Acting on a brownian probe : from optical forces to optimal thermodynamic protocols

Yoseline Rosales Cabara

UNIVERSITÉ DE STRASBOURG

ÉCOLE DOCTORALE ED222

UMR 7006

THÈSE présentée par :

Yoseline ROSALES CABARA

soutenue le : 9 **Juillet 2020**

pour obtenir le grade de : **Docteur de l'université de Strasbourg**

Discipline/ Spécialité : Physique

Acting on a Brownian probe : from optical forces to optimal thermodynamic protocols

Agir sur une sonde Brownienne : des forces optiques aux protocoles thermodynamiques optimaux

THÈSE dirigée par :

M. GENET Cyriaque — Dr., ISIS, Université de Strasbourg, CNRS

RAPPORTEURS :

M. REYNAUD Serge — Dr., Laboratoire Kastler-Brossel, Sorbonne Université, CNRS

M. WENGER Jérôme — Dr., Institut Fresnel, Aix-Marseille Université, CNRS

AUTRES MEMBRES DU JURY :

M. MANFREDI Giovanni — Dr., IPCMS, Université de Strasbourg, CNRS

In the loving memory of
my grandparents, Elia and César

Acknowledgements

The past few years as a Ph.D. candidate has been a time of incredible growth, and I would like to express my deepest gratitude for those who have accompanied me and helped me along the way.

I would like to acknowledge my reviewers, Prof. Serge Reynaud and Prof. Jérôme Wenger for their time, their interest on the manuscript and especially their valuable insights on my work, as well as Prof. Giovanni Manfredi accepting to be the president of the jury and for guiding so warmly the Ph.D. defence.

I do not have enough words to express how grateful I am to my supervisor, Cyriaque Genet, for giving me the opportunity to be part of such prestigious group and learn from so many brilliant people, thanks to him I could contribute my bit to his great ideas and managed to take this important step. I will always be thankful for everything he taught me with such enthusiasm. I was lucky to have a supervisor that is so dedicated to his students, offering unique guidance and support. His vision and passion will always be a source of inspiration.

I would like to warmly thank Prof. Thomas Ebbesen for welcoming in his group, for his friendliness and great leadership, and for encouraging me to pursue anything without limits.

Thank you both for your support and for believing in me more than I did myself.

Special thanks to Eloise Devaux and James Hutchinson, for their kindness and for setting such a nice work environment and making everyone feel as a very special part of the group.

I am very grateful to my collaborators, Prof. Giovanni Manfredi, as his work, together with Prof. Paul-Antoine Hervieux and Prof. Laurent Mertz made me discover the very exciting field of stochastic thermodynamics, which cascaded into so many new ideas. I would like to thank Lisa Poulikakos and Prof. David Norris for their expertise and time, their contribution was essential for me to learn about chiral light-matter interactions, as well as Antoine Canaguier-Durand and Hugo Wendehenne for their works on force metrology.

I owe a great deal to Gabriel Schnoering, who had the patience to share with me a bit of his endless knowledge from the start to the end and whose tenacious work has made possible so many results, without him I would not have what to write. I would like to thank him for all his time, support and very fast responses despite the distance.

I am also indebted to the new "trappists", Samuel Albert, Rémi Goerlich and Minghao Li, who taught me more than I could teach them. I am very happy to have shared

precious moments with such extraordinary people as the former and current members of the Laboratoire des Nanostructures. The wholesome coffee breaks with Jérôme and Bianca, the thoughtful discussions with Anoop, Stefano and Thibault, Robrecht's delicious chocolate mousse, the sport sessions with Gian-Lorenzo, Oussama and Marcus. I have to thank Kuidong, Yantao, Kripa, Daichi and Kalai for always gifting me with a beautiful smile, as well as Xiaolan, Hadi, Jino, Yaowei and Atef.

I would like to thank the other ISIS members that I had the chance to make good friendships, as well as my friends from Strasbourg and elsewhere. I am very grateful to the Zambrini-Cruzeiro family, Ana Bela, Jean-Claude and Emmanuel, for their contagious passion for science and their affection.

I would like to thank the Initiative d'Excellence (IDEX) program for the economic support. I am also indebted to Marie-Claude Jouaiti for her very efficient help and advice with the administrative documents. In this context, I would also like to thank the administrative and technical staff of ISIS, Muriel, Thierry, Jean-Louis, Fabien, Fabienne and Philip, for their and kindness and for saving many scientists in distress.

I would like to thank my parents, Jacqueline and Fernando, for their love and support that stood by me at any cost, as well as the rest of my big family, who have been very close to me despite the distance, their good vibes crossed the entire atlantic and filled me with joy and force every day of my studies.

Last but not least, I wish to thank my boyfriend Marco, for his constant positive attitude and patience, for the daily smile he manages to bring out of me no matter the situation, and his family, who have always made me feel like one of them.

Contents

1 Introduction
Thermal fluctuations at small scales

The separation of scales, such as in energy, time, or sizes, has enabled physicists to establish models that accurately describe and predict the behaviour of natural processes. The deep insight provided by powerful models for many different systems stem from treating the different levels of description as independent of each other. Yet, an important aspect of science is to achieve unified frameworks capable of describing processes not from the viewpoint of scale division but from interconnected theories through which it is possible to move across the limits. One of such theories is statistical mechanics, which successfully yielded thermodynamic results observed in macroscopic systems without ignoring the evolution of the microscopic, complex, degrees of freedom [1, 2]. Statistical physics conveys the powerful message that it is not necessary to know the specific state of each atom, molecule or organism that forms a system, in order to be able to provide, at a collective level, the inexorable rules obeyed by the ensemble. The study of gases is paradigmatic since it offers a clear illustration of how the description of its properties is more easily accessible by statistical inference than by solving the full set of equations of motion of the constituent particles.

Statistical physics was enriched at an even deeper level when physicists began to realize that fluctuation themselves can provide valuable tools to understand diverse nonequilibrium processes [3–5]. Despite the great progress that we have witnessed over the past few decades on the understanding of a variety of out-of-equilibrium systems, there is still no general teatrise. As Kubo pointed out, *"the concept of non equilibrium is perhaps too broad to be unified by a few principles"* [6]. Most of the processes occurring in nature happen out-of-equilibrium [7, 8], and being out-of-equilibrium causes the breakdown of a fundamental symmetry: the time invariance of the evolution equations. Such asymmetry manifests itself as dissipation of energy and, according to the second law of thermodynamics, dissipative processes are characterised by entropy production. Many paradoxes have nourished the debate concerning the interpretation of the second law and on how irreversibility arises from a system composed of microscopic degrees of freedom that obey time-reversible equations of motion [9, 10]. Nowadays, the statistical nature of the second law has not only been verified experimentally [11], but it has too a well-defined theoretical support which came from the development of a relatively new framework, known as the Fluctuation Theorems (FT) [12–15], which will be discussed in more detail in Chapter 4.

The first relation between fluctuations and dissipation was provided by Einstein's

analysis of Brownian motion in one of his notorious articles published in 1905 [16–18]. Brownian motion represents the incessant erratic motion observed on a mesoscopic object suspended in a fluid, named after the botanist Robert Brown who was the first to study the phenomenon systematically, in 1827 looking at grains of pollen suspended on water [19]. On Brownian motion, Einstein demonstrated the relation between the ensemble average of velocity time correlations and the diffusion coefficient directly related to the viscous drag through the temperature [6]. Such a relation is known as the Fluctuation-Dissipation Theorem (FDT), and links the averages of the time correlations of fluctuating quantities to macroscopic observables [3, 6]. It was then established as a general approach to treat any system slightly away from equilibrium after the works of Nyquist, Onsager, Kubo and others [5, 19, 20].

Experimentally, Einstein's results have been fully verified by the diligent experimental works of Jean Perrin in 1907 that ended a long lasting debate between the atomistic and the equivalentist hypothesis in favor of the former [18]. Since then, Brownian motion has established itself as a key concept in statistical physics mainly by its ability to probe the complexity of interacting individual microscopic objects and reveal predictable thermodynamic behaviours at the macroscopic level.

Among the many formulations of Brownian motion, the Langevin equation is probably the most privileged and convenient in an experimental context. The first central hypothesis of Langevin's approach is a very sharp separation of the time scales between the fast molecular degrees of freedom and the relatively slow degrees of freedom of the particle (the d.o.f. accessible by the observer) [21, 22]. The second hypothesis uses the central limit theorem, by modeling the transfer of momentum between the particle and the numerous and random molecular impacts of the fluid as a Gaussian random process [21]. With these features, the Langevin equation describes the Brownian dynamics as a balance of forces, composed by an inertial term, a viscous term, due to the friction of the particle with the fluid, and a stochastic term, known as the thermal force, from which stems the erratic character of the motion.

As the first stochastic differential equation, the Langevin equation is considered to be at the origin of stochastic calculus [19, 20]. Nowadays, stochastic calculus represents an important branch of physics and mathematics, and has broad impact in the different disciplines, well beyond the natural sciences [23]. Whether applied for stock market fluctuations or population dynamics, the tools provided by stochastic calculus have succeeded in understanding many aspects of complex systems where intuition is hard to build considering the too large number of intervening factors and degrees of freedom. An interesting example is given by the applications in epidemiology, where stochastic models assess the dynamics of the spread of infectious diseases, providing insights of the key factors that allow to evaluate the results of different containment strategies [24].

In physics, the study of Brownian dynamics has recently been enriched by a powerful experimental technique: optical tweezers [14, 25, 26]. This technique consists

in optically trapping unique Brownian objects in well controlled environments, and it gives direct access to their stochastic evolutions. Remarkably, optical trapping experiments are usually well described using the Langevin approach because the experimental control available on an optical trap allows one to induce, shape, modulate, etc, the different terms forming the Langevin equation: an interaction potential, additional external force fields (of conservative or non-conservative nature), a control on temperature and viscosity. Overall, optical traps, through the possibility to induce tailored and well controled optical forces, have allowed the study of Brownian systems from totally new perspectives.

The experimental contributions of optical trapping experiments together with the theoretical approach of Langevin equation have led to the emergence of a new field: Stochastic Thermodynamics [14, 27], a rich approach to describe fluctuating nonequilibrium phenomena, whose results had a strong impact in many applications, going from explanation of metabolic processes in living systems [7] to quantum field theories [28].

Stochastic thermodynamics encompasses every aspect of small systems in nonequilibrium situations, such as colloids, biopolymers such as RNA and DNA, proteins, enzymes and molecular motors [14]. Such small biosystems execute essential tasks in our organism, for example gene transcription by the formation of small loops in DNA molecules [7, 29], or serotonin release that regulates our anxiety is carried out through the intervention of molecular motors such as the kinesin family [30]. Single-molecule biophysics was revolutionized by the advent of optical tweezers and other micromanipulation and imaging techniques [31], the most notable findings concerned the characterization of the mechanical properties of DNA such as the stretching [32] and torsional effects [33], and also the dynamics of motor proteins [34]. Stochastic thermodynamics has made it possible to study in depth the role of fluctuations in such systems, and provided the tools to access to information such as the free-energy landscapes of biomolecules or the efficiencies of such molecular motors. With relevant energy scales, of the order of k_BT, and fluctuations of the same magnitude, such systems are extremely sensitive to and actually driven by thermal fluctuations. For example, molecular motors use chemical energies from the hydrolysis of ATP to rectify thermal fluctuations or extract useful energy from the bath [35]. As a consequence molecular motors can occasionally operate in reverse and reach efficiencies as high as 60% [7].

At such small scales, the ability to rectify thermal fluctuations is one fundamental feature for the operating principle of microscopic engines [36]. This is clearly seen in the operation of biological molecular motors [7, 35]. Such systems live in environments where fluctuations dominate the average behaviour. Fluctuations experienced by these molecules are an integral part of their mechanism [14]. The efficiencies of molecular machines, in terms of energy consumed versus useful work, are above any macroscopic

counterpart. Thanks to the fluctuating environment such motors sometimes work backwards, by absorbing a few k_BT of energy from the environment rather than dissipating it.

The idea of converting thermal fluctuations into useful work dates back to Feynman's ratchet [37], conceived as a mechanism capable of rectifying thermal fluctuations under non-homogeneous external conditions [36, 38, 39]. Recently a Feynman ratchet was setup experimentally by means of optical tweezers [40].

In small stochastic systems, one can distinguish between three types of out-of-equilibrium situations. First, one can prepare the system in an initial state of non-equilibrium and study its relaxation towards equilibrium. Second, one can disturb the system by external time-dependent forces, fields, fluxes, or unbalanced chemical reactions. Third, if the external disturbance does not depend on time (or is periodic), the system can reach a nonequilibrium steady state (NESS). For all these situations, there are rigorous theoretical results [7, 14, 26]. In all cases, even in nonequilibrium situations, the temperature of the medium is well defined [14]. This property, together with the existence of a separation of time scales between the degrees of freedom of the observables and the degrees of freedom associated with the thermal bath allow a consistent thermodynamic description.

In an article published in 1998, Ken Sekimoto showed how the Langevin equation can be endowed with a thermodynamic interpretation [41]. As a consequence, thermodynamic quantities, such as heat, work and internal energy, as well as the first law of thermodynamics can be defined at the level of single stochastic trajectories of a Brownian object, therefore such quantities become fluctuating themselves and follow specific statistical laws. Later, it was proposed that quantities such as entropy become fluctuating [15] and then demonstrated that entropy can be also defined at the level of single stochastic trajectories [42]. These where the building blocks used for the foundation of the field of Stochastic thermodynamics, whose pillars are the Fluctuation Theorems [12, 13, 15]. These relations shed new light on the principles governing fluctuations in such thermodynamic quantities [7, 8, 14, 26, 43]. It should be noted that this framework goes beyond linear or quasi-equilibrium response conditions, and can be applied to a large number of systems disturbed by non-conservative forces through arbitrarily time-dependent protocols [44], even in the case of feedback control [45, 46]. Formally, the generality of the fluctuation theorems can be attributed to the way in which the probability distributions of certain observables behave in the presence of forces that break some dynamic symmetry, for example, non-conservative and or time-dependent forces [15, 47].

Because all such experiments require extreme control of the environments, external parameters and external force fields applied, optical tweezers are privileged tools in this context. They have not only been instrumental for the investigation of biological systems [31], they also constitute reliable and flexible tools for measuring weak forces in

different environments. Through the thermal position fluctuations of the particle one can indeed measure small displacements and perform 3D mapping of nonconservative force fields [48]. The accuracy level offered in this type of experiments have made it possible to measure the instantaneous velocity of a Brownian particle in rarefied gases and verify the Maxwell-Boltzmann velocity distribution [49, 50], an experiment that Einstein thought impossible [16, 17]. Such experiments paved the way for developing methods that gave access to the quantum ground state of mechanical motion [51]. The high precision reached on levitated nano-objects through the techniques of optical trapping and laser cooling [52] has enabled the possibility to map the vectorial nature of the optomechanical interaction [53] and the strong coupling between mechanical modes of a trapped oscillator [54].

The following paragraphs discuss some experimental milestones in the recent research field of stochastic thermodynamics of small systems, all studies performed with diverse optical trapping configurations. Of course, we do not intend to provide here an exhaustive review but rather to discuss the ideas conveyed in some of the selected experiments.

Experimental observations of information to energy conversion

The second law of thermodynamics states that in order to decrease the entropy of a system, a reservoir must "pay" for that decrease and must have therefore its own entropy increasing. This, for example, precludes infinite production of energy or work. There have been countless debates on the interpretation of this law. In 1948, after Claude Shannon defined the information entropy, *information*, became a real physical quantity with a unit [55]. Thus, as a physical quantity, *information* should be subjected to physical laws, in particular thermodynamic ones [56–58]. This approach turned the question whether is it possible to extract mechanical work from the information of the state of the system [59]. Debates on the role of information in thermodynamics actually started in the early days of the establishment of thermodynamic laws, when Maxwell devised a simple and ingenious *gedankenexperiment*, to illustrate a hypothetical violation of the second law. The idea consisted in considering a vessel made of two compartments of equal volume and adiabatic walls. The two partitions were occupied by the same gas of same temperature, given by the mean velocity of the molecules. The wall separating the two compartments contained a molecule-sized window that opens and closes in a controlled way by an intelligent being, dubbed the Maxwell's dæmon by Lord Kelvin [26, 60]. Depending on the velocity of the molecule that reaches the window, the dæmon decides whether to open the window or not, thus separating the fast molecules from the slow ones in the different compartments, managing to raise the temperature of one side and lowering the temperature of the other.

Later, in 1929, Leó Szilárd simplified Maxwell's thought experiment by changing the working substance from a gas to a single particle. The volume V containing the particle is divided in two partitions of equal volume at a certain instant, at which the dæmon intervenes, measuring the position of the particle. Such system has two possible outcomes, either the particle is on the left or in the right [60]. As the dæmon knows where the particle is located, he uses this information to exchange the partition wall with a piston and then leaves the one-particle gas perform an isothermal expansion going back to the initial volume, in this way the Szilárd engine is capable of extracting a work [61]:

$$W = \int_{V/2}^{V} p dV = \mathrm{k_B T} \int_{V/2}^{V} \frac{dV}{V} = \mathrm{k_B T} \ln 2$$

cyclically. After the process, according to the first law, the reservoir has given an amount $Q = W$ decreasing its entropy by an amount $\Delta S = \mathrm{k_B} \ln 2$ and thus violating the second law. Szilárd concluded that a measurement must then be associated with a certain entropy production which balances such entropy decrease. At the time, this hypothesis was criticized with the argument that entropy was a measurable quantity and does not depend on the information that the observer has on the system [57, 58].

In 1961, Rolf Landauer, proposed that in a computer there are specific degrees of freedom in charge of encoding logical states and that such logical states evolve irreversibly. A logical operation is accompanied by entropy increase in the other degrees of freedom and in the environment [56]. In particular, he showed, that the erasure of a bit of information requires at least an amount, $\mathrm{k_B T} \ln 2$ of work which is dissipated into the environment [26, 62]. Using this argument, Charles Bennett solved the apparent violation of the second law in a Szilárd's engine. Since there are two possible locations for the particle, left or right, the dæmon is equivalent to a one-bit memory system, which at each cycle has to be reset [63, 64]. According to Landauer's principle, the cost of memory erasure of the dæmon is $W_{erasure} \geq \mathrm{k_B T} \ln 2$, which is the work one has to inject, and therefore the work extracted by the engine is actually $W - W_{erasure} \geq 0$, and thus the second law is not violated.

For the reasons summarized above, it is not surprising that the first experimental demonstration employing feedback as Maxwell's dæmon to convert information into energy was performed on an optically trapped Brownian particle [65]. The particle was placed in an staircase-like potential, as the one on the left panel of Fig. 1.1 made with an electric field gradient. The height of the steps were set to ca. 1 $\mathrm{k_B T}$. Due to thermal fluctuations the particle makes jumps between the steps stochastically, however due to the nature of the staircase, downward jumps are more frequent than upward, thus in average, the particle falls down the stairs. The feedback protocol consisted in measuring the particle's position, and when this latter performs an upward jump, a block emulated by an electric field, is placed to prevent a subsequent downward jump from that point. Repeating this protocol a certain number of times, and assuming that the block is placed reversibly, the particle was able to climb up the stairs and gain free

energy.

A similar feedback protocol was used to make a Brownian particle move against a fluid flow without the use of an external force [66] and studied the role of the frequency of measurements on the work extracted and the information gain. The colloidal particle was trapped in a channel filled with a flowing fluid, as shown in the right panel of figure 1.1, the feedback loop consisted in moving a wall of light upstream towards the particle whenever the particle was observed to move stochastically in the opposite direction of the fluid flow.

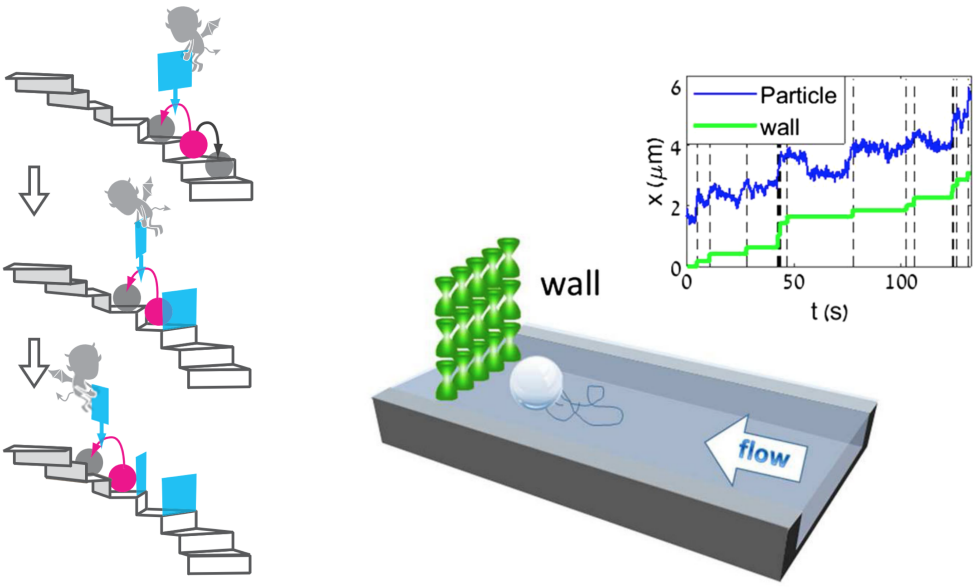

FIGURE 1.1: Experimental realizations of Szilárd engines with an optically trapped colloidal particle. Left panel: Maxwell's dæmon feedback protocol to achieve the Brownian particle to climb up the staircase. Right panel: Stochastic motion of the Brownian particle moving upstream along with the barrier implemented with the feedback protocol. Figures adapted from refs. [65, 66].

No long after the first experimental realization of a Szilárd engine [65], an optically trapped Brownian particle was also used to experimentally test the Landauer's principle [62]. The erasure of one-bit memory was emulated by the particle in a bistable potential whose barrier could be modulated, see left panel on fig. 1.2. The erasure cycle starts with the particle in state 1, which is considered when the particle is in the left well, then the barrier is lowered during 1s and kept low for a duration, τ, in which an external force is applied to move the particle to the right well, then the cycle is closed by raising the height of barrier and removing the external force. The dissipated heat is measured for a cycle and on average from many repetitions of the protocol. The average dissipated heat as a function of the transfer duration from one well to the other is shown in the right panel of figure 1.2 below. The Landauer's bound is attained for transfers performed quasistatically.

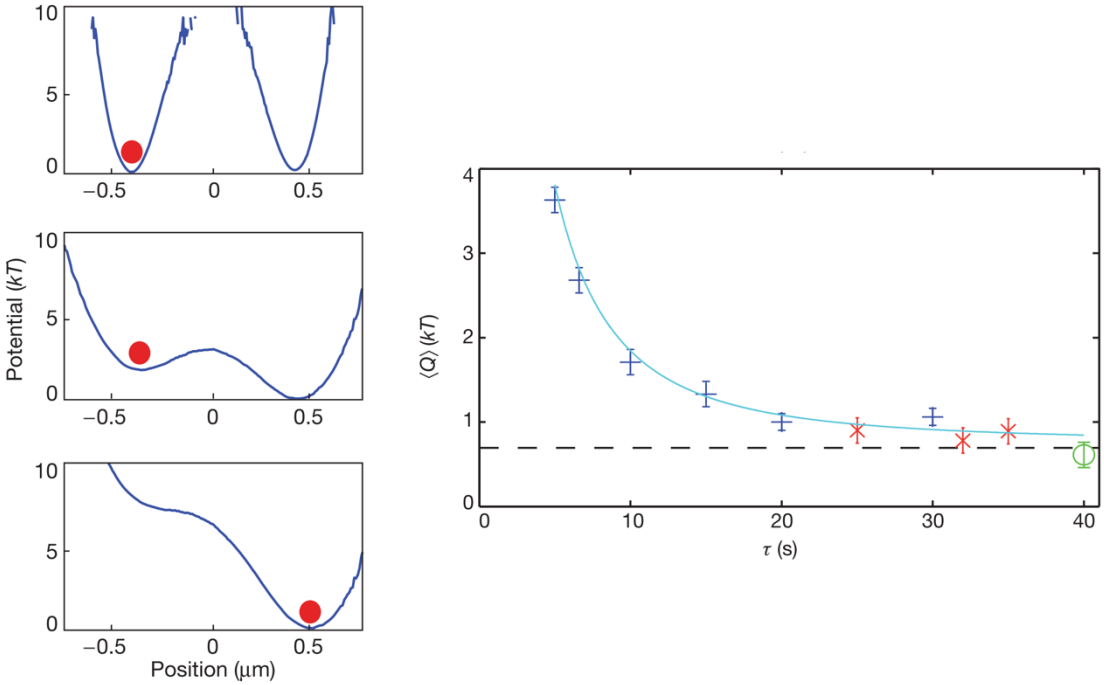

FIGURE 1.2: Experimental verification of Landauer's principle. Left panel: Different stages of the erasure cycle. Right panel: Mean dissipated heat for an erasure cycle as a function of transfer duration, τ. The dashed line represents Landauer's bound. Figures reproduced from ref. [62].

Thermal engines in a regime where fluctuations dominate the average behaviour

At the macroscale, the laws of thermodynamics impose important limitations for the operation of thermal engines. Let us consider, in a very simplified way, the operation of a combustion engine in a car. A spark causes the explosion of a given quantity of fuel, producing a lot of energy in the form of heat. Part of the thermal energy is transferred to the engine's pistons, which effectuate a cycle, allowing the complex gear system to start the car moving. But inevitably, part of the heat absorbed to do work is transferred to the environment, which has a temperature much lower than that of the gases used for the combustion [67]. A direct implication of the second law, just the way Carnot expressed it, is that no engine can perform optimally, defining the efficiency as the fraction of heat absorbed that is used to perform work. Unfailingly, a part of that heat is released to a colder reservoir, and consequently the efficiency of any cyclical process in a thermal machine is always less than 100%. In fact, Carnot found that there is an optimal cyclic process for an engine that operates between two different thermal reservoirs at different temperatures, such that no real engine can have a greater efficiency than that of a thermal machine operating under this cycle, called the Carnot cycle. This process consists of an isothermal expansion of the gas followed by

an adiabatic expansion and then a closing of the cycle with an isothermal compression followed by a adiabatic compression [68].

The prototypical simplicity of a Brownian particle in an optical trap makes it an ideal test tool for implementing thermodynamic cycles and explore necessary aspects involved in artificial micrometer sized heat engines, since these are not simply the miniaturized version of the well known macroscopic heat engines [69] of the early days of thermodynamics. At small scales, it is not straightforward to put a Brownian system in contact with two reservoirs at different temperatures in order to extract work, however a Brownian particle moving in an asymmetric can serve as an isothermal motor, as in the case of ratchets [36].

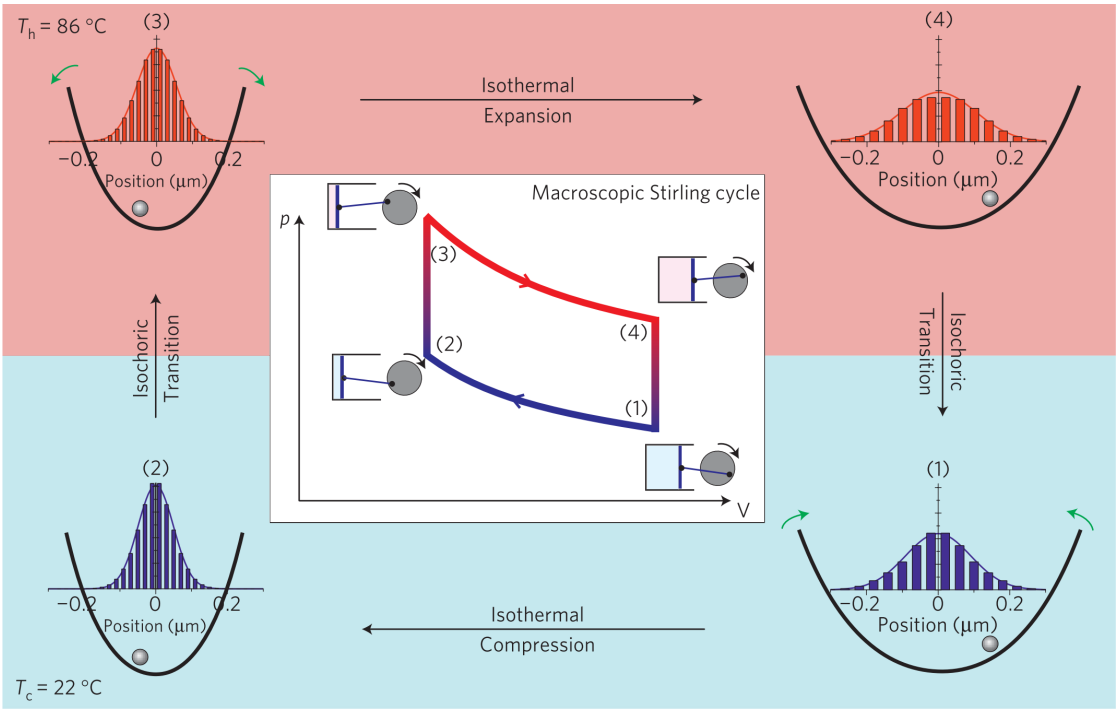

FIGURE 1.3: Stirling cycle at the microscale: (1) → (2) Isothermal increase of the stiffness of the optical trapping potential (isothermal compression). (2) → (3) Instantaneous temperature increase at fixed optical potential (isochoric process). (3) → (4) Isothermal decrease of trap stiffness (isothermal expansion) (4) → (1) Instantaneous temperature decrease at fixed optical potential (isochoric process). The histograms show the measured particle probability distributions of the corresponding stationary states. Inset: Stirling process in the pressure-volume diagram representation, where the enclosed area amounts to the work extracted by the machine. Reproduced from ref. [69]

A non-isothermal microscopic heat engine was realized by Blickle and Bechinger [70]. The engine consists on a single Brownian particle confined in a optical potential whose stiffness is time dependent. The tempperature of the surrounding fluid was "instantly" changed at the different stages of the thermodynamic cycle, yielding isochoric transformations. This was achieved by means of a second laser with a wavelength

matching the absorption peak of water and a temperature sensitive dye. In this way, they were capable of raising the temperature from 22°C to 90°C in less than 10 ms. With the control of the stiffness of the trapping potential and the temperature of the bath, the trapped Brownian particle was able to recreate a microscopic version of the Stirling cycle as shown in fig. 1.3 above. An engine capable of extracting about $20k_BT$ from the heat bath.

Instead of abrupt changes of temperature at a give stiffness of the trap, Martinez *et al.* used an external source of electrostatic noise in order to control the kinetic temperature of the trapped Brownian particle [71] devised a way to mimic the effects of a thermal bath on a trapped Brownian particle. With the simultaneous control of the effective temperature and the trap stiffness, they were able to realize adiabatic transitions within a cycle [36, 72], paving the way for a miniaturized realization of a Carnot engine, with the Brownian particle as the working substance [73]. As expected, in an environment dominated by thermal fluctuations, they observed that the fundamental Carnot limit for the efficiency can be exceeded.

Today there is an increasing number of proposals and prototypes for artificial engines at the micro and nanoscale, in all kind of environments [74, 75]. Thanks to the progress of nanoscience and the tools of manipulation in biology, hybrid systems combining biological and artificial systems are starting to become a reality, for example transistors made by combining proteins, nanoparticles and quantum dots [76].

It is not yet clear how biological molecular machines are optimized, however for the artificial small engines it is still a challenge. There are numerous novel theoretical studies for the optimization of nonequilibrium processes at the mesoscale [44, 77–80], especially concerning the trade-off between power fluctuations and efficiency [81, 82]. With all this progress on stochastic control and optimization, it is perhaps not absurd to consider the feasibility of artificial heat engines that could potentially outperform molecular motors.

1.1 Thesis outline

In this thesis we act on a Brownian probe with conservative and nonconservative optical force fields that can be integrated and modulated by means of a versatile optical trapping setup. As discussed throughout this introduction, such system has an experimental relevance for its flexibility and good control at the micro and nanoscales and the tractability of its theoretical model which is very advantageous to offer when proposing simple methods to explore fundamental notions of forces and energetics.

The framework of the Langevin equation forms the backbone of this thesis, as it offers the possibility to study the effects of manipulating each of its terms independently. By means of our optical trapping setup we are able to control the external force term and the potential term, the first with the purpose of constructing a force microscope that would be capable of measuring chiral forces at the nanoscale and the latter for performing optimal transformations between thermal equilibrium states. With this introduction, the manuscript is structured in six chapters, which are outlined in the following paragraphs.

- **Chapter 2** is dedicated to the physics of optical trapping and the description of our experimental setup. The chapter starts with a brief historical introduction on light forces and takes a retrospective look on the early days of optical trapping. Then presents a more rigorous description of the optical forces involved in the trapping mechanism. An alternative configuration of the standard single-beam trapping method is presented, such modification consists in focusing the trapping laser in front of a reflective surface, creating a standing wave pattern and is advantageous for the stable trapping of metallic nanoparticles. We detail the different components of the experimental setup such as the detection methods, how we follow the dynamics of the trapped bead in real time and the interferometric imaging system, essential for discriminating single objects from aggregates. As in our laboratory we are particularly interested in the influence of chirality in light-matter interactions, we have tested the capacity of our set-up to trap chiral nanoparticles as a first step towards the selective manipulation of chiral nano-objects. Such particles are metallic and of non-spherical, we explain the essential considerations for trapping such objects and characterize their dynamics. We then implement an enantiomeric recognition method based on polarimetry that allows us to recognize which enantiomeric form of the chiral nano-object is in the trap. This study has been published in ref. [83].

- **Chapter 3** explores the potential of the standing wave optical trap as a high resolution force microscope in presence of thermal noise. Stably trapped single metallic nanoparticles are used as highly sensitive probes for external radiation pressure exerted by an additional laser. This second beam acts independently of the trapping dynamics and is modulated sinusoidally in such a way that the force can be detected at the frequency of modulation. Potential temperature elevation issues are carefully assessed to validate the metallic nanoparticles as optimal

probes. Two detection methods are investigated for extracting the smallest measurable force and then compared in terms of force and position resolution. The fundamental aspects of a force measurement at the thermal limit are exposed, emphasizing how the the measurement bandwidth is constrained by the global stability of the setup. The work covered in this chapter has been published in ref. [84].

- **Chapter 4** deals with transformations between equilibrium states of a Brownian particle trapped in a potential under compression and expansion, evaluating the system from the perspective of stochastic thermodynamics. The chapter begins with an analogy between the trapped Brownian particle and the concept of the ideal gas in a piston. Then we explain the experimental and analytical methods to obtain the thermodynamic quantities at the level of single trajectories and at the level of the ensemble. Two transformation protocols and their time-reversed counterparts are studied with the tools of stochastic energetics and fluctuation theorems, which gives the notions necessary for the experiments studied in Chapter 5.

- **Chapter 5** studies the control of transformations of our Brownian system, designing theoretically a strategy for optimising the dissipation and the transfer duration on an equal footing, unveiling a universal time-energy bound that can only be reached under optimal control conditions, such strategy is implemented experimentally with different parameters to construct and verify such universality curve. The chapter starts by explaining the notion of relaxation time and proceeds walks through the optimisation methodology. We situate our results with previous works concerned with acceleration of transitions between states and optimization of the energetic cost. We will discuss how optimisation problems are currently a major concern in the field of stochastic thermodynamics, especially in the context of nano-engines that we have briefly mentioned above. These efforts have been published in ref. [85].

- **Chapter 6** concludes the thesis by putting some of the results presented in the manuscript into perspectives with respect to the current trends in the field of stochastic energetics.

2 Standing wave optical trap and chiral metallic nanostructures

2.1 Mechanical light-matter interactions

Since Kepler who suggested in the seventeenth century that comet tails were pushed by sun emanations away from it, light has been suspected to exert mechanical forces on material objects. More than two centuries later, Maxwell, developing the electromagnetic theory [86], formalized the concept of light radiation pressure. By showing that light carries linear momentum, Maxwell simply explained radiation pressure by a transfer of momentum $\Delta\mathbf{p} = \mathbf{p}_{\text{incident}} - \mathbf{p}_{\text{reflected}}$ between an illuminating beam of light and a reflecting surface of given area S. Characterizing the surface by a reflectivity R and an absorption A (assuming thus that $1 - T = R + A$) illuminated at normal incidence, the time average momentum transfer writes as

$$\langle \frac{\Delta\mathbf{p}}{\Delta t} \rangle_T = (2R + A) \times S\frac{I}{c}, \tag{2.1}$$

where I is the irradiance of the light beam, in [Wm^{-2}] units. A pictorial view of the process is shown in Fig. 2.1, for the case of a semi-reflecting surface.

The irradiance of the sun on earth's outer atmosphere is ca. 1100 [Wm^{-2}]. Equation 2.1 leads to an exerted solar radiation pressure of $\sim 4\,\mu$Pa, which compared to the atmospheric pressure, is more than ten orders of magnitude smaller. This point naturally led the first experimentalists decided to test and measure radiation pressures to do so by applying a radiant flux as high as possible on the smallest possible area.

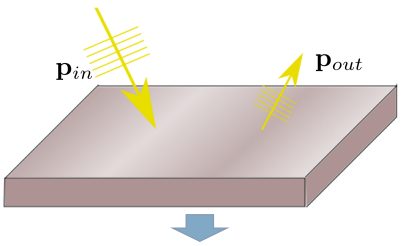

FIGURE 2.1: Conceptual illustration of the change of momentum $\Delta\mathbf{p} = \mathbf{p}_{in} - \mathbf{p}_{out}$ of a plane wave impinging on a surface resulting in mechanical displacement.

The first experimental observations of such forces were performed by P.N. Lebedev in tour-de-force experiment (published in 1901 [87]) where he measured, using reflecting winglets suspended on torsional balances radiation pressure forces down to 3×10^{-10} N with a precision better than 6%. These experiments were followed by the ones of Nichols and Hull [88], who like Lebedev, ended up being limited by thermal perturbations induced on the measurement system by the illuminating light beam,

such as convective and radiometric effects. This is probably why these outstanding experiments remained for a long time practically the only ones that managed to observe light induced forces, until Arthur Ashkin revived the idea of observing the mechanical interaction of light with small objects by using focalized lasers with which very high irradiance of very small area (diffraction limited focal spots) can be reached.

The birth of optical manipulation

Ashkins' successful attempts took place when using transparent microspheres suspended in water [89]. Resorting to transparent microspheres through which light absorption is reduced was the solution proposed by Ashkin to minimize the radiometric force. Such issues remain indeed problematic in experiments involving lasers. Shinning an intense laser on a particle inevitably heats the surrounding fluid, and thereby inevitably induces photophoretic forces that can become several orders of magnitude stronger than radiation pressure.

These experiments led, after more than 15 years, to the observation of additional transverse forces guiding the particles towards the beam waist [25, 90]. Such forces, coined as *gradient forces*, arise from the strong electric field gradients that can be created near the focus of a laser beam. Achieving very stable trapping through such gradient forces generated with a single laser beam by using high NA immersion microscope objectives led to considerably increasing the trapping potentialities of Ashkin's experiments that became capable of operating in the Rayleigh size regime. This in particular paved the way to atom trapping and cooling experiments.

Operating mainly with such gradient force effects, so-called optical tweezers developped into powerful noninvasive tools in the fields of biology and physics. During the last three decades, their performance has constantly improved with the aim of manipulating small objects such as nanoparticles and bio-molecules. As discussed in Chapters 4 and 5, they appeared as ideal tools for testing non-equilibrium statistical physics with a great variety of stochastic protocols that can be implemented [7].

In order to describe the forces at play in an optical tweezer, Ashkin elaborated a simple ray-optics explanation, looking at momentum exchanges between the trapping laser beam and the particle [90]. This point of view is illustrated in figure 2.2. For a refractive index of the particle, n_p, larger than the refractive index of the surrounding medium, n_m, as would be the case of a polystyrene bead ($n_p = 1.59$) immersed in water ($n_m = 1.33$), the particle can be considered as a small lens and the beam as formed by rays that travel with well defined directions perpendicular to the wavefronts. As rays enter the particle, a portion gets reflected and the remaining refracted. In figure 2.2, we see two incoming rays of wave vectors $k_{i,1}$ and $k_{i,2}$ refracted by a bead situated at a certain distance from the laser focal point, refracted again with new wave vectors $k_{f,1}$,$k_{f,2}$ as they exit the particle's volume. This directional change of rays' momenta gives rise to a force following light momentum conservation. Physically, this force acts on the bead to

restore axial and transverse displacements from the trapping focus. Such force has two components, one acting in the direction of propagation, which is the scattering force, and one normal to the direction of propagation, which corresponds the gradient force.

As radiation pressure tends to push the particles along the direction of propagation, the electric field gradient confines the particle near the focus of the beam, giving the possibility to trap and manipulate objects. To enhance the latter effect and enable stable three dimensional trapping of high refractive index particles, Ashkin implemented a two counter-propagating beams configuration. In this arrangement, radiation pressure from both beams would be compensated, stabilising the particle axially while being confined laterally by the gradient force. We will describe below our standing wave trap that shares some aspects with counter-propagating trapping beam confugurations.

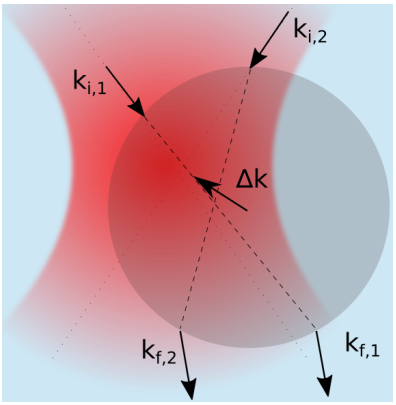

FIGURE 2.2: Qualitative view of the momentum exchanges taking place in an optical trap in the regime of geometric optics.

2.2 Optical forces in the dipolar approximation

Ashkin's model is set within the regime of geometric optics where the particle diameter is assumed to be much larger than the wavelength of the trapping laser (at least 10λ). Even in this regime, this simple model however fails to account for important effects that are well observed experimentally, such as multipolar resonance effects. More rigourous approaches are available, such as Lorenz-Mie theoretical description of the interaction between the large particle and the laser trapping beam [91]. In this context, an important body of work has been carried out using different calculation strategies, and numerical and computational methods. For example, a representation for the forces on a dielectric particle has been derived by considering an explicit series of partial waves [92]. Ganic and colleagues presented exact calculations based on a vectorial theory of diffraction [93]. The group lead by Helena Rubinsztein-Dunlop developed computational tools using the generalized Lorentz-Mie theory and the T-matrix [94] permitting even to calculate forces on non-spherical particles[95].

Although theoretical calculations of high precision can be obtained, it is important to keep in mind that the experiments are far from the idealized configurations assumed in theoretical work. Many effects are intertwined experimentally within the force signals, such as thermo-hydrodynamic coupling effects, local heterogeneities within the fluidic cell, electrostatic influence of charge stabilization of the colloidal assemblies, etc., all making difficult a high-precision level comparison between theory and experiment. This explains why, in practice, we have rather looked for an apposite framework

within which our experiments can be physically interpreted.

This framework corresponds to the Rayleigh regime where the size of the particle is taken sufficiently small ($D \ll \lambda$) so that the electric field can be considered homogeneous over the full volume of the particle. In such a case, the particle is described by a dipole (or an ensemble of dipoles enclosed within the volume V of the particle [96, 97]) induced by the illuminating electromagnetic field, neglecting in the case of a not too strong field, higher multipolar terms.

Harada and Asakura showed, in the paraxial approximation, that this approach is very precise for cases where the radius of the particle is less than $\lambda/20$ [96]. Depsite this, and very interestingly in the context of optical trapping, they demonstrated that the Rayleigh regime can extend its range of validity with respect to the gradient force term, until the size of the particle reaches a size comparable (yet smaller) to the trapping laser beam waist.

Dealing with an homogeneous electromagnetic field inside the volume of the particle, the complex dipolar moment associated with the particle can be written as $\mathbf{p} = \mathbf{p}_0 e^{-i\omega t}$. It is related to the complex harmonic electric field of frequency ω through the complex polarizability[1] $\alpha(\omega)$ and the real refractive index $n(\omega)$, $\mathbf{p}_0(\mathbf{r}) = n^2 \alpha \mathbf{E}_0$.

Considering monochromatic fields of angular frequency ω, such as the lasers employed in trapping experiments, $\mathcal{E}(\mathbf{r}, t) = \mathbb{R}\mathrm{e}\{\mathbf{E}_0(\mathbf{r}) e^{-i\omega t}\}$, $\mathcal{H}(\mathbf{r}, t) = \mathbb{R}\mathrm{e}\{\mathbf{H}_0(\mathbf{r}) e^{-i\omega t}\}$, the instantaneous force exerted on the electric dipole is given by the Lorentz law [99]:

$$\mathbf{F} = (\mathcal{P} \cdot \nabla)\mathcal{E} + \mu_0 \dot{\mathcal{P}} \times \mathcal{H} \tag{2.2}$$

with $\mathcal{P} = \mathbb{R}\mathrm{e}\{\mathbf{p}\}$. From the complex fields one can introduce the quantity:

$$\mathbf{f}_0 = (\mathbf{E}_0 \cdot \nabla)\mathbf{E}_0^* + \mathbf{E}_0 \times (\nabla \times \mathbf{E}_0^*) \tag{2.3}$$

whose decomposition in real and imaginary parts allow to express the net force as:

$$\mathbf{F}_{\text{reactive}} = \frac{n^2}{2} \mathbb{R}\mathrm{e}\{\alpha\} \mathbb{R}\mathrm{e}\{\mathbf{f}_0\} \qquad \mathbf{F}_{\text{dissipative}} = -\frac{n^2}{2} \mathbb{I}\mathrm{m}\{\alpha\} \mathbb{I}\mathrm{m}\{\mathbf{f}_0\}. \tag{2.4}$$

In such expression the dissipative and reactive terms can be clearly identified. Note that this identification turns out to be very important for interpreting many experiments performed in nano-optics [48, 100–102]. In the regime of ray optics in contrast, such a separation of force fields into conservative and dissipative components loses its meaning.

[1] in most materials, given by the Clausius-Mosotti relation. In some cases a correction is supplied to take into account the field scattered by the dipole [98]. In the adopted notation, taken from ref. [99], the equations are valid for both cases, i.e. including or not the radiated field by the dipole.

The interpretation of the reactive and dissipative components is straightforward when considering an electric field, linearly polarized (such as delivered by a simple laser). In this case, the electric field of amplitude ρ and phase ϕ can be expressed as $\mathbf{E}(\mathbf{r}) = \rho(\mathbf{r})e^{i\phi(\mathbf{r})}\hat{\mathbf{y}}$, so that the term $\mathbf{f_0}$ reduces to:

$$\mathbb{R}\mathrm{e}\{\mathbf{f}_0\} = \frac{1}{2}\nabla\rho^2 \qquad\qquad \mathbb{I}\mathrm{m}\{\mathbf{f}_0\} = -\rho^2\nabla\phi.$$

These expressions immediately connect with the fact that the reactive force is associated with the gradient force and the dissipative part, associated with the phase gradient, corresponds, as such, to optical radiation pressure force.

In nano-optics, optical excitation usually correspond to more complex polarization cases, that can be framed most generally with amplitude and phase definitions given component-by-component. Each component $E^j = \rho_j e^{i\phi_j}$ of the electric field can now be different with $\phi_x \neq \phi_y \neq \phi_z$. The term $\mathbf{f_0}$ is now given by:

$$\mathbb{R}\mathrm{e}\{\mathbf{f}_0\} = \frac{1}{2}\nabla\sum_j \rho_j^2 \qquad\qquad \mathbb{I}\mathrm{m}\{\mathbf{f}_0\} = -\sum_j \rho_j^2\nabla\phi_j.$$

In this case, the imaginary component is expressed as a weighted average of phase gradients, which can be seen as a generalization of a phase gradient.

Replacing the complex fields in the expression of the Lorentz force, eq.2.2 and taking the time average gives:

$$\langle\mathbf{F}\rangle_T = \underbrace{\frac{n^2}{4}\,\mathbb{R}\mathrm{e}\{\alpha\}\nabla||\mathbf{E}_0||^2}_{\text{reactive}} + \underbrace{n^2\omega\mu_0\,\mathbb{I}\mathrm{m}\{\alpha\}(\mathbf{\Pi} - \frac{\nabla\times\mathbf{\Phi}_E}{2\omega\mu_0})}_{\text{dissipative}}, \tag{2.5}$$

where $\mathbf{\Pi} = \langle\mathcal{E}\times\mathcal{H}\rangle_T$ the time-averaged Poynting vector, $\mathbf{\Phi}_E = \mathcal{E}\times\dot{\mathcal{E}}/\omega$ the time-independent electric polarization ellipticity and μ_0 the free-space permeability. This leads to an interesting decomposition of the time-averaged Poynting vector in orbital and spin parts:

$$\mathbf{\Pi} = \underbrace{-\frac{1}{2\omega\mu_0}\,\mathbb{I}\mathrm{m}\{\mathbf{f}_0\}}_{\mathbf{\Pi}_O} + \underbrace{\frac{1}{2\omega\mu_0}\nabla\times\mathbf{\Phi}_E}_{\mathbf{\Pi}_S}. \tag{2.6}$$

This separation shows that a non-vanishing curl of the electric ellipticity leads to interpreting radiation pressure as arising from $\mathbf{\Pi}_O$ and not $\mathbf{\Pi}$. This framework highlights the relation between the phase-gradient and the orbital energy flow responsible for radiation pressure, as discussed in details in the group [99, 103].

The two contributions lead to a net force that is non-conservative. However in situations where the gradient force is significantly stronger than radiation pressure, as it happens in single beam traps, the force acting inside the trap can be considered as arising from an optical potential. In this case, the motional dynamics of the particle

inside the optical tweezer is performed within a potential energy well.

2.3 Experimental setup

We now describe the optical trap and detection methods used throughout this manuscript. A schematized description of our trap is given in figure 2.3. Our trap consists in a single TEM_{00} laser beam (Coherent OBIS LX, $\lambda = 785$nm, optically isolated using a Faraday isolator (Newport ISO-04-780-MP), focused by a water-immersion microscope objective of 1.2 numerical aperture (NA) into a microfluidic cell containing a dispersion of charge-stabilized Brownian dielectric spheres purchased at PolySphere GmbH.

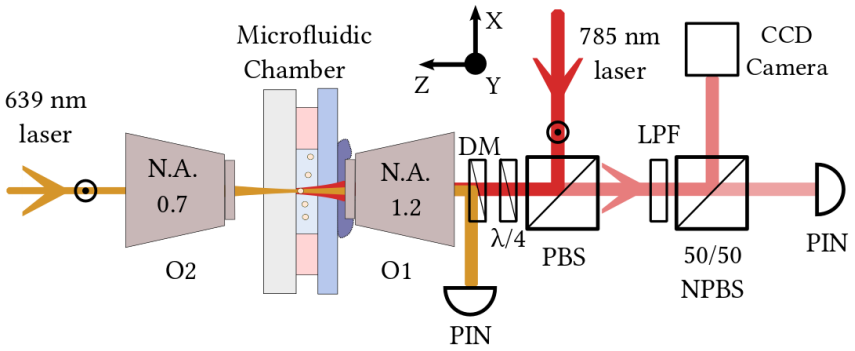

FIGURE 2.3: Trapping and the two alternative detection methods, in forward scattering and backscattering. The trapping 785 nm laser is focused in vicinity of the end-surfaces constituting the microfluidic chamber, using a NA=1.2 water-immersion microscope objective. In order to have a collimated beam slightly overfilling the back aperture of the microscope objective, the beam is magnified $3\times$ through a $4-f$ lens relay system not shown here. Figure adapted from [84].

Real-time displacements of the bead around the equilibrium position inside the trapping potential are usually recorded by monitoring the intensity variations associated with the interference pattern resulting from the coherent superposition of the incident beam and the scattered light by the nanoparticle. More precisely, these variations of the light intensity are due to the Gouy phase changes between the incident and scattered field related to the axial position fluctuations of the bead in the focal region. This technique is commonly referred as Back Focal Plane (BFP) interferometry since the position sensing device is placed in a plane conjugated to the BFP of the collection objective. In our case, we exploit the reflection of the trapping laser at the end-interface of the microfluidic cell (as discussed further down), which implies that the trapping objective also serves as a collection objective in the reflected path. The detector that we use in order to record precisely the intensity variations is a PIN photodiode (Thorlabs Det10A2) of 350 MHz bandwidth.

A 50-50 non-polarizing beam-splitter (NPBS) is placed between the PIN photodiode and the trapping objective in order to send 50% of the recollected light to a CCD camera. This allows us to visualize the trapping spot during the experiments and perform necessary optical adjustments. The voltage generated by the PIN detector is simultaneously sent to an acquisition card (National Instruments PCI-6251) for data collection and to an oscilloscope that monitors the signal in real time.

In the experiments detailed in Chapters 4 and 5, the position-tracking of the trapped bead is performed using an additional laser (wavelength at 639 nm, 70 mW, Thorlabs laser diode) that enters the trapping volume by means of a dry microscope objective (O2) of NA= 0.7 –see figure 2.3. A 45° dichroic mirror (DM) separates the scattered 639 nm beam sent to a PIN-photodiode from the reflected trapping 785 nm laser. In this configuration, a combination of a polarizing beam-splitter cube (PBS) and a quarter wave plate ($\lambda/4$) placed between the source of the 785 nm laser and the trapping objective (O1) is used to reduce back-reflections from the microfluidic chamber (or other optical elements) back to the laser source. Such a system yields an additional optical isolation of approximately 20 dB to the initial optical isolation stage. With a glass-slides composing the microfluidic chamber giving reflections of ca. 3%, such stringent isolations are necessary in order to avoid any feedback into the diode laser.

For all the experiments, the objectives (O1 and O2) have to remain conjugated. It is important that their relative lateral positions remain fixed, so that the only degree of freedom is the axial relative distance between the two objectives. This corresponds to a variable axial distance between the sample and objective O1, or equivalently between the sample and objective O2. The three axes of the sample holder can be driven independently by three piezo-electric actuators (Newport PZA12, travel range 12.7 mm, motion precision 30 nm) enabling lateral scanning of the sample and adjustment of the axial distance between the trapping objective and the fluidic chamber. This relative distance is actually controlled by a system of two coupled piezo-actuators, one for the long range displacement and one for fine adjustments (Newport NPA50SGV6). The latter can be operated under closed loop with a resolution of 1 nm over a travel range of 40 μm. The axial axis of the second objective, O2, is also piezo-controlled, with its position with respect to the sample therefore adjustable once the sample-to-trapping objective distance is fixed. On the contrary, the trapping objective is carefully fixed in order to maintain the alignment with the rest of the elements of the optical path.

A standing wave optical trap

Many of our experiments are performed using an alternative arrangement of the counter-propagating configuration proposed by Ashkin, a modification conceived by Pavel Zemánek in 1998 [104]. This modification consists on focusing the trapping beam on a reflective surface such that the interference between the incident and reflected

waves creates a deep optical potential in which the particle's motion is confined without the need of high numerical aperture optics. The interference between the incident and reflected beams results indeed in a strong reduction of the axial scattering force that can be easily much smaller than the gradient force induced by the focusing effect of the objective [83].

In our group, such a configuration was first implemented in combination with nanostructured mirrors in order to investigate the mechanical effects of resonant and delocalized surface plasmons (SP) on the trapping dynamics of the trapped bead, aiming in particular at increasing as much as possible the "trapping efficiency" (i.e. stifness vs. trapping laser power) of the trap [105]. A standing wave configuation was also used in order to generate bistable potentials and to study, from a thermodynamical perspective, the dynamics of a trapped Brownian particle at the cross-over between stable and bistable regimes [106]. In this context, inter-well stochastic synchronization effects using external forcing have been studied by Gabriel Schnoering [107].

Assuming that the reflected wave only differs by amplitude and phase from the incident wave, the axial component of the gradient force can be approximated as [104]:

$$F_{grad}(z,r) = -\frac{4\alpha}{\pi c}\frac{P}{w^2}\rho e^{-2r^2w^2}\sin(\phi), \qquad (2.7)$$

using a Gaussian beam in the paraxial approximation, with $r = \sqrt{x^2+y^2}$ the radial coordinate, w the beam waist, ρ the amplitude of Fresnel reflection coefficient of the surface, P the total beam power, and α the (dipolar) polarizability of the trapped bead. In the vicinity of the mirror the phase factor can be simplified to $\phi \simeq 2kz + \psi$, with ψ the phase shift added to the wave after the reflection on the surface. Stable equilibrium positions occur at $\phi = 2\pi l$, with l an integer, at which the particles will be trapped in the antinodes $l\lambda/2 - \psi/2k$ of the standing wave pattern separated by $\lambda/2$. In these antinodes, the radial component of the gradient force is almost 4 times stronger than for the case of a highly focused single beam trap for the same intensity. The radial position of the maximal radial component is localized in the same position as for a single-beam trap.

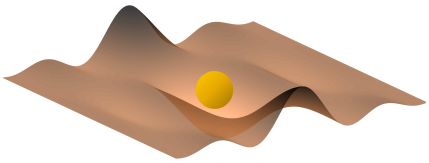

FIGURE 2.4: Pictorial view of the standing wave potential landscape. A small metallic bead is axially confined by "light walls" formed by the standing wave. In such a configuration, the Poynting vectors of the incident and reflected beams compensate each other in such a way that the transverse confinement is merely ensured by the gradient force.

This configuration proves to be very efficient for trapping metallic nanoparticles. As discussed below and in Chapter 3, this is an important asset of our trapping configuration. It is indeed difficult to achieve three-dimensional stable optical trapping of large metallic nanoparticles (i.e., radii larger than 50 nm) in fluids using standard laser intensity conditions [108–110]. This difficulty remains a strong limitation despite the potential offered by metallic nanoparticles, in particular in the context of

biophysics, nanosensing, and spectroscopy. In a standing wave configuration, single metallic nanoparticles turn out to be axially confined in the anti-nodes of the standing wave pattern, and the transverse immobilization ensured by the gradient force that entirely determines the trapping stability due to the compensation between the Poynting vectors between the incident and reflected beams.

We finally stress that the high reflecting surface used to create the standing wave optical trap requires a strong attenuation of the back-reflected beam at least of 6 orders of magnitude [107]. In addition therefore to the PBS-$\lambda/4$ plate combination, an additional optical isolation stage is incorporated which consists of a Faraday isolator (Newport ISO-04-780-MP) placed right at the exit of the laser, ensuring a 30-38 dB level of isolation.

Microfluidic cell

In our experiments, we have always used colloidal dispersions of dielectric or metallic nanoparticles in deionized water in order to increase the screening length and avoid formation of aggregates.

The dispersion, deposited on a microscope glass slide sealed using a cover glass with an adhesive spacer (Invitrogen SecureSeal imaging spacers) of 120μm thickness. This fluidic cell chamber is then fixed to a vertical sample holder integrated in the setup.

The fact that the microfluidic cell can be made either using a microscope slide or a 0° dichroic mirror gives to our setup a interesting versatility. Indeed, depending on the choice of the reflecting surface, the trapping laser can either be transmitted (forming a single-beam trap) or reflected for a standing-wave trap configuration. The single-beam mode is used for trapping micron sized dielectric particles while, as discussed above, the standing-wave trap is important when aiming for a stable trap for large metallic nanoparticles. In this case, the mirror is dip-coated for ca. 5 min in a 5% wt polystyrene sulfonate solution in order to reduce electrostatic interactions between the metallic particles and the mirror.

For the experiments presetend below in this chapter or in Chapter 3, we use a 0° dichroic mirror (Thorlabs FM01R) highly reflective (99.4 %) at the trapping wavelength (785 nm) while transparent (93.5%) for an auxiliary laser beam of wavelength 639 nm and an additional imaging laser at 594 nm (in this case, a transparency of 94.9%).

2.3.1 Interferometric imaging

The variety of nanoobjects, dielectric or metallic, involved in our experiments demands a good capacity in diagnosing what is falls and eventually what is stabilized in the optical trap. But obviously, objects whose sizes lie below the diffraction limit cannot be resolved precisely. For tackling this issue, we resort to an interferometric imaging

strategy that has been proposed and developped by the group of Vahid Sandoghdar. This technique is known as Interferometric Scattering Microscopy (abbreviated iSCAT or ISM). In [111], they implemented an iSCAT approach and demonstrated the localization of gold nanoparticles of 5 nm radius. After this first implementation, a series of variations based on the same methodology have been proposed [112]. Today, iSCAT has has been applied in many contexts, from investigating viruses and DNA to quantum dots and metallic nanoparticles [112] proving its efficacy and adaptability. For instance, an interferometric scattering mass spectrometry iSCAMS have been implemented [113], giving an unexpected and striking illustration of the value of the method.

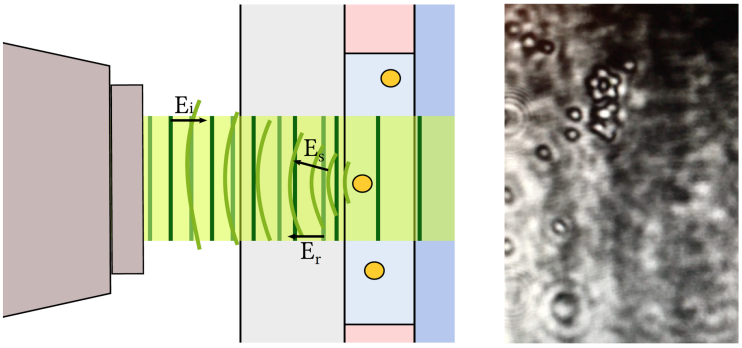

FIGURE 2.5: iSCAT mechanism: When illuminating a suspension of nanoparticles in an acqueous solution, a fraction of the scattered field E_s travels back in the opposite direction of the incident field and interferes with the reflection at the glass/water interface. The image on the right shows an iSCAT image of a very concentrated solution of polystyrene microparticles.

The iSCAT idea is to detect an illuminated single nanoobject by means of an interference between the field it scatters and a reference field, given by the reflection of the incident illuminating beam on a glass/water interface as -schematized in figure 2.5. The approach offers a label-free detection of objects in the fluid against a bright background. Let us consider a spherical scatterer of radius R. The response of this object to the incident field of intensity E_i is $E_s = sE_i$, with $s = |s|e^{i\varphi_s}$ the scattering amplitude, proportional in the Rayleigh regime (i.e. when $R \ll \lambda/2\pi$) to the complex polarizability of the nanoparticle:

$$\alpha(\lambda) = \varepsilon_m(\lambda)\frac{4\pi R^3}{3}\frac{\varepsilon_{NP}(\lambda) - \varepsilon_m(\lambda)}{\varepsilon_{NP}(\lambda) + \varepsilon_m(\lambda)} \tag{2.8}$$

with λ the wavelength of the incident field ,ε_{NP} the complex dielectric function of the nanoparticle, and ε_m of the surrounding medium (in our case, water).

As one immediately notices, the scattering intensity $I_s = |E_s|^2 \propto \alpha^2|E_i|^2$ drops with $V^2 \propto R^6$. Taking into account the reflection $E_r = rE_i$ of the incident beam at the interface with a reflection amplitude $r = |r|e^{i\varphi_r}$, the intensity at the detector will

be given by the superposition of the scattered and the reflected light:

$$I_{ISM} = \eta|E_r + E_s|^2 = \eta(|r|^2 + |s|^2 + 2|r||s|\sin\varphi)|E_i|^2, \tag{2.9}$$

where $\eta = \eta(\lambda)$ is the detection efficiency, and φ containing the phase difference $\varphi_r - \varphi_s$ between the interfering fields.

When the object is very small, I_s becomes negligible. The cross-term stemming from the interference between E_s and E_r then determines the ISM signal:

$$I_{ISM} = \eta I_r(1 - 2\frac{|s|}{|r|}\sin\varphi), \tag{2.10}$$

with a contrast with respect to the reflected intensity written as [114]:

$$\frac{I_{ISM}}{I_r} = 1 - \frac{2|r||s|\sin\varphi}{|r|^2} \tag{2.11}$$

In this case, the particle appears as a dark spot on top of a constant bright background. In practice, this background is not homogeneous since the ISM signal also reveals all impurities, roughness, etc., present on the surface of the sample. Note that it is possible to remove the background $I_{ISM} - I_r$ in order to improve the contrast [112], as $I_{ISM} - I_r$. Finally, ISM signals are quite insensitive to spurious reflections along the optical path, because these have amplitudes smaller than the signal from the reflection of the sample.

In order to setup a interferometric scattering microscopy within our optical trap, we used the dichroic mirror described above as the bottom mirror of the fluidic cell and injected a third laser (Excelsior, Spectra Physics, λ =594 nm, 50mW) into the cell, as depicted in figure 2.6. The beam enters the fluidic chamber colinearly with the trapping beam, but in the opposite direction of propagation. Prior to this step, the beam passes through a beam expander and subsequently through a plano-convex lens (L1) in order to be focused at the back focal plane of objective O_2. This enabled the beam to propagate through the sample as a plane wave and to illuminate a sufficiently wide area (several hundred of μm^2) around the object, or equivalently along the axis of the trapping beam. As mentioned previously, a portion of the beam is reflected at the glass/water (or dichroic mirror/water) interface and interferes with the back-scattered light by the objects in the fluid. The sample image is formed on a CCD camera placed in a conjugate plane formed using a tube lens (L2).

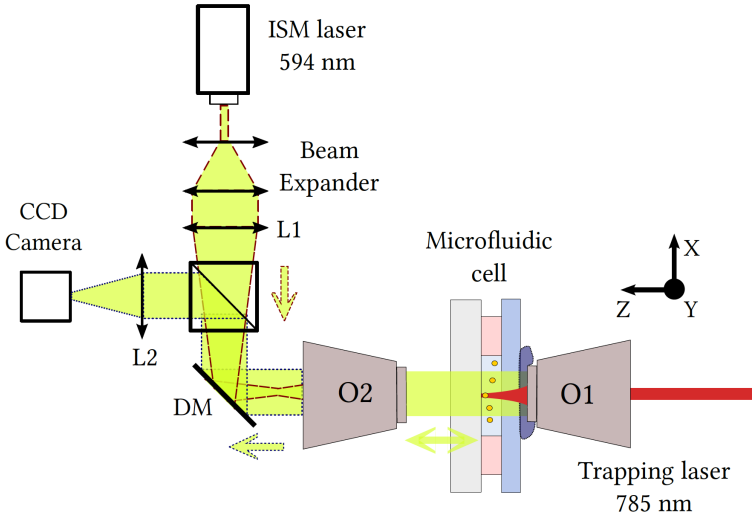

FIGURE 2.6: Optical illumination set-up (not to scale.) An additional plane wave counterpropagating the trapping laser gets reflected at the water/glass interface, and back-scattered by the nanoparticles in the fluidic chamber, the scattered and reflected beam interfere forming an image on a camera situated on a conjugate plane of the back focal plane of objective O2. Figure adapted from reference [83].

Once installed, the ISM line constitutes an important tool for diagnosing the quality of colloidal (both dielectric and metallic –see below) dispersions, and for determining the nature of the trapped object in the trap volume, as well as counting how many objects are in the trapping volume. It helps us in determining the diffusive properties related to the sizes of all small objects dispersed in the fluid through (i) the shape of the imaged spot and its contrast, and (ii) through the blinking dynamics of the image on the CCD video, which strongly depends on the size of the object. Small objects, with large average diffusion rates, will span the phase φ through diffusion more rapidly than larger ones. Importantly for the experiments, ISM allows us to scan through the sample in order to assess the quality of dispersion and select the object to be trapped relatively fast. To rapidly trap any particle, one can adjust the relative distance or trap strength to catch the particle, according to its image in the camera, or conversely move the trap away when there are objects approaching once a single particle is already trapped. Therefore, one can work at very low NP concentrations without having to wait hours to catch the particle of choice. One can simply scan across the sample until finding the diffusing object with the expected characteristics that will therefore be trapped by simply switching on the trapping laser.

2.4 Brownian dynamics of a trapped spherical bead

Objects held in optical potentials have typically sizes ranging from 10 nm to 10 μm. Such objects, suspended in a fluid, undergo a perpetual random motion (Brownian motion) due to the collisions with the fluid molecules. To describe the interplay of forces acting on Brownian particles, a convenient approach is to use the fact that

in the region near equilibrium, the interaction between the particle and the optical trap can be approximated by a harmonic potential, where the particle is confined and oscillates with an amplitude that depends on the thermal energy k_BT and the trap stiffness κ. This noise driven motion of a bead in a harmonic potential is described by a Langevin equation:

$$m\ddot{x}(t) + \gamma\dot{x}(t) + \kappa x(t) = F_{\text{th}}(t), \tag{2.12}$$

where $\kappa x(t)$ is the restoring force of the trap, $\gamma\dot{x}(t)$, the force due to the viscous friction. The drag coefficient is given by the Stokes law, $\gamma = 6\pi\rho\nu R$, for a spherical particle of radius R placed far from any wall, immersed in a fluid of density ρ and kinematic viscosity ν. In the case for a polystyrene particle of radius $R = 0.5\,\mu$m in water at room temperature, $\rho = 997.86\text{kg}\,\text{m}^{-3}$, $\nu = 0.89 \times 10^{-6}\text{m}^2\,\text{s}^{-1}$ the Stokes drag is $\gamma = 8.39 \times 10^{-9}\text{kg}\,\text{s}^{-1}$.

The term $F_{\text{th}}(t) = \sqrt{2k_BT\gamma}\eta(t)$ is the Langevin thermal force that describes the effect of stochastic collisions between the particle and the fluid molecules. In water at room temperature, these collisions occur in very short time scales, $\tau \sim 10^{-12}$ s. During a characteristic time of the motion of the bead, a large number of stochastic kicks take place and the total effect can be modeled with a delta-correlated Gaussian noise,

$$\langle\eta(t)\rangle = 0 \qquad\qquad \langle\eta(t)\eta(t')\rangle = \delta(t - t') \tag{2.13}$$

where the average $\langle\cdots\rangle$ taken over many realizations of the Gaussian process.

The first term of the l.h.s. of equation 2.12 is the inertial contribution, where m is the mass of the bead. In a typical optical trap that immobilizes a polystyrene bead of radius $R = 0.5$ μm in water at room temperature, the inertial term can safely neglected since the characteristic decay time of the kinetic energy due to friction $\tau_v = m/\gamma \sim 10^{-7}$s is, at least, four orders of magnitude shorter than the relaxation time for positions $\tau_x = \gamma/\kappa \sim 10^{-3}$ s. This scaling $\tau_v \ll \tau_x$ corresponds to the overdamped limit (low Reynolds number) for Equation 2.12. A typical time series of the positions of a polystyrene microsphere of radius $R = 0.5$ μm confined in a trap of stiffness $\kappa = 18\,\text{pN}/\mu\text{m}$ is displayed in figure 2.7 below.

Introducing the trap characteristic frequency as $f_c = \kappa/(2\pi\gamma)$ and the Einstein relation for the diffusion coefficient $D = k_BT/\gamma$, the equation of overdamped motion can be written as:

$$\dot{x}(t) + 2\pi f_c x(t) = \sqrt{2D}\eta(t). \tag{2.14}$$

The cut-off frequency, f_c characterises the spectral cross-over between the low-frequency confined dynamics and the high-frequency free Brownian diffusion. It is therefore useful to determine how the position fluctuations are distributed over the different frequencies. This information can be retrieved by computing the power spectral density (PSD), which is basically the Fourier transform of the auto-correlation function of the position signal $x(t)$.

To compute analytically the PSD of the time trace of the position fluctuations, we first compute Fourier transform of eq. 2.14,

$$2\pi\gamma(f_c - if)\hat{x}[f] = \hat{F}_{\text{th}}[f]$$

with $\hat{x}[f] = \int_{-\infty}^{+\infty} x(t)e^{-2i\pi ft}dt$. Then, we take the square modulus $2|\hat{x}[f]|^2 = S_x[f]$, with the one-sided PSD of positions given by:

$$S_x[f] = \frac{|\hat{F}_{Th}[f]|^2}{4\pi^2\gamma^2(f_c^2 + f^2)} = \frac{D}{\pi^2(f_c^2 + f^2)}, \tag{2.15}$$

taking the value for the thermal fluctuations PSD $S_{Th}[f] = |\hat{F}_{Th}[f]|^2 = 4\gamma k_B T$ fixed by the fluctuation-dissipation theorem [3, 115].

The spectral density for the position noise is therefore a Lorentzian with a low-frequency plateau fixed at $S_{Th}[f]/\kappa^2$. At higher frequencies, the PSD falls as $1/f^2$, the frequency dependency of free Brownian diffusion.

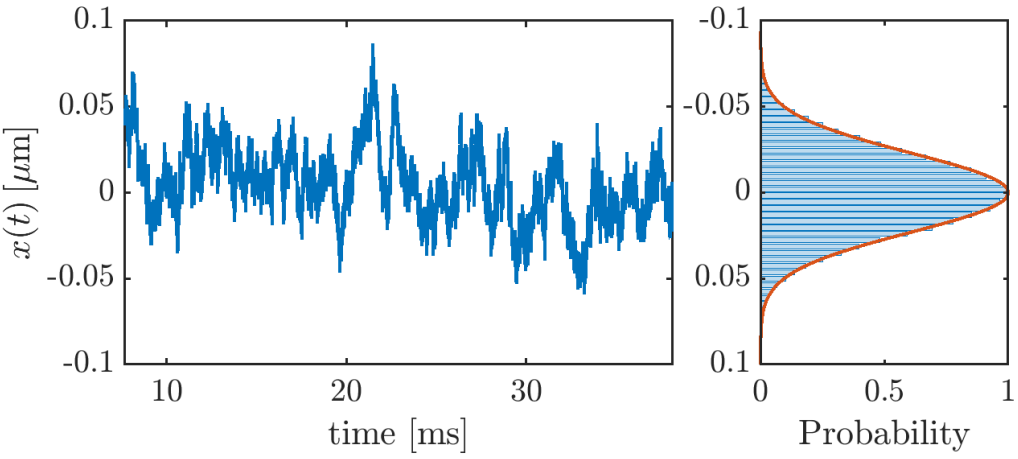

FIGURE 2.7: Left panel: Extract of the temporal trace of the positions of a trapped polystyrene microsphere of radius 0.5 μm along the optical axis corresponding at $x = 0$. Right panel: The corresponding ccupation histogram of positions.

Experimentally, we deal with a discrete time series of voltage values recorded using the PIN-photodiode. These values are proportional to the displacement of the bead. We fit the Lorentzian PSD $L = D^{ex}/(\pi^2(f_{ex}^2 + f^2))$ with two free parameters D^{ex} and f_{ex}^2 from which we extract the PSD roll-off frequency f_c, hence the trap stiffness κ and the diffusion coefficient. Given in arbitrary voltage units, these values are compared to the value $D = k_B T/\gamma$ expected from the known properties of the fluid. This leads to define the conversion factor between voltages (in volts units) and spatial displacements (in meters) of the bead inside the trap. This is one of the advantages of this calibration

method based on the PSD where no prior calibration of the detection system itself is needed. The PSD for the time series plotted in figure 2.7 is displayed in figure 2.8, where the cutoff frequency is found to be $f_c = 340$Hz which corresponds to a stiffness of $18\,\mathrm{pN}/\mu\mathrm{m}$.

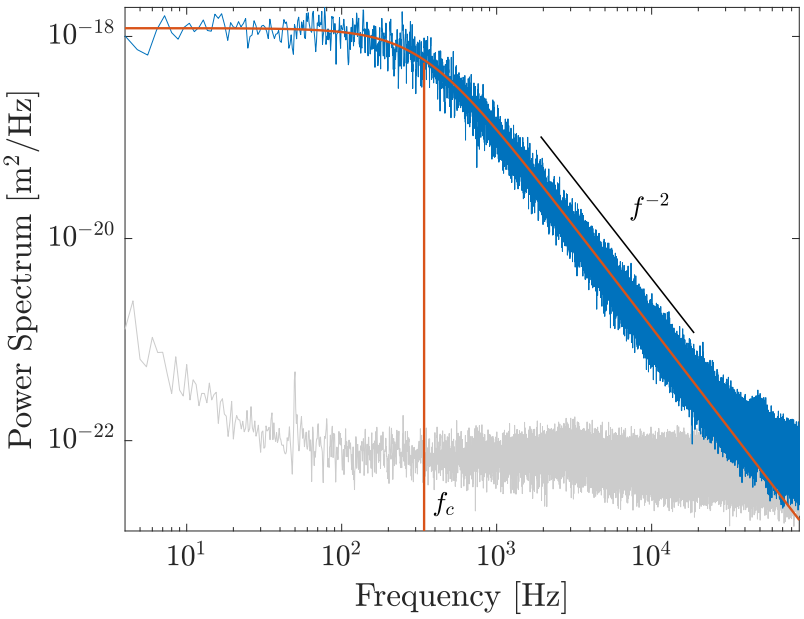

FIGURE 2.8: The power spectrum of a trapped polystyrene microsphere of radius 0.5 μm is shown in blue, superposed to a the power spectrum of the noise floor in grey, taken without a bead in the trap. The solid orange line shows the Lorentzian fit, the cutoff frequency obtained from the fit is $f_c = 340Hz$ and the conversion factor from volts to meters is $6.89 \times 10^{-7}\,\mathrm{m/V}$. One can observe two regimes, in the low frequency regime, before the cut-off frequency f_c represents the position flucutations of the bead confined in the trapping potential, at higher frequencies we observe the free Brownian motion spectral beahviour f^2. The bottom PSD (in grey) corresponds to the experimental noise floor.

The separation of time scales between the degrees of freedom of the bath and the degrees of freedom of the particle allows to have a well defined temperature of the system. Under such thermalized conditions, the distribution of positions $\rho(x(t))$ of the particle in the tweezers can be described by Boltzmann statistics:

$$\rho(x) = Z^{-1} e^{-U(x)/k_B T} \tag{2.16}$$

where $U(x)$ corresponds to the harmonic potential inside which the Brownian bead moves and $Z = \int_{-\infty}^{+\infty} e^{U(x)/k_B T} dx$ is the partition function of the system. The probability density function (PDF) of positions is obtained simply by building, throughout the time series, an histogram of occupied positions as presented in panel (b) of figure 2.7. As

clearly seen, the probability density is a Gaussian which width is given by the stiffness

$$\rho(x) = \frac{1}{\sqrt{2\pi\sigma_x^2}} e^{-x^2/2\sigma_x^2} \qquad \sigma_x^2 = \langle x^2 \rangle = \frac{k_B T}{\kappa}, \tag{2.17}$$

as expected from the equipartition theorem. The trapping potential can be reconstructed from the PDF, up to a constant ($k_B T \ln Z$):

$$U(x) = k_B T \ln(\rho(x)), \tag{2.18}$$

where a quadratic fit can be used to extract the trap stiffness. The experimental occupation histogram in figure 2.7 shows the Gaussian character of the PDF.

2.5 Trapping single chiral nanoparticles

As an illustration of the asset of our optical trap configuration, we present now experiments that optically trapped single metallic (gold) chiral nanopyramids (NPy). Such experiments rely on specific features of our setup, capable to operate in a standing wave configuration for stable trapping of metallic nanoparticles with the open nature of the trapping cavity (i.e. an optical access offered in the fluidic cell by the use of a 0° dichroic mirror) that allows the incorporation of additional laser beams intervening in the trapping volume without affecting the trapping dynamics. It appears cleary through these experimental results that the combination of the standing wave configuration of the trap with the interferometric imaging diversifies and expands the capacities of the setup to trap in well-controlled conditions metallic nanoobjects with more complex shapes, in particular chiral ones, that actually very difficult, if not impossible, to trap using standard single-beam traps. In addition, our setup allows to recognize precisley the type of trapped object by implementing and combining an interferometric scattering microscopy together with, using a third laser acting as a weak probe for circular dichroic scattering, a polarization analysis that enable us to perform an *in situ* recognition of the enantiomeric form of the trapped chiral NPy.

As we now discuss, trapping single chiral objects lead to carry new physical discussions grounded on fundamental concepts, which are at the core of many current debates and discussions like the conservation law of optical chirality or the notion of chiral scattering. Remarkably, these discussions lead to turning operational such concepts in the experimental study of chiral matter at the nanoscale, as exemplified in our use of chiral symmetries in the context of optical trapping. In particular, invoking the conservation law of optical chirality [116] enables a new experimental development for single-particle enantiomeric recognition. The results that we now present have been made possible by collaborating with the Optical Materials Engineering Laboratory of Prof. David J. Norris at ETH-Zurich, in particular with Lisa V. Poulikakos during her PhD thesis.

2.5.1 Complex chiral colloids

Outstanding anisotropic etching techniques mastered in D.J. Norris' laboratory at ETH-Zürich resulted in the fabrication of three-dimensional chiral nanostructures of pyramidal shape, with specific handedness depending on the choice of high-index off-cut silicon wafers [117]. Scanning Electron Microscope images are displayed in figure 2.9. The sharp-edges of such complex structures exhibit intense chiral near fields that are more twisted than circularly polarized light, as studied in [118]. Such "twisted" near fields correspond to now coined *superchiral* near fields. Remarkably, such chiral nanostructures have strong chiroptical signatures as revealed in their extremely strong circular dichroism (CDpeaked at 639 nm, as seen on the CD spectra given on figure 2.9.

These colloidal chiral nanopyramids (NPys) are obviously apposite systems for our experiments and we prepared, with the help of Lisa V. Poulikakos, enantiomerically pure dispersions of gold chiral NPy colloids in charge-stabilized solutions using trisodium citrate buffer at a pH of 7.32. The choice of the buffer leads to a dispersion of chiral NPys of typical sizes of 150 nm. The CD spectra clearly show on figure 2.9 a sign inversion between two NPy dispersions of opposite handedness.

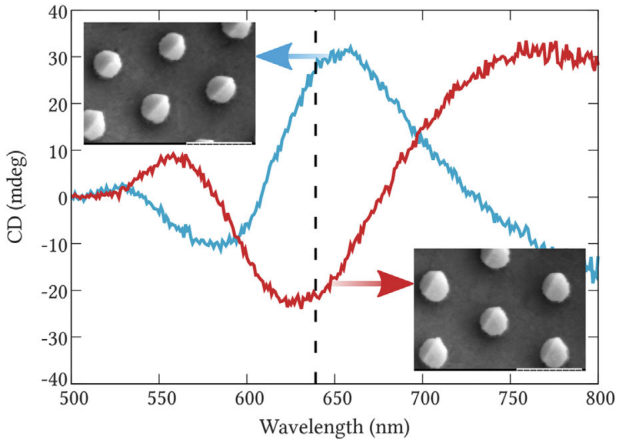

FIGURE 2.9: Circular dichroism (CD) spectra measured through a 1 cm thick cuvette for right-handed (red) and left-handed (blue) enantiomerically pure NPy dispersions. The dashed line represents the wavelength of the probe laser used in our experiment (see below). The corresponding SEM images of the NPys, taken directly after lift-off, are displayed as insets for the left-handed (left upper corner) and right-handed (right lower corner) NPys. The scale bars correspond 500 nm. Reproduced from ref. [83].

2.5.2 Trapping single chiral nanopyramids

In order to trap these NPys, our trap, schematized in figure 2.10, uses a standing wave configuration where the circularly polarized TEM_{00} 785 nm trapping beam (power 45 mW) is focused in the microfluidic chamber by a water immersion objective (60×, 1.2 NA) and then reflected by a 0° dichroic mirror placed at a distance ca. 2 μm from the beam waist. The trapping dynamics is monitored in three dimensions: the

back-reflected light (on-optical axis motion) is recorded by a PIN-photodiode and the instantaneous transverse and axial motions of the trapped NPy are recorded using a quadrant photodiode (QPD).

In order to reduce electrostatic attraction that lead to unwanted adhesion of the NPys on the walls of the fluidic cell, we negatively charge both the dichroic end-mirror by dip-coating it for 5 min in a 5 % wt., and the NPys by diluting the colloidal dispersion within a citrate buffer solution. Despite this, the quality of the dispersion degrades over time, and the NPys start forming aggregates so that, after a certain time, no single NPy is left available for trapping. This puts a constraint on the available time for repeated experiments on different trapped objects that must be accounted for when doing our experiments. By their sizes, the aggregates are actually more prone to be trapped. In order to discriminate between a cluster of NPys and a single NPy, we use the Interferometric Scattering Microscopy (ISM) signal. There, the phase-dependent blinking dynamics of an ISM image strongly depends on the size of the object. For the sake of experimental reproducibility, we only keep trapped objects which blinking dynamics corresponds to the closest possible to the diffusive dynamics found by observing through the ISM compartively sized 150 nm Au nanospheres.

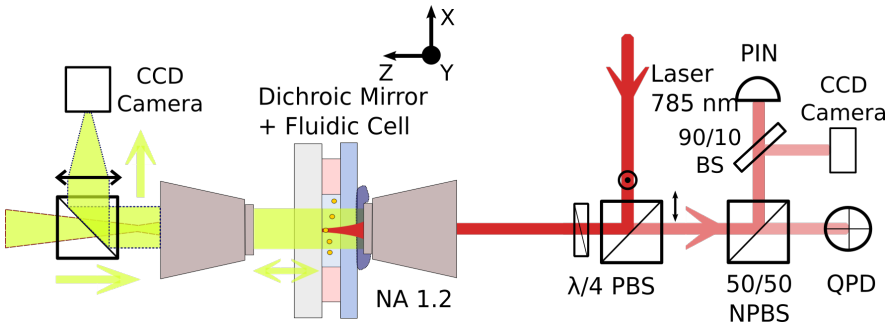

FIGURE 2.10: Schematics of the standing wave optical trap (SWOT), consisting in a circularly polarized TEM_{00} beam from a 785 nm diode-laser (power 45 mW, Excelsior) sent into a water immersion objective (60×, 1.2 NA) and focused in a water cell (deionized water, 120 μm thick). The beam is reflected by a dichroic mirror placed at a distance ca. 3 μm from the beam waist, creating a standing wave pattern within which a single NPy can be trapped. A low-power laser beam of 15 μW (594 nm, 50 mW, Excelsior, Spectra Physics) is focused at the back focal plane of an objective (NA 0.6, 40×) behind the SWOT dichroic end-mirror, transparent at 594 nm. This allows to have the laser beam almost like a plane wave between the two objectives. A fraction of this beam is scattered back at the mirror/water interface and another fraction from the NPy trapped in the fluid. The interference between these scattered beams is imaged back on a CCD camera by a tube lens. Adapted from [83].

A single chiral NPy has very specific scattering signatures, when freely diffusing and when optically trapped. Stable trapping of single NPys in three dimensions is

demonstrated in figure 2.11, where the Gaussian histogram of the axial position fluctuations shows the good confinement of the NPy. The power spectral densities (PSD) acquired for 36 seconds along the three spatial dimensions show almost the Lorentzian shape associated with a harmonic trapping potential. A Lorentzian fit for each PSD shows that above the roll-off frequencies, they precisely match the f^{-2} signature of the free Brownian motion. However, in the lower frequency ranges, below the roll-off frequency, broadly distributed correlations are observed with a power law $S_z[f] \propto f^{\alpha}$ deviating from to the expected Lorentzian plateau $k_B T/\gamma\pi^2$. This is observed most notably in the axial PSD. The exponent α slightly depends on the position of the end-mirror with respect to the waist of the trapping beam. In the case shown in figure 2.11 the exponent is $\alpha \sim -0.49$ and is the largest measured. Curiously, this exponent takes place in the best trapping conditions of the standing wave optical trap. Because it lies below the $1/f$ noise spectral signature, we attribute this deviation to the peculiar geometry of the NPys, with uneven facets, diffusing within a limited trap volume [83]. This observation deserves to be investigated in details, for it opens new questions on the influence of (chiral) geometries in the context of optical trapping.

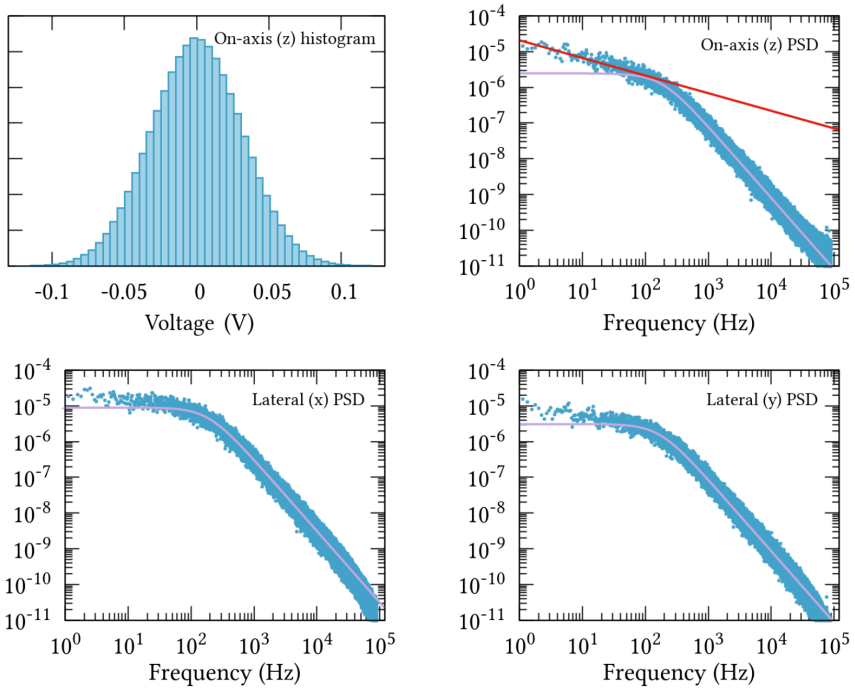

FIGURE 2.11: (a) The intensity histogram of positions along the optical axis shows a Gaussian like distribution. (b–d) Axial and transverse power spectral densities (PSD) of a trapped chiral NPy, acquired for duration of 36 s and averaged 8×. The continuous purple curves represent, for each case, the best Lorentzian fits. The red line shows the best fit of the on-axis data on the low frequency part of the spectrum (from 1 to 200 Hz). Its linear scaling is characterized by a slope of 0.49. Reproduced from [83]

2.5.3 Dissipation of optical chirality and recognition protocol

Once the NPy is stably trapped, the open character of our trap allows for a far-field polarization analysis of the signal scattered by a probe beam illuminating the NPy inside the trapping volume. This leads to define a recognition protocol of the enantiomeric form of the trapped NPy, as we now explain.

This protocol can be understood as a consequence of the conservation law of optical chirality [116]. As discussed by Lisa Poulikakos *et al.*, a lossy, dispersive chiral object upon a non-chiral excitation selectively dissipates optical chirality and must therefore break, in the scattering, the initial balance in left vs right circular polarizations of the excitation field. This unbalanced scattering is determined in direct relation with the chiral nature of the scattering object, hence its enantiomeric form. We note that this law of conservation is directly related to the concept of "Circular Dichroism Differential Scattering" proposed earlier by Tinoco Jr. and Bustamante in the context of chiroptical molecular studies [119].

It is interesting to discuss the nature of the conservation law of optical chirality in connection with the Poynting's theorem that describes the conservation of energy in a lossy, dispersive medium. For time average harmonic complex fields (as defined in Section 1.2), the conservation law writes as [116, 120]:

$$-2\omega \int_{\mathrm{V}} \mathbb{I}\mathrm{m}\{w_{\mathrm{e}} - w_{\mathrm{m}}\} d\mathrm{V} + \int_{\mathrm{S}} \mathbb{R}\mathrm{e}\{\mathbf{\Pi} \cdot \hat{\mathbf{n}}\} d\mathrm{A} = 0, \tag{2.19}$$

where the first integral is taken over a volume V surrounding the medium and the second over the surface S enclosing the volume (with a elementary surface term A), and where $\hat{\mathbf{n}}$ the unit vector normal to the surface. The harmonic electric and magnetic energy densities are $w_{\mathrm{e}} = \frac{1}{4}(\mathbf{E} \cdot \mathbf{D}^*)$ and $w_{\mathrm{m}} = \frac{1}{4}(\mathbf{B} \cdot \mathbf{H}^*)$ respectively. The imaginary term therefore quantifies how much energy is dissipated inside the volume which corresponds to an output energy flux given by the Poynting vector $\mathbf{\Pi} = \mathbf{E} \times \mathbf{H}^*$. We remind that $\nabla \times \mathbf{E} = i\omega\mathbf{B}$ and $\nabla \times \mathbf{H} = -i\omega\mathbf{D}$ for harmonic complex fields (electric displacement D and complex magnetic induction $\mathbf{B}$).

Akin to the Poynting's theorem, it was noted very long ago by D.M. Lipkin [121] and more recently by Y. Tang and A.E. Cohen [122] that the optical chirality of an electromagnetic field could be measured by a local chiral density and a local chiral flux that are both related through a conservation law similar to the energetic one. In strict analogy with the Poynting's theorem, L.V. Poulikakos proposed to quantify the amount of optical chirality that can be dissipated in a chiral lossy, dispersive object by the generation of a non-zero chiral flux, following the law [116]:

$$-2\omega \int_{\mathrm{V}} \mathbb{I}\mathrm{m}\{\mathcal{K}_{\mathrm{e}} - \mathcal{K}_{\mathrm{m}}\} d\mathrm{V} + \int_{\mathrm{S}} \mathbb{R}\mathrm{e}\{\mathbf{\Phi} \cdot \hat{\mathbf{n}}\} d\mathrm{A}, \tag{2.20}$$

where the complex electric and magnetic chirality densities write as:

$$\mathcal{K}_{\mathrm{e}} = \frac{1}{8}[\mathbf{D}^* \cdot (\nabla \times \mathbf{E}) + \mathbf{E} \cdot (\nabla \times \mathbf{D}^*)] \tag{2.21}$$

$$\mathcal{K}_{\mathrm{m}} = \frac{1}{8}[\mathbf{H}^* \cdot (\nabla \times \mathbf{B}) + \mathbf{B} \cdot (\nabla \times \mathbf{H}^*)]. \tag{2.22}$$

Quoting Y. Tang and A.E. Cohen, such quantities "embody the geometrical picture that in a chiral field, the field lines wrap around a central axis, but also have a component parallel to that axis" [116, 122]. The optical chirality flux is written as:

$$\mathbf{\Phi} = \frac{1}{4}[\mathbf{E} \times (\nabla \times \mathbf{H}^*) - \mathbf{H}^* \times (\nabla \times \mathbf{E})]. \tag{2.23}$$

The implication of this law is that the dissipation of optical chirality $\mathbb{I}\mathrm{m}\{\mathcal{K}_{\mathrm{e}} - \mathcal{K}_{\mathrm{m}}\}$ translates into the generation of a non-zero chirality flux $\mathbf{\Phi}$ that corresponds to a far-field quantity, and as such easily measurable. It turns out, as expected, that this quantity is simply related to the third component of the Stokes vector S_3 measuring the balance in left vs. right circular polarization in the polarization state of the scattered field. Our recognition strategy will be based on the fact that the optical chirality flux becomes easily accessible through polarization analysis intensity measurements, considering that the sign of the balance is strictly dependent on the enantiomeric-dependent selective dissipation of left and right circularly polarized light in the chiral scatter, as described by the conservation law of optical chirality. This is simply summarized in figure 2.12 – reproduced from [118] – which describes schematically a chiral scattering mechanism. Upon achiral excitation using a linearly polarized field (in other words, a field that combines equal weights of left and right circular polarization) a lossy, dispersive chiral material will selective dissipate chirality in its scattering, breaking in the far-field the circular polarization balance. This is directly quantified by measuring the S_3 Stokes vector.

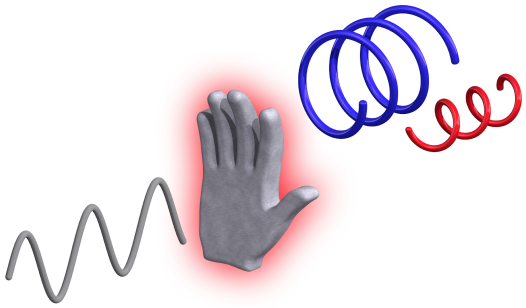

FIGURE 2.12: A chiral structure (a hand, e.g.) made of a homogeneous isotropic lossy dispersive medium is excited with vertically polarized light. As linear polarization is an equal superposition of left- and right-handed circular polarization, the incoming optical chirality flux is zero. If the structure then selectively dissipates optical chirality of one handedness, a nonzero outgoing optical chirality flux must be generated. In this case, the only chiral light contained in the scattered field is due to the structure. Figure reproduced from ref. [118].

2.5.4 Chiral scattering by metallic nanopyramids

In order to describe the chiral scattering properties of a chiral nanopyramids, let us use a Jones matrix representation. In the paraxial approximation, the Jones matrix is a simple 2×2 matrix which structure for a 3D chiral object is known and described in details in [123]. For instance, in the basis of circularly polarized states (σ_L, σ_R), the Jones matrix of the + enantiomer can be written as:

$$J_+ = \begin{pmatrix} \alpha & \gamma \\ \gamma e^{2i\theta} & \beta \end{pmatrix}, \tag{2.24}$$

where the diagonal elements (α, β) represent the "circular dichroic" strength of the NPy and the off-diagonal elements correspond to the fact that the NPy takes a preferential orientation inside the trap as depicted in fig. 2.13, where the base-to-tip axis of the NPy forms an angle $\theta/2$ with respect to the x-axis. We observe indeed experimentally on the ISM images that each NPy adopts a stable averaged position inside the trap which corresponds to the scheme of Fig. 2.13 inside the trap.

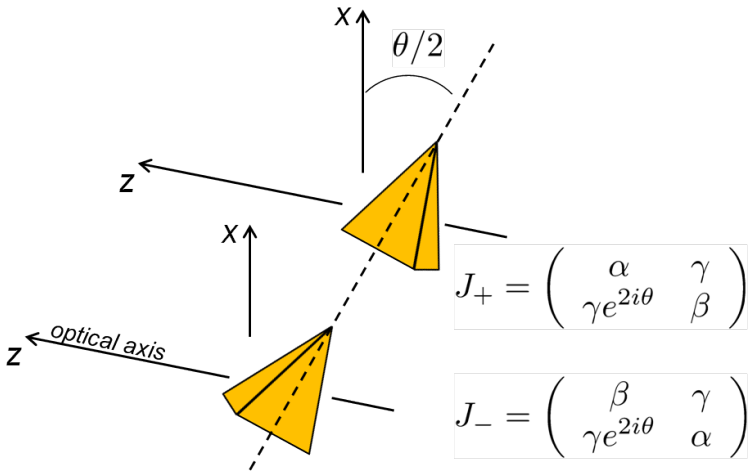

FIGURE 2.13: Schematics explaining the structure of the Jones matrices that can be associated with the NPy enantiomers. Due to its slight pyramidal anisotropy of shape, the + enantiomer is immobilized inside the optical trap in a preferred direction that makes an angle $\theta/2$ with the x-axis of the optical axis $-z$. The Jones matrix of the - enantiomer is deduced by mirror symmetry.

In this simple Jones formalism, the mirror symmetry operation that exchanges the + enantiomer into its − mirror image writes as [123]:

$$\Pi_\theta = \begin{pmatrix} 0 & e^{-i\theta} \\ e^{-i\theta} & 0 \end{pmatrix} \tag{2.25}$$

for an in-plane symmetry axis making an angle $\theta/2$ with respect to the x-direction. The enantiomeric exchange from + to − enantiomer is then described by:

$$J_- = \Pi_\theta \cdot J_+ \cdot \Pi_\theta^{-1} = \begin{pmatrix} \beta & \gamma \\ \gamma e^{2i\theta} & \alpha \end{pmatrix}. \tag{2.26}$$

This formalism enables us to write directly the scattered field as $\phi_{sca}^{\pm} = J^{\pm}\phi_{in}$ depending on which eneatiomeric for is optically trapped inside the trap. Following the law of conservation of optical chirality [116], such a lossy, dispersive NPy will selectively dissipate optical chirality of one handedness more than the other, hence breaking in the scattered field the initial L vs. R balance of polarization of the illuminating beam. As a consequence, a non-zero chirality flux will be generated. The important point is that this balance breaking can be directly measured as the third component of the Stokes vector of the scattered field [116]. In our experiments, it is rather the total field $\phi_{tot}^{\pm} = \phi_{in} + \phi_{sca}^{\pm}$ that we have access to, and the third Stokes parameter associated to it can be written as:

$$S_3^{\pm} = \langle |\phi_{tot}^{\pm}|_L^2 - |\phi_{tot}^{\pm}|_R^2 \rangle. \tag{2.27}$$

In order to evaluate the parameter, we start by assuming rotational invariance of the chiral optical responses of the NPy. This corresponds to a reasonable angular averaging process over the different orientations that can be exposed due to the faceted structure

of the NPys will being trapped and diffusing inside the trap. With such angular averaging, the enantiomeric Jones matrices become diagonal with:

$$J_+ = \begin{pmatrix} \alpha & 0 \\ 0 & \beta \end{pmatrix} \tag{2.28}$$

$$J_- = \begin{pmatrix} \beta & 0 \\ 0 & \alpha \end{pmatrix}. \tag{2.29}$$

In this case the Stokes parameter normalized to $\langle|\phi_{in}|^2\rangle$ is:

$$S_3^+ = (\alpha - \beta) + \frac{1}{2}(\alpha^2 - \beta^2) = -S_3^-. \tag{2.30}$$

The chiral recognition process relies on the global sign inversion related to the $\pm$ nature of the enantiomer. The first term of Eq. (2.30) stems from the interference between the incident field and the scattered field. Since $\phi_{sca}^{\pm}$ is enantioselectively altered, the interfering term is proportional to the relative difference $\pm(\alpha-\beta)$ and hence to the circular dichroism of the single $\pm$ enantiomer. This term actually corresponds to the concpet of "CD Differential Scaterring" introduced in [119]. The second term $\pm(\alpha^2-\beta^2)/2$ represents the chiral field directly scattered by the trapped NPy. As such, it measures the optical chirality flux, in agreement with the prediction that optical chirality flux of opposite sign is generated by chiral objects of opposite handedness [124]. The recognition efficiency of our protocol relies in the global sign inversion of S_3 depending on the optically trapped $\pm$ enantiomer. For our experiments performed in the visible range, the NPys, with their pockets and tips, behave as weak light scatterers. This implies that $|\phi_{\mathrm{in}}/\phi_{\mathrm{sca}}^{\pm}| \gg 1$ so that the recognition essentially operates through the dominant CD contribution.

Experimentally, in addition to the 785 nm trapping laser, we insert a second laser, linearly (vertically) polarized acting as ϕ_{in}, inside the trap volume co-linearly with the trapping beam. This laser is slightly focused behind the trap, but to avoid exerting any force on the trapped NPy, its power is kept as low as possible (100 μW) with respect to the polarization analysis (see below). To maximize the selective dissipation of optical chirality $(\alpha-\beta)$ with respect to handedness, this second laser is tuned to the CD maximum of the NPy at 639 nm, see Fig. **??**. With a dichroic end-mirror, our configuration ensures that the 785 nm laser is reflected, creating the SWOT, while the 639 nm laser is perfectly transmitted by the mirror. In this way, we are able to perform the S_3 polarization analysis behind the trap volume by collecting, through an imaging objective (NA 0.6, 40×), the light transmitted and scattered in the forward direction by the NPy.

The interference signal $\phi_{tot}^{\pm}$ is then sent to a photodetector through a polarization analysis stage made of a quarter-wave plate at 45°, followed by a half-wave plate, and a Wollaston prism. The quater-wave plate converts the unbalanced beam $\phi_{tot}^{\pm}$ into a superposition of horizontal $|H\rangle$ and vertical $|V\rangle$ polarization states and the Wollaston prism separates spatially the two linear orthogonal $|H\rangle, |V\rangle$ states into two beams

with a diverging angle of 20°. The intensities of these two channels are measured by a balanced photodetector (New Focus Balanced Photoreceiver Model 2307) and then substracted. The $S_3 = \langle I_H - I_V \rangle$ values are measured by a fast oscilloscope, averaging over an acquisition time of $\delta t = 50\mu$s.

Once the polarization analysis is performed, the NPy is released from the trap by blocking the trapping laser and the trap is re-opened after ca. 1 min in order to catch a new NPy which is, in turn, analyzed in the same way. This procedure is repeated on two different dispersions of opposite enantiomers prepared in identical fluidic cells (identical dichroic mirrors and cover glasses) in the same way (stabilization and concentration). The two samples are analyzed in a sequential manner, following the same polarization preparation and analysis. One advantage of our experimental protocol using a Wollaston prism is that the optical settings (and in particular polarization optics) are left untouched when interchanging the fluidic cells. The measurements performed for each cell are repeated three times for validity for each + and − enantiomers. The single NPy trapping condition is carefully verified each time with the ISM method, and only the scattering intensities and imaging signatures corresponding to the smallest, thus single, objects are measured.

2.5.5 In-situ recognition experimental results

The results are gathered in Fig. 2.14. The averaged values ($\overline{S_3^+} = -39 \pm 4$ mV and $\overline{S_3^-} = 28 \pm 6$ mV) clearly show that the + and − enantiomeric signals can be distinguished through the polarization analysis. The reproducibility of the S_3 measurements for different NPys trapped from one given dispersion and within the same optical landscape suggests a constant equilibrium position of the NPys inside the optical trap. Despite this, the recorded values do not display the exact sign inversion in the S_3 component between the two enantiomers expected from Eq. (**??**). As discussed below in more details, we explain this from (*i*) the fact that the NPys adopt a preferred orientation inside the optical trap, and (*ii*) from residual alignment errors in the polarization preparation and analysis stages. These effects only offset the $S_3^{\pm}$ values by the same constant quantity, independently from the enantiomeric form. Therefore, the meaningful quantity to monitor is the difference $\Delta_{S_3} = \overline{S_3^+} - \overline{S_3^-} = -67 \pm 10$ mV for which the deviation from zero directly measures the NPy's preferential dissipation of incident left- or right-handed circularly polarized light, i.e. the NPy circular dichroism $\propto (\alpha - \beta)$.

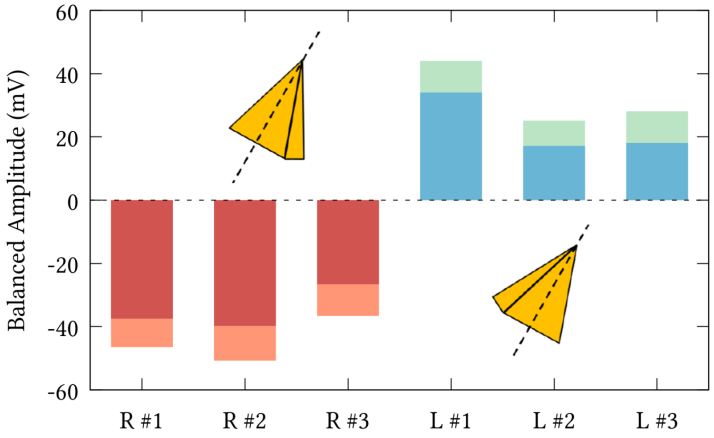

FIGURE 2.14: S_3 Stokes measurements for two dispersions of chiral NPys of opposite handedness. The red bars correspond to different chiral right + NPy labeled from 1 to 3 while the blue bars are three different left ,àí enantiomers. Errors, given by the lighter top of each bar, represent the standard deviation in measuring the S_3 parameter of each trapped NPy. The signal clearly exhibits nonoverlapping intensity differences between the ± enantiomers. We use a fast oscilloscope to measure all S_3 values, averaging over an acquisition time of $\delta t = 50\mu$s. Each measurement sequence for a given dispersion is performed in less than 15 min, and the entire comparative study was shorter than 30 min. These requirements are important in order to avoid fluidic drifts and NPy aggregation to affect the stability of the setup. Reproduced from [83].

Orientational issues

As emphasized above, describing the Jones matrices associated with each enantiomeric form of the NPys with the simple circular dichroism (CD) matrices given in Eq. (2.29) actually amounts to assuming some kind of rotational invariance of the chiral optical responses. This condition leads to the usual optical activity transmission matrices found for instance for isotropic chiral media such as molecular solutions. But at the single chiral object level, ISM images revealed that NPys take a preferred orientation inside the optical trap due to their pyramidal shapes. In such conditions, one loses rotational invariance, and the Jones matrices are no longer diagonal but rather determined by Eq. (2.24). With such matrices, we evaluate the time-averaged intensity $S_3^{\pm} = \langle |\phi_{\rm tot}^{\pm}|_L^2 - |\phi_{\rm tot}^{\pm}|_R^2 \rangle$ component of the Stokes vector associated with the total field $\phi_{\rm tot}^{\pm} = \phi_{\rm in} + J_{\pm}\phi_{\rm in}$. To first order in (α, β), we then evaluate

$$S_3^{+} = (\alpha - \beta) + \partial \quad (2.31)$$

$$S_3^{-} = (\beta - \alpha) + \partial, \quad (2.32)$$

showing an additional constant contribution $\partial = \gamma\,(1 - \cos(2\theta))$ with respect to the simple CD case presented above in Eq. (2.30). This contribution however is consistent with our data that do not show the perfect sign inversion expected from this simple CD case, stressing that it is indeed the difference $\Delta_{S_3} = \overline{S_3^{+}} - \overline{S_3^{-}}$ which is meaningful

in the context of optical trapped chiral objects.

Such evaluations of the Stokes vectors rely on one main assumption: the enantiomers are structural mirror images from each other, with $(\alpha, \beta, \gamma)_+ = (\alpha, \beta, \gamma)_-$. This assumption cannot be absolutely true but we have indications that it is reasonable. First, as far as the α, β parameters are concerned, it is reasonable from the opposite profiles of the CD spectra associated with each enantiomers -see Fig. 2.9. Then, it is also reasonable from the relatively small variations in the three successive S_3 measurement obtained for each $\pm$ enantiomers. Considering the reliability of the fabrication process of the NPys, in particular from an enantiomorphic point of view, the small variations observed when trapping both $\pm$ NPys imply that $(\alpha, \beta, \gamma)_+ \sim (\alpha, \beta, \gamma)_-$.

Potential impact of polarization errors

Finally, we evaluate the potential errors introduced by slight misalignements of the polarization optics in the preparation and analysis sequences of the recognition experiments.

Our polarimetry takes the advantage of using a Wollaston prism that analyzes left vs. right handed circular polarized σ_+, σ_- states through a mere intensity balanced detection. It hence avoids having to manipulate and rotate any wave plate during the analysis. For an empty trap, the half-wave plate ($\lambda/2$) placed before the prism (but after the collection objective, as shown in Fig. 2.15) is adjusted to precisely compensate slight misalignments between the prism and the balanced detector. When set, the $\lambda/2$ wave plate yields zero in the balanced detection for an linearly polarized input state and absolute maximum (minimum) for σ_+ (σ_-). In the analysis sequence therefore, the main source of errors, however very small, will come from the alignment of the fast axis of the quarter-wave plate ($\lambda/4$).

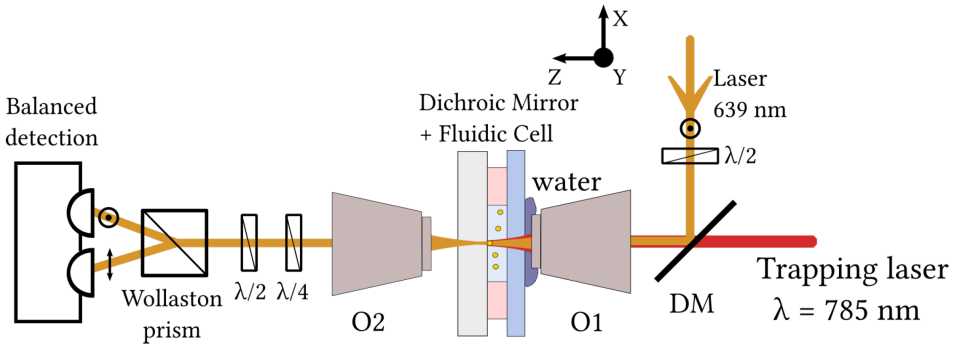

FIGURE 2.15: Polarization preparation and analysis sequences involved in the enantiomeric recognition protocol. The 45° dichroic mirror allows injecting inside the trap the 639 nm laser. This laser is scattered at the waist of the trapping beam by the NPy enantiomer and hence serves as the polarization probe. The preparation sequence is insured by the first half-wave plate ($\lambda/2$) and we treat the 45° dichroic mirror - $\lambda/2$ wave plate as a phase retarding wave plate. The analysis involves a second half-wave plate ($\lambda/2$ behind the collection objective O2) and a quarter-wave plate ($\lambda/4$) which fast axes are respectively set to $\pi/2+\theta_{\lambda/2}$ and $\pi/4+\theta_{\lambda/4}$.

In the preparation sequence in contrast, the presence of a 45° dichroic mirror (DM in Fig. 2.15) induces polarization errors that have to be discussed carefully. Because the reflection amplitudes for s and p polarizations are different on DM, we use a motorized half-wave plate to set the input linear polarization of the 639 nm laser normal to the plane of incidence of the beam on the 45° dichroic mirror, i.e. as close to the vertical y axis as possible (see frame on Fig. 2.15). This corresponds to an orientation of the field $\vartheta = \pi/2+\delta$ of the half-wave plate fast axis, but with an unavoidable small offset δ. Then, in order to keep the discussion of polarization errors general, we simply model the $\lambda/2$-DM system as a general phase retarding wave plate with $\tilde{J}(\pi/2+\delta,\eta,\varphi)$, where η is the relative phase retardation between the fast and slow axes, and φ the circular retardance (following the conventions of [125]).

The polarization analysis sequence can then be written in a straightforward way. We start with the incident field ϕ_{in} linearly polarized, first sent through the half-wave plate-DM system as $\tilde{\phi}_{\text{in}} = \tilde{J}(\pi/2+\delta,\eta,\varphi)\phi_{\text{in}}$. This field then illuminates the chiral sample inside the trap and is transmitted as $\tilde{\phi}^{\pm}_{\text{tot}} = \tilde{\phi}_{\text{in}} + J^{\pm}\tilde{\phi}_{\text{in}}$. As explained in the main text, we measure the $S_3^{\pm}$ parameters from a balanced detection of intensities ΔI in the horizontal $|H\rangle$ and vertical $|V\rangle$ states of polarization after the Wollaston prism. This balanced detection yields:

$$\begin{aligned}\Delta I \;=\; & |\langle H|J_{\frac{\lambda}{4}}(\pi/4+\theta_{\lambda/4})\cdot J_{\frac{\lambda}{2}}(\pi/2+\theta_{\lambda/2})|\tilde{\phi}^{\pm}_{\text{tot}}\rangle|^2 \\ & -|\langle V|J_{\frac{\lambda}{4}}(\pi/4+\theta_{\lambda/4})\cdot J_{\frac{\lambda}{2}}(\pi/2+\theta_{\lambda/2})|\tilde{\phi}^{\pm}_{\text{tot}}\rangle|^2,\end{aligned} \tag{2.33}$$

where $J_{\frac{\lambda}{4}}(\pi/4+\theta_{\lambda/4})$ and $J_{\frac{\lambda}{2}}(\pi/2+\theta_{\lambda/2})$ are the Jones matrices associated with the

analysis quarter- and half-wave plates. They include in $\theta_{\lambda/4}$ and $\theta_{\lambda/2}$ small deviations from the perfect $\pi/4$ and $\pi/2$ orientations of the fast axes.

Due to these deviations and the $\lambda/2$-DM system, we are confronted to a residual contribution δI from the direct transmission that is not perfectly canceled in the balanced detection. This residual contribution can be expanded to second order in the errors as

$$\delta I \sim -2(8\delta\eta\theta_{\lambda/4}\theta_{\lambda/2} - 4\theta_{\lambda/4}\theta_{\lambda/2} + \delta\eta) \tag{2.34}$$

This additive term, which does not depend on the enantiomeric form of the NPy, therefore acts exactly on the same level as the orientational effect discussed above: it forbids to measure the expected exact sign inversion between the S_3^+ and S_3^- parameters. But as discussed above, it can be eliminated by measuring the difference in the Stokes parameters for the two enantiomers. From the polarization analysis point of view, this difference then only depends on the relative orientation of the wave plates. The difference can be derived at the second-order in potential polarization misalignment errors (and at the first order in the (α, β) chiral response) as:

$$S_3^+ - S_3^- \sim (\alpha - \beta) \cdot \left(1 + 8\theta_{\lambda/4}\theta_{\lambda/2}\right). \tag{2.35}$$

We emphasize that the $(\pi/4, \pi/2)$ orientations of the fast axes of the analysis quarter- and half-wave plates are actually the best controlled parameters of the entire polarimetric protocol. This implies that the angular deviations $(\theta_{\lambda/4}, \theta_{\lambda/2})$ are much too small to change the overall sign of the $S_3^+ - S_3^-$ difference. We can hence safely conclude that this difference is robust to polarization errors both in the preparation and in the analysis sequences, providing for that reason a reliable observable for recognizing the two different NPy enantiomers.

2.6 Conclusion and perspectives

These experiments illustrate well the versatility of our optical trap, constructed on a standing wave configuration. Such a configuration has enabled us (i) to stably trap chiral shaped metallic nanopyramids of 150 nm size, (ii) to monitor these sub-wavelength particles during the whole experiments and controlling their number and sizes inside the trap volume using an built-in interferometric imaging microscopy, and (iii) to perform polarimetry analysis that led to a capacity for *in situ* chiral recognition of such single nanopyramids exploiting the law of conservation of optical chirality.

Considering the few remarkable experiments that have been performed at the micrometer scale [126, 127] or with two-dimensional objects [124, 128], our demonstration of stable optical trapping of single chiral nano-objects in three-dimensions is an important step in the development of new experimental methods for controlling and manipulating chiral nano-objects [129]. The concomitant capacity of our optical tweezer for *in situ* chiral recognition gives the possibility to perform chiroptical studies on single

artificial chiral objects at the nanometer scales with an unprecedented level of control. In fact, such experiments take an important step towards the possibility to selectively manipulate chiral matter via new modes of actuations. A strong drive for us towards these experiments is the perspective of revealing and exploiting chiral optical forces at the nanoscale. There is indeed a high expectation that chiral optical forces could constitute an alternative and viable strategy for chiral mechanical separation [103, 130, 131]. In this context, our setup appears in an optimal position. As we will discuss in the next Chapter, our optical trap can also turn into a high-resolution force measurement microscope. Such a combination of possibilities gathered around a single setup gives promissing oppotunities for assessing the applicative potential of all-optical strategies in the vast and cross-disciplinary realm of chirality.

3 Thermally limited force microscopy in an optical trap

3.1 Introduction

The experiments presented in this Chapter can be read as the continuous effort, initiated in the previous Chapter, towards measuring chiral optical forces at the nanoscale. Such forces, as already emphasized, are notoriously weak: optimistic predictions give forces at the fN level involving *"strongly chiral"* artificial objects [103]). Moreover, they are usually superimposed to non-chiral conventional optical forces, such as radiation pressure, which are expected to dominate, by ca. 2 orders of magnitude. In such conditions, and besides the capacity to optically trap single chiral nanoobjects, it is also important to assess the potential of our setup for measuring weak force signals, and to this aim devising the most efficient force detection strategies.

In this Chapter therefore, we will discuss in detail the limitations put by thermal fluctuations, first on the force sensitivity, and then on the best force resolution level that one can reach in our standing wave trap configuration. These discussions are common in the context of weak force measurement experiments. For instance for micromechanical systems, such as Atomic Force Microscopes (AFM), it is important to optimize the mechanical properties of the probe (such as an AFM cantilever) in order to reduce the drag acting on it as much as possible. In such case indeed, the fundamental limit put on the minimal detectable force is set by the coupling to the external bath. Using nanoresonators in ultra-high vacuum conditions, the optomechanics community has achieved force resolutions at the zeptonewton (i.e. 10^{-21} N) level [132]. In liquids at room temperature, where drag effects are important, the group of F. Capasso reached a subfemtonewton (i.e. $< 10^{-15}$ N) resolution level using a Total Internal Reflection Force microscope (TIRF) [133, 134]. This work draws an interesting relation between the TIRF expected sensitivity and the resolution level that actually made us realize how important a global stability test of the entire experiment setup is, in order to fix the appropriate measurement bandwidth, as discussed further down.

3.2 Optically trapped Brownian motion under external forcing

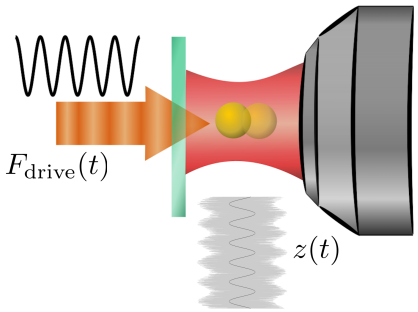

FIGURE 3.1: Thermal position fluctuations $z(t)$ of the trapped bead under the influence of an external sinusoidal force $F_{\text{ext}}(t)$.

For an optically trapped bead in a harmonic potential and on which is exerted an external (radiation pressure, e.g.) force field $F_{\text{ext}}(t)$, the Langevin equation (in the overdamped regime) writes as:

$$\gamma\dot{z}(t) + \kappa z(t) = F_{\text{th}}(t) + F_{\text{ext}}(t), \qquad (3.1)$$

where $z(t)$ is the instantaneous position of a trapped nanoparticle, $\dot{z}(t)$ its time derivative, $\gamma = 6\pi\eta R$ is the Stokes drag built on the dynamical viscosity of water at room temperature ($\eta \sim 10^{-3}$ Pa/s) and the radius R of the trapped bead. The trapping force $\kappa z(t)$ stems from a harmonic potential. F_{th} is the fluctuating thermal force whose magnitude is related to the dissipative drag coefficient γ as a result of the fluctuation-dissipation theorem (FDT):

$$F_{\text{th}} = \sqrt{2k_BT\gamma}\eta(t) \qquad (3.2)$$

that ensures thermodynamic equilibrium. Molecular collisions are assumed to happen in times much shorter than the relaxation time of positions, and described effectively by a Gaussian stochastic process $\eta(t)$ uncorrelated in time. Given the large number of successive impacts that compensate on average, the process $\eta(t)$ is characterized by the following properties:

$$\langle\eta(t)\rangle = 0 \qquad\qquad \langle\eta(t')\eta(t)\rangle = \delta(t'-t).$$

The thermal force is not affected by the trapping potential since this latter does not change the properties of the fluid, however the thermal fluctuations of the bead in the trap are constrained by the stiffness. Assuming a harmonic potential the variance of the position noise is given by equipartition, $\sigma_x^2 = k_BT/\kappa$.

At thermal equilibrium, when no other sources are present, the bead dynamics within the trap is entirely driven by the thermal force ($F_{\text{ext}} = 0$), in this case, the Fourier transform of the Langevin equation, $\hat{z}(f) = \chi(f)\hat{F}_{\text{th}}[f]$, leads to define the mechanical susceptibility:

$$\chi[f] = \frac{1}{\kappa - i2\pi\gamma f} \qquad (3.3)$$

which measures the spectral response of the Brownian system. Using the FDT that relates the power spectral density of the thermal noise to the friction term of the

mechanical susceptibility [135]:

$$S_{\mathrm{th}}(f) = |\hat{F}_{\mathrm{th}}(f)|^2 = -\frac{k_{\mathrm{B}}T}{\pi f}\mathrm{Im}\left(\frac{1}{\chi[f]}\right) \tag{3.4}$$

leads to $\hat{F}_{\mathrm{th}}(f) = \sqrt{2k_BT\gamma}\hat{\eta}(f)$.

The motional PSD describes how the power is distributed among the different frequency components. Usually, one works over an interval of positive frequencies $0 < f < +\infty$, hence evaluating the *one-sided* PSD [136]:

$$S_z(f) = |\hat{z}(f)|^2 + |\hat{z}(-f)|^2.$$

Since the process $z(t)$ is real, the two parts are equal, and we write

$$S_z(f) = 2|\hat{z}(f)|^2. \tag{3.5}$$

The corresponding one-sided PSD has a simple Lorentzian shape:

$$S_z[f] = \frac{k_BT}{\gamma\pi^2(f^2 + f_T^2)} = \frac{D}{\pi^2(f^2 + f_T^2)} \tag{3.6}$$

where we have introduced the diffusion coefficient given by the Einstein relation: $D = k_BT/\gamma$. The roll-off frequency f_T depends on the ratio of the stiffness of the potential κ and the dissipative term γ through $f_T = \frac{\kappa}{2\pi\gamma}$. This roll-frequency separates two regimes of diffusion. For frequencies $f < f_T$, the PSD is constant to a plateau value $S_z(f < f_T) = 4\gamma k_BT/\kappa^2$ that characterizes Brownian fluctuations of the particle confined by the potential. For higher frequencies ($f > f_T$), i.e. for shorter times than γ/κ, the particle essentially does not see the effect of the harmonic potential and behaves as a free Brownian particle, with a typical PSD decrease following a $1/f^2$ law. From this, one concludes that in the lower frequency range of the PSD, the trapped bead acts as a mechanical low-pass filter of cut-off frequency equal to f_T, where higher frequency spurious signals do not contaminate the particle's motional dynamics at long times.

We now want to evaluate the response of the trapped bead, when added to the stochastic mechanical action exerted by the surrounding bath on the trapped bead, an external source perturbs its dynamics. More precisely, we are interested in the influence of external radiation pressure pushing the bead along the trapping potential but being exerted in a completely independent way from the trap. The action of this force is designed to be harmonically modulated at a fixed frequency f_0 as:

$$F_{\mathrm{ext}}(t) = F_{\mathrm{DC}} + F_{\mathrm{AC}}\cos(2\pi f_0 t) \tag{3.7}$$

To be considered as a genuinely independent action, the beam exerting external radiation pressure has to fulfill a few conditions:

- The external radiation pressure is exerted independently of the trapping force, and does not perturb the trapping dynamics. We will see in the next section that such force can be induced using a weakly focalized beam that does not trap the bead.

- The radiation pressure force field is uniform within the whole trapping volume in such a way that its action on the probe is not position dependent and thus the detected radiation pressure is not modulated by the Brownian diffusion of the bead itself within the trapping volume. This conditions is not obviously met in other recent experiments, see [133] for instance.

- The action of the sinusoidal F_{drive} on the bead is uncorrelated from the thermal noise. This will allow us to superpose the two PSD contributions

$$S_z^d(f) = S_z^{\text{th}}(f) + S_z^{\text{drive}}(f), \tag{3.8}$$

  where $S_z^{\text{th}}(f)$ gives the PSD associated with the thermal position fluctuations of the bead in the trap, and $S_z^{\text{drive}}(f)$ the contribution to the motional PSD $S_z^d(f)$ of the sinusoidal forcing.

Assuming that the response of the bead to the external radiation pressure is linear, the Langevin equation taking into account the external force is:

$$\gamma\dot{z}(t) + \kappa z(t) = F_{\text{th}}(t) + F_{\text{ext}}(t). \tag{3.9}$$

In our experiments, the instantaneous position of the bead $z(t)$ is measured using a *p-i-n* photodiode (see Chapter 2) which signal is sent through a low-noise pre-amplifier in which a high pass filter is set at 0.03 Hz to remove the DC force contribution. As derived in Appendix A, the one-sided PSD of the bead evaluated from Eq. 3.9 is given by:

$$S_z^d(f) = \frac{1}{(f^2 + f_T^2)}\left[\frac{D}{\pi^2} + \frac{F_{\text{AC}}^2}{8\pi^2\gamma^2}\delta(f - f_0)\right] \tag{3.10}$$

where the Dirac peak contribution at $f_0 = 43333\,\text{Hz}$ corresponds to the harmonic modulation. We emphasize that we have carefully verified the sinusoidal nature of the modulation signal of the radiation pressure laser beam intensity. In such condition, the signature of the external harmonic drive is directly observed as a peak superimposed on the motional PSD at the modulation frequency f_0, as clearly seen in 3.2. Such a clear emergence of the force peak is a consequence of the fact that the beam exerting the external force does not perturb the trapping dynamics. In this figure, the large peak amplitude measured corresponds to a modulation ratio of $I_{\text{mod}}/I_{\text{static}} = 0.3$ with a PSD measured from a motional temporal trace integrated over 10 s at a sampling rate of 1 MHz.

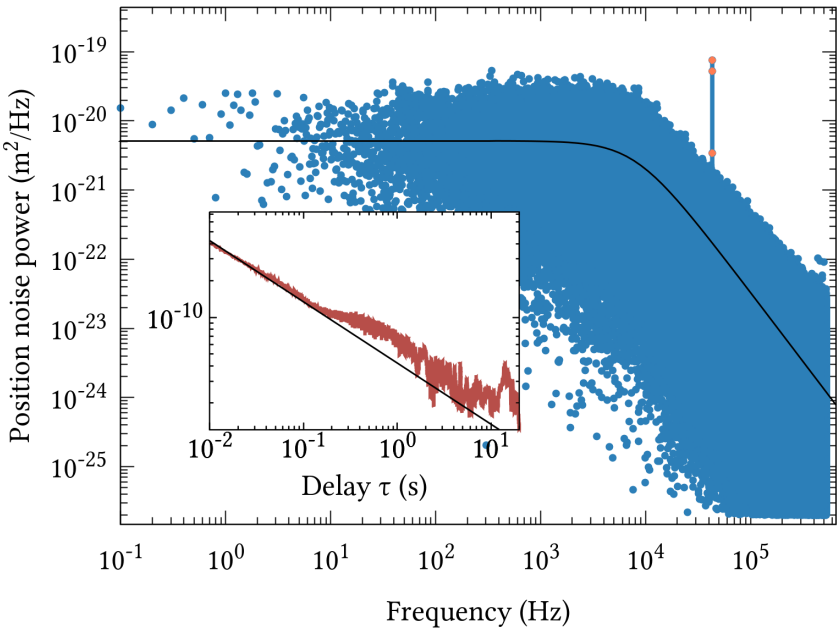

FIGURE 3.2: Experimental one-sided PSD acquired over $\tau_{opt} = 10$ s at 1 MHz is shown in the main panel. From the Lorentzian fit, shown as a solid line, we extract the best-fitted roll-off frequency $f_T = 8\,\text{kHz}$ and a calibration factor $\beta = 1.2 \times 10^{-7}\,\text{m/V}$. Inset: The Allan deviation $\sigma_z(\tau)$ of a trapped gold nanosphere without external drive. The black solid line has a slope of $-1/2$ which corresponds to white noise.

The effect of the filtered-out DC component is to shift the minimum of the potential along the optical axis. The bead ends up fluctuating around the shifted minimum within an effective attractive potential schematized in figure 3.3. On top of the thermal fluctuations, the motion of the bead under the influence of F_{AC} is as if it were virtually pushed and pulled sinusoidally at a frequency f_0 around the new effective equilibrium position.

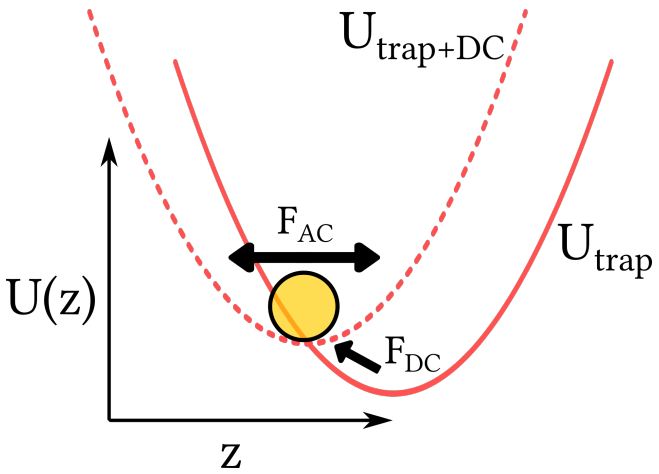

FIGURE 3.3: Simplified energy landscape of the trapped nanosphere under the influence of an external oscillating radiation pressure force, including both DC and AC force components.

The coupling to the bath will determine the force detection limits of our optical trap envisioned as a force microscope. We will now specifically address the problem of defining the force resolution of our setup, by presenting our experimental approach that led us to measure radiation pressure at the fN resolution level.

3.3 Qualifying the setup as a force microscope

As stressed above, our force microscope is designed in such a way that external radiation pressure can be injected independently from the trap and detected by the nanoparticle. We use gold nanospheres of radius $R = 75$ nm (BBI Solutions) that yield large extinction cross-sections for the wavelength of the laser exerting radiation pressure, $\lambda_P = 639\,\text{nm}$. The large extinction cross-sections make such nanospheres highly sensitive probes to external radiation pressure, exhibiting large displacements inside the trap volume even at low radiation pressure laser powers. The size was chosen in order to have a good compromise between extinction cross-sections and the reduction of the Stokes drag $\gamma = 6\pi\eta R$. Considering that the thermal noise depends only on the temperature and the drag, this choice of a small radius will increase the sensitivity of our setup, as we will discuss further below.

In the previous Chapter we have seen that large gold nanoparticles are rather difficult to stably trap using conventional laser tweezers, we have thus resorted to our standing wave configuration, in which the nanospheres can be immobilized in the antinodes of the standing wave pattern. The end-mirror is a 0° dichroic mirror which reflects the trapping laser ($\lambda_T = 785\,\text{nm}$) and transmits the beam exerting the external radiation pressure, which we call the pushing laser, ($\lambda_P = 639\,\text{nm}$). This latter enters collinearly with the trapping laser but propagates in the opposite direction.

Whereas the trapping beam overfills the water immersion microscope objective (NA 1.2, ×100), the pushing laser does not fill the entrance pupil of the corresponding objective (NA 0.7, ×0.7) and hence is only weakly focused in order to avoid any gradient force that would, if induced, perturb the trapping dynamics. In such a configuration the external force field is uniform within the trapping volume, so that the second point rose above –i.e. no Brownian modulation of the measured radiation pressure- is insured. This allows to operate the force microscope in the dynamic mode, where the intensity of the force signal is harmonically modulated and thereby detected at the modulation frequency f_0. With therefore a power of the pushing laser sinusoidally driven around a mean value $\langle P\rangle_t$ as:

$$P_P = \langle P\rangle_t + P_{\text{mod}} \cos 2\pi f_0 t, \tag{3.11}$$

the resulting harmonic force takes the form:

$$F_{\text{ext}}(t) = F_{\text{DC}} + F_{\text{AC}} \cos(2\pi f_0 t) \tag{3.12}$$

with F_{DC} being proportional to $\langle P \rangle_t^2$ and F_{AC} to P_{mod}^2. The experimental configuration used to implement this scheme is described in figure 3.5. The pushing beam entering behind the dichroic mirror of the fluidic cell is delivered by a linearly polarized laser diode at 639 nm (Thorlabs LP639-SF70). The power of the pushing laser is controlled by a function generator (Agilent Technologies 33220A) which generates a sinusoidal waveform with a computer controlled frequency and amplitude. The function generator also sends the output to a lock-in amplifier to serve as reference for this alternative detection (see below for more details).

The advantage of our sinusoidal modulation with respect to other periodic modulations such as square functions, used for instance in ref. [137] or by employing a chopper, as in ref. [133], is that no harmonics are present after the main peak, not even at high modulation strengths, as clearly observed in figure 3.2 that display only the harmonic peak alone associated with the excitation, without any odd harmonics.

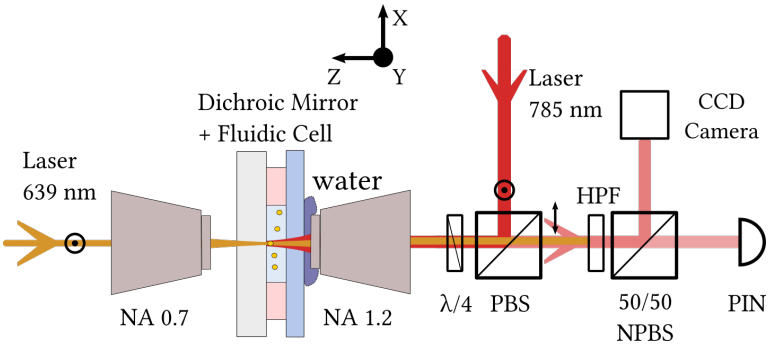

FIGURE 3.4: The force microscope

The recording of the instantaneous position of the gold nanosphere is made on the light scattered by the particle, collected back into the trapping objective and sent by means of a polarizing beam-splitter (PBS) to a fast *p-i-n* photodiode (Thorlabs Det10A). Importantly, a 650-nm high-pass filter (HPF) is added in the path in order to prevent any contamination of the scattered signal by the pushing beam. Prior to the photodiode a nonpolarizing beam splitter (NPBS) divides the signal and send a fraction of it to a CCD camera that allows real-time video monitoring the trapping spot.

The photodiode detected signal, is passed through a low-noise pre-amplifier with high pass filter set at 0.03 Hz, hence removing the DC contribution. The signal is then sent to both a 16-bit acquisition card (National Instruments NI-6251) and a lock-in amplifier (Stanford Research SR830).

3.3.1 Measurement Bandwidth

In weak force measurements, it is crucially important to identify the limited stability of the experimental setup in standard conditions in order to put an upper bound on the available measurement time. This fixes the available measurement bandwidth, and

thus the level of resolution that can be ultimately reached by the setup.

Despite being housed and acoustically/vibrationally isolated, the interferometric nature of our trap makes it very sensitive to all external perturbations: besides intrinsic Brownian noise, our system is subject to other natural noises, air currents, evaporation in the cell, acoustic vibrations, electrical noise in the acquisition chain. In this case, one can expect deviations from the true measure of the position that are statistically not well behaved, for example, the presence of Flicker-like $(1/f)$ noise. Such sources of non-stationarity will lead to deviations that cannot be evaluated with conventional statistical tools.

It is therefore very important to be able to determine our optimal data acquisition time τ_{opt} beyond which the various sources of noise have eventually drifted the entire setup out of the thermodynamic response given by Eq. 3.6 [138].

As discussed in details in a recent work in the group [139], the stability of the entire setup can be carefully assessed using an Allan variance-based analysis. This type of analysis gives unambiguous indications of the relevant timescales over which the system is only driven by thermal (Gaussian) noise and those above which it becomes dominated by other noise sources or detrimental drift effects.

The Allan variance is obtained by subsampling a long time trace and can be computed as [107, 139, 140]:

$$\sigma_z^2(\tau) = \Big\{ \sum_{i=0}^{1} \Big[\frac{z((i+1)\tau) - z(i\tau)}{\tau} \Big]^2 - \frac{1}{2} \Big[\sum_{i=0}^{1} \frac{z((i+1)\tau) - z(i\tau)}{\tau} \Big]^2 \Big\} \tag{3.13}$$

which monitors the evolution of the difference taken between successive means of the trapped bead position $z(t)$ separated by a time interval τ.

The inset of Fig. 3.2 shows the result for the Allan deviation $\sigma_z(\tau)$ calculated on a trapped gold nanosphere without external drive. For time delays shorter than 0.1 s, $\sigma_z(\tau)$ has a slope of 1/2 this indicates that the system is dominated by thermal noise [140]. For longer timescales, one can observe a slight departure from the thermally driven dynamics of the bead appears, system is subject to drift. At 10 s, it usually ranges between 1.2 and 2 depending on the trapped Au NP and its distance to the end mirror. At this transition, the departure still follows a thermal noise spectrum, implying thus that the system can be considered stable. At longer time delays, it clearly appears that the system is dominated by drift effects and clearly not thermally limited anymore.

This analysis gives us a simple criterion for choosing the optimal bandwidth at which a measurement can be performed when aiming at resolving the minimal force at the thermal limit. In our experiments, this limited bandwidth turns out to be ca.

$\Delta f_{\text{opt}} = 0.1$ Hz. Beyond such limit, it is not possible to average a large number of measurements repeated for long acquisition times to increase the experimental sensitivity. This clearly contrasts with the naive view of an optical trap as a "no-drift" system for which one thinks possible to subsample a (very) long tracking sequence into many PSDs that are eventually averaged. Beyond the thermal limit, such procedure can lead to increasing errors in the measured force. As it is seen on the Allan deviation, one position measurement performed over 1 s. is already not solely thermally driven. Averaging our signal acquired over 10 s. as 10×1 s. will necessarily add non-thermal noise observed at 1 s. The ratio between the signal measured and the thermal floor due to other noise contributions being comparable between 1 and 10 s., errors would simply be $10\times$ larger on the averaged position dynamics than for a single measurement of 10 s. In our case therefore, averaging the PSD cannot provide any improvement in the force measurement.

3.3.2 Power spectrum calibration and extraction of the force peak

The *p-i-n* photodiode provides a voltage, the power spectrum associated to this signal, $S_I(f)$ has units of $\text{V}/\sqrt{\text{Hz}}$, a Lorentzian fit of the form, eq. 3.6, taken without the interval where the force peak lies and starting at 10 Hz, provides the best fitted values for D and f_T. The value D is calibrated to the diffusion coefficient $D_{FDT} = \kappa_B T/\gamma$, given by the fluctuation-dissipation theorem, assuming the known properties of the fluid, T, γ. The conversion factor from photodiode volts to meters is given by $\beta = D_{FDT}/D$, consequently the calibrated PSD is obtained as $S_z(f) = \beta^2 S_I(f)$.

The procedure to extract the peak in the spectrum due to F_{AC} is the following. Once the power spectrum is acquired and the Lorentzian fit is performed, one can localize the peak, and substract the thermal contribution:

$$\frac{D}{\pi^2(f^2 + f_T^2)}. \tag{3.14}$$

One is then left with the value $S_z(f_0)$ around f_0. In practice, the spectral density of the peak is distributed over a finite frequency range Δf_{AC} which is approximately 0.4 Hz and centered at f_0. The peak is therefore the sum of all the spectral contributions I_i within this frequency range Δf_{AC}, $I = \sum_i I_i$. The peak has to also be calibrated as $I = \beta^2 I$. The force sensitivity is given by :

$$F_{\text{AC}} = \sqrt{8\pi^2\gamma^2 I(f_0^2 + f_T^2)} \tag{3.15}$$

As shown in figure 3.2, the PSD is an extremely erratic function, at each frequency there are various points which consist in independent events distributed as a Gaussian, the standard deviation of the power spectral density equals its value $\sigma_z(f) = S_z(f)$. However, averaging the PSD necessarily reduces the frequency band- width because

each signal series involved in the averaging is measured on a shorter timescale. As a consequence of this reduction in bandwidth, the width of the peak associated with the external modulated force is increased and its height is reduced. This implies that the improvement associated with the reduction of the PSD variance is lost when the peak is measured at a smaller bandwidth.

Taking the minimal measurable peak spectral density $I_{\min}$ as one standard deviation $\sigma_z[f]$ of the PSD, the sensitivity of the optical force microscope is expected to be thermally limited at $\sqrt{8\pi^2\gamma^2\sigma_z[f]\,(f_0^2+f_T^2)}$ which equals $2\sqrt{2k_{\mathrm{B}}T\gamma}$, using the property that for a continuous response driven by Gaussian white noise: $\sigma_z(f) = S_z(f)$. As expected therefore with Gaussian white noise, the thermal force sensitivity depends only on the fluid properties and the radius of the NP via the Stokes drag, as for an AFM, where reducing dissipation sources is a key target to increase resolution [141]. In this respect, the possibility for trapping a Au nanoparticle of radius $R = 75$ nm is a good compromise between the $\sqrt{R}$ dependence of the Stokes-drag contribution, which must be reduced as much as possible to increase the thermally limited force sensitivity, and the R^3 dependence of the absorption cross section, which determines the strength of the radiation pressure.

In practice, starting with large F_{AC} values, one first measures over the optimal bandwidth Δf_{opt} the ac force signal at f_{opt} through a high peak spectral intensity $I \gg \sigma_z(f)$. Figure 3.7 (a) gathers such force measurements obtained with a single trapped Au nanoparticle for a relatively large optical modulation ratio. We stress that all f_0 peak spectral intensities $S_z(f)$ are measured from a PSD (or with a lock- in amplifier, as discussed below) acquired with a bandwidth of $f_{\mathrm{opt}} = 0.1$ Hz, hence at noise levels similar to the noise level of the PSD shown in Fig. 3.2.

Reducing the optical modulation ratio, one faces a relative increase of unavoidable noise (thermal, external, vibrations, etc.) with respect to the force signal. This noise contribution is analyzed through Allan-deviation analysis. After 10 s, this deviation (seen in the inset in Fig. 2) reaches, at worst, twice the thermal contribution. This sets the optimal experimental sensitivity to $2 \times (2\sqrt{2k_{\mathrm{B}}T\gamma}) = 9.2$ fN/ $\sqrt{\mathrm{Hz}}$ for our experimental conditions (single Au NP, radius 75 nm, trapped in water at room temperature). This sensitivity is valid only for experiments with timescale shorter than τ_{opt}.

3.3.3 Lock-in detection

Another advantage of the sinusoidal forcing is the use of a lock-in amplifier for the detection of the position of the particle. Lock-in amplifiers are instruments typically used in experiments when it is desired to detect a signal in the presence of overwhelming noise, such system measures the amplitude and phase when the device under test is probed by a pure periodic signal by combining methods of time and frequency domains.

The algorithm consists on sending the input noisy signal and the reference into a frequency mixer, in our particular case, a function generator emits a sinusoidal voltage $V(t)$ that controls the pushing laser and simultaneously is sent to the lock-in amplifier as a reference $V_{\text{ref}}(t) = V(t)$, the resulting modulated pushing beam is injected into the force microscope where is probed by the trapped gold nanoparticle. The temporal trace of the position is detected by a *p-i-n* photodiode which in turn sends a voltage $V_{\text{sig}}(t)$ to the lock-in amplifier. We have seen that $V_{\text{sig}}(t)$ contains is proportional to the thermal position fluctuations of the bead in the trap and contains also the influence of the sinusoidal pushing. Prior to lock-in detection $V_{\text{sig}}(t)$ is sent to a low-noise preamplifier and and high-pass filtered with a cut-off frequency set at 0.03 Hz to remove the DC component.

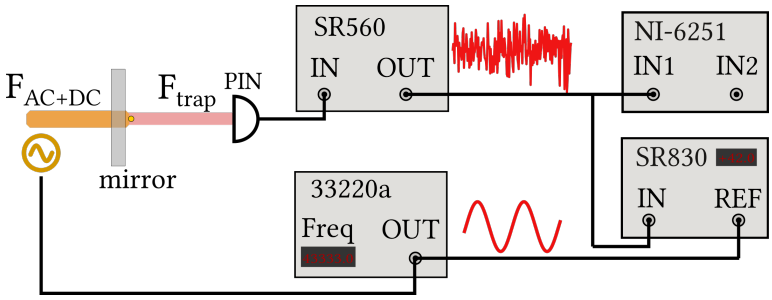

FIGURE 3.5: Lock-in detection method

The signal mixing consists in multipling the two inputs $V_{\text{ref}}(t)$ and $V_{\text{sig}}(t)$:

$$V_{\text{ref}}(t)V_{\text{sig}}(t) = R\cos(2\pi ft + \theta)\cos(2\pi ft) \tag{3.16}$$

which in the frequency domain will appear as a peak at twice the frequency, $2f$, and outputs the voltage of such peak.

The voltage values provided by the lock-in have to be calibrated by means of the self-calibrated Power Spectral Density, since both detection methods provide values proportional to $S_z^d(f_0)$. For a single drive frequency, f_0 the modulation amplitude is set to a high value and then progressively lowered, in this regime of strong drive, the linearity of the lock-in output signal is calibrated to the linearity of the power spectral intensity peak at f_0 measured from the PSD and converted, as F_{AC}, to newtons.

The lock-in amplifier can be modeled as a Lorentzian band-pass filter centered at the modulation frequency, and a narrow spectral bandwidth set by the Allan variance. Such that the position noise becomes $\delta z = \sqrt{\Delta f S_z^d(f_0)}$. For sufficiently high modulation frequencies, this mode of operations shifts the resolution threshold away from the $1/f$ noise contribution. The position noise determines the thermally limited resolution of the force.

3.3.4 Heating effects

Because the trap stiffness κ_T, directly proportional to the field intensity, depends on the viscosity $\eta(T)$, it is clear that a wrong estimation of the fluid temperature can have dramatic implications on calibrating the setup and measuring forces. Optical powers at the waists of tightly focused light beams can reach significant levels (of the order of MW/cm^2), and metallic objects are subject to strong elevations of temperature, around 1500 K/W for Au NPs of 150 nm at λ_T. This would correspond for our experiments to an increase in temperature of ca. 40 K which gives, for water, a change in viscosity by a factor two. In order to check, and if necessary, estimate such unwanted thermal contributions, we varied the trapping beam intensity for different Au NPs stably trapped, and at different mirror-waist distances (see Supplementary Material, Sec. B). No deviations to linearity for trap stiffnesses as a function of the laser power were observed, suggesting a constant surrounding viscosity for all trapping laser intensities. Importantly therefore, heating of the trapped Au NP in our system, if present, has a negligible impact in calibrating the setup and measuring an external force.

The temperature elevation at the surface of the metallic sphere under laser irradiation can be estimated considering its size R and absorption cross-section σ_{abs} as well as the water thermal conductivity k_s and the irradiance I using the following expression:

$$\Delta T = \frac{\sigma_{abs} I}{4\pi k_s R}. \tag{3.17}$$

Such effect has been measured experimentally looking, for instance, at trap stiffness variations, shift of the localized plasmon resonances or thermal damaging of a supporting membrane. These experiments provide a value of thermal elevation of ca. 500 K/W for Au spheres of 100 nm under a Gaussian illumination at wavelength 1064 nm. These values are in relatively good agreement with Eq. (3.17).

Adjusting this value for our 150 nm spheres illuminated at 785 nm provides temperature elevations over 1500 K/W, which corresponds, considering the ∼25 mW of our laser, an increase of 40 K. The viscosity of water $\eta = \eta(T)$ being strongly dependent on temperature variations, this increase is expected to give a factor 2 change in the viscosity -η(T = 300 K) = 0.85 and η(T = 340 K) = 0.42- that necessarily would alter our external force estimation by the same factor.

But such a change is not observed in our experiments. We carefully checked this by varying, through a rotating optical density, the trapping laser power for single Au NPs (150 nm) trapped at different distances from the mirror. As clearly seen in Fig. 3.6, the roll-off frequencies for all trapping conditions follow a linear behavior. Considering that the trap stiffness $\kappa_T = 12\pi^2\eta(T)Rf_T$ is assumed to be directly proportional to the trapping laser intensity, this linear dependence shows that the viscosity $\eta(T)$ of water inside the trap remains constant throughout the variations of intensity. We can therefore conclude that no significant thermal effect is at play on the dynamics of the

trapped object.

This *a priori* surprising results hints towards the complex patterns for stable trapping of spherical Au NP in a standing-wave optical trap. In our experiments, and in order to be consistent with this thermal result, one must imagine that the NP is trapped slightly aside from field intensity maxima. Our system appears analogous to a cage with optical walls along the optical axis, preventing the NP to cross anti-nodes of the interference pattern, while being maintained laterally from the residual gradient contributions.

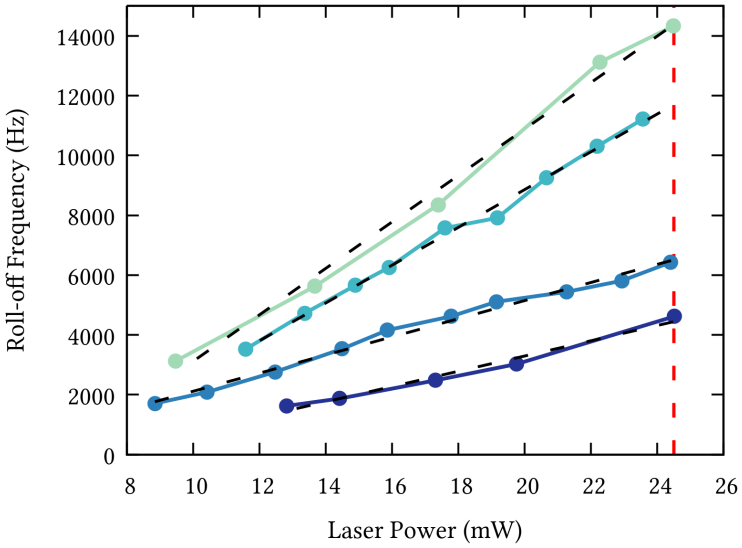

FIGURE 3.6: Evolution of the trap stiffness with incident trapping laser powers depicted for 4 different Au spheres of 150 nm and at different stable trapping positions. Regardless of the mirror-waist distances, the trap stiffnesses, while different, increase linearly with increasing laser power. The behavior is expected when the drag term γ is constant which in our case depends only the viscosity of the fluid and therefore temperature. This verifies that the potential heating of the trapped NPs remains low enough as to not induce any significant variations of the surrounding viscosity. The second top line is offset by -1000 Hz to ease readability. The red dashed line (24.5 mW) corresponds to the trapping laser intensity which is used in experiments.

Finally, no changes were observed in the trap stiffness with the external DC force present. The external pushing field is a few orders of magnitude weaker than the trapping beam and does not induce changes in the fluid properties despite its higher absorption cross-section.

3.4 Force measurements

We now present in Fig. 3.7 optical force measurements done over Δf_{opt}. The measurements are performed at the modulation frequency $f_0 = 43\ 333$ Hz and displayed as a

function of the ratio between the modulation of the pushing-beam amplitude I_{mod} set by the function generator and the static pressure contribution I_{static}. They are done with both the lock-in amplifier and the PSD, measuring the intensity peaks on the PSD plot (pink crosses) with the relevant spectral bins populated by the external force and distributed over Δf_{AC}. The force, as expected, varies linearly (blue shade in Fig. 3.7) with the pushing-laser modulation intensity.

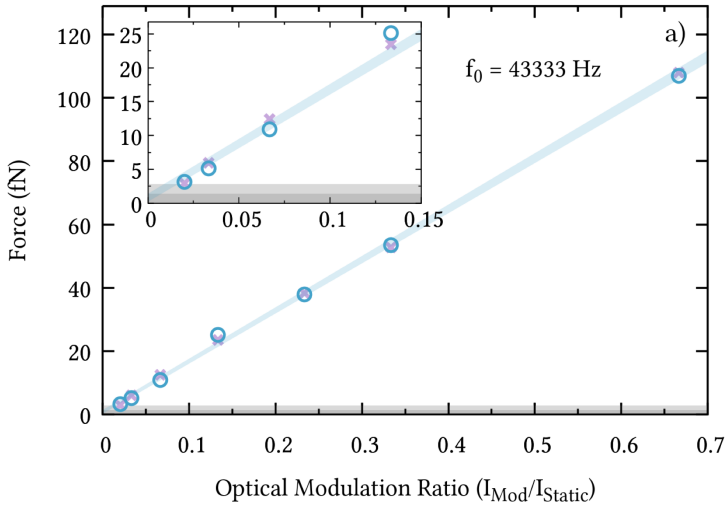

FIGURE 3.7: Evolution of the force measured by the intensity peak on the PSD (blue circles) and by the lock-in amplifier (pink crosses) at the modulation frequency f_0 =43 kHz, as a function of the modulated pushing beam amplitude controlled by the function generator. The linearity of measured forces with modulation amplitudes is apparent and quantified by an uncertainty interval (a deviation to linearity to $\pm 1\sigma$) on the whole measurement series shown as a shaded blue area. Dark and light grey shaded areas represent one and two thermal forces of F_{th} and $2 \times F_{\mathrm{th}}$, respectively, at the chosen bandwidth $\Delta f_{\mathrm{opt}} = 0.1$ Hz.We reach a dynamical range of detection of $F_{\mathrm{DC}}/F_{\mathrm{min}} \sim 50$.

Working at the optimal bandwidth, we expect in these conditions a resolution of $2 \times (2\sqrt{2\mathrm{k_B T}\gamma}) \times \sqrt{\Delta f_{\mathrm{opt}}} = 2.9$ fN, which corresponds to the minimal force that can be measured by our microscope as discussed above. All measurements of external forces below $2 \times F_{\mathrm{opt}}$ are discarded considering that in such cases, the corresponding force signal cannot be discriminated from the noise with a sufficient confidence level. Remarkably, as seen in the inset in Fig. 3(a), our system enables us to measure radiation pressures down to 3 fN (i.e., at the level of the expected resolution) directly from the f_0 modulation peak of the PSD. In agreement with these values, a Mie computation with field intensities estimated at the experimental limit yields a force of 4 fN exerted on the 150 nm Au sphere, a value in good agreement with our measurements.

We also verified that, as a consequence of the property $\sigma_z(f) = S_z(f)$, the minimal force measured does not depend on the choice of the modulation frequency. To do so, we repeated our experiments for different driving frequencies f_0 corresponding to confined ($f_0 < f_T$) or freely ($f_0 > f_T$) diffusing Brownian motion within the trap. The

results are gathered in Fig. 3.8 below. All measured series minimal forces detected above the stringent resolution criterion of $2F_{\mathrm{th}} \sim 3$ fN. Remarkably, while the bandwidth was chosen to account for a worst-case stability scenario for a single NP, the good linearity of the overall series (taking up to a few minutes) suggests that longer acquisition times do not deviate much, for good series, from the Allan variance at 10 s. This could allow for even shorter bandwidth when considering single measurements and must further be evaluated from a much longer acquisition time Allan variance computation, difficult to perform with colloidal suspensions and the chosen acquisition card.

Our data confirm that for our over-damped Brownian particle, the measured external force, and in our case, the minimal measurable external force, remains constant regardless of the driving frequency. This is seen experimentally with driving frequencies f_0 equal to 1331, 10331, 43333 and 97579 Hz, spanning two orders of magnitude and across the trap roll-off frequency. The results are gathered in Fig. 3.9. These results in a sense can be expected: the thermal force depends only on the coupling of the object to the fluid, no matter where in the frequency spectrum the force is driven and detected through the motional PSD.

Finally, we stress that the force resolution is independent of the static DC radiation-pressure component. The smallest force measured F_{min} is almost 50 times smaller than F_{DC} determined to be approximately 160 fN from the slope of the force versus modulation ratio. This gives to our setup one important feature, namely a potential capacity to detect small optical force modulations within a strong background. This feature can indeed become an asset in the context of chiral optical force detection where one could envision inducing on a chiral nanoobject optically trapped chiral radiation pressure modulations by alternating at f_0 the polarization of the trapping beam from linear to circular polarization states. This will impart a small additional AC chiral force signal on the DC component of the achiral radiation pressure contribution that is always present, whatever the polarization state is. The results just presented above give hope for detecting, within the dynamical mode strategy of this chapter, chiral force signals ca. 2 orders of magnitude smaller that non-chiral radiation pressure terms.

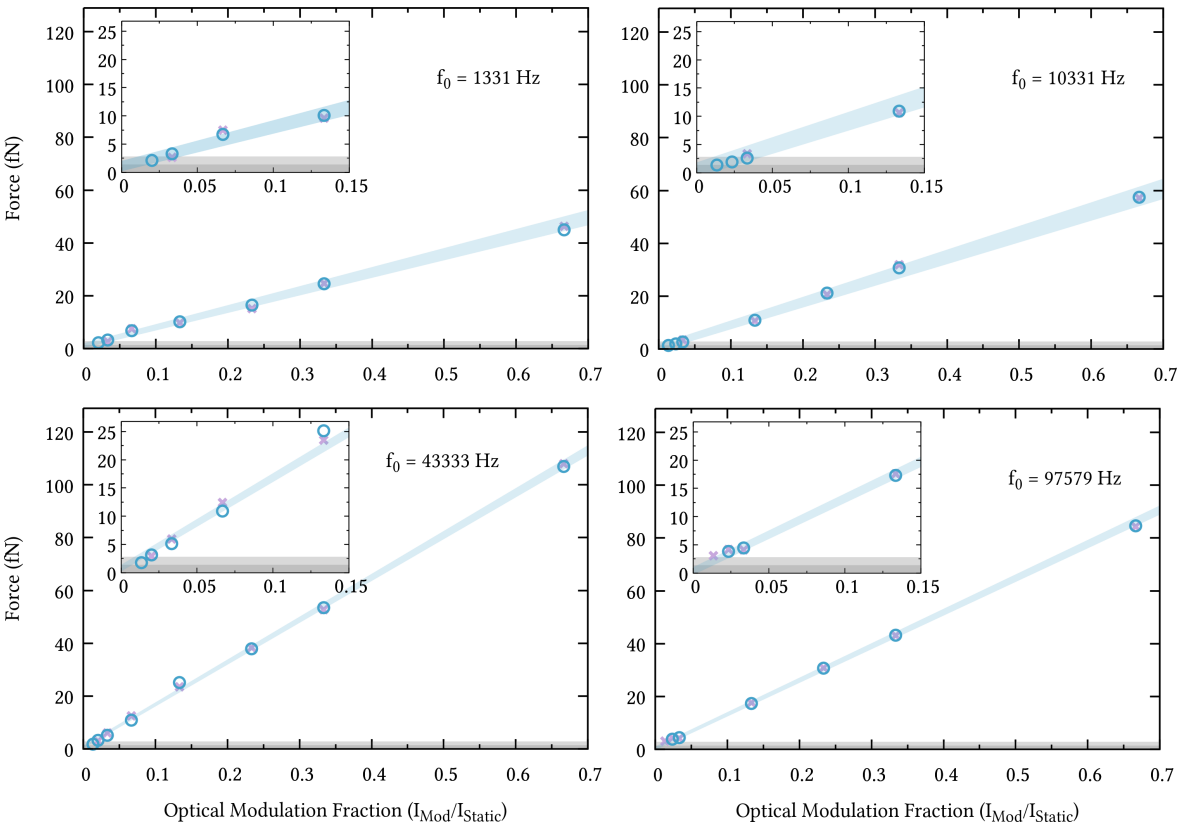

FIGURE 3.8: Measured external forces driven at f_0 exerted on optically trapped single Au NPs of 150 nm at frequencies of 1331, 10 331, 43 333, and 97 579 Hz. The amplitude of the drive is modulated with respect to the mean intensity of the 639 nm optical beam. The crosses are measured external forces from the PSDs and the circles represent forces measured by the lock-in amplifier after its response is linearly calibrated from strong external drives.Each value has a bandwidth $f = 0.1$ Hz. The linearity of measured forces with modulation amplitude is quantified through an uncertainty interval (a deviation from linearity of $\pm 1\sigma$) on the whole measurement series. Dark and light shaded areas represent one and two thermal forces of F_{th} and $2 \times F_{\mathrm{th}}$, respectively, at the chosen bandwidth (0.1 Hz).

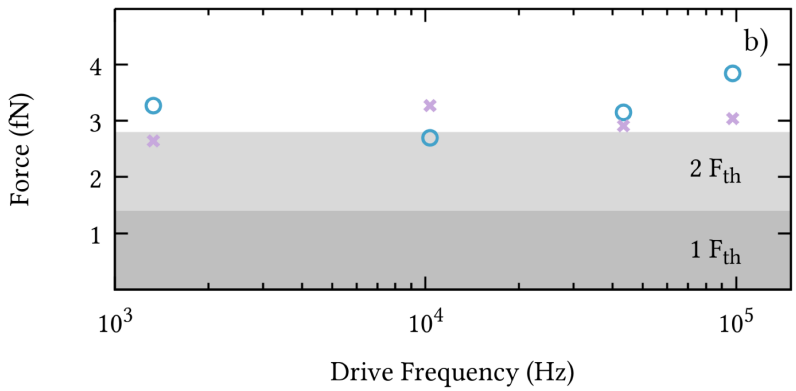

FIGURE 3.9: Smallest measurable external force measured by the lock-in amplifier (red crosses) and the spectral peak stracted from the PSD, for different modulations in frequency across 2 full orders of magnitude. No fundamental difference between the force measured in the different spectral regions : the smallest measured force stays constant at ca. 3 fN throughout the whole drive-frequency range with both methods. Dark and light shaded areas represent one and two thermal forces of F_{th} and $2 \times F_{\mathrm{th}}$, respectively, at the chosen 0.1 Hz bandwidth.

3.5 Position resolution

The discussion on forces is of course different if one looks at positions. Indeed, measuring $S_z^{\mathrm{d}}[f]$ by selecting spectral bins on the PSD over a sufficiently narrow spectral bandwidth $\Delta f_{\mathrm{AC}} \ll f_0$, or equivalently operating through a lock-in amplifier, corresponds to a band-pass filter centered on the modulation frequency f_0. In such conditions, the position noise is given by $\delta z_{\mathrm{min}} \sim \sqrt{\Delta f \cdot S_z[f_0]}$. Contrasting with the thermal limit for force measurements, position noises therefore depend on the modulation frequency, for high-resolution in position it is therefore convenient to modulate at high frequencies.

An isometric representation of the PSD for different external drive frequencies f_0 is displayed on Fig. 3.10. Displacements associated with the smallest external forces measured by the lock-in amplifier are superimposed on the graph as red crosses as a function of f_0. As clearly seen, they lie within the PSD noise levels, separated only by a factor ca. 2 from the Lorentzian fits. The f_0 dependence yields δz_{min} that rapidly decrease with f^2 as soon as the free Brownian regime is dominant for $f_0 > f_T$. Furthermore, the large f_T values provide sub-Å levels of resolution in position for all drive frequencies f_0 and displacements of 10^{-11} m reached at $f_0 \sim 100$ kHz.

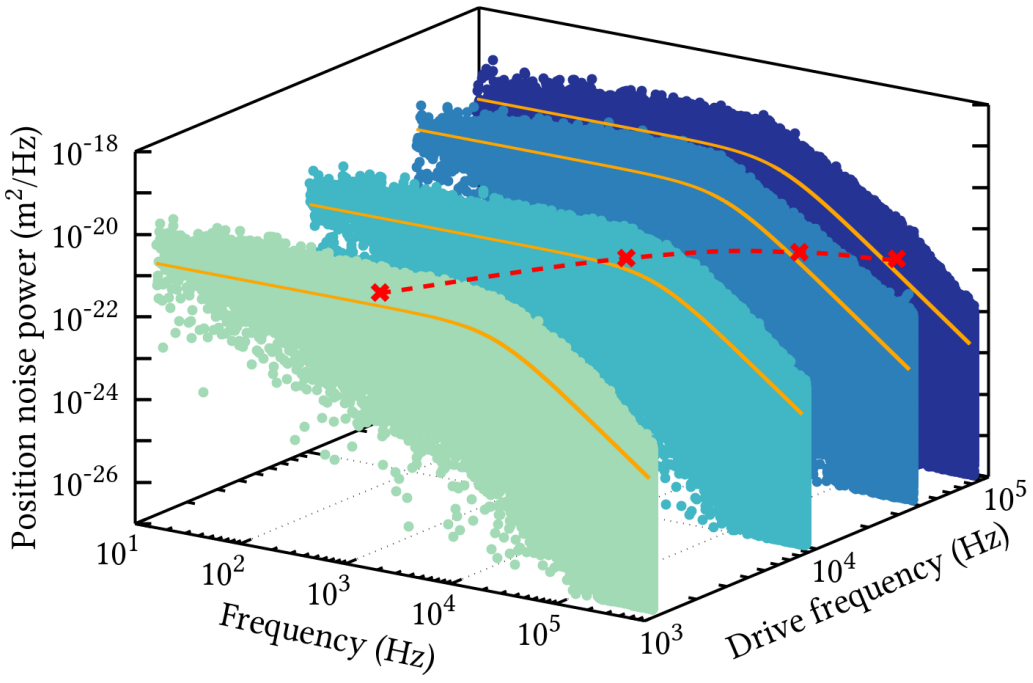

FIGURE 3.10: Isometric representation of the PSD as a function of the external drive frequency f_0 (going from ∼1 kHz to ∼100 kHz). The position resolution measured by the lock-in amplifier (and converted back to noise powers) are superimposed on the graph as crosses as a function of f_0. The smallest measured displacement amplitude is less than 1 angstrom and diminishes even further as the drive frequency departs from the Lorentzian plateau and reaches the free Brownian regime (f^{-2} at high frequencies in the PSD plot). The fit line (in orange) in each PSD plot represents the thermal contribution to the dis- placement. All measurements are acquired over thermally limited acquisition time $\tau_{\text{opt}} = 10$ s. Experiments are performed with different nanospheres and at different distances from the mirror. This results in different trap stiffnesses for the different series acquired. The roll-off frequencies are 17 kHz for $f_0 = 1331$ Hz, 18.5 kHz for $f_0 = 10331$ Hz, 8 kHz for $f_0 = 43333$ Hz, and 7.2 kHz for $f_0 = 97579$ Hz.

3.6 Conclusion

The careful assessment of the conditions for stability of our experiment through Allan-deviation analysis validates our setup as a high-resolution optical force microscope. Over a thermally limited bandwidth of 0.1 Hz, we are able to consistently measure radiation pressure down to approximately 3 fN. This result should also be appreciated in relation to a dynamical range $F_{\text{DC}}/F_{\text{AC}}$ of approximately 2 orders of magnitudes. This range, together with the capacity to reach femtonewton force-resolution levels in

water at room temperature with relatively short acquisition times in the absence of any induced heating, is particularly important when one is aiming at studying new types of optical force fields, in particular in the context of evanescent and surface-plasmon optics, optical spin-orbit interactions, and chiral optical forces.
The concomitant subangstrom displacement resolution offered by our setup also opens new possibilities in the context of short-distance forces, such as Casimir-like interactions or optical binding effects, where adjustable roll-off frequencies allow tuning of the diffusion volume of the trapped NP, and thereby giving a capacity of localization on nanometer scales. This capacity could be important for resolving nonlinear force signals, such as found at the level of self-organized supramolecular assemblies in mechanochemistry. In this context, the reliability and resolution provided by our force microscope could help in exploring connections between optical force and chemical signals.

4 Thermodynamic transformations in an optical trap

4.1 Introduction

In the preceding chapter we have used a harmonically trapped Brownian particle in order to measure radiation pressure at the thermal limit. The strategy consisted in modulating the source of external radiation pressure in such a way that the particle was pushed periodically along the trapping landscape. The energy supplied by the periodic forcing was dissipated to the environment through the frictional force $\gamma\dot{x}$, which via the fluctuation-dissipation theorem, is related to the thermal force $F_{\rm th}(t) = \sqrt{2k_BT\gamma}\xi(t)$, the source that stochastically injects energy to the system and maintains it in thermal equilibrium with its surroundings.

The dynamics of the bead resulted from a linear combination of the thermal force and the controlled radiation pressure. Thus, with such a probe, the smallest resolvable external force was limited to the thermal force, whose magnitude can only be influenced by the coupling to the bath, through the Stokes drag γ and the temperature T.

For our analysis, we adopted the linear response approach, in which the displacement $x(t)$ of the optically trapped bead is connected through the Langevin equation to the thermal force, the trapping potential and the external radiation pressure F_{ext}:

$$\gamma\dot{x}(t) = -\kappa x(t) + F_{ext}(t) + F_{\rm th}(t) \tag{4.1}$$

where $\gamma\dot{x}$ is the viscous drag, $-\kappa x$ the trapping force and $F_{\rm th} = \sqrt{2k_BT\gamma}\xi(t)$, is the thermal force characterized by delta-correlated noise of zero mean, $\langle\xi(t)\xi(t')\rangle = \delta(t-t')$, $\langle\xi(t)\rangle = 0$. In such overdamped regime, the time scale at which the energy of the system is dissipated into the bath is given by γ/κ, which is the time the particle takes to relax within the harmonic potential of stiffness κ, at a given friction γ. We call this relaxation time of positions, "the trap characteristic time" $\tau_{\rm relax}$. In our experiments, we do not have access to faster degrees of freedom. Typically, the relaxation time of the velocities of a polystyrene bead of mass $m = 5.52 \times 10^{-16}$ kg is $\tau_v = m/\gamma \sim 10^{-8}$ s, with $\gamma = 8.39 \times 10^{-9}$ kg s^{-1}, the Stoke's drag for a bead of radius $R = 1$ μm.

Under the periodic forcing studied in Chapter 3, the particle enters a stationary state known as a non-equilibrium steady state (NESS) [142, 143], a state reached by a system when driven out of equilibrium by non-conservative forces and in which the

system constantly dissipates heat to the surrounding bath. No longer described by the canonical distribution, a NESS can not be studied with the standard tools of classical thermodynamics. But in the past decade, significant theoretical [143, 144] and experimental [145–147] progress made possible a consistent description of such states extending thermodynamics to arbitrary irreversible states. This brings us to the main discussion of the present chapter, the thermodynamics of a trapped Brownian particle. At this stage indeed, one wonders whether it makes sense to talk about thermodynamics of such a small system with certainly not ca. 10^{23} degrees of freedom. This is precisely the purpose of a relatively recent field of research known as "Stochastic Thermodynamics" [26, 27, 148], where the Langevin equation itself is endowed with a thermodynamic interpretation [21, 41]. K. Sekimoto attributed heat and work to single stochastic trajectories [41], when later in 2005, U. Seifert, assigned entropy production at the level of individual trajectories [42], establishing the foundation of the field.

This field nowadays is very well developed with fast-paced theoretical advances. The literature on the topic is very extensive, with an exhaustive review with more than 600 references that can be found in ref. [14]. Today, developments in stochastic thermodynamics have allowed the recovery of equilibrium properties of systems measured only out of equilibrium [149], measurement of irreversibility of processes [15], the quantitative measurement of the direction of time's arrow [150], and many more fundamental results related to small systems and systems driven arbitrarily far from equilibrium. An essential family of results forming the backbone of stochastic thermodynamics are the celebrated fluctuation theorems, a set of exact relations that shed new light on the principles that govern energy fluctuations in a wide group of model systems. It should be noted that these relationships go beyond the conditions of linear response or quasi-equilibrium, and can be applied to a large number of systems perturbed by conservative or non-conservative forces through arbitrarily time-dependent protocols [43].

This chapter aims at presenting a simple stochastic thermodynamics approach in the context of our optical trapping experiments, in order to understand the meaning and validity of thermodynamic predictions at the level of a single microscopic particle. In the same way the ideal gas represents the most convenient system to derive thermodynamics results from statistical mechanics, the thermodynamic interpretation of the Langevin equation reveals how a single particle in an optical trap constitutes "the gas and piston" model in the thermodynamics of small systems [7, 47]. A pictorial view of such analogy is shown in Fig. 4.1. An ideal gas contained in a vessel with a movable piston can be subjected to changes of state if one exerts work on the system by compressing the gas or conversely the gas can exert work on the piston if its temperature increases. The same occurs to a Brownian particle confined in a trapping potential, when increasing the laser power, increases the stiffness of the potential. This forces the bead to fluctuate in a smaller volume, a situation that can be considered as analog to the compression of the gas by diminishing the available volume in the vessel.

Optical trapping experiments give access to fundamental models that allow to derive the connection between the macroscopic and microscopic worlds from a thermodynamical perspective. An optical trap with a Brownian particle offers an experimental playground to test and develop theoretical models. In particular, a colloidal particle in a time dependent harmonic potential becomes a very interesting system for studying the emergence of macroscopic irreversible behaviors from the reversible dynamics at the microscopic scale. This simply stems from the capacity to perform ensemble averages over large number of trajectories of the trapped particle. At the level of a single particle, the individual trajectories constitute the microstates and their ensembles represent the behavior of the macrostate.

Both, the piston-gas and the trapped Brownian particle are simple systems, coupled to a single heat reservoir, and can be driven out of equilibrium by an external time dependent perturbation.

In this Chapter, we will start from a "macroscopic" thermodynamics viewpoint in order to remind some classical results obtained when describing processes generated by the action of a piston on an ideal gas. This introduction in section 4.2 will help understanding the significance of the results one can obtain when looking at optical trapping experiments in the framework of stochastic thermodynamics. With such a system, section 4.3 will show how the information at the single trajectory and the ensemble levels can be obtained. Section 4.3.3 introduces the measurement of stochastic heat, work and internal energy at the single trajectory level. Macroscopic behaviors are then derived through ensemble averages, leading to address the problem of dissipation in such fluctuating systems. This of course is connected to the possibility to perform reversible transformations, as discussed in section 4.3.6. The connection is made clear with the Jarzysnki Equality and Crooks Fluctuation Theorems, presented in sections 4.4.1 and 4.4.2. These sections lead to the concept of stochastic entropy, presented in section 4.4.3, closing the chapter on the Integral Fluctuation Theorem for entropy production in section 4.4.4, which is the fluctuation theorem stochastic entropy production obeys, and a generalization of the Second Law of thermodynamics to small systems.

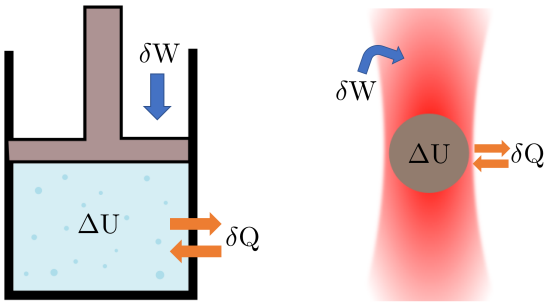

FIGURE 4.1: Analogy between the gas-piston model in classical thermodynamics and its microscopic counterpart, the optical trap and Brownian particle system. The change of internal energy ΔU of the system (gas/Brownian particle) is given by the heat exchanged δQ with the environment and the work exerted δW on the system by the piston/trap.

This Chapter therefore introduces all the tools and concepts that are necessary when discussing the connections between reversibility and dissipation at the level of thermodynamic transformations imposed on single systems. As discussed in the next Chapter, such transformations on such systems, when looked from a stochastic viewpoint, open interesting perspectives and opportunities for the control of single sub-micro/nano systems.

4.2 Entropy changes for isothermal compression of an ideal gas enclosed in a moving piston

The ideal gas is defined as a gas consisting of non-interacting particles that do not possess internal degrees of freedom. It provides a simple system that allows one to derive many results of classical thermodynamics. Let us remind here some of its properties.

We consider an ideal gas, constituted by N particles, enclosed in a vessel made of diathermal walls that allow heat flows between the gas and the surroundings. A moving piston closes the vessel and fixes the available volume V for the gas. The position of the piston can be controlled by an external agent. The system is in contact with a thermal reservoir of constant temperature T. The equation of state of the gas is $PV = Nk_BT$, with P the pressure the gas exerts on the walls of the container and k_B the Boltzmann constant. One can alter the state of the gas by changing the volume of the container, or by varying the pressure of the gas, for example by supplying heat, thus changing the temperature.

We examine an isothermal compression, in which the available volume V decreases in a controlled manner by manipulating the moving piston while keeping the vessel in contact with the bath of constant temperature. The motion of the piston can be performed according to a prescribed protocol. The volume $V(t)$ being proportional to the position of the piston $x(t)$ can be considered as the control parameter. The internal

energy of the gas is $U = c_V N k_B T$ where c_V is the specific heat capacity at constant volume. The internal energy only depends on the temperature, hence for an isothermal process, $\Delta T = 0$, the internal energy of the gas before and after the transformation remains unchanged, $\Delta U = 0$. Thus, the first law of thermodynamics, $\Delta U = W + Q$, grants the possibility to perform the transformation along a reversible or an irreversible path, $W_{\text{rev}} + Q_{\text{rev}} = W_{\text{irrev}} + Q_{\text{irrev}}$. The only thermodynamic restrictions put on the possible processes compatible with the first law, are imposed by the second law of thermodynamics. This law assesses the entropy production, ΔS associated with the change from the initial to the final state. When compressing an ideal gas, the entropy $S(U, V)$ changes according to:

$$\begin{aligned} dS &= \frac{dU}{T} + \frac{PdV}{T} \\ &= c_V N k_B \frac{dT}{T} + N k_B T \frac{dV}{V} \\ &= c_V N k_B d[\ln T] + N k_B d[\ln V], \end{aligned} \tag{4.2}$$

with the first term vanishing when the process is carried out at constant temperature. We investigate two limiting cases of protocols for driving the state of the gas between two equilibria.

- In the first protocol, known as a STEP, the gas starts at thermal equilibrium with the bath until the piston position is changed instantaneously, resulting in an abrupt reduction of the available volume. The gas is driven out of equilibrium and takes its natural relaxation time to equilibrate at the new state, the relaxation timescale depends on the work parameter and the coupling to the heat bath.

- In the second protocol, the transformation is carried out slowly enough so the gas can be considered at equilibrium at each elementary stage of the transformation and therefore during the whole process.

4.2.1 Case 1: Isothermal compression of an ideal gas: STEP protocol

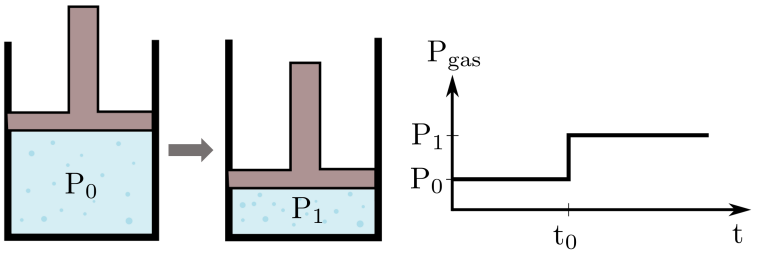

FIGURE 4.2: Isothermal compression of an ideal gas. At time t_0 the volume is abruptly changed from the initial V_0 to V_1. The pressure is then expected to increase from $P_0 = \frac{N k_B T}{V_0}$ to $P_1 = \frac{N k_B T}{V_1}$ according to the compression rate $\xi = V_0/V_1 = P_1/P_0 > 1$.

With a sudden compression, the volume of the container is instantaneously changed from V_0 to V_1, as illustrated in Fig. 4.4, while keeping the temperature constant, $T_0 = T_1 = T$. The pressure of the initial and final state can be found respectively from the equation of state, $P_0 = Nk_BT/V_0$, $P_1 = Nk_BT/V_1$. In this isothermal transformation, the compression factor is given by $\xi = \frac{P_1}{P_0} = \frac{V_0}{V_1} > 1$. The entropy change for the gas (system) is according to eq. 4.2:

$$\Delta S_{gas} = Nk_B \int_{V_0}^{V_1} d\ln V = -Nk_B \ln \xi < 0 \tag{4.3}$$

The first law of thermodynamics tells us that any work applied to the system will either increase the internal energy of the gas or will be dissipated as heat to the surroundings according to $W + Q = \Delta U$. Since the process here is isothermal, the internal energy does not change and the work thus results in heat exchanged with the thermostat. Therefore the entropy change of the bath stems from the heat exchanged with the gas:

$$\Delta S_{bath} = -\frac{Q}{T} \tag{4.4}$$

with $\delta W = -P_1 dV$ i.e. $W = -P_1V_1(1-\xi) = -Nk_BT(1-\xi)$, thus $Q = Nk_BT(1-\xi)$ according to the first law. One then derives:

$$\Delta S_{bath} = -Nk_B(1-\xi) > 0. \tag{4.5}$$

This allows us to evaluate the total entropy change of the "universe" given by entropy change of the system and the entropy change of the surrounding bath as:

$$\begin{aligned} \Delta S_{tot} &= \Delta S_{gas} + \Delta S_{bath} \\ &= Nk_B(\xi - 1 - \ln \xi) > 0, \end{aligned} \tag{4.6}$$

a positive quantity that can only be taken as the signature of irreversibility. This is what Sommerfeld calls "*The Second part of the Second Law*": the entropy of an isolated system can only increase [151].

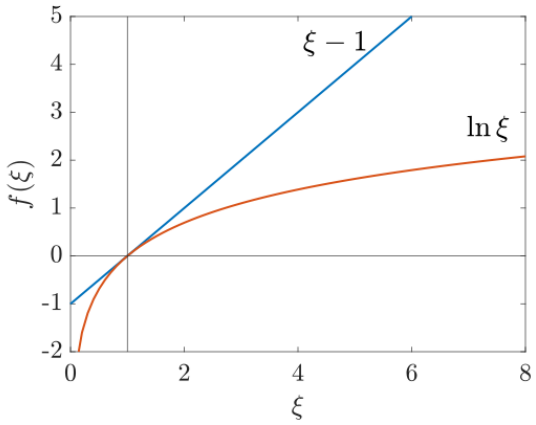

FIGURE 4.3: Comparison of the entropy increase of the system and the bath as a function of the compression rate. A concave function $f(x)$ is such that for any $x_1 \neq x_2$, $\frac{1}{2}(f(x_1) + f(x_2)) \leq \frac{1}{2} f(x_1 + x_2)$.

This entropy production can be recasted in terms of expended work and exchanged heat:

$$\begin{aligned} \Delta S_{tot} &= \Delta S_{sys} + \Delta S_{bath} > 0 \\ &= \Delta S_{sys} - \frac{Q}{T} = \Delta S_{sys} - \frac{\Delta U - W}{T} \end{aligned} \tag{4.7}$$

$$\implies \Delta(\underbrace{U - TS_{sys}}_{F}) < W, \tag{4.8}$$

where $F = U - TS$ characterises the equilibrium state and depends only on the temperature and the control parameter, which in this case is the volume of the vessel. F is known as the Helmholtz free energy, and in statistical mechanics it is a very useful quantity. It allows indeed, to retrieve information regarding the probability associated to a given state since it is related to the partition function, according to $F = -k_B T \ln Z$.

The formulation 4.8 of the second law stresses that the minimum amount of work required to transform a system from a state A to an state B is given by the free-energy difference between these states $\Delta F = F_B - F_A$. If during the transformation the system has been driven out-of-equilibrium, the produced entropy does not allow the system to return to its initial state, unless paying an extra amount of work, known as the dissipated work, $W_{diss} = W - \Delta F$, which is the work needed to compensate dissipation. Lost in the bath, such work is proportional to the entropy production, and the constant of proportionality is the temperature of the bath, $W_{diss} = T\Delta S_{tot}$.

The two expressions, eq. 4.7 and 4.8 encompass the essence of the Second Law of Thermodynamics, which tells us that if the process has been carried out irreversibly, the entropy production of the universe (system + environment) is always positive, breaking the time-reversal symmetry characteristic of the underlying microscopic dynamics. The second interpretation of the Second Law, pointed out by Lord Kelvin, says that in any

thermodynamic process that transforms heat into work, the maximum amount of work that can be extracted is ΔF. In other words, there is always a certain amount of work W_{diss} lost in the bath. This sets a fundamental limit to the power and efficiency of thermal engines.

4.2.2 Case 2: Isothermal compression of an ideal gas: reversible limit

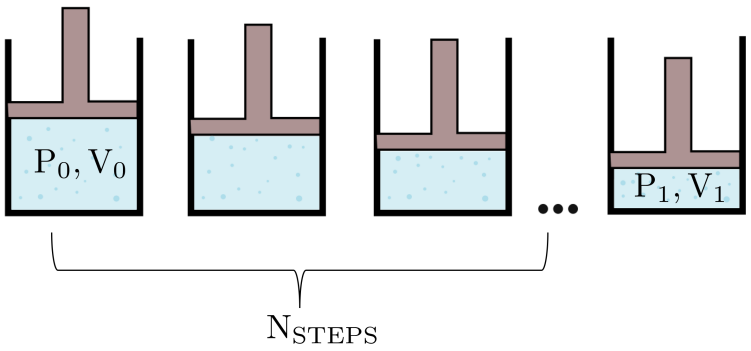

FIGURE 4.4: Quasi-static compression: instead of an abrupt change of the piston, the piston is moved very slowly, which is equivalent of saying that the motion of the piston is composed by $\tilde{N}$ infinitesimal STEPS.

Now we examine a reversible process described in Fig. 4.4, involving the same change $V_0 \to V_1$ compression discussed in case 1. But the compression this time it is carried out infinitely slowly throughout $\tilde{N}$ infinitesimal STEP transforms, that each are at equilibrium. The infinitesimal compression rate is:

$$\varepsilon = \frac{P_{j+1}}{P_j}$$

with P_j the pressure of state j, and $j = 0, 1, ..., \tilde{N} - 1$. After $\tilde{N}$ identical compressions, the total compression rate is:

$$\xi = \frac{P_1}{P_0} = \varepsilon^{\tilde{N}},$$

with thus $\varepsilon = \xi^{1/\tilde{N}} = e^{\frac{1}{\tilde{N}} \ln \xi}$. According to eq. 4.6, the total entropy change associated to an infinitesimal compression ε is:

$$\delta S_{tot} = N k_B (\varepsilon - 1 - \ln \varepsilon),$$

implying thus that the total entropy change of the whole process is $\Delta S_{tot} = \tilde{N} \delta S_{tot}$. Since $\tilde{N} \gg 1$, we can write $\varepsilon = 1 + h$, where $h \sim \frac{\ln \xi}{\tilde{N}} + \mathcal{O}(\frac{1}{\tilde{N}})$ arises from a Taylor expansion of $e^{\frac{1}{\tilde{N}} \ln \xi}$. With this approximation we have:

$$\varepsilon - 1 - \ln \varepsilon = h - \ln (1 + h) \sim \frac{h^2}{2} + \mathcal{O}(h^2)$$

and $h - \ln 1 + h \sim \frac{1}{2}(\frac{\ln \xi}{\tilde{N}})^2 + \mathcal{O}(\frac{1}{\tilde{N}})$. In the limit of a large number of infinitesimal steps, the total entropy change is:

$$\begin{aligned}\Delta S_{tot} &\sim \tilde{N} N k_B \frac{1}{2}(\frac{\ln \xi}{\tilde{N}})^2 + \mathcal{O}(\frac{1}{\tilde{N}}) \\ &\sim N k_B \frac{(\ln \xi)^2}{2\tilde{N}} + \mathcal{O}(\frac{1}{\tilde{N}}) \underset{\tilde{N} \gg 1}{\longrightarrow} 0\end{aligned}$$

This shows that in the quasi-static limit $\tilde{N} \gg 1$, we have:

- $\Delta S_{tot} = 0$, that is:
- $W = \Delta F \Rightarrow W_{diss} = 0$.

Macroscopically, when the piston is moved slowly enough to maintain the gas at equilibrium, the gas can be driven back to the initial state without paying extra energy, and (without accounting for the random behavior of microscopic degrees of freedom), the gas can be considered as passing through the same sequence of equilibrium states as it went through when compressed, since no entropy is produced during the compression.

In classical thermodynamics, the extensive quantities involved, i.e. heat, work and entropy, are regarded as deterministic quantities. If the process is repeated a large number of times, the measured values of such quantities are expected to give the same result. At the thermodynamic limit, with the number of particles $N \sim 10^{23}$, the mean values of extensive quantities increase linearly with the number of particles, whereas their fluctuations decrease as $1/\sqrt{N}$. The predictions of classical thermodynamics are therefore consistent for macroscopic deterministic results and one single experiment is sufficient in order to describe the behavior of the system under thermodynamic transformations. The question is what happens when the scales are reduced, notably to the level of a single particle, as in the case of our trapped colloidal bead? In such systems, whose energy fluctuations are of the same order of the mean energies involved, thermodynamic predictions have to be interpreted statistically. As an example, we show in Fig. 4.5, the results of one of our experiments, in which the Brownian particle is confined in a trapping volume undergoing a quasi-static compression. The measured work values for individual realizations of the process are distributed statistically, and some of these values violate the second law of thermodynamics. This notion of stochastic thermodynamic quantities and their associated distributions will be investigated further in the chapter.

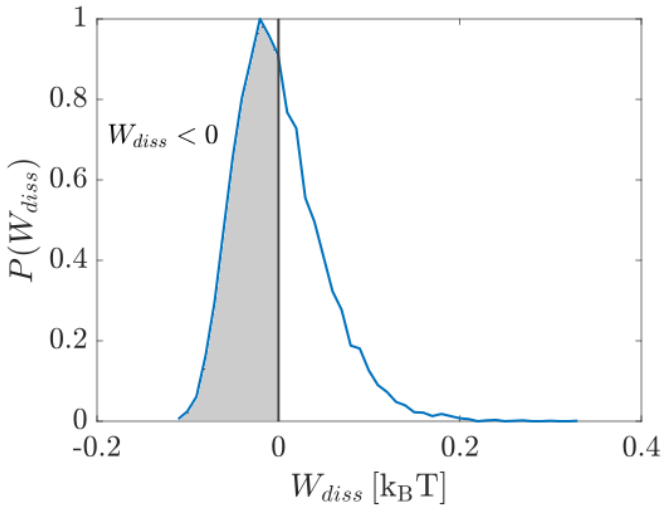

FIGURE 4.5: The second law, has to be interpreted statistically. Among the fluctuating work values, for a quasistatic protocol (for experimental details, see section 4.3.6) indeed, we can observe, events for which $W < \Delta F$. At the micron scale, dealing with a single Brownian object, occasional violations of the second law are observable, *"in which random fluctuations interfere constructively in a manner that facilitates the process"* [152].

4.3 Isothermal compression at the level of a single particle confined in an optical trap

The reactive gradient trapping force of the optical trap limits the diffusion of the Brownian particle to a certain volume. Such a force can be considered as deriving from a harmonic potential[1] $U(\kappa, x) = \kappa x^2/2$, where the stiffness of the trap, κ, is proportional to the polarizability of the bead and the averaged intensity I of the trapping laser. If we probe the position of the particle, $x(t_j)$, within this potential at a given instant t_j, it is not possible to conclude whether the particle is thermalized or not. Therefore one usually records the position of the particle during a long enough interval of time τ. From this stochastic trajectory $x(\tau)$, which can be considered as an ensemble of discrete points in time $\{t_j\}_j$, one can construct a histogram, such as the one displayed in Fig. 4.6, which represents the occupation probability of the particle inside the potential.

At thermal equilibrium, the distribution that determines this histogram is given by:

$$\rho(x) = \frac{e^{-U(\kappa,x)/k_BT}}{\int_{x(\tau)} dx e^{-U(\kappa,x)/k_BT}} \tag{4.9}$$

where k_B is the Boltzmann constant and T the temperature of the surrounding bath. The denominator ensures normalization of probability and represents the partition

[1]For simplicity we proceed all discussions in one dimension, the conclusions in three dimensions are analog.

function, with the integration path taken along the full trajectory $x(\tau)$. In the case of a harmonic potential, $\rho(x)$ is a Gaussian of zero-mean and variance:

$$\sigma_x^2 = \frac{k_B T}{\kappa}$$

which satisfies the equipartition theorem. Figure 4.6 shows how one can retrieve the confining potential from the thermally driven fluctuations.

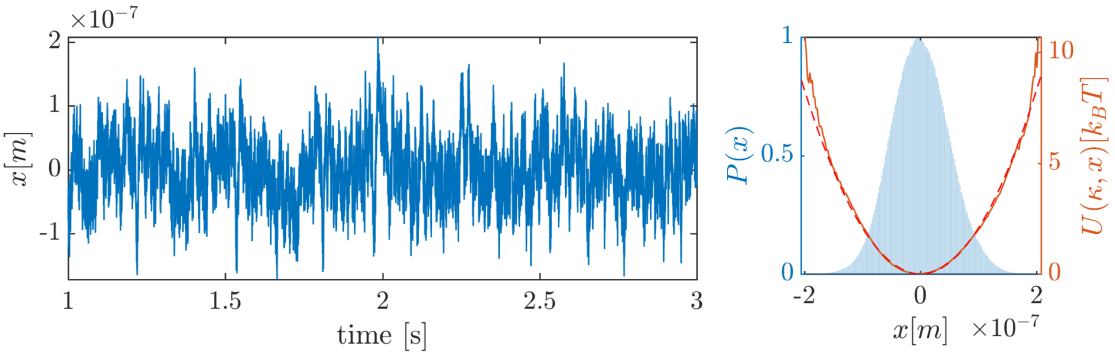

FIGURE 4.6: Left panel: Extract of the temporal trace of the thermal position fluctuations of a polystyrene bead of radius 500 nm trapped in a potential $U(\kappa, x)$ of stiffness $\kappa = 1.7\,\mathrm{pN}/\mu\mathrm{m}$ acquired during $\tau = 10$ seconds at a sampling rate of 262.144 kHz. Right panel: Corresponding histogram of the axial position fluctuations. Superposed as an orange solid line, is the potential $U(\kappa, x)$ calculated from the histogram by inverting eq. 4.9 with $U = -k_B T \ln \rho + C$, the constant C being determined by the partition function. The dashed red line shows a parabolic fit assuming harmonicity.

We now extend the analysis discussed for the ideal gas in a moving piston to the situation of a Brownian particle confined in an optical potential. In our optical trap, an isothermal compression can be realized by changing the trapping potential $U_i = \kappa_i x^2/2$ to a stiffer one $U_f = \kappa_f x^2/2$ with $\kappa_f > \kappa_i$. The role of the control parameter is played by the trap stiffness which can follow any driving protocol $\kappa(t)$ that transforms the state of the system from an initial to a final configuration. The advantage of such system is that no matter how far from equilibrium the system is driven, the surrounding fluid still behaves like a bath of constant temperature T at equilibrium.

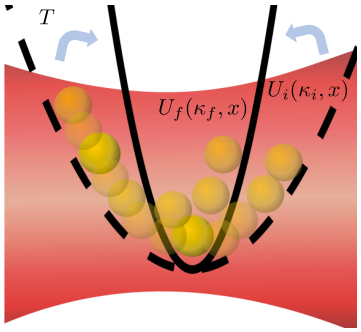

FIGURE 4.7: Conceptual illustration of a trap compression along the optical axis

If we perform the trap compression repeatedly, preparing the system at the same κ_i and following the same driving protocol $\kappa(t)$, we can study how the thermal fluctuations of the particle in the trap affect the work values which, being measured for each

realization are random variables.

4.3.1 Implementing a protocol $\kappa(t)$

The laser output power is controlled by an external time varying voltage supplied by a function generator (Agilent 33220A) as depicted in Fig. 4.8. Such voltage can take any arbitrary waveform designed by the user. In our experiment, we use Matlab to send the desired waveforms $V(t)$ to the function generator. As aforementioned, since $\kappa(t) \propto I(t)$ the trapping potential evolves accordingly. More details are given in section 4.3.2.

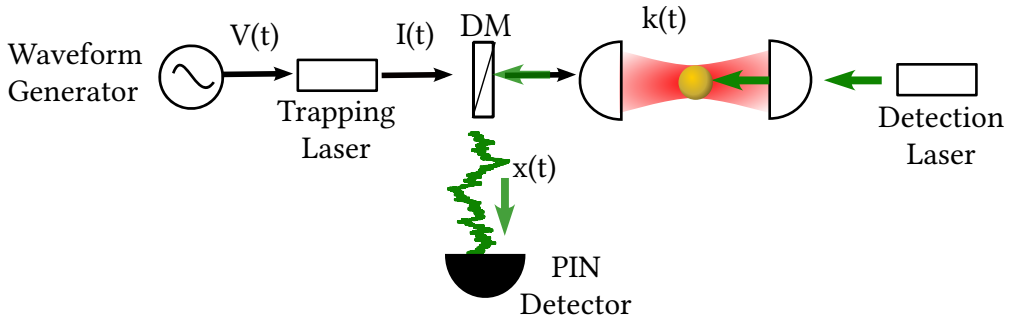

FIGURE 4.8: Set-up scheme showing how the trap stiffness $\kappa(t)$ is modulated and how the instantaneous position $x(t)$ of the bead under the protocol is independently detected. The computer programmed waveform is sent as a time-varying voltage $V(t)$ to the trapping laser. An auxiliary laser, arriving from the opposite direction of the propagation of the trapping beam probes the position of the particle. The scattered light by the particle is sent to a PIN photodiode by means of a dichroic mirror (DM) that separates the trapping beam and the scattered detection beam containing the bead fluctuations.

We first implement a STEP protocol that drives the system from $\kappa_i = 4$ to $\kappa_f = 6\,\mathrm{pN}\mu\mathrm{m}^{-1}$, the compression factor is given by $\xi = \kappa_f/\kappa_i$. To ensure such an abrupt increase of κ, characteristic of a STEP protocol, the laser power has to increase in a time shorter than the equilibration time, which for our overdamped system is given by $\tau^f_{relax} = 2\gamma/\kappa_f = 2.8\,\mathrm{ms}$. From our laser specifications (laser OBIS, Coherent), we expect to increase the laser intensity in less than $0.7\,\mu\mathrm{s}$, with the rise time of the voltage generator expected to be 5 ns. In practice, we observe that the STEP "instantaneous" transition takes place rather within $7.63\,\mu\mathrm{s}$, which still remains significantly shorter than τ^f_{relax}. On the other hand, in our approach where we repeat large number of compression cycles, the duration of the plateaus where $\kappa(t) = \kappa_i$ or κ_f has to be longer than the corresponding relaxation time (τ^f_{relax} for $\Delta\kappa > 0$ and $\tau^i_{relax} = \gamma/\kappa_i$ for $\Delta\kappa < 0$) in order to guarantee the proper equilibration of the system in between cycles. This approach is described in the top right panel of Fig. 4.9. There, the potential is maintained with a constant stiffness of $\kappa_i = 4\,\mathrm{pN}\mu\mathrm{m}^{-1}$ during 12.5 ms, followed by the abrupt change $\Delta\kappa$ and then $\kappa(t)$ is maintained again constant at the final value $\kappa(t) = \kappa_f = 6\,\mathrm{pN}\mu\mathrm{m}^{-1}$ during 12.5 ms before a new cycle starts.

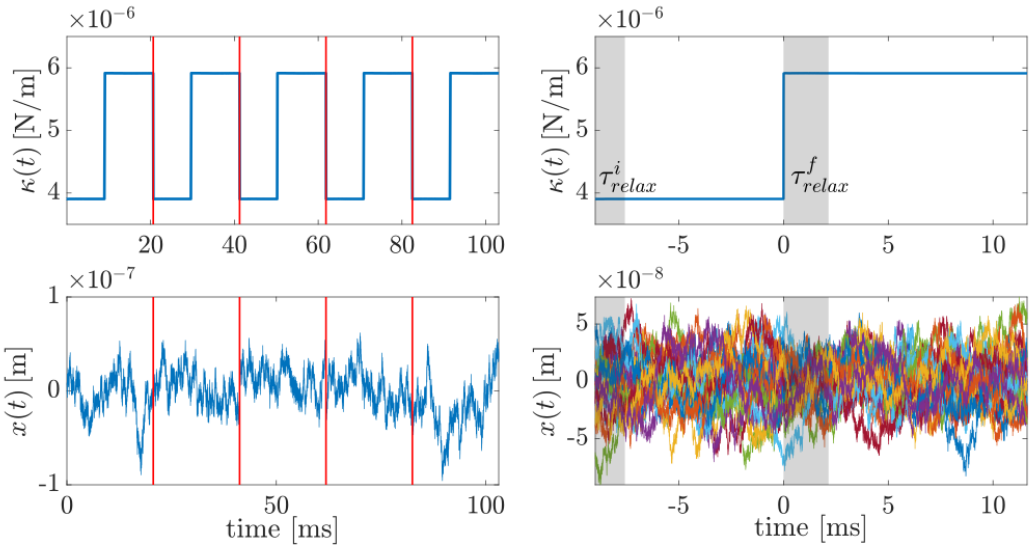

FIGURE 4.9: Procedure followed in order to obtain an ensemble of independent trajectories undergoing the same transformation. Several cycles of the STEP compression protocol $\kappa(t)$ are shown on top of the right panel. The corresponding stochastic position of the particle $x(t)$ experiencing the cyclic modulation of the potential stiffness appears in the bottom. The red vertical lines depict how to section the long temporal trace in order to obtain the ensemble of trajectories undergoing a single STEP as illustrated on the right panel. The shaded areas indicate the timescale at which the system is out-of-equilibrium. The first zones, $t \leq |\tau^f_{relax}|$ and $t \leq |\tau^i_{relax}|$, are removed before analysis.

When the system is at thermal equilibrium with κ fixed, constructing the occupation probability $\rho(x_j(t))$ from a single trajectory will be the same as constructing an occupation probability from an ensemble of trajectories at a given time instant t_i, $\rho(x_j(t)) = \rho(\{x(t_i)\})$. However when the stiffness becomes time dependent $\kappa = \kappa(t)$ this is no longer the case, because the system now is not stationary. In such situation it makes no more sense to construct an occupation probability from a single trajectory. One has to resort to an ensemble of trajectories, that is, a set of trajectories subjected to the same change of the control parameter, and to evaluate the distribution for a particular time instant t_j.

Under trapping laser intensity modulations, the instantaneous axial motion $x(t)$ of the bead is monitored using an auxiliary laser propagating in the opposite direction of the trapping beam, cf. fig. 4.8. With this additional laser we construct an ensemble of trajectories by recording the instantaneous position of the particle undergoing a cyclic change of potential, with a driving protocol repeated $N = 2 \times 10^4$ times. The time series of the position measurements constitutes a long temporal trace $x(t)$ that can be sectioned into trajectories of equal length $\{x_i(\tau)\}$ $(i = 1..N)$, each corresponding to a single cycle of the compression protocol. Under proper sectioning as discussed above, the trajectories can be considered independent of each other, and all starting with initial points drawn from the same probability distribution $\rho(\kappa_i, x)$. On the left panel of Fig. 4.9, we can see several cycles of the STEP protocol driving the system

from κ_i to κ_f and the corresponding stochastic position of the particle experiencing the cyclic modulation of stiffness. The figure on the right shows a single cycle of $\kappa(t)$ which represents the desired STEP protocol, and below, the ensemble of 2×10^4 independent trajectories that correspond to a single cycle. It is on this ensemble that the occupation probability $\rho(\{x(t_i)\})$ is constructed.

4.3.2 Calibration

When modulating the trapping beam intensity according to the prescribed protocol, the trapping laser is operated externally with a voltage generator and the intensity $I(t)$ is proportional to the voltage $V_{\text{mod}}(t)$ provided. To determine the conversion factor between $\kappa(t)$ and $V_{\text{mod}}(t)$, a calibration is performed prior to the experiment. The procedure consists in measuring the trap stiffnesses associated with a series of consecutive DC voltages applied to the laser. The calibration curve shown in the left panel of Fig. 4.10 corresponds to a linear fit of the evolution of the measured trap stiffness as a function of the DC voltages. The shaded area represents a 95% confidence interval for the estimated linear regression parameters taking into account the weights of the uncertainties of the individual κ points. The errorbars of the data points are determined by combining the error of the Lorentzian fit of the PSD and the uncertainty on the Stokes drag $\gamma = 6\pi R\eta$ due to the polystyrene sphere radius dispersion $\delta R/R = 2.8\%$.

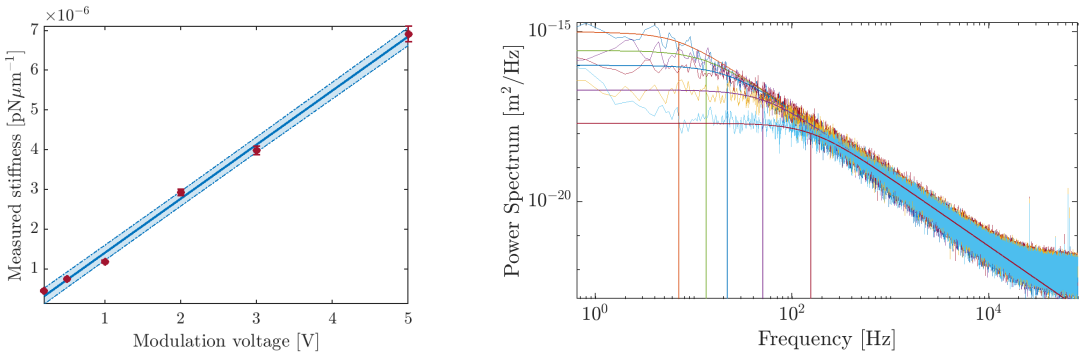

FIGURE 4.10: Left panel: Calibration of the function generator voltages. The red symbols represent the measured values of κ extracted from the PSD's, shown in the right panel, as a function of the DC voltage that fixes the laser intensity. The shaded area depict the linear fit confidence interval. Right panel: The motional power spectra for the different steady trapping laser intensities, the solid lines are the Lorentzian fits and the vertical represent the location of f_c of each fit.

Such calibration is also useful for determining the limits of stiffness variations that can be reached with our system and design the protocols accordingly. Because of the thermal equilibration waiting times, the time intervals during which $\kappa(t)$ is kept constant will depend on the specific values of κ_i and κ_f, thus having an impact on the duration of the cycles and the total experimental time. Such constraints are important to identify.

4.3.3 Stochastic energetics

As we have quickly mentioned above, it is possible to give a thermodynamic interpretation to a single stochastic trajectory, Ken Sekimoto [21, 41] proposed that stochastic processes, for example described by Langevin equations, can be viewed at an intermediate level which takes into account the effects of the microscopic degrees of freedom while allowing to introduce control parameters in the same way as in the context of classical thermodynamics. With this view and the fact that energy must be conserved also at the level of a single stochastic trajectory, Langevin equations are endowed with a thermodynamic interpretation for equilibrium and non-equilibrium processes.

The balance of forces of a Brownian particle in a harmonic potential $U(\kappa, x)$, at thermal equilibrium with a homogeneous stationary fluid is set by the Langevin equation:

$$-\gamma\frac{dx}{dt} - \frac{dU}{dx} + F_{\text{th}}(t) = 0 \tag{4.10}$$

where $\gamma\dot{x}$ is the frictional force, γ the Stokes drag coefficient, which relates the dissipative force to the fluctuating thermal force $F_{\text{th}} = \sqrt{2k_BT\gamma}\eta(t)$. The normalized white noise process $\eta(t)$ can be represented as a time-derivative of a Wiener process with the following properties:

$$\langle\eta(t)\rangle = 0 \qquad\qquad \langle\eta(t)\eta(t')\rangle = \delta(t'-t)$$

The Brownian system is assumed to be a spherical particle. In the overdamped regime and at equilibrium (no work exerted on the system) any change in the internal energy of this system is mostly due to changes in the potential energy, $dE = dU$, considering variations in kinetic energy negligible.

At thermal equilibrium, any infinitesimal change in the bead's position within the potential, $dx(t)$, is driven by thermal fluctuations via $F_{\text{th}}(t)$. Since there are no external force sources acting on the particle and since the potential is fixed, equation 4.10 can be regrouped and interpreted as an infinitesimal variation in potential energy due to heat exchanged with the bath [14, 41]:

$$\underbrace{\frac{dU}{dx}dx(t)}_{dU} = \underbrace{\Big(-\gamma\frac{dx}{dt} + F_{Th}(t)\Big)\circ dx(t)}_{-\delta Q} \tag{4.11}$$

hence, dU and δQ become stochastic quantities due to the Langevin force $F_{\text{th}}(t) = \sqrt{2k_BT\gamma}\eta(t)$. We adopted the convention of a positive sign when the heat flows from the system to the bath. We will use the notation $q = Q[x(t)]$, $u = U[x(t)]$ to emphasize that the energetics are expressed at the level of a single trajectory $x(t)$.

In our experiments, because the bead is trapped far from any wall and is not subject to multiplicative noise [153], γ is independent of x and t. The stochastic integrals are

written in the Stratonovich form[2], denoted with the symbol $\circ$, which corresponds to employing the usual rules of integration. The same assumptions prevail in the rest of the manuscript and we will therefore drop the symbol $\circ$ from now on. (See Appendix A).

Injecting work into the system

The same reasoning employed in equation 4.11 can be extended to the case in which the trap stiffness κ, i.e. the external control parameter, is varied from κ_i to $\kappa_f > \kappa_i$ according to a driving protocol $\kappa(t)$. Now that in our case of a harmonic potential, $U = \frac{1}{2}\kappa x^2$ depends on $\kappa(t)$ and $x(t)$, the dynamical change in the potential energy is:

$$dU = \frac{\partial U}{\partial \kappa} d\kappa + \frac{\partial U}{\partial x} dx \tag{4.12}$$

Combining eq. 4.12 with the energetic balance defined previously eq. 4.10:

$$\underbrace{(-\gamma \frac{dx}{dt} + F_{\text{th}}(t))dx}_{-\delta q} = dU \underbrace{-\frac{\partial U}{\partial \kappa} d\kappa}_{\delta w}, \tag{4.13}$$

we arrive with eq. 4.13 to the first law of stochastic thermodynamics, with a microscopic expression for the work exerted on the system when the control parameter changes by a small amount dk.

The work performed along the trajectory of duration $\tau = t_f - t_0$ when the control parameter is increased from κ_i to κ_f depends on the specific trajectory $x(\tau)$, therefore it is expressed as a functional of the trajectory:

$$w[x(\tau)] = \int_{\kappa_i}^{\kappa_f} \frac{\partial U}{\partial \kappa}\, d\kappa(t) = \frac{1}{2} \int_{t_0}^{t_f} \frac{d\kappa}{dt} x^2(t)\, dt, \tag{4.14}$$

where the last equality corresponds to the a harmonic trapping potential $U(\kappa, x) = \frac{1}{2}\kappa x^2$.

In order to extract the heat dissipated along the trajectory, we resort to the chain rule of the internal energy, equation 4.12, and write:

$$q[x(\tau)] = \int_{x(t_0)}^{x(t_f)} \frac{\partial U}{\partial x} dx(t) = -\frac{1}{2} \int_{t_0}^{t_f} \kappa(t) \frac{d(x^2(t))}{dt} dt. \tag{4.15}$$

[2]In Stratonovich calculus, the discretization of integrals is as following [27, 36]:

$$\int f(x(t)) \circ dx(t) = \lim_{\Delta t \to 0} \sum f(\overline{x}(t))(x(t + \Delta t - x(t)))$$

with $\overline{x}(t) = \frac{x(t)+x(t+\Delta t)}{2}$.

This method allows one to extract the heat simply from the particle's trajectory and the control parameter, without having to evaluate the stochastic thermal force.

Numerically, we can compute the integrals, eq. 4.14 and eq. 4.15, as definite integrals or as cumulative integrals. In the first case, the integral over the duration of the entire process gives a single value, which is the total work w_{tot} or total heat q_{tot} associated to that particular trajectory $x(t)$. Obviously, thermal fluctuations lead to different total values of the energetics. When computing the total values for many realizations, one can construct a probability distribution of such total values, q_{tot} and w_{tot}. The probability distributions of such values are shown in Fig. 4.11 below. In the case of the (internal) potential energy, since there is no integral to compute, and Δu is independent of the path taken, the values for the total internal energy change over an interval $\tau = t_f - t_i$ can be obtained as $\Delta u = u(\kappa(t_f), x(t_f)) - u(\kappa(t_i), x(t_i))$. By evaluating the distributions $P(q)$ and $P(u)$, it is not possible to detect the effect of the STEP protocol because thermal fluctuations induce larger fluctuations of q_{tot} and u_{tot}, as can be seen by comparing the distribution of the total work values $P(w)$, whose largest fluctuation is about $3\,\mathrm{k_B T}$.

On the other hand, when computing the cumulative integral, one obtains a sequence of values $\{q(t_j)\}_j$ resulting from the cumulative integral from t_0 to $t_0, t_1, t_2, t_3, t_4, ..., t_f$ that grows sequentially. This is considered as a stochastic heat trajectory $q[x(t)]$ associated to a single trajectory $x(t)$ (and similarly for the work $w[x(t)]$), as shown in Figs. 4.12 and 4.13. The stochastic functional of the internal energy, $u[x(t)]$, is trivially obtained from the product of $\kappa(t)$ and $x^2(t)$, as $u[x(t)] = \frac{1}{2}\kappa(t)x^2(t)$.

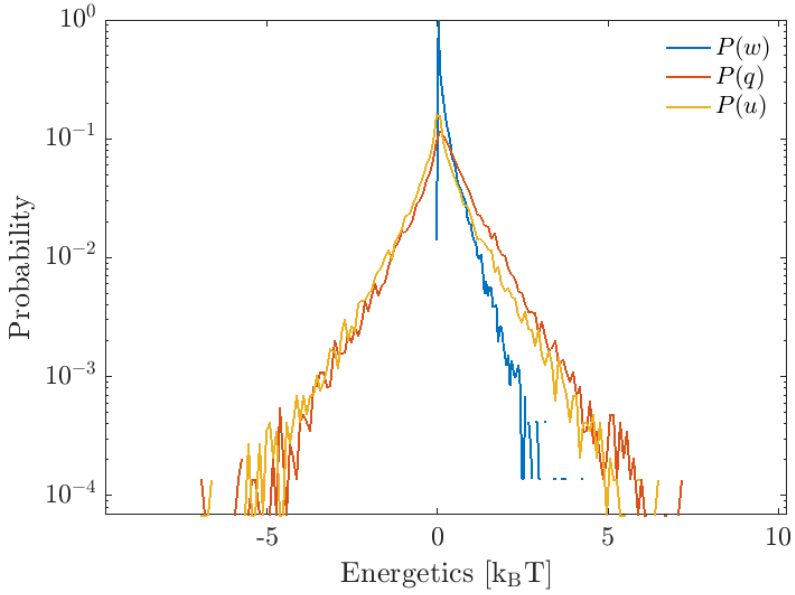

FIGURE 4.11: Upon repetitions of the STEP protocol, we obtain the total values of heat, work and internal energy for each trajectory. The blue curve represents the distribution of w_{tot}, the orange curve the distributions of the total heat and the yellow curve the internal energy change. The $y-$axis is in logarithmic scale.

Fig. 4.12 displays the instantaneous fluctuations of the potential energy as the particle explores the fixed harmonic potential. The potential energy $u[x(t)]$ is calculated as $\kappa(t)x^2(t)/2$ for constant $\kappa(t) = \kappa_i$. In this given realization, we can observe fluctuations of the potential energy that are as large as $2\,k_BT$. The stochastic heat $q[x(t)]$ is calculated as the cumulative integral $-\frac{1}{2}\int_{t_0}^{t_f} \kappa(t)\frac{d(x^2(t))}{dt}dt$ for constant $\kappa(t) = \kappa_i$.

Since the system is at thermal equilibrium, the strong coupling with the bath ensures that the dissipated heat instantaneously compensates the fluctuations of energy. This can be seen with the two curves associated respectively to $q(t)$ and $u(t)$ that mirror each other. The fluctuations of each of these functionals are constrained: the heat is defined negative so that its fluctuations can never be positive, and conversely, energy fluctuations never go negative. Their sum $\delta[x(t)] = q[x(t)] + u[x(t)] - w[x(t)]$ $(w[x(t)] = 0)$ is centered to zero as expected from the first law of thermodynamics, showing the consistency of such a trajectory-dependent view with thermodynamic balance.

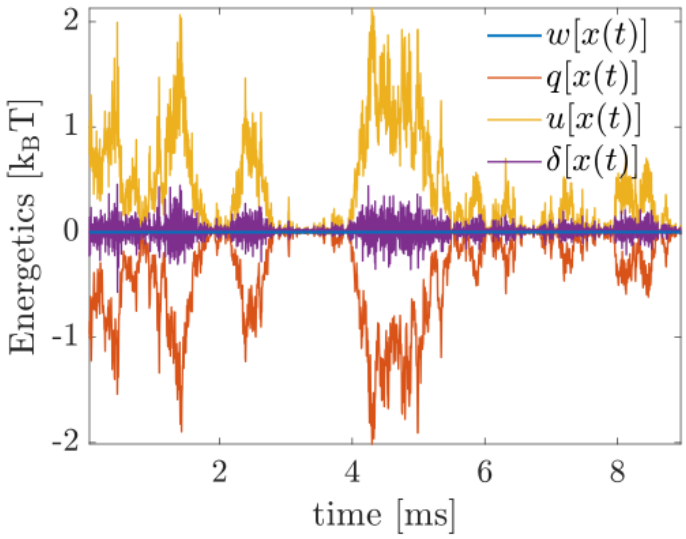

FIGURE 4.12: When the Brownian system is at thermal equilibrium, the increase in the potential energy of the system along a single trajectory $u[x(t)]$ (orange curve) is compensated by the heat dissipated to the bath $q[x(t)]$ (in blue). The energy balance is confirmed at the level of a single trajectory, $q[x(t)] + u[x(t)] = \delta[x(t)]$ centered to zero (in yellow).

We now examine a case in which work is injected to the system. Fig. 4.13 displays the temporal fluctuations of the different energetics, u, q, w for a single realization $x(t)$, when the trap undergoes a STEP compression. The internal energy and the heat are calculated as explained in the previous paragraph but considering now a time-dependent $\kappa(t)$. The stochastic work is computed as the cumulative integral of eq. 4.14. In this realization, the work exerted on the system, $w[x(t)]$, is dissipated into the surroundings in the form of heat. As expected for an isothermal process, the internal energy does not change, besides evidently, the fluctuations induced by $F_{\rm th}(t)$, which are also compensated by the heat released to the bath. At every given instant, the trapped bead receives a kick from the thermal bath that increases its potential energy. This gain in potential energy is then released as heat (by several collisions with the surrounding molecules of the bath) in a timescale given by $\sim \gamma/\kappa_f$.

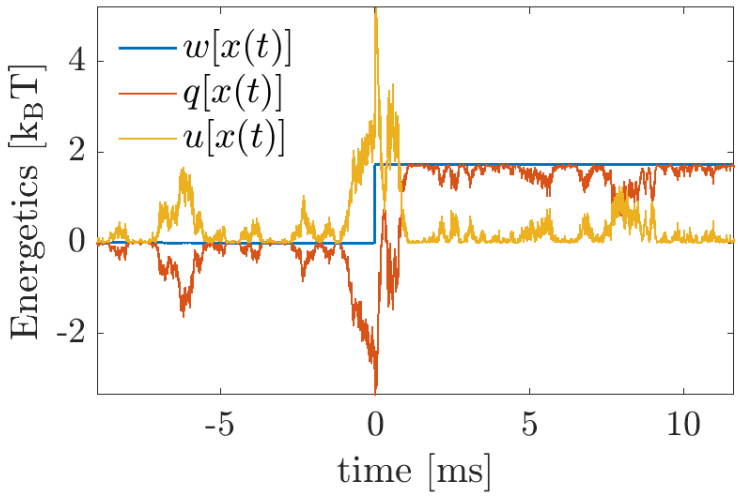

FIGURE 4.13: Top panel: Temporal fluctuations of heat, $q[x(t)]$ (orange), work $w[x(t)]$ (blue), and internal energy $u[x(t)]$ (yellow) for a single trajectory $x(t)$ undergoing a STEP protocol $\kappa(t)$. In this out-of-equilibrium situation we observe that w is totally dissipated by q.

As expected for an isothermal process, one sees no change in the internal energy in Fig. 4.13 when comparing both sides of the STEP. The isothermality is observed for several realizations of $x(t)$ upon compression with the STEP protocol, as shown in Fig. 4.14, where the temporal traces of the internal energy present fluctuations whose lower bound is zero. Superimposed to the single realizations is the ensemble average of the internal energy over 2×10^4 trajectories, see below. Taking the ensemble average, we can see that the fluctuations wash out, the cumulative temporal evolution of the ensemble average validates the isothermal character, $\Delta U = 0 \Leftrightarrow W = Q$, of the process almost at all times. For such an abrupt switch of the control parameter, with the transition from κ_i to κ_f happening in less than τ_{relax}, the overdamped system is driven out of equilibrium, and relaxes to the new equilibrium state in a time-scale[3] of the order of γ/κ_f. For times right after the transition, that are shorter than the relaxation time, the applied work is not compensated by the dissipated heat. As a consequence, a transient change in internal energy occurs. Fig. 4.15 below shows, respectively, the work and heat extracted for different realizations of the process $x(t)$ undergoing a STEP protocol. The temporal evolution of their respective ensemble averages is superimposed to the individual trajectories.

[3]The notion of the relaxation time between two equilibria will be discussed in detail in chapter 5.

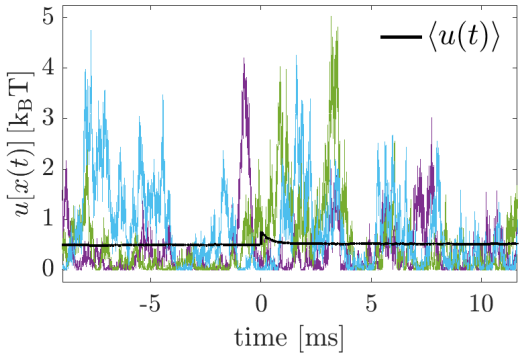

FIGURE 4.14: Several realizations of the internal energy of the system, when the trap is compressed with a STEP protocol. The bold black line represents the ensemble average of the cumulative internal energy extracted from 2×10^4 trajectories.

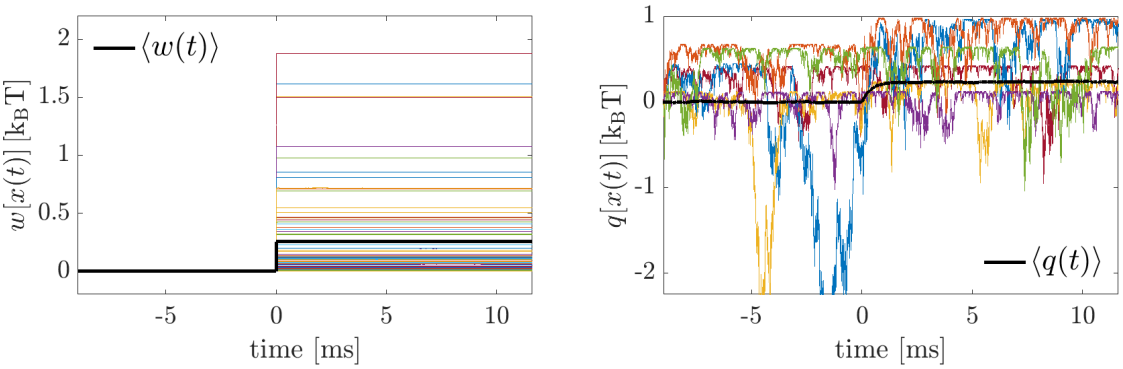

FIGURE 4.15: Heat and work trajectories for different cycles of the STEP protocol, that drives the stiffness of the confining potential from κ_i to κ_f. The bold black solid lines represent the ensemble averages, $\langle w(t) \rangle$, $\langle q(t) \rangle$.

The different heat trajectories display very large fluctuations, which are constrained by the temperature T and κ. From one realization to another, only the magnitude of the work $w[x(t)]$ corresponding to the STEP fluctuates. Each trajectory appears very smooth, without significant fluctuations over time that are comparable to the amplitude of the fluctuation at the transition. This can be easily understood from the fact that when $\kappa(t)$ is constant, no work is applied. Since the derivative $d\kappa/dt$ for a STEP protocol is zero everywhere except at the transition, the integral 4.14 only evaluates the fluctuation of $x^2(t)$ at the transition time as depicted in Fig. 4.16 below.

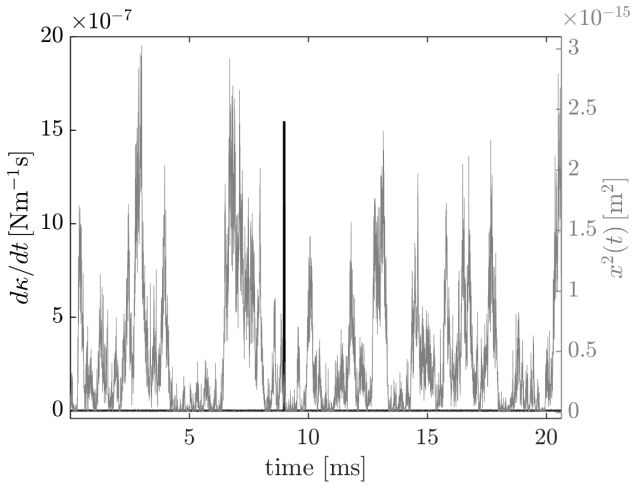

FIGURE 4.16: Illustration of the terms to be evaluated in the work integral, eq. 4.14 for a STEP protocol at the level of a single stochastic trajectory. The black solid line represents $d\kappa/dt$ and $x^2(t)$ is shown as the grey, highly fluctuating curve.

First law of thermodynamics for stochastic trajectories

Now that we have identified the stochastic heat, work and internal energy at the level of single trajectories we can proceed to verify the trajectory-dependent version of the first law. In realizations such as the ones displayed in Figs. 4.12 and 4.13, the first law is perfectly validated at the level of single trajectories, in those cases, the trajectory-dependent sum $\delta[x(t)]$ of $q[x(t)]$,$u[x(t)]$ and $w[x(t)]$ has a zero temporal mean with some instantaneous small fluctuations. However when observing $\delta[x(t)]$ for several realizations of the compression process as shown in Fig. 4.17, we can see that for some realizations the instantaneous fluctuations of $\delta[x(t)]$ do not fall at zero for all cycles. This indicates that some additional energy must be taken into account when studying the first principle in this particular experiment.

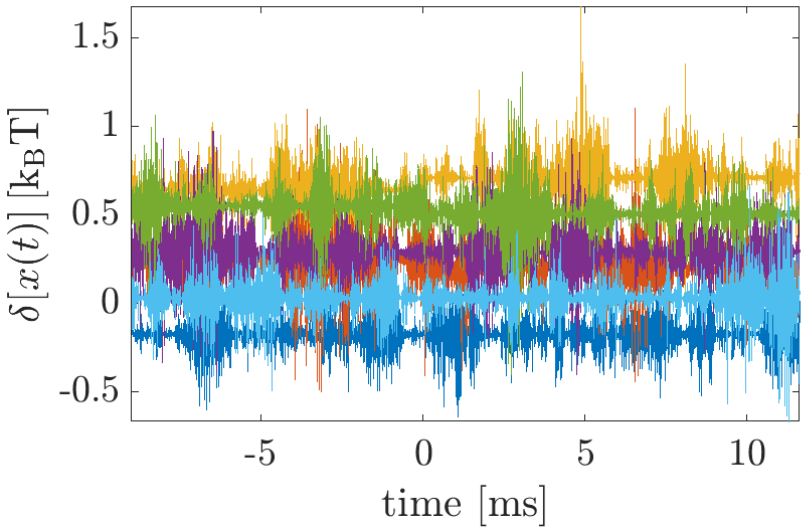

FIGURE 4.17: Trajectory-dependent deviation to the first law, $\delta[x(t)] = q[x(t)] - w[x(t)] + u[x(t)]$ for different trajectories undergoing the same STEP compression.

To evaluate the precision within which we can measure the conservation of energy of the system, we adopt a similar approach as the one described in reference [70]. We calculate the total values of the injected work w_{tot} and dissipated heat q_{tot} corresponding to a single cycle, and $\Delta u = u(\kappa_f, x(t_f), t_f) - u(\kappa_i, x(t_i), t_i)$ for the total energy difference. We then compute these values for all the cycles. From each of these values we can extract the corresponding deviation $\delta = q_{tot} - w_{tot} + \Delta u$ and evaluate its distribution $\rho(\delta)$, as shown in the right panel of Fig. 4.18.

How the total values of the thermodynamic quantities, q_{tot}, w_{tot} and Δu, fluctuate from one realization to the next is shown in Fig. 4.18. As expected, the distribution of the values of the deviation, $\delta = \Delta q - \Delta w + \Delta u$, is centered at zero, validating the fact that the first law holds on average. The distribution is symmetric around zero with a standard deviation of $0.17\,k_B T$, associated with the experimental precision that the setup offers, taking into account discretization effects due to the measured trajectory with a finite sampling frequency, $f_s = 2^{18}$ Hz, and due to the numerical computation of integrals eq. 4.15 and eq. 4.14.

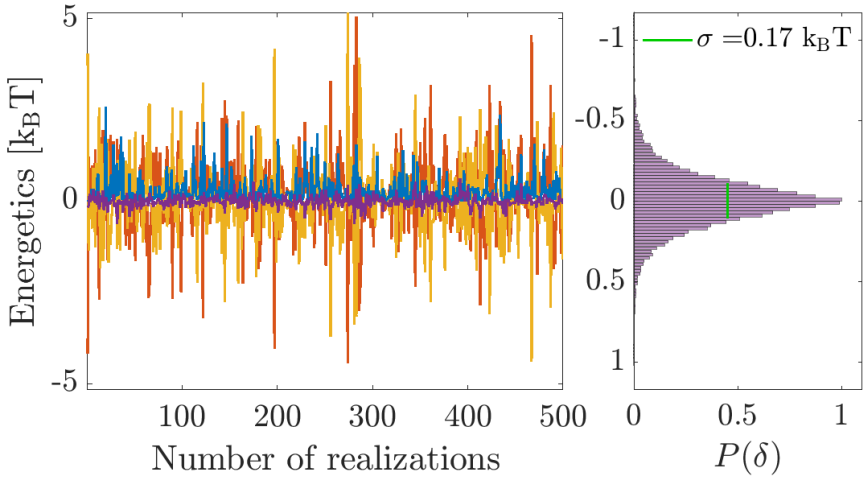

FIGURE 4.18: Left panel: Fluctuations, from one cycle to another, of the total heat (orange), total work (blue) and total energy change (yellow) of the system. In dark purple are the corresponding fluctuations of the values of δ from one cycle to the next. Right panel: Distribution of the residue $\delta = q_{tot} - w_{tot} - \Delta u$ to the first law. The variance of the distribution is $0.17 k_B T$.

4.3.4 Ensemble behavior

Taking the ensemble average over the 2×10^4 trajectories of thermodynamic functionals reveals the deterministic behavior of the energetics at play when performing a sudden trap compression. The temporal evolution of the mean cumulative heat, work and internal energy are shown in Fig. 4.19 below.

Because of the instantaneous switch of $\kappa(t)$, the work shows an abrupt increase from $0\,\mathrm{k_B T}$ (equilibrium) to $0.25 \pm 0.02\,\mathrm{k_B T}$, as expected when going from the single trajectory work:

$$w(t) = \int_{\kappa_i}^{\kappa_f} \frac{\partial U}{\partial \kappa} d\kappa = \frac{1}{2}(\kappa_f - \kappa_i) x^2(t),$$

to the ensemble average:

$$\langle w(t) \rangle = \frac{1}{2}(\kappa_f - \kappa_i) \langle x^2(t=0) \rangle$$

with $\langle x^2(t=0) \rangle$ given by the equipartition theorem:

$$\langle x^2(t=0) \rangle = \frac{k_B T}{\kappa_i}.$$

This leads to measure an ensemble averaged work equal to:

$$\langle w(t) \rangle = \frac{k_B T}{2} \frac{(\kappa_f - \kappa_i)}{\kappa_i} = 0.25\,\mathrm{k_B T}.$$

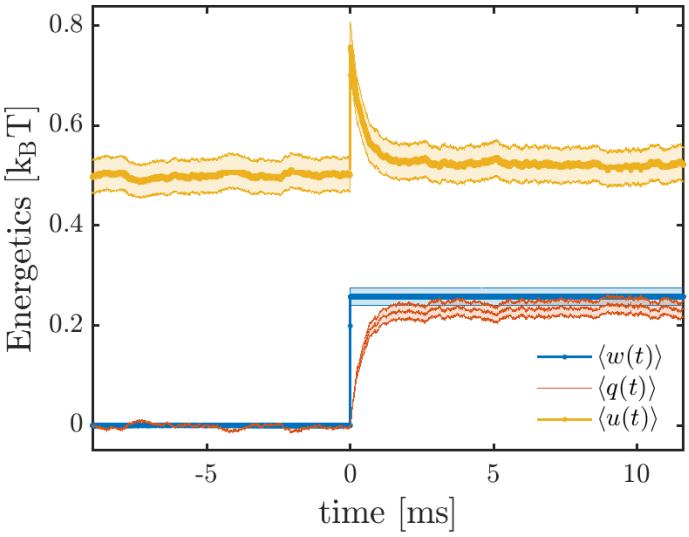

FIGURE 4.19: Temporal evolution of the mean cumulative work (blue), heat (orange) and internal energy (yellow) associated with the STEP protocol for increasing κ_i to $\kappa_f = 1.5\,\kappa_i$. The shaded areas represent the combination of statistical and systematic uncertainties detailed below in the main text.

The behavior of the mean cumulative heat $\langle q(t)\rangle$ and the mean cumulative energy $\langle u(t)\rangle$ can be analyzed together. As κ is switched, a sudden amount of work is injected into the system. For an isothermal transformation like this one, such added source of energy must be dissipated into the bath in order to leave the internal energy unchanged. This compensation, however, is not instantaneous. Just as in the case of the ideal gas, the system is driven out of equilibrium and displays a transient increase in internal energy accompanied with a slow release of heat that take place during an interval of time given by τ_{relax}. Once the system reaches equilibrium, the energy exchange ceases and $\langle q(t)\rangle = \langle w(t)\rangle$ as expected.

In our experiments, we consider that the temperature of the surrounding bath remains unchanged during the whole experiment. Consequently, as discussed in the gas-piston model, the internal energy is likely to remain unchanged during the process. Besides the transient characteristic of the out-of-equilibrium behavior, we expect that once the system is equilibrated in the new state, the corresponding internal energy is the same as before the STEP. Yet in Fig. 4.19, we can observe that this is not exactly the case. There remains a difference of ca. $0.03\,k_BT$ between the initial and final equilibrium values of the mean energies. Such a difference can be also spotted between the heat and work, once the system has relaxed in the new thermal equilibrium, with $\langle w(t)\rangle \neq \langle q(t)\rangle$. Even though such discrepancy does not appear to be significant since it falls perfectly within the errorbars, it might still indicate that the total work could be slightly overestimated. A potential cause for a misestimation could be that the true stiffness of the trap has slightly departed from the initial calibration value. For computing the energetics, we use indeed the voltage waveform converted to stiffness

units by means of the prior calibration. Such a procedure therefore does not directly yield the measured stiffness. This is a difficulty that remains because extracting the stiffness instantaneously relies recording instantaneous positions. However, when the system is out-of-equilibrium, such a position-based extraction of the stiffnesses does not work because $\kappa(t)$ can change on shorter timescales than τ_{relax}.

4.3.5 Uncertainties

The confidence intervals represented as shaded surfaces in Fig. 4.19 combine the PSD calibration uncertainties of $x(t)$ and $\kappa(t)$ and the statistical uncertainties arising from averaging over the ensemble of trajectories.

A single stochastic trajectory, $w[x(\tau)]$, $q[x(\tau)]$ or $u[x(\tau)]$ computed from equations eq. 4.14 and 4.15, is subjected to calibration uncertainties of x and κ in the following way:

$$\delta w = \frac{1}{2}\int_{t_0}^{t_f}\left[\frac{d\delta\kappa}{dt}x^2(t) + \frac{d\kappa}{dt}\delta x^2(t)\right]\,dt \tag{4.16}$$

$$\delta q = -\frac{1}{2}\int_{t_0}^{t_f}\left[\kappa(t)\frac{d\delta x^2(t)}{dt} + \delta\kappa(t)\frac{dx^2(t)}{dt}\right]\,dt \tag{4.17}$$

$$\delta u = \frac{1}{2}\Big(\kappa(t)\delta x^2(t) + \delta\kappa(t)x^2(t)\Big). \tag{4.18}$$

The ensemble average of the work can be obtained as:

$$\langle w\rangle = \frac{1}{N}\sum_{i=1}^{N} w_i, \tag{4.19}$$

where w_i is the stochastic work of the $i-th$ realization of the protocol. The associated statistical uncertainty is then given by the statistical deviation of the mean:

$$\sigma_{\langle w\rangle} = \frac{\sigma_w}{\sqrt{N}} \tag{4.20}$$

with σ_w the estimator of the standard deviation:

$$\sigma_w = \sqrt{\frac{1}{N-1}\sum_{i=1}^{N}(w_i - \langle w\rangle)^2}. \tag{4.21}$$

Doing the same treatment for the uncertainties δw_i, we can combine in quadrature [154] the statistical and systematic uncertainties to obtain the total error as:

$$\Delta w = \sqrt{\sigma^2_{\langle w\rangle} + \langle\delta w\rangle^2 + \sigma^2_{\langle\delta w\rangle}}. \tag{4.22}$$

In the same way, $\langle q \rangle \pm \Delta q$ and $\langle u \rangle \pm \Delta u$ are calculated. These uncertainties appear as the shaded surfaces in Fig. 4.19.

4.3.6 Slow switching protocol

The premises of the ideal gas and the movable piston offer valuable intuition on the expected macroscopic behavior of our system. As discussed in the previous section, the first scenario we evaluated was the sudden compression of the trap, implemented with the STEP protocol, in which the stiffness is increased instantaneously[4], approximately 200 times faster than the characteristic time of the trap $\sim \gamma/\kappa_f$. With such a protocol, the system is driven out of equilibrium. For an abrupt increase of work, the mean cumulative energetics revealed a transient interchange of internal energy and released heat, taking place during the same characteristic time. Once the system reaches thermal equilibrium in the final state, the dissipated heat compensates the injected work to leave the internal energy unchanged in agreement with the first law of thermodynamics.

We now study the effects of a protocol analogue to the quasi-static transformation presented in section 4.2 for the gas-piston model. This protocol intends to keep the system at equilibrium at each instant of the transfer between the initial and final state. To this purpose, optical confinement has to be increased very slowly. To do so, we implement the simplest protocol, called a RAMP, in which κ_i evolves towards κ_f linearly during 28 ms, i.e. approximately during $10\,\tau_{relax}$. The calibrated waveform corresponding to one cycle of the RAMP protocol is contrasted with the STEP in Fig. 4.20. For a single cycle of the RAMP we can observe three cycles of the STEP. A single cycle of the RAMP protocol lasts 71 ms, with the intervals of constant κ, 25 ms for $\kappa(t) = \kappa_i$ and 18 ms for κ_f.

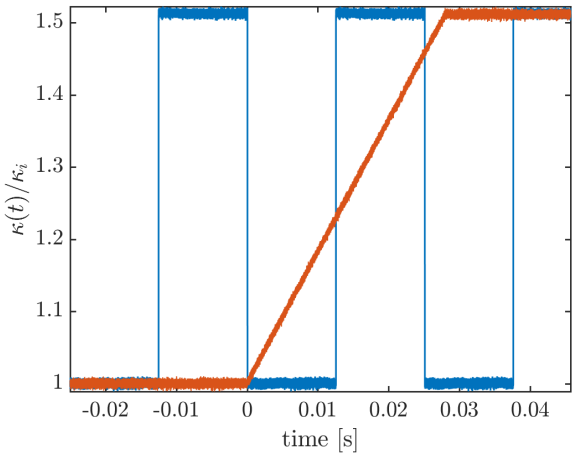

FIGURE 4.20: RAMP protocol (in orange), representing the quasi-static variation of a control parameter, on top of three cycles of the STEP protocol (in blue) for the same transition $\kappa_i = 4 \rightarrow \kappa_f = 6\,\mathrm{pN}\mu\mathrm{m}^{-1}$.

[4]For our experimental limitations, "instantaneously" means during 7.6 μs, to be compared with $\tau_{relax} = 1.4$ ms for a targeted $\kappa_f = 6\,\mathrm{pN}\mu\mathrm{m}^{-1}$.

The energetic fluctuations as the trap becomes progressively stiffer are shown in Fig. 4.21 for different repetitions of the protocol. Instantaneous fluctuations close to $6\,k_BT$ in internal energy are compensated by heat fluctuations. In contrast to the stochastic work trajectories of the STEP, $w[x(\tau)]$ of the RAMP fluctuates during the whole transition interval.

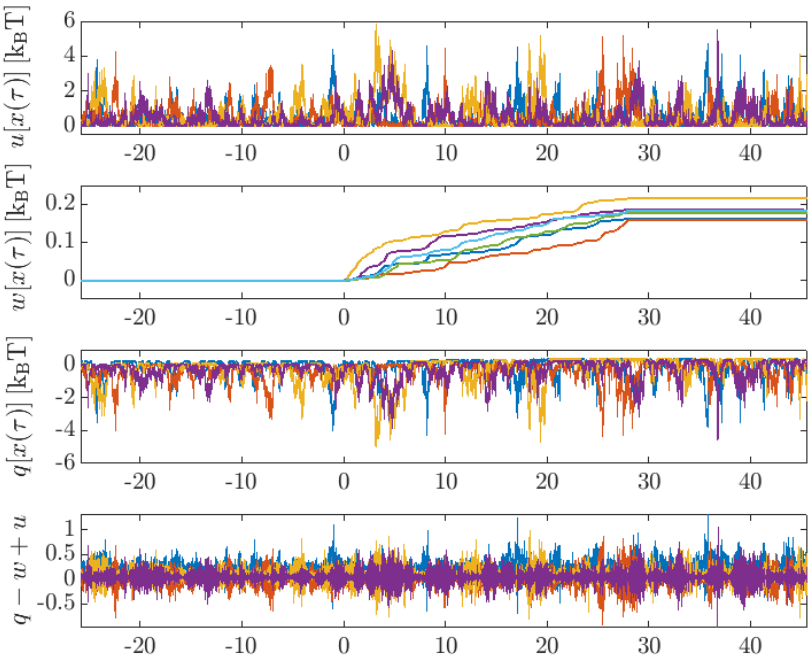

FIGURE 4.21: Several realizations of the stochastic energetics for different trajectories undergoing the RAMP protocol presented in Fig.4.20.

The probability distribution of the heat and work fluctuations for the STEP and RAMP protocols appear in fig.4.22. The distributions of heat fluctuations are similar for both protocols. Since these are large, and are compensated by the energy fluctuations, it is not possible to detect the influence of the driving scheme from distribution of the dissipated heat values. In contrast, work distributions show striking differences between the two protocols, the work fluctuations associated with the STEP protocol are significantly larger than in the case of the quasistatic drive. Already at the level of fluctuations we can conclude that the STEP protocol is more dissipative than the RAMP. From a linear response perspective, the dissipated work can be directly estimated from the variance of the fluctuations [8, 155, 156]:

$$W_{diss} = \frac{\sigma_W^2}{2k_BT} \tag{4.23}$$

which gives $W_{diss} = 0.07\,k_BT$ for the STEP and $0.001\,k_BT$ only for the RAMP, the latter value falling below the experimental uncertainties. The STEP protocol is roughly 50 times more dissipative than this particular RAMP protocol, for a 5 times faster

transformation, considering the transformation completed once the system is fully relaxed in the final state. At this point, we can thus clearly see that driving a system out of equilibrium results in inevitable dissipation.

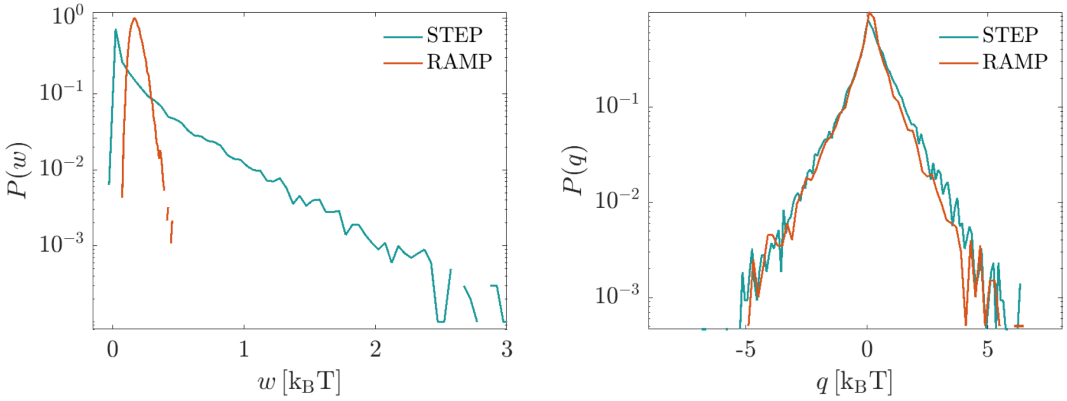

FIGURE 4.22: Probability distributions of the work (left panel) and heat fluctuations (right panel) for a STEP and a RAMP protocol.

On the macroscopic level, the behavior of the ensemble averages of the different cumulative energetics, $\langle w[x(t)]\rangle$,$\langle q[x(t)]\rangle$ and $\langle u[x(t)]\rangle$ are shown in Fig. 4.23. Unlike the STEP case, the internal energy stays constant during the entire RAMP transformation. The mean work is compensated by the mean heat at all times, and the system does not exhibit any significant departure from equilibrium. However, looking attentively, one can observe a small difference between the mean work and mean heat in the final state, as well as a slight deviation of the constant evolution of the mean internal energy. This change in internal energy is exactly the same as for the STEP. Fig. 4.23 confirms that $\Delta U = Q_{rev} + W_{rev} = Q_{diss} + W_{diss}$, that is, the energy difference depends only on the difference of states, unlike the heat and work which depend on the path taken during the transformation, which can be reversible (subscript rev) or dissipative ($diss$). Additionally, if the process is isothermal, we expect $\Delta U = 0$. This is practically verified, by measuring a deviation less than $0.02\,\mathrm{k_B T}$, which coincides exactly with the value of the experimental uncertainty. Such discrepancy is therefore not significant to be considered as a physical departure of equilibrium or even less as a change in the bath temperature. As discussed previously for the case of a STEP protocol, such a small deviation could be due to an overestimation of the work as a consequence of a wrong calibration of the stiffness or a degradation of the signal over time.

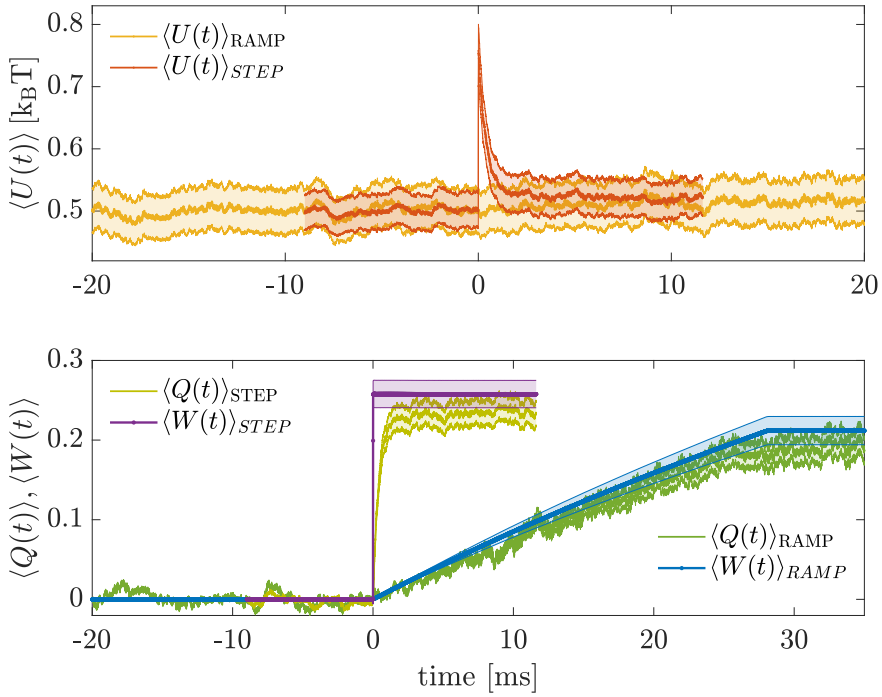

FIGURE 4.23: Comparison of the temporal evolution of the ensemble averaged cumulative energetics associated to the RAMP and STEP protocols.

By definition, there is no dissipation when performing a reversible transformation, thus the injected work is simply the free-energy difference between the initial and final states $\Delta F = F(T,\kappa_f) - F(T,\kappa_i)$, with $F(T,\kappa) = -k_BT \ln Z$ and $Z(T,\kappa)$ the partition function of an overdamped system:

$$Z(T,\kappa) = \int dx e^{-U(\kappa,x)/k_BT} = \int dx e^{\frac{1}{2}\frac{\kappa x^2}{k_BT}} = \sqrt{\frac{2\pi k_BT}{\kappa}} \tag{4.24}$$

$$\Delta F = -k_BT \ln \frac{Z(T,\kappa_f)}{Z(T,\kappa_i)} = k_BT \ln \sqrt{\frac{\kappa_f}{\kappa_i}}. \tag{4.25}$$

The expression for ΔF is very similar to the one for the compression of the ideal gas $\Delta F = Nk_BT \ln \xi$, with the stiffness equivalent $\sqrt{\kappa_f}/\kappa_i$ of the compression factor $\xi = V_f/V_i$. The free energy of the confined particle depends on the square-root of the potential stiffness just as the free energy of the confined gas depends on the position (volume) of the piston. Any driving scheme that performs the transition faster than the relaxation time will pay an energetic price which is quantified by the dissipative work $W_{diss} = W_{tot} - \Delta F$. The work the RAMP performs is $W_{tot} = 0.21 \pm 0.02\,\mathrm{k_BT}$ and the free energy difference, as calculated from eq. 4.25, is $\Delta F = 0.21 \pm 0.04$, validating that such protocol can be considered as reversible indeed. These values are also consistent with eq. 4.23.

4.4 Fluctuation theorems and the second law

The identification of work and heat at the level of single trajectories of the Brownian particle has given us some insight on the transformation between equilibrium states at two scales. At the macroscopic level, we have recovered for the trapped Brownian particle the deterministic behavior similar to the behavior of the compression of an ideal gas, by performing ensemble averages of the trajectory-dependent thermodynamic functionals. The microscopic behavior was investigated by analysing single events of the transformation. The specific distribution of work values obtained from different repetitions of the compression process is a signature of how irreversible the transformation is. When the compression is performed abruptly according to the STEP protocol, such distributions exhibit large tails with large fluctuating work values. When the system is driven from the initial to the final state while maintaining the system at equilibrium during the whole transformation, as done with the RAMP protocol, the fluctuations are relatively small. Thus large fluctuations are a direct consequence of driving the system out of equilibrium and are associated to inevitable dissipation.

One essential consequence of the stochasticity of the thermodynamic functionals is the existence of trajectories violating the Second Law. Such trajectories yield $W_{diss} < 0$ as illustrated in the result of the RAMP protocol, Fig. 4.5. It is possible to interpret such events as single realizations that convert all absorbed heat into useful work, a process forbidden by the Second Law and unimaginable at the macroscopic scale. Having seen that the dissipative work is directly related to entropy production, we can say that a quasi-static transformation as the RAMP protocol has a similar number of trajectories that consume entropy as trajectories that produce entropy. In contrast, as the driving protocol forces the system to depart from equilibrium, the number of events of entropy consumption decreases.

Fluctuations seem to provide essential and fundamental information on how thermodynamic irreversible behavior emerges from a stochastic system. Entropy being an extensive quantity, we can expect that as the system grows or as the process is observed during longer time intervals, realizations in which dissipation is negative decrease in number. The study of the distribution of such fluctuations can precisely show how fast this number of events decreases. This is precisely the purpose of Fluctuation Theorems (FT) that quantify the previous statement. The first FT [12] was originally derived in the context of non-equilibrium steady states of certain dissipative dynamic systems where the first violations of the Second Law were observed. Other approaches have then been developed towards more general stochastic systems in order to explain such symmetries. IN particular, FT were generalized to systems following Langevin-type dynamics [13].

Concretely, FT are exact relations expressing universal properties of the probability distribution $p(X)$ for trajectory functionals $X[x(t)]$ like work and heat [14]. They can be phenomenologically classified in "integral" and "detailed fluctuation theorems".

Integral fluctuation theorems are of the form:

$$\langle e^{-X} \rangle = 1 \tag{4.26}$$

for averages over many realizations of $X[x(t)]$. Detailed fluctuation theorems, formulated for the same observables, relate the probability distributions of X, and of itself under some symmetry transformation, typically time reversal, and can be written as [14]:

$$\frac{p(X)}{p(-X)} = e^{X}. \tag{4.27}$$

In most of the cases, the quantity in the exponent represents a convenient measure of the asymmetry of the system with respect to the transformation. In the case of time-reversal, such quantity is entropy increase, which in our case, is directly related to the dissipative work.

In this section we review a few FT relevant in the context of this manuscript. For the cases we have studied up to now, in which the system is driven between two equilibrium states, there exist two fundamental relations. The first, known as the Jarzynski equality, is classified as an integral fluctuation theorem, and the second, known as the Crooks Fluctuation Theorem, is more general and falls under the category of detailed fluctuation theorems. What is important however, is that both relations can be simply written in terms of dissipative work.

4.4.1 The Jarzynski equality

Up to now, we have seen how under repetition of the protocol $\kappa(t)$, either the STEP or the RAMP, measured work values fluctuate from cycle to cycle, with in average $\langle W \rangle \geq \Delta F$ (with the equality reached for the RAMP protocol). In both cases, at the level of single trajectories, there is a significant amount of trajectories for which $W < \Delta F$. The Jarzynski equality [149] tells us that if we average the exponential of all the fluctuating work values, this reduces to:

$$\langle e^{-W/k_BT} \rangle = e^{-\Delta F/k_BT} \tag{4.28}$$

or equivalently,

$$\langle e^{-W_{diss}/k_BT} \rangle = 1 \tag{4.29}$$

in which, $\langle\,\rangle$ denotes the average performed over a large number of experiments, repeated by following the same protocol $\kappa(t)$. This result holds for all nonequilibrium processes driven by any time-dependent perturbation. What is important is to note that this equality can only be true if there are trajectories for which $W_{diss} \leq 0$ [8]. This equality is not only a statistical generalization of the Second Law[5], but has an

[5]Which can be retrieved by using Jensen's inequality, $e^{\langle -W_{diss}/k_BT \rangle} \leq \langle e^{-W_{diss}/k_BT} \rangle \Rightarrow \langle W_{diss} \rangle \geq 0$.

additional powerful meaning: *"equilibrium information is subtly encoded in the microscopic response of a system driven out of equilibrium"* [47].

For this reason, the Jarzynski equality has proven to be very interesting to exploit for systems in which equilibration is difficult to characterize and/or when equilibrium quantities, such as free energies, are unknown. The Jarzynski equality actually explains how, through a series of perturbations that drive the system out of equilibrium, one can retrieve ΔF by applying any type of transformation. This approach was successfully demonstrated in the case of a RNA molecule, in which the free energy landscape was obtained by repeating a given stretching process [156]. Such results have impacted a lot the field of biomechanics and molecular motors as reviewed in this article [7].

Using a collection of measured work values w_{tot}, obtained while repeating on the optical trap the same protocol a large number of times, we are in position to study the convergence of the relation given in eq. 4.28, as a function of the number of trajectories involved in the ensemble average. We do this by comparing the two limits of continuous protocols: the instantaneous switch, i.e. the STEP protocol on the one hand, and the reversible switch, the RAMP protocol, on the other.

In our case, the simple nature of our system gives us access to ΔF, as explained above –see eq. 4.25. This allows us to determine how many realizations of the protocol are necessary in order to satisfy Jarzynski equality. Fig. 4.24 shows the convergence $\langle e^{-W/k_BT} \rangle \to e^{-\Delta F/k_BT}$ using work values extracted from the STEP and RAMP protocols.

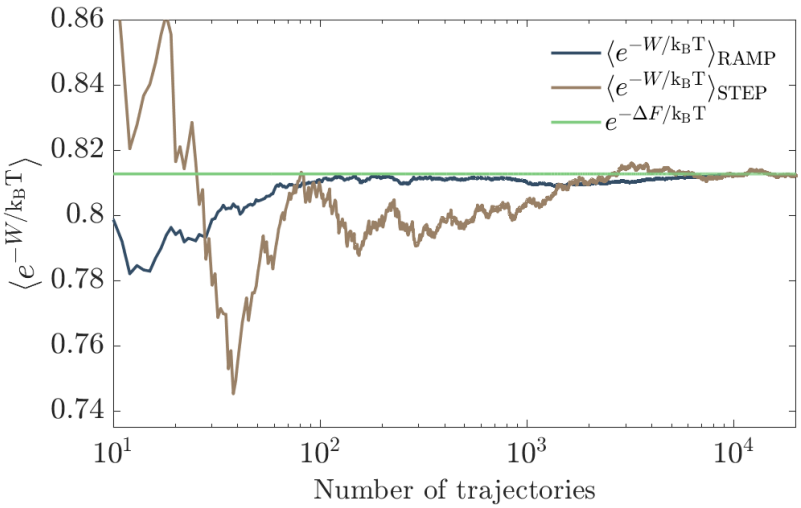

FIGURE 4.24: Convergence of the Jarzynski equality, $\langle e^{-W/k_BT} \rangle \to e^{-\Delta F/k_BT}$ (green horizontal line) both for the STEP (brown curve) and the RAMP (dark blue) driving protocols. The size of the ensemble of increments (number of trajectories) are shown in logarithmic scale.

For measurements performed with the STEP protocol, more than 5000 trajectories are needed to estimate the free energy difference, whereas with the RAMP protocol, the

convergence to $e^{-\Delta F/k_BT}$ is reached after roughly 200 realizations only. This difference naturally stems from the fact that with more dissipation resulting from the driving protocol, less chances of finding trajectories with $W_{diss} < 0$ are. In fact, the maximal number of violating trajectories occurs in the reversible limit, in which *"the number of trajectories for which $W_{diss} < 0$ equals the number of trajectories with $W_{diss} > 0$"* [8]. In our case, the shorter the transition between the two equilibrium states set by the control parameter is, the more trajectories are needed to estimate ΔF. For the RAMP protocol, the distribution of work values measured for the different trajectories were shown in Fig. 4.5 above.

After roughly 50 trajectories convergence is attained from below $e^{-\Delta F/k_BT}$, for both protocols, this is due to the dominating contribution of trajectories with $W > \Delta F$, as expected from Jensen's inequality [157], $f(\langle x \rangle) \leq \langle f(x) \rangle$, where f is a convex function.

For measurements obtained with the STEP protocol, we can see that $\langle e^{-W/k_BT} \rangle$ as a function of the number of trajectories involved in the average, fluctuates more significantly than for the RAMP case. However, in both protocols, the occurrence of sudden jumps through the convergence suggest events for which $W < \Delta F$. Such events have large contributions to the exponential average which, as such, is very sensitive to rare events [158, 159].

4.4.2 Crooks Fluctuation Theorem and Stochastic Entropy Production

The possibility to observe violations of the Second Law when compressing the optical trap is reduced as more dissipation takes place during the process. In a dissipative transformation, as the system grows, or as the process is observed during longer times, the probability of observing trajectories with negative dissipation becomes exponentially smaller than the probability of observing trajectories with positive dissipation. The FT particularly relevant for our system that quantifies this is the Crooks Fluctuation Theorem (CFT) [15]. Inspired by the general form of already existing entropy production FT, G. Crooks found a symmetry relation for the probabilities of entropy production in the forward and time-reversed transformation of a stochastic system driven by a time-dependent perturbation. For systems that depart from equilibrium and whose entropy production is related to W_{diss}, as in the case of the gas-piston model discussed in section 4.2, the CFT can be formulated in terms of the work distributions evaluated along the forward and reverse paths.

Consider the trap compression we have been studying. As explained above, our experiments build ensemble averages by repeating the chosen protocol $\kappa(t)$ in a cyclic manner. This method leads to passing periodically through a sequence of equilibrium states $\kappa_i \to \kappa_f \to \kappa_i$. Depending on where we section the cycles of $\kappa(t)$, we can have access to the process in the forward direction or its reverse. The forward protocol is

the one we have been examining until now, namely the trap compression, in which $\kappa(t)$ is varied from κ_i to κ_f. In the reverse process, which depicts a trap expansion, $\kappa(t)$ evolves from κ_f to κ_i, written as $\kappa_R(t) = \kappa_F(\tau - t)$, with F and R denoting "forward" and "reverse" and τ the total duration of the forward protocol. The time evolutions of the control parameter of such conjugate processes are shown in Fig. 4.25 below.

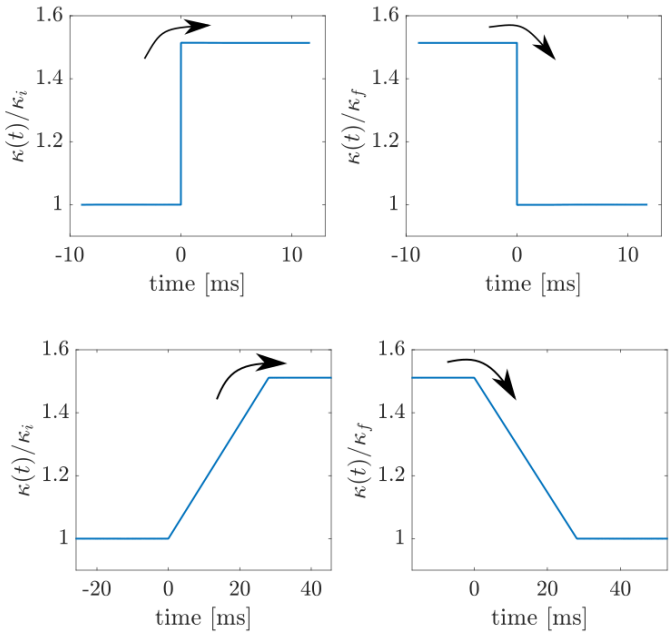

FIGURE 4.25: Forward and reverse paths of the work parameter of the STEP and RAMP protocols.

The distribution of work values obtained from a large number of repetitions of the protocol $\kappa(t)$ in the forward $P_F(W)$ and time-reversed $P_R(-W)$ paths are related according to CFT as [15]:

$$\frac{P_F(W)}{P_R(-W)} = e^{W_{diss}/k_BT}. \tag{4.30}$$

Therefore, the more dissipation, the more these distributions differ from each other [14]. Figure 4.26 below shows the experimental verification of eq. 4.30 for the trap compression and expansion following the STEP protocol.

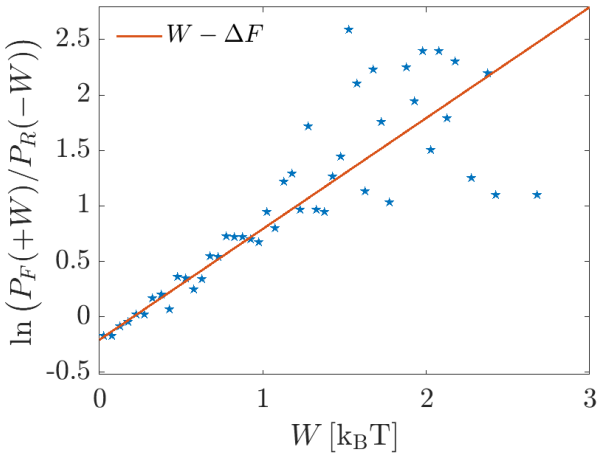

FIGURE 4.26: Verification of eq. 4.30 with the STEP protocol. The blue markers represent $\ln\left(P_F(W)/P_R(-W)\right)$ drawn from the distributions of the measured work values associated to the compression and expansion of the trap. The solid line represents the corresponding dissipative work W_{diss} of the transformation.

The spreading of points show how the values $P_F(w)$ and $P_R(-w)$ start to differ more for larger work fluctuations. This can be clearly seen in the work distributions displayed in the left panel Fig. 4.27 below. The right panel shows the same distributions of work values in the forward and reversed directions of the RAMP protocol.

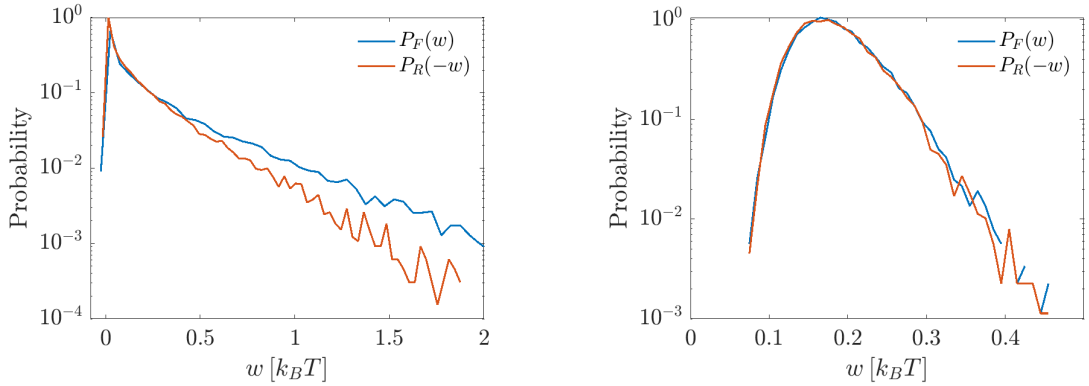

FIGURE 4.27: Distribution of the work fluctuations when the system is under the forward and reverse protocols of the STEP and the RAMP.

In the case of the RAMP protocol the distributions are exactly the same as expected from a reversible process. The particular small compression ($\kappa_f = 1.5\kappa_i$), even with the STEP protocol, causes only very little dissipation. This explains why we observe the distributions $P_F(w)$ and $P_R(-w)$ nearly coinciding for the most probable values of work fluctuations, while starting to differ for larger fluctuations.

It is interesting to note that the Jarzynski's equality can be derived simply from eq. 4.30, by considering the following sequence [15]:

$$\begin{aligned}\langle e^{-W/k_BT}\rangle &= \int e^{-W/k_BT}P_F(W)dW \\ &= \int e^{-W/k_BT}e^{W_{diss}/k_BT}P_R(-W)dW \\ &= e^{-\Delta F/k_BT}\int P_R(-W)dW = e^{-\Delta F/k_BT}.\end{aligned}$$

4.4.3 Stochastic entropy production

As mentioned above, the general formulation of the CFT involves entropy production terms [15]:

$$\frac{P_F(+\Delta s_{tot})}{P_R(-\Delta s_{tot})} = e^{+\Delta s_{tot}}, \tag{4.31}$$

with Δs_{tot} the total entropy production measured over a finite time interval, which in our case is taken before and after the transition, but long enough to make sure that the system is relaxed in both states. Eq. 4.31 implies 4.30, since for systems that start at equilibrium, the entropy production is $\Delta s_{tot} = (W - \Delta F)/T = W_{diss}/T$ [15].

We have presented, in section 4.3.3, how for a single realization of the compression process, work and heat become stochastic functionals of the trajectory, $w[x(\tau)]$, $q[x(\tau)]$. Remarkably, this reasoning can be extended to entropy production, as originally proposed by U. Seifert in [42].

In a single cycle of $\kappa(t)$, the instantaneous heat dissipated by the system to the surroundings is $q[x(t)]$. The instantaneous increase of the entropy of the bath is thus expected to be $s_{bath}[x(t)] = q[x(t)]/T$ [15, 27]. Concomitantly, there is also an entropy variation associated with the change in the microscopic state of the system. For a given state that occurs with probability $p(x)$, the amount of information required to describe that state is [15]:

$$s_{sys}(x) = -k_B \ln p(x) \tag{4.32}$$

which is the Gibbs/Shannon definition of entropy of a microscopic state. Starting from this, U. Seifert found the expression for a trajectory-dependent entropy of the system $s_{sys}[x(t)]$ [42], for a system characterized by overdamped Langevin dynamics. He did so by evaluating the probability $p(x,t)$, obtained from the Fokker-Planck equation, along the stochastic trajectory $x(t)$ [27, 42]. The stochastic entropy of our colloidal particle is:

$$s_{sys}[x(t)] = -k_B \ln p(x,t), \tag{4.33}$$

which is associated to a single trajectory. This relation, however, subtly involves the ensemble of trajectories in order to evaluate the probability distribution, $p(x,t)$ along

the trajectory of interest $x(t)$.

Experimentally, the procedure is straightforward: we construct the instantaneous distribution $p(x,t)$ from an ensemble of trajectories subjected to the same change in the control parameter as described in section 4.3, Fig. 4.9. From this ensemble of trajectories, we proceed to build a distribution of positions at each instant t_j, and thus define $p(x(t_j),t_j)$. The stochastic entropy $s_{sys}[x(t)]$ is then obtained by evaluating the value $p(x(t_j),t_j)$ of the selected trajectory $x(t_j)$ at each instant t_j, as depicted in the figure 4.28 below.

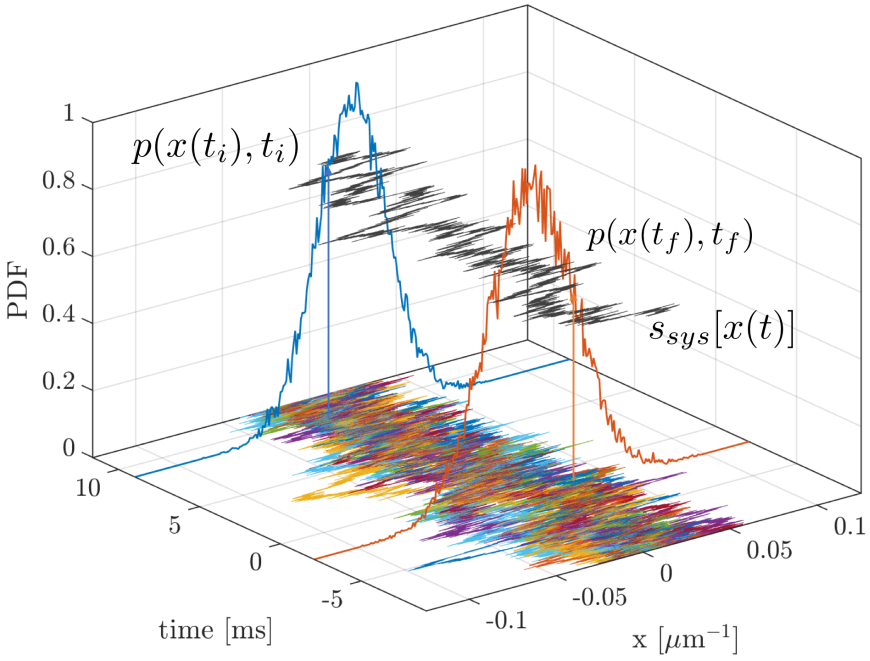

FIGURE 4.28: Illustration of the scheme for evaluating the probabilities $p(x,t)$ along a selected trajectory $x(t)$. The blue and orange lines represent the $p(x,t)$ distributions at the instants, t_i and t_f, distributions built from the instantaneous distributions of positions from the ensemble of trajectories shown in the plane (time, x). The trajectory-dependent entropy of the system is evaluated step-wise following eq. 4.33 as displayed in the black curve.

The trajectory-dependent entropy production for an isolated system can be obtained as $s_{tot}[x(t)] = s_{sys}[x(t)] + s_{bath}[x(t)]$. The stochastic nature of s_{tot} and the associated trajectory-dependent entropy of the bath and of the system are shown in the left panel of figure 4.29, for a single cycle of the STEP protocol.

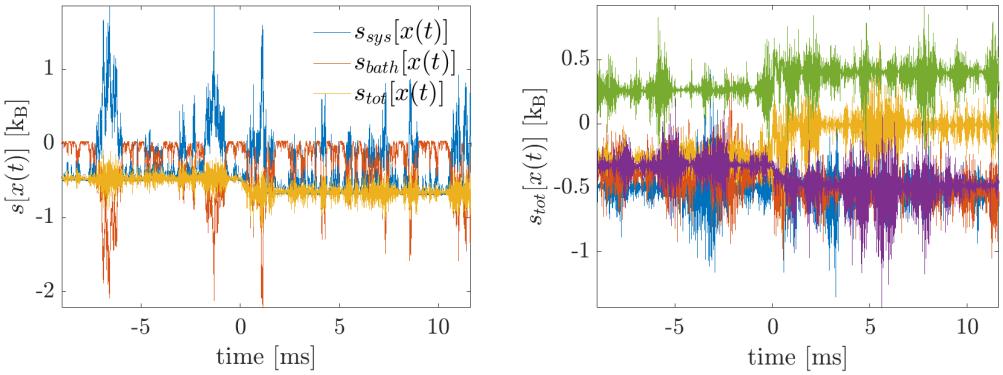

FIGURE 4.29: Instantaneous fluctuations of the trajectory-dependent entropies. Left panel: $s_{sys}[x(t)]$,$s_{bath}[x(t)]$ and $s_{tot}[x(t)] = s_{sys}[x(t)] + s_{bath}[x(t)]$ for a single realization of the STEP compression, $x(t)$. Right panel: $s_{tot}[x(t)]$ for different cycles of the STEP process.

The left panel of Fig. 4.29 presents a case in which the stochastic entropy production decreases. In the panel on the right, several realizations of the process result in different outcomes: some compression cycles show entropy annihilating trajectories and some others show entropy creating trajectories. We can also see that, at equilibrium, before the STEP is applied (i.e. $t < 0$) s_{tot} also fluctuates. The distribution of fluctuating values of entropy production when the system is at equilibrium is displayed in Fig. 4.30, under a constant κ. As expected, the total entropy production fluctuates around zero, with equal number of trajectories producing negative entropy and positive entropy.

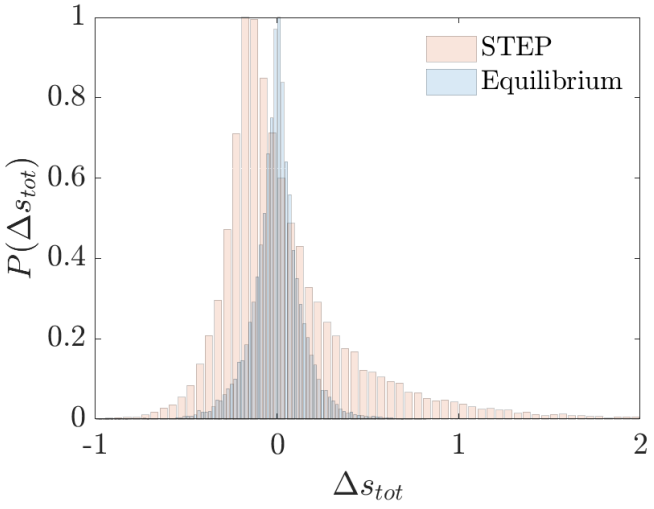

FIGURE 4.30: Comparison of the distributions of the entropy production for a STEP transformation and at equilibrium. The standard deviation of the equilibrium distribution is $\sigma = 0.13\,\mathrm{k_B}$ which increases to $\sigma = 0.39\,\mathrm{k_B}$ when the irreversible compression is takes place.

From the definitions of the entropy of the bath and the entropy of the system at the trajectory level, we can evaluate the differences $\Delta s_{sys} = s_{sys}(t_f) - s_{sys}(t_i)$ for a given interval of time, in which t_i and t_f are time instants in which the system is already

relaxed in the initial and final equilibrium state respectively. The change of entropy associated to the compression of the trapping potential is:

$$\Delta s_{tot} = \Delta s_{sys} + \Delta s_{bath}. \tag{4.34}$$

These measured values fluctuate from trajectory to trajectory, the distributions of fluctuations of these quantities Δs are displayed in Fig. 4.31, for the compression and expansion of the trap following the STEP and RAMP protocols. In all cases, the change in system entropy fluctuates around zero with no net entropy increase, the amplitude of fluctuations are the same for all the processes, the RAMP and the STEP in the forward and backward directions, since the system entropy depends only on the states and not the driving scheme, as emphasized already for the Jarzynski equality.

Because the distributions of Δs_{bath} look similar in the forward and backward directions of both protocols, it is difficult to detect the effect of the protocol just by looking at the distribution of these stochastic values. As discussed in the description of heat fluctuations, at the level of a single cycle, the dynamical fluctuations due to the thermal force are large compared to the effects of the small $\Delta\kappa$ of the protocol and therefore difficult to detect when looking at the distribution of the dissipated heat. Here, the same situation occurs for the entropy of the bath: Δs_{bath} exhibits large fluctuations going beyond $\pm 5\, k_B$ units in both protocols. However, when examining the distribution of Δs_{tot} one can notice two interesting features in the case of the STEP: the distribution of the forward process has significantly larger fluctuations than the reverse process, and both distributions are asymmetric. When the quasistatic transformation is applied the distribution of entropy production values is the same along the forward and reversed paths. We plot the ratio $\ln\left(P_F(+\Delta s_{tot})/P_R(-\Delta s_{tot})\right)$ as a function of Δs_{tot} in Fig. 4.32, in order to verify if the entropy production fluctuations satisfy eq. 4.31, even though most of the values satisfy the relation, we observe some departures in the values that fall in the tails of the distributions. This is consistent with what we have observed in the case of work fluctuations.

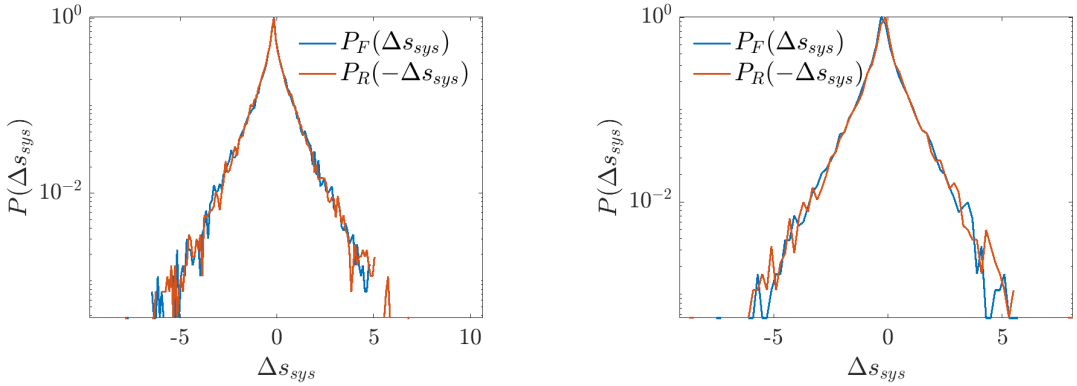

(A) $P(\Delta s_{sys})$ STEP (B) $P(\Delta s_{sys})$ RAMP

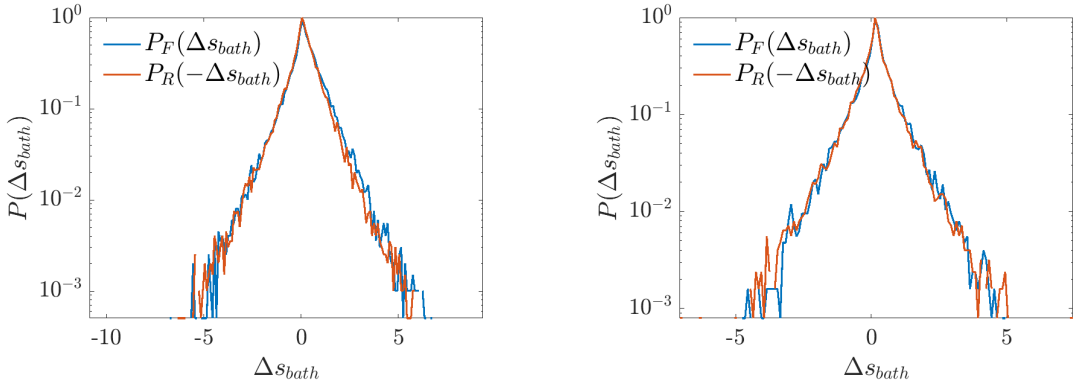

(C) $P(\Delta s_{bath})$ STEP (D) $P(\Delta s_{bath})$ RAMP

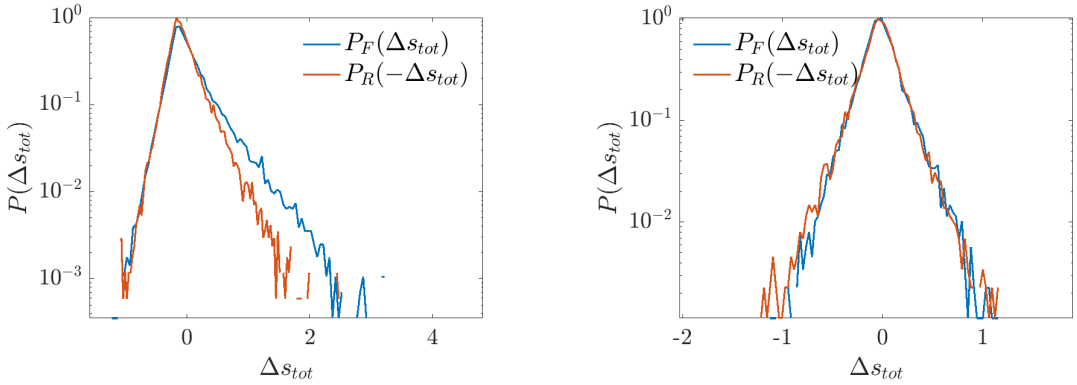

(E) $P(\Delta s_{tot})$ STEP (F) $P(\Delta s_{tot})$ RAMP

FIGURE 4.31: Probability distributions of the fluctuations of measured values of entropy change, for the entropy of the system, panels 4.31a,4.31b, of the bath, panels 4.31c and 4.31d and of the total entropy production, panels 4.31e and 4.31f, for the system under compression (forward direction) and expansion (reverse) with the STEP and RAMP protocols.

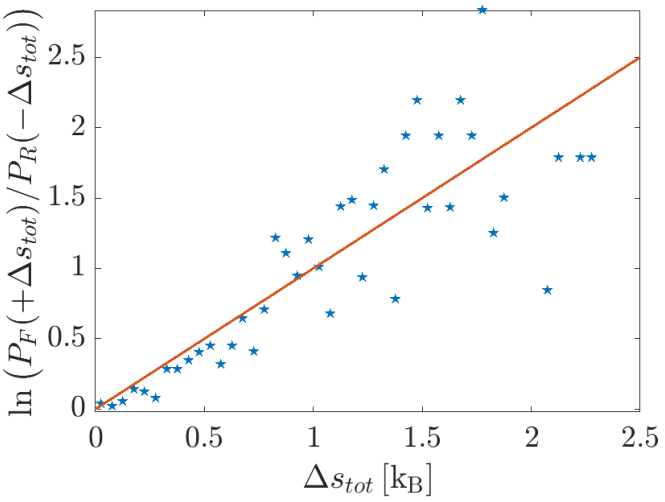

FIGURE 4.32: Verification of eq. 4.31 for the STEP protocol. The blue markers are the results of the ratio of probabilities of the values Δs_{tot} from the distributions shown in Fig. 4.31. The solid line is $+\Delta s_{tot}$.

By taking the ensemble average over all the realizations of the STEP protocol, we obtain the time-dependence of the mean cumulative entropy of the system and of the bath, $\langle s_{bath}[x(t)]\rangle$, $\langle s_{sys}[x(t)]\rangle$, together with the resulting time evolution of the macroscopic entropy s_{tot} produced by the abrupt compression. These evolutions are shown in Fig. 4.33

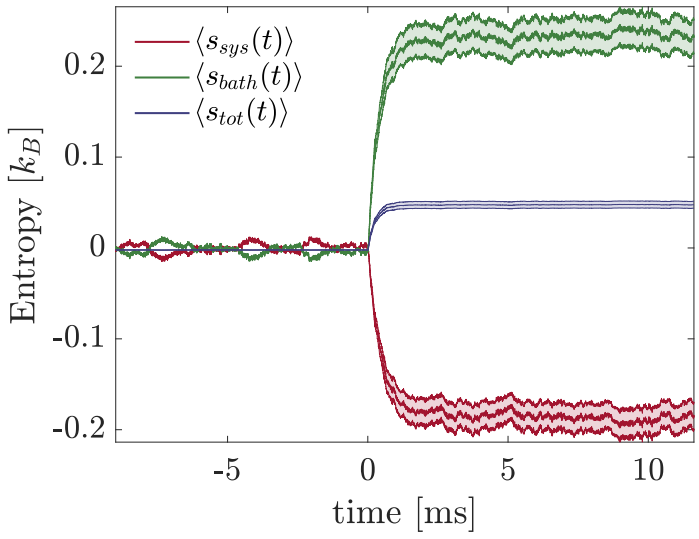

FIGURE 4.33: Temporal evolution of the ensemble averages of the different entropies, for an abrupt compression of the trap induced by the STEP protocol.

Similarly, we obtain the time-evolution of the ensemble averages of the entropy for the RAMP protocol, shown in Fig. 4.34.

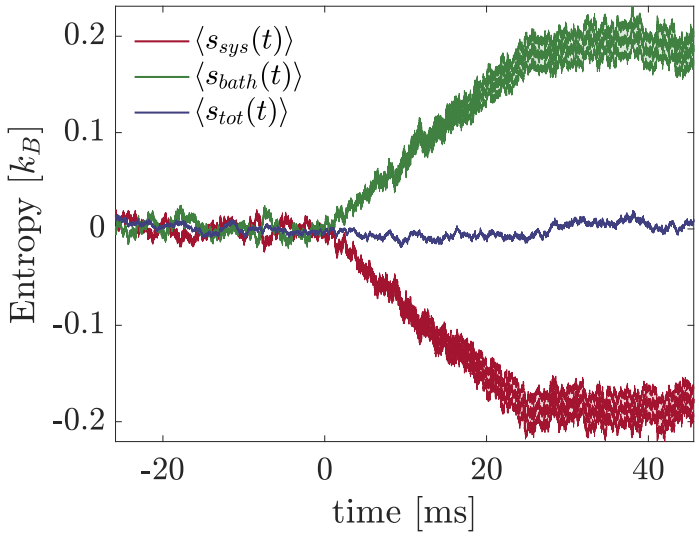

FIGURE 4.34: Temporal evolution of the ensemble averages of the different entropies, for a progressive compression of the trap induced by the RAMP protocol.

The contrasting behavior of the temporal evolution of the mean cumulative entropy production for the two limiting cases of the work parameter is illustrated in Fig. 4.35. When the trap is closed abruptly as prescribed by the STEP protocol, total entropy production increases monotonically as the system relaxes to the new equilibrium state where it saturates to a new value $\Delta s_{tot} = 0.05\,[\mathrm{k_B}]$, signature of an irreversible process that can be detected only with an ensemble average over a large number of trajectories. In contrast, when the stiffness is slowly increased in the case of the RAMP protocol, the total entropy production fluctuates around zero with no net entropy increase.

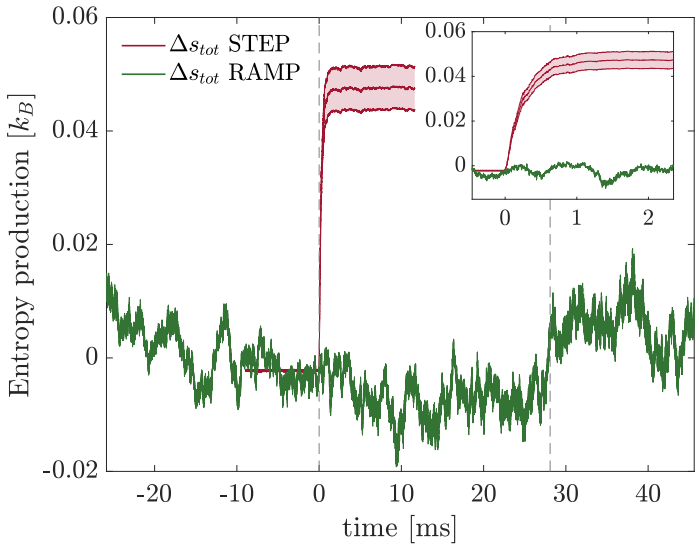

FIGURE 4.35: Time-evolution of the total entropy production for the RAMP and the STEP protocols, the two vertical dashed lines showing where the RAMP protocol starts and ends. The inset is a close-up over the entropy production related to the STEP protocol as the system is evolving towards thermal equilibrium.

The entropy change of the system is the same for both protocols, since it depends only on the initial and final states. The entropy production therefore is solely due to the change in entropy of the bath, which in this case is due to the fraction of the exerted work dissipated into the bath according to $W_{diss} = T\Delta s_{tot}$.

4.4.4 Integral Fluctuation Theorem for Stochastic Entropy Production

Measured work values satisfy Jarzysnki and Crooks FT. Stochastic entropy production satisfies too an integral fluctuation theorem, derived by Seifert [42] following the definition of trajectory-dependent entropy production. This entropy production FT writes as:

$$\langle e^{-\Delta s_{tot}} \rangle = 1. \tag{4.35}$$

Using Jensen's inequality [157], $e^{-\langle \Delta s_{tot} \rangle} \leq \langle e^{-\Delta s_{tot}} \rangle$ leads to verify indeed that:

$$\langle \Delta s_{tot} \rangle \geq 0, \tag{4.36}$$

and hence recovering the Second Law of Thermodynamics.

In the same light as for the Jarzynski equality, we have performed ensemble averages of different sizes and observed the convergence of this entropy FT as a function of the number of trajectories for a compression and expansion of the trap under the STEP protocol. The results are displayed in Fig. 4.36. Convergence is reached roughly after 1000 trajectories in both cases, the forward (compression) and backward (expansion)

processes. The fact that the average over more than 1000 trajectories is found slightly above 1, precisely around 1.02 is due to our limited experimental precision.

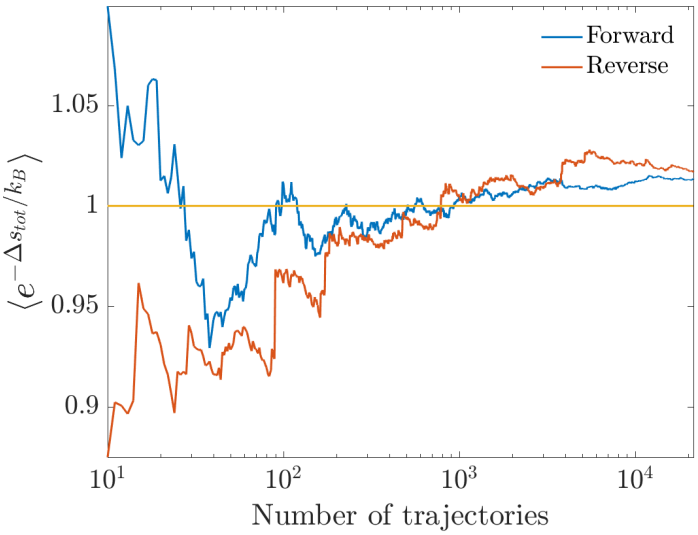

FIGURE 4.36: Convergence of $\langle e^{-\Delta s_{tot}} \rangle$ to 1, as a function of the number of trajectories involved in the average, for the forward and reversed processes of the STEP protocol.

4.5 Conclusion

In this chapter, we have studied thermodynamic transformations between equilibrium states at the level of a single Brownian particle. We first focused on a process analog to the compression of an ideal gas in a vessel induced by a moving piston. This was achieved by trapping the particle in a fixed optical potential and increasing confinement by increasing the trap stiffness. The trap stiffness therefore, played the role of control parameter, and it was changed over time to drive the system from the initial equilibrium state within the initial potential $U(\kappa_i, x)$ to the final equilibrium state in $U(\kappa_f, x)$. In order to perform this transformation, we implemented (i) a STEP protocol, which represents an instantaneous change of κ and (ii) a RAMP, in which $\kappa(t)$ is slowly increased from κ_i to κ_f.

Using Sekimoto's approach, we identified heat, work and internal energy for such processes at the level of single stochastic trajectories. In this framework, these thermodynamic quantities associated to the transformation become random vairables that fluctuate from realization to realization. We discussed in particular how their statistical distributions give powerful information on the dissipative nature of the driving protocol. Besides the fact that the shape of the probability distribution of the work fluctuations depends on the temporal evolution on the specific protocol $\kappa(t)$, the magnitude of the fluctuations depends on how far from equilibrium the protocol drives the system in order to achieve the transformation.

We also showed, repeating the protocols a large number of times, how to recover the deterministic macroscopic behavior by taking the ensemble average of the thermodynamic functionals of heat and work associated to the single stochastic trajectories, undergoing the same change of control parameter. The time-evolution of such ensemble thermodynamic quantities for the system driven out-of-equilibrium when performing the STEP protocol reveals how the exchange of injected work and released heat evolve to keep the internal energy unchanged in the case of the RAMP protocol.

When observing the work fluctuations taking place when the optical trap is compressed applying the RAMP or STEP protocol, we detected the presence of some trajectories that violate the Second Law of thermodynamics. We therefore devoted the last part of the chapter to the definition and implementation of specific fluctuation theorems that give essential information on the fluctuation dynamics at play in the processes investigated with our system. We first focused on the Jarzynski equality, which emphasizes that events violating the Second Law contribute to ensemble averages in a way that they allow to determining the equilibrium free-energy differences between the initial and final states involved in the transformation induced by any type of driving protocol. Investigating the Crooks fluctuation theorem led us to investigate further work fluctuations. The CFT revealed in particular how the asymmetry between the compression process and its time-reversed (expansion) is directly linked to the mean dissipated work. This FT hence explained the emergence of irreversibility at the macroscopic level from our microscopic measurements.

These discussions on irreversibility and dissipation led us to investigate the fluctuations of entropy, in which the CFT offers again a valuable insight. Following Seifert's method to obtain entropy production at the level of a single stochastic trajectory, we obtained the probability distributions of entropy production for the compression and expansion of the trap under the STEP and RAMP protocols. We then verified with our data the validity of the CFT and the integral fluctuation theorem for stochastic entropy production, observing the existence and importance of entropy annihilating trajectories that were also manifest previously, but viewed from the work point of view.

Overall, the aim of this chapter was to provide the central concepts necessary for the presentation of the results of the last chapter of the manuscript, where we address the problem of optimizing such transformations between two equilibrium states.

5 Optimal thermodynamic control

5.1 Introduction

In the previous chapter, we have seen how the Brownian particle trapped in an optical potential represents the piston-gas model for testing the results of stochastic thermodynamics. We have tested two intuitive protocols that drive the system between two equilibrium states: one long enough to be considered as quasistatic and an other, a step-like protocol characterized by an abrupt change in the optical trap stiffness. By recording the trajectory of the Brownian particle in the optical potential undergoing a large number of cycles of the STEP protocol we were able to construct an ensemble of trajectories characterized by the same change of external conditions, i.e. stiffness variation.

Such a step-like protocol constitutes the simplest protocol for transferring the Brownian particle between two equilibrium states. For such a transfer, the relaxation time is simply determined by the γ/κ_f. It has been shown both theoretically and experimentally that this duration can be arbitrarily shorten by implementing a specific protocol that essentially consists in a very strong compression/expansion sequence *i.e.* through a very energetic cost.

In this Chapter, we are interested in the constrained relation between transfer duration and energetic cost. We define and demonstrate the possibility of optimal transfer protocols that lead to the best possible compromise between the shortening of the transfer duration and its associated energetic cost. This project is a result of a collaboration that intertwines the theoretical works of Prof. G. Manfredi and Prof. P.A. Hervieux, IPCMS Strasbourg, and Prof. Laurent Merz, NYU-Shanghai and our experiments.

5.2 Dynamical evolution of Brownian particle in a potential under compression

In the previous chapter we have seen how the probability distribution of positions can be constructed from an ensemble of trajectories, since the trap remains harmonic at all times of the evolution of the stiffness, the linearity of Langevin equation guarantees that the PDF of positions remains Gaussian at all times too [160]. A Gaussian can be fully described by its first and second moments, the mean and the variance. When the stiffness of the potential changes with time, the mean stays fixed, but the variance

evolves accordingly.

It is possible to obtain the equation of motion of the variance directly from the overdamped Langevin equation:

$$\gamma \frac{dx}{dt} = -\kappa x(t) + F_{\text{th}}(t), \tag{5.1}$$

where $F_{\text{th}}(t) = \sqrt{2k_BT\gamma}\xi(t) = \sqrt{2D}\xi(t)$ the Langevin force. We take the approach of A. Manoliu and C. Kittel [161], multiplying the Langevin equation by $x(t)$,

$$\gamma \frac{dx}{dt}(x(t)) = (-\kappa x(t) + F_{th}(t))\, x(t) \tag{5.2}$$

$$\frac{\gamma}{2}\frac{dx^2}{dt} = -\kappa x^2(t) + F_{th}(t)x(t) \tag{5.3}$$

and taking the ensemble average:

$$\frac{\gamma}{2}\underbrace{\langle \frac{dx^2}{dt} \rangle}_{d\langle x^2\rangle/dt} = -\kappa\langle x^2\rangle + \langle F_{th}(t)x(t)\rangle \tag{5.4}$$

we are left to compute the correlation function $\langle F_{th}(t)x(t)\rangle$. For that we use the solution to the overdamped Langevin equation, and calling the correlation time $\tau = \gamma/\kappa$, we can write:

$$x(t) = x_0 e^{-t/\tau} + \int_0^t dt' e^{-(t-t')/\tau} F_{th}(t') \tag{5.5}$$

then, we multiply by the stochastic force and take the ensemble average:

$$\langle F_{th}(t)x(t)\rangle = \underbrace{\langle x_0 F_{Th} e^{-t/\tau}\rangle}_{0} + \langle \int_0^t dt' F_{Th}(t) F_{Th}(t') e^{(t'-t)/\tau}\rangle \tag{5.6}$$

$$\langle F_{th}(t)x(t)\rangle = 2k_BT\gamma \underbrace{\int_0^t dt' \delta(t-t') e^{(t'-t)/\tau})}_{1/2} \tag{5.7}$$

The last integral can be rigourously demonstrated by using stochastic integrals [1]. Thus:

$$\frac{\gamma}{2}\frac{d\langle x^2\rangle}{dt} = -\kappa\langle x^2\rangle + k_BT\gamma \tag{5.8}$$

for simplicity we call $\langle x^2(t)\rangle \equiv s(t)$ so the previous equation writes:

$$\frac{ds}{dt} = -\frac{2\kappa}{\gamma}s(t) + 2D \tag{5.9}$$

with κ the stiffness of the potential, γ the Stokes drag and D the diffusion coefficient.

[1] The integral of half of a distribution function is done by using Stratonovich convention. See Appendix A

This equation describes the deterministic dynamical evolution of the system. The solution of this equation in the case of a fixed harmonic potential ($\dot{\kappa} = 0$) is:

$$s(t) = \frac{D\gamma}{\kappa}(1 - e^{-2\kappa t/\gamma}) \tag{5.10}$$

from which we can extract the relaxation time of the variance of the position PDF, when this latter reaches the equilibrium distribution, $\tau_{relax} = 2\gamma/\kappa$. At $t \gg \tau_{relax}$, we recover the equipartition theorem:

$$\kappa s = k_B T \tag{5.11}$$

which plays the role of a dynamical criterion for the system to be considered at thermal equilibrium with its surroundings.

Time-dependent trapping potential As we have seen in the previous Chapter, section 4.3.1, optical traps are very advantageous for applying arbitrary driving schemes to the control parameter thanks to the simple relation $\kappa(t) \propto I(t)$. When the potential changes between two configurations, $U(\kappa_i, x)$ and $U(\kappa_f, x)$, due to a time-dependent stiffness $\kappa(t)$, the potential stays harmonic at all times of the transformation. In the figure below 5.1, we show, at the level of a single trajectory, how the trapped Brownian particle thermally explores the optical potential undergoing a compression with a STEP protocol.

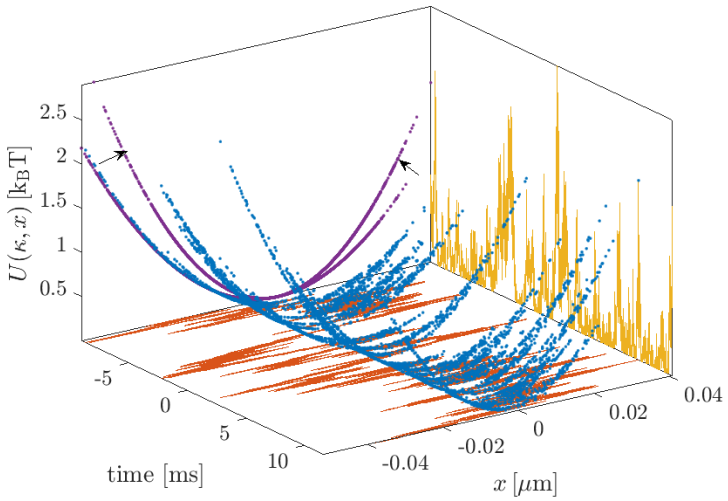

FIGURE 5.1: Trajectory dependent energy fluctuations as a function of time (yellow curve) and as a function of the trajectory (blue). Each blue dot represents the sampled energy position of the particle within the potential. The trapping potential was evolving according to the STEP protocol, studied in the previous Chapter, from $U(\kappa_i, x)$ to $U(\kappa_f, x)$. These are projected in the (x, U)-plane as purple curves.

The dynamical effects of such protocol at the ensemble level can be monitored directly on the variance, $s(t)$. The time evolution of $s(t)$ for a STEP protocol that

performs a trap compression characterized by κ_i going to $\kappa_f \gg \kappa_i$, can be found by solving equation 5.9, with the boundary conditions $s(0) = s_i = k_B T/\kappa_i$ and $s(t_f) = s_f = k_B T/\kappa_f$:

$$s(t) = s_i e^{-2\kappa_f t/\gamma} + s_f(1 - e^{-2\kappa_f t/\gamma}) \tag{5.12}$$

As an example, we plot the analytical evolution $s(t)$ as an orange solid line on top of an experimental ensemble variance represented as the blue curve in Fig. 5.2. The system approaches the new equilibrium state characterized by a variance $s_f = k_B T/\kappa_f$ after a time τ_{relax} given by $2\gamma/\kappa_f$, which is indicated as the green dashed line in the figure.

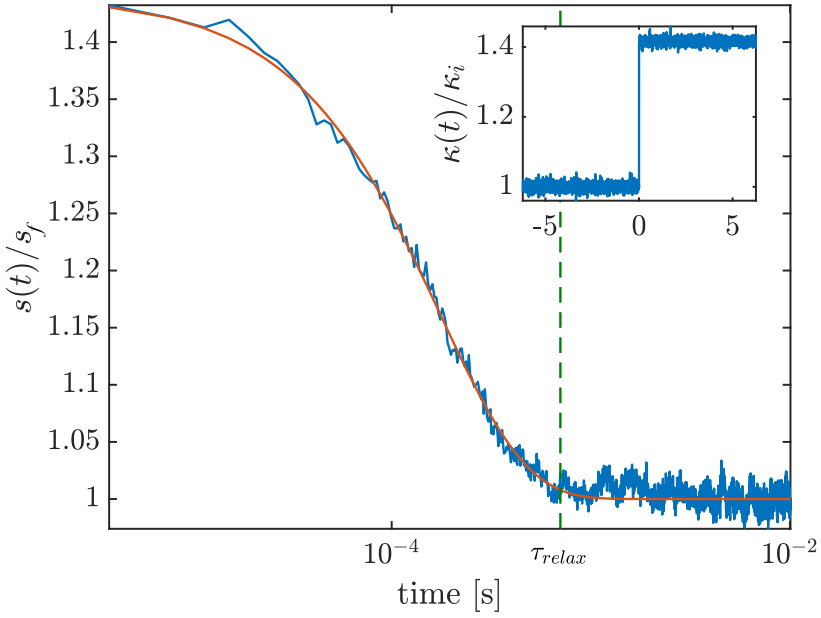

FIGURE 5.2: Example of the variance evolution of a trap under compression following a STEP protocol. The blue solid curve represents the temporal evolution of the measured ensemble variance $s(t)$ normalized to the final variance $s_f = 1.72 \times 10^{-16} m^2$. The stiffness of the potential evolves from $\kappa_i = 1.69 \times 10^{-5}$N/m to $\kappa_f = 2.39 \times 10^{-5}$N/m. The orange solid line on top of the measured variance is the analytical solution of the variance evolution, equation 5.12. The vertical green dashed line indicates the relaxation time $\tau_{relax} = 2\gamma/\kappa_f = 7 \times 10^{-4} s$. Inset: Time evolution of the control parameter $\kappa(t)$ following a STEP protocol, normalized to the initial stiffness κ_i.

The ensemble cumulative energetics associated to the transformations, as discussed in the previous chapter, section 4.3.3, can be now expressed in terms of the variance $s(t)$:

$$W(t) = \langle w(t) \rangle = \int_0^{t_f} s(t)\dot{\kappa} dt \qquad Q(t) = \langle q(t) \rangle = \int_0^{t_f} \dot{s}\kappa(t) dt \tag{5.13}$$

following a convention for a positive flow when the heat is transferred from the trapped microsphere to the bath, usually taken in stochastic thermodynamics [70].

In section 4.3.1, we described the procedure to build the ensemble of trajectories, from which at each instant, $t = t_j$, of the time evolution of the trapping potential, we can extract the distribution of positions $p(x(t_j), t_j)$, as illustrated in Fig. 4.29. Such PDF is a Gaussian of zero mean, $\mu_x(t_j) = 0$, and variance $s(t_j)$. We can therefore extract the instantaneous ensemble variance over N repetitions of the driving protocol. We use a Matlab routine which gives the estimator:

$$\sigma_x^2(t_j) = \sum_{i=1}^{N} \frac{|x_i(t_j) - \mu_x(t_j)|^2}{N-1} \tag{5.14}$$

where t_j is a specific time instant, $x_i(t_j)$ is the instantaneous position of a given trajectory i, $\mu_x(t_j)$ the ensemble mean at time t_j. The statistical uncertainties for the instantaneous ensemble variances are obtained following a χ^2 law with $N-1$ degrees of freedom where $N = N_{cycles}$ is the number of independent trajectories $x_i(t)$ undergoing one cycle of the protocol $\kappa(t)$, these uncertainties have to be complemented with the systematic errors of calibration between positional units and measured voltages.

PSD calibration uncertainties: Under a trapping laser intensity, the registered *p-i-n* voltage values $V(t)$ that correspond to the position fluctuations of the trapped bead are converted into displacement units using the best-fit parameter of the Lorentzian fit of the PSD of the trajectory (at constant κ). The fit parameter D_{fit} is compared to the diffusion coefficient $D = k_B T/\gamma$ expected from the Fluctuation-Dissipation Theorem, assuming known temperature and viscosity. This gives a conversion factor $\beta = \sqrt{D/D_{\text{fit}}}$ from *p-i-n* voltages to meters. The uncertainty on the position sensitivity is obtained from standard error propagation including the uncertainty on the viscosity resulting from the $\delta R/R = 2.8\%$ size dispersion deviation of the trapped beads.

Instantaneous positions are thus given from the conversion factor as $x(t) = (\beta \pm \delta\beta)V(t)$, and therefore the variance, up to first-order in uncertainty, $x^2(t) = (\beta^2 \pm 2\beta\delta\beta)V^2(t)$, (since the mean position $\langle x(t)\rangle = \mu_x(t) = 0$). The total error of the variance writes as:

$$s(t_j) = \sigma_x^2(t_j) \pm \underbrace{(\delta\sigma_{\chi^2}^2(t_j) + \beta\delta\beta\sigma_x^2(t_j))}_{\delta s(t_j)}, \tag{5.15}$$

where $\sigma_x^2(t_j) = \sum_{i=1}^{N} |x_i(t_j) - \mu(t_j)|^2/(N-1)$ is the estimator of the instantaneous ensemble variance over N cycles, $\delta\sigma_{\chi^2}^2$ corresponds to the statistical uncertainty in the motional variance determination (see above) and $\delta\beta\sigma_x^2$ the PSD calibration uncertainty just discussed.

The temporal average variances related to the initial an final stiffness s_i and s_f are obtained from temporal average. Assuming Δt as the interval over which $\kappa(t)$ remains constant (either at κ_i or κ_f), the temporal average $\overline{\cdots}$ of the corresponding variance

is:

$$\overline{s} = \frac{1}{\Delta t}\sum_{j=1}^{n} s(t_j), \tag{5.16}$$

taking Δt as the interval over which $\kappa(t)$ remains constant (either at κ_i or κ_f) and $n = \Delta t \cdot f_s$ with $f_s = 262$ kHz, the sampling frequency. The standard deviation of the temporal average is simply evaluated as:

$$\delta_t \overline{s} = \sqrt{\frac{1}{\Delta t}\sum_{j=1}^{n} |s(t_j) - \langle s \rangle_t|^2} \tag{5.17}$$

The stationary variances s_i and s_f and their uncertainties are thus simply given by:

$$s_{i,f} = \overline{s} \pm \underbrace{\left(\delta_t \overline{s} + \overline{\delta s} + \delta_t \overline{\delta s}\right)}_{\delta_t s_{i,f}}, \tag{5.18}$$

where $\overline{\delta s} = 1/\Delta t \sum_{j=1}^{n} \delta s(t_j)$.

5.3 Accelerated equilibration

The reversible and irreversible driving schemes discussed in the previous chapter show that even with an abrupt change of the control parameter as performed with the STEP protocol, the shortest time at which the system reaches equilibrium is limited to $\tau_{relax} = 2\gamma/\kappa$. Nevertheless, if two states are related by a quasistatic transformation, it is possible to design alternative driving protocols that transform the system from an initial, $U(\kappa_i, x)$ to a target state, $U(\kappa_f, x)$, in a time shorter than τ_{relax}. Martinez *et al.* designed a novel protocol, called *'Engineered Swift Equilibration'* (ESE) [160], which was the first proposition of accelerated equilibration protocols to a system in contact with a thermostat. Such protocols aim at short-cutting quasi-static relaxations however by paying a high energetic cost. They first applied the ESE protocol to drive a Brownian particle held in an optical trap between two equilibrium configurations of the potential, characterized by an initial stiffness κ_i and a final κ_f. In their experimental configuration, the ESE protocol allowed the system to reach the final equilibrium state 100 times faster than the natural relaxation time, they subsequently demonstrated the applicability on a underdamped system, an AFM cantilever whose equilibrium position is displaced [162]. Below we briefly explain their analytical method, for the overdamped case.

As discussed above, the evolution of the system during the transition towards the new equilibrium state is monitored through the position PDF which is a Gaussian during the whole process. Defining the variable $\alpha(t) = \kappa(t)/\mathrm{k_B}T$, the PDF can be written as:

$$\rho(x,t) = \sqrt{\frac{\alpha(t)}{\pi}} e^{-\alpha(t)x^2} \tag{5.19}$$

By imposing $\alpha(0) = \frac{\kappa_i}{2k_BT}$ and $\alpha(t_f) = \frac{\kappa_f}{2k_BT}$, i.e. thermal equilibrium at initial and final times and plugging Eq. 5.19 into the overdamped Fokker-Planck equation:

$$\frac{\partial}{\partial x}\rho(x,t) = \frac{1}{\gamma}\frac{\partial}{\partial x}\left[\rho(x,t)\frac{\partial U}{\partial x}\right] + D\frac{\partial^2}{\partial x^2}\rho(x,t), \tag{5.20}$$

leads to a differential equation for $\alpha(t)$:

$$\dot{\alpha} = \frac{2\kappa}{\gamma}\alpha - \frac{4k_BT}{\gamma}\alpha^2 \tag{5.21}$$

Their strategy relies on choosing arbitrarily a solution of the differential equation for α supplied with the boundary conditions, and a simple choice is a third degree polynomial, calling the re-scaled time as $\hat{t} = t/t_f$, and $\Delta\kappa = \kappa_f - \kappa_i$:

$$\alpha(\hat{t}) = \frac{1}{2k_BT}[\kappa_i + \Delta\kappa(3\hat{t}^2 - 2\hat{t}^3)] \tag{5.22}$$

This solution satisfies equation 5.21:

$$\kappa(t) = \frac{\gamma}{2\alpha(t)}\left[\dot{\alpha}(t) + \frac{4\mathrm{k_B}T}{\gamma}\alpha^2(t)\right] \tag{5.23}$$

$$= \frac{\gamma}{2}\frac{\dot{\alpha}}{\alpha} + 2\mathrm{k_B}T\alpha \tag{5.24}$$

In this way, with such solution and the imposed boundary conditions, they were able to impose a relaxation in a time $t_f \ll \tau_{relax}$, while driving the control parameter as:

$$\kappa_{\mathrm{ESE}}(t) = \frac{3\gamma\Delta\kappa\hat{t}(1-\hat{t})/t_f}{\kappa_i + \Delta\kappa(3\hat{t}^2 - 2\hat{t}^3)} + \kappa_i + \Delta\kappa(3\hat{t}^2 - 2\hat{t}^3) \tag{5.25}$$

We compare the results of such ESE protocol with the standard sudden switch of stiffness, the STEP protocol, using as observable the variance $s(t)$. In the figure 5.3 below we show the protocols and the time evolution of the resulting variance.

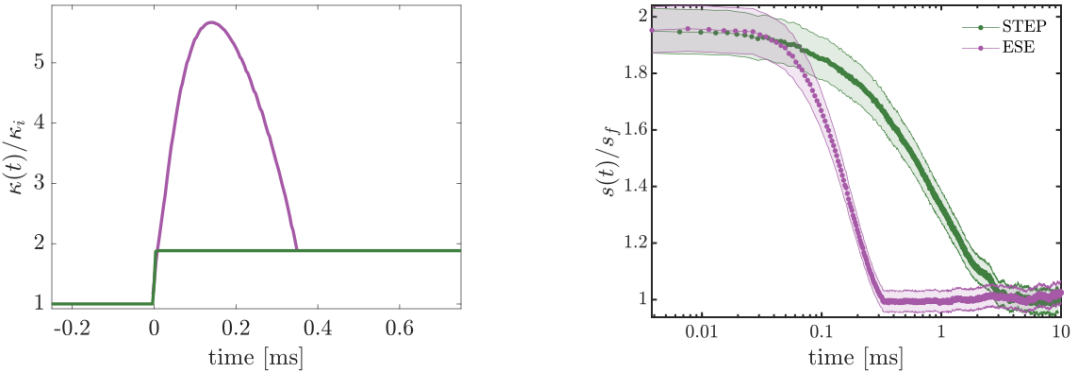

FIGURE 5.3: Left panel: Time evolution of the protocols, $\kappa(t)$ normalized to the initial stiffness κ_i. The STEP protocol is represented by the green solid line and the ESE protocol is the pink line. Right panel: The temporal evolution of the ensemble variances as a result of the modulations with the ESE and STEP protocols. The color codes are the same as for the left panel. The shaded areas represent 95% confidence intervals. The variance $s(t)$ is normalized to its final equilibrium value $s_f = \mathrm{k_B}T/\kappa_f$.

When the trap is compressed following the STEP protocol, the particle starts at equilibrium in the potential $U = \kappa_i x^2/2$, with $\kappa_i = 2.77 \pm 0.08\,\mathrm{pN}/\mu\mathrm{m}$, then at $t = 0$, the stiffness is suddenly switched to $\kappa_f = 5.22 \pm 0.15\,\mathrm{pN}/\mu\mathrm{m}$. The variance $s(t)$ evolves according to Eq. 5.12 until the system reaches the new equilibrium state in the potential $U = \kappa_f x^2/2$, after $\tau_{relax} = 3.22$ ms. For the same $\Delta\kappa$, we impose that the system reaches the new equilibrium state in a time 10 times faster than τ_{relax} by driving the stiffness with the ESE protocol, Eq. 5.25. As seen in the left panel, in order to perform such an acceleration, κ_{ESE} goes up to a maximum value approximately six times higher than its initial value and then decreases towards κ_f in the time imposed, which in this case is, $t_f = 0.34$ ms. At $t = 0$, the variance $s(t)$ evolves from $s_i = 1.5 \times 10^{-15}\mathrm{m}^2$ as $1/2\alpha$ (Eq. 5.21) and after $\Delta t = t_f$ reaches the final equilibrium value $s_f = 7.7 \times 10^{-16}\mathrm{m}^2$.

Figure 5.4 displays the temporal evolution of the mean cumulative energetics associated to the trap compression following the STEP and ESE protocols. The mean cumulative work of the STEP protocol is depicted in green, and as seen previously, reaches immediately $W_{\mathrm{step}} = 0.45 \pm 0.04\ k_{\mathrm{B}}T$. In contrast, the heat, plotted in brown, achieves the equilibrium value $W = Q$ with $Q_{\mathrm{step}} = 0.45 \pm 0.04\ k_{\mathrm{B}}T$ only after τ_{relax}. In the right panel we see the evolution of the mean cumulative work for the ESE protocol, displayed in pink, which increases up to a maximum as confinement is increased, then work is dissipated to the environment, resulting in a total work expended of $W_{\mathrm{ESE}} = 1.142 \pm 0.075\ k_{\mathrm{B}}T$. The mean cumulative heat generated through the ESE protocol is displayed in yellow, superimposed to the W_{ESE}, and monotonically increases as the system dissipates heat continuously until the system is completely relaxed in the new equilibrium, with total heat $Q_{\mathrm{ESE}} = 1.142 \pm 0.076\ k_{\mathrm{B}}T$. At equilibrium, the heat and work stay constant, $W = Q$, both curves reach equilibrium at the imposed

time Δt. To perform such a transformation in such short time, the work expense is 2.5 times higher than the STEP protocol. In their experiment [160], Martinez *et al.*, use the ESE protocol to perform a transition from $\kappa_i = 0.5\,\mathrm{pN}/\mu\mathrm{m}$ to $\kappa_f = 1\,\mathrm{pN}/\mu\mathrm{m}$, in a time 30 times faster than τ_{relax}, and it comes at a price 20 times higher than using the STEP protocol.

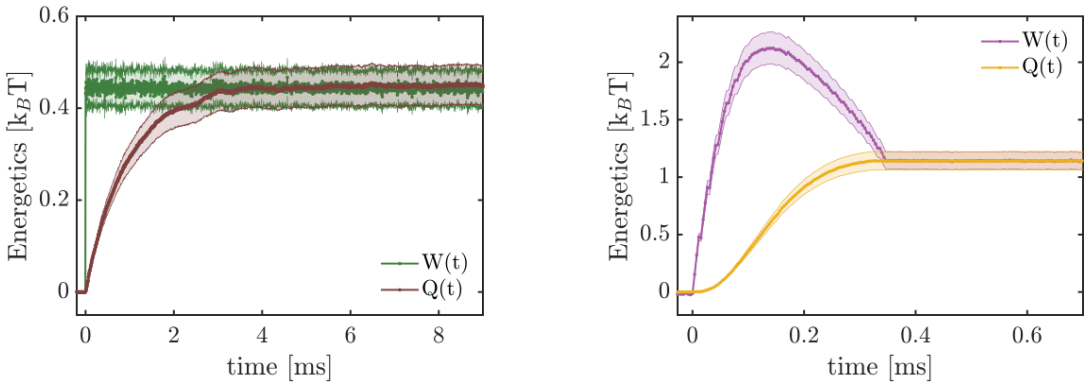

FIGURE 5.4: Temporal evolution of the mean cumulative energetics of the STEP protocol (Left panel), and the ESE protocol (Right panel). The shaded areas represent the errorbars.

5.4 Optimization strategy

Our aim is to control the relaxation dynamics of the trapped bead when the potential is changed between two configurations, in such a way that for the minimal energetic cost the system equilibrates as fast as possible, especially faster than the natural relaxation time given by the ratio of the viscosity and the stiffness of the final trapping potential. The advantage of an optical trap is in its harmonic nature, the clear relation between the stiffness an the variance. And thus we can base our optimization strategy on the direct influence of the control parameter $\kappa(t)$ on the evolution of $s(t)$. At equilibrium, the two variables are related as, $s_i\kappa_i = s_f\kappa_f = k_BT$. And the interplay of the two is also revealed in the energetics, as shown in equations 5.13. We thus seek, for the time evolution of the control parameter $\kappa(t)$ that optimises the compromise of transfer duration and energetic cost, and this can be readily tackled with the approaches of calculus of variations (See Appendix C).

In our case, $s(t)$ and $\kappa(t)$ are monotonically varying functions of time, this renders the calculations simpler. Instead of the time, κ or s can be considered as the independent variable of the problem. This approach allows us to define a parameter space (s, κ) in which the optimization problem can be clearly stated, as we will in the following paragraphs.

Choosing s as the independent variable of the problem, the control parameter, $\kappa(t)$ can be written as $\hat{\kappa}[s(t)]$. The quantities that we want to optimize such as the transfer

duration and the work can now be written as functionals of the curve $\hat{\kappa}[s]$ From Eqs. 5.9 and 5.13 we obtain:

$$\Delta t[\hat{\kappa}(s)] = \int_0^{t_f} dt = \frac{1}{2}\int_{s_i}^{s_f} \frac{\gamma\, ds}{D\gamma - s\,\hat{\kappa}(s)} \tag{5.26}$$

$$W[\hat{\kappa}(s)] = -\frac{1}{2}\int_{s_i}^{s_f} \hat{\kappa}(s)ds + \underbrace{\frac{1}{2}\left(\kappa_f s_f - \kappa_i s_i\right)}_{=0}, \tag{5.27}$$

In variational calculus [163], for a curve $\hat{\kappa}(s)$ in the (s,κ)-space, we can define a differentiable function $L(\hat{\kappa},\hat{\kappa}',s)$, where $\hat{\kappa}' \equiv d\hat{\kappa}/ds$, known as the Lagrangian, and a differentiable functional :

$$J[\hat{\kappa}(s)] = \int_{s_i}^{s_f} L(\hat{\kappa},\hat{\kappa}',s)ds \tag{5.28}$$

such that the curve $\hat{\kappa}(s)$ is an extremal of the functional $J[\hat{\kappa}(s)]$ on the space of curves joining (s_i,κ_i) and (s_f,κ_f), if it satisfies the Euler-Lagrange equation:

$$\frac{d}{ds}\frac{\partial L}{\partial \hat{\kappa}'} - \frac{\partial L}{\partial \hat{\kappa}} = 0 \tag{5.29}$$

The idea originates from analytical mechanics [163], where the motion of a mechanical system, whose extremals are solutions of Newton's equations of motion in a potential, coincide with the extremals of a functional $S[\mathbf{q}(t)] = \int_{t_0}^{t_f} L(\mathbf{q},\dot{\mathbf{q}},t)dt$, known as the action, where $\mathbf{q}(t)$ are generalized coordinates and $L(\mathbf{q},\dot{\mathbf{q}},t)$ is the Lagrangian of the system, representing the difference between kinetic and potential energy. In such mechanical system, the Euler-Lagrange equations are nothing other than Newton's equation of motion.

To define the Lagrangian in our case, or the functional $J[\hat{\kappa}(s)]$, we use the Lagrange multiplier technique, in which the Lagrangian takes the form of a linear combination of the objective function, and the constraints with the Lagrange multipliers, see Appendix C. We can write $J[\hat{\kappa}(s)]$ as a compromise between transfer duration, eq. 5.26 and work, eq. 5.27 as:

$$J[\hat{\kappa}(s)] = \int_{s_i}^{s_f} \frac{\gamma ds}{D\gamma - s\,\hat{\kappa}(s)} - \lambda\int_{s_i}^{s_f} \hat{\kappa}(s)ds, \tag{5.30}$$

where λ is a Lagrange multiplier that regulates the trade-off between transfer duration and work, and will have units of [time/energy], that is $[s/J]$ or $[s/k_BT]$. Within this framework, the optimization strategy can be interpreted as the search for the trajectory in the (s,κ)-space that minimizes $J[\hat{\kappa}(s)]$ while keeping the extrema fixed at equilibrium, i.e. $s_i\kappa_i = s_f\kappa_f = k_{\mathrm{B}}T = D\gamma$. With:

$$L(\hat{\kappa},\hat{\kappa}',s) = \frac{\gamma}{D\gamma - s\,\hat{\kappa}(s)} - \lambda\hat{\kappa}(s), \tag{5.31}$$

Eq. 5.29 yields:

$$s\,\hat{\kappa}(s) = D\gamma + \sqrt{\frac{\gamma s}{\lambda}} \tag{5.32}$$

The expressions of the transfer duration and work can be obtained by plugging eq. 5.32 into equations 5.26 and 5.27:

$$\Delta t = t_f = \sqrt{\gamma\lambda}\left(s_i^{1/2} - s_f^{1/2}\right) \tag{5.33}$$

$$W = \mathrm{k_B}T\ln\left(\frac{s_i}{s_f}\right) + \sqrt{\frac{\gamma}{\lambda}}\left(s_i^{1/2} - s_f^{1/2}\right). \tag{5.34}$$

Depending on the value λ, different situations can be described from the above equations, for instance, in the limiting case, $\lambda \to \infty$, one recovers the quasistatic solution, $s\kappa = D\gamma = \mathrm{k_B}T$, with infinite duration and a expended work equal to the free energy difference, $W_{\mathrm{QS}} = \Delta F = \frac{1}{2}\mathrm{k_B}T\ln(s_i/s_f)$. For finite λ and making use of Eq. (5.32), Eq. (5.9) can be rewritten as:

$$\frac{ds}{dt} = -2\sqrt{\frac{s}{\gamma\lambda}} \tag{5.35}$$

which possesses the general solution:

$$s(t) = \left(\sqrt{s_i} - \frac{t}{\sqrt{\gamma\lambda}}\right)^2. \tag{5.36}$$

This equation represents the evolution of the variance when the trap is compressed following the optimal protocol for the stiffness $\kappa_{\mathrm{opt}}(t)$, whose expression can be obtained by inserting Eq. 5.36 into Eq. (5.32):

$$\kappa(t) = \frac{D\gamma + \sqrt{\gamma s_i/\lambda} - t/\lambda}{\left(\sqrt{s_i} - t/\sqrt{\gamma\lambda}\right)^2}, \tag{5.37}$$

this temporal evolution ensures the minimal trade-off between Δt and W, in other words, generates a transfer between two equilibrium states as "fast and cheap" as possible.

In our case, the Euler-Lagrange equation is purely algebraic, so that one cannot enforce the initial and final conditions, unlike other strategies consisting in solving differential equations to find the suitable evolution for $\kappa(t)$. Except for the quasi-static limit, Eq. 5.37 does not satisfy the conditions for which the system is at thermal equilibrium in the initial and final states. In order to ensure that $s_{i,f}\kappa_{i,f} = k_B T$, we need to add to Eq. 5.37 two discontinuities (See Appendix C). The optimal protocol, shown in Fig 5.5, thus, consists of three successive sequences:

① At time $t = t_i$, the trap stiffness is suddenly changed from $\kappa_i = D\gamma/s_i$ (initial equilibrium) to $\kappa(t_i^+) = \kappa_i^+$, such that: $\kappa_i^+ - \kappa_i = \sqrt{\gamma/(\lambda s_i)}$, while keeping the variance equal to s_i;

② Between t_i^+ and t_f^-, the stiffness varies according to Eq. 5.37, reaching $\kappa(t_f^-) \equiv \kappa_f^- = D\gamma/s_f + \sqrt{\gamma/(\lambda s_f)}$;

③ At time $t = t_f$, the stiffness is suddenly changed from κ_f^- to $\kappa_f = D\gamma/s_f$ (final equilibrium), while keeping the variance equal to s_f.

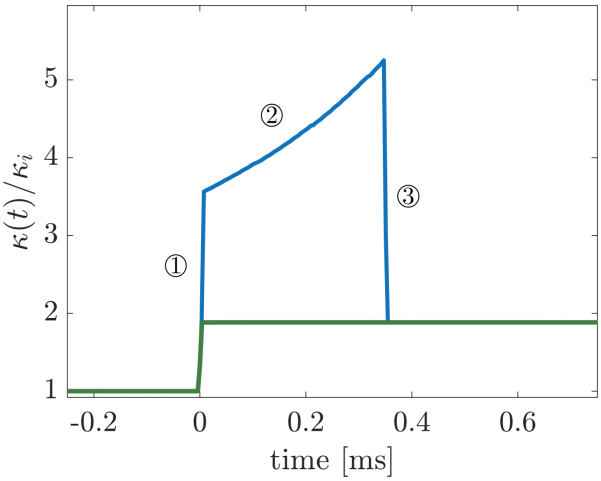

FIGURE 5.5: Three succesive sequences constituting the temporal evolution of the optimal protocol. $\kappa_{\text{opt}}(t)$ (blue curve) is compared to the STEP protocol (in green) for the same transition $\Delta\kappa$. The two protocols are normalized to κ_i.

Discontinuities are part of optimization problems, as emphasized in [44, 164], and depending on the system, they can have a clear interpretation, in our case, their presence forces thermal equilibrium at initial and final sequences of the protocol.

To implement experimentally such optimal protocols the procedure is as follows:

- We choose the initial and targeted equilibrium states, by setting κ_i and κ_f, this fixes the characteristic natural relaxation time $\tau_{relax} = 2\gamma/\kappa_f$ associated to the final trapping potential $U(x, \kappa_f) = \kappa_f x^2/2$, and the values of s_i and s_f from equipartition.

- We choose to accelerate the transition n times compared to the characteristic τ_{relax}, this gives the protocol duration $\Delta t_{\text{opt}} = \tau_{relax}/n$, or simply the desired Δt_{opt}.

- In turn, from Eq. 5.33, these choices fix the Lagrange multiplier λ as:

$$\lambda = \frac{\Delta t_{\text{opt}}^2}{\gamma(s_i^{1/2} - s_f^{1/2})^2} \tag{5.38}$$

  and consequently the jumps, ① and ③, in figure 5.5.

We perform the experiment for the same transition described in the case of the ESE and the STEP protocols, see Fig. 5.3. The results are shown in Fig. 5.6 below. The stiffness of the potential is fixed to $\kappa_i = 2.77 \pm 0.08\,\mathrm{pN}/\mu\mathrm{m}$ during the first 30 ms of the cycle, then at $t = 0$ the stiffness evolves according to the optimal protocol containing the three sequences described above, and at time $t_f = \Delta t \sim \tau_{relax}/10 = 3.47 \times 10^{-4}$ s, the stiffness reaches the final equilibrium value $\kappa_f = 5.22 \pm 0.15\,\mathrm{pN}/\mu\mathrm{m}$ and is maintained at this value during (20 - Δt) ms, the protocol is repeated 24000 times, and each cycle lasts 50 ms.

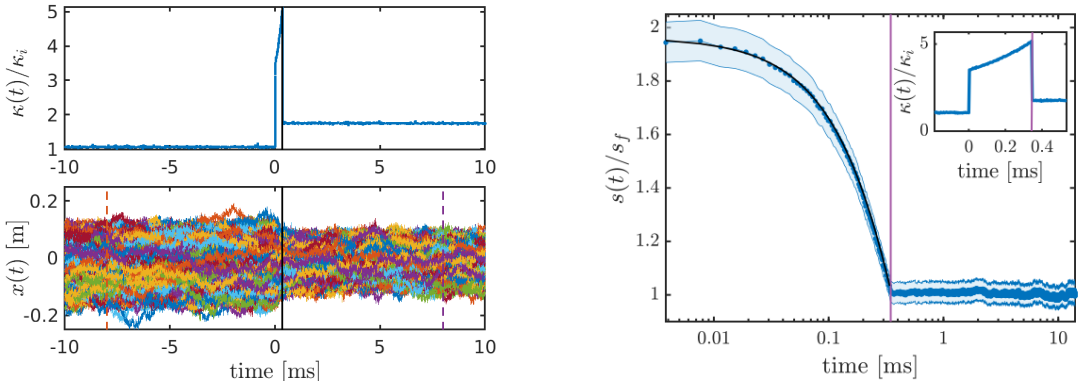

FIGURE 5.6: Experimental results of the optimal protocol. Left panel displays the ensemble of trajectories undergoing one cycle of the the optimal protocol $\kappa_{\mathrm{opt}}(t)$ shown on top. The black vertical lines indicate t_f. Right panel shows the temporal evolution of the corresponding ensemble variance $s(t)$ with a 95% confidence interval.

The temporal evolution of the variance shows that the system is fully relaxed at the final equilibrium $s_f = \kappa_f/k_BT$, exactly at time $t_f = \Delta t$. $s(t)$ evolves in excellent agreement with the theory, as displayed in Fig. 5.6 with the superimposed black continuous line, which represents the theoretical evolution, Eq. 5.36, calculated with the experimental values, s_i and λ. The Lagrange multiplier for this protocol was $\lambda = (5.29 \pm 0.08) \times 10^{-4}\,[\mathrm{s}/k_BT]$. In figure 5.7 below, we compare these results with those obtained using ESE and STEP protocols.

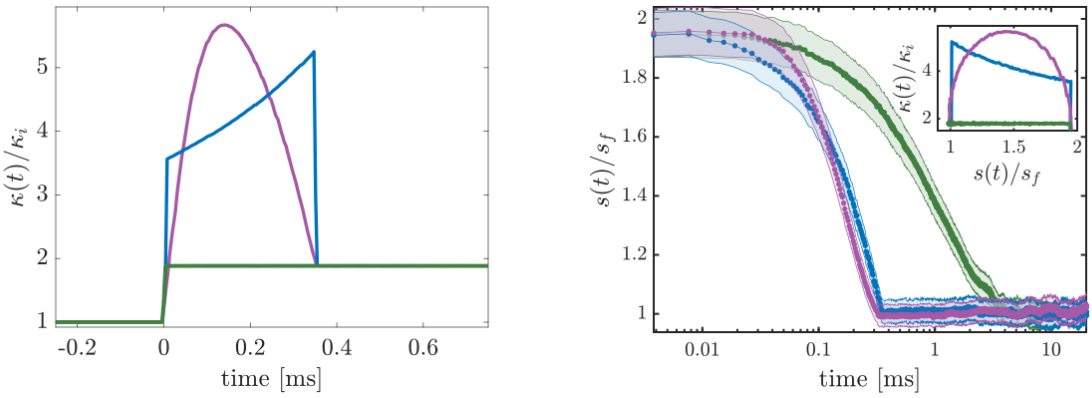

FIGURE 5.7: Left panel: $\kappa(t)$ for the ESE (pink), STEP (green) and optimal (green) protocols. Right panel: Associated variance evolutions. Inset: The trajectories of the different driving schemes in the (s, κ)-space.

When the stiffness instantly disrupts the system, as with the STEP protocol, the PDF of positions exponentially relaxes to the final equilibrium PDF characterized with a variance s_f. It can be observed that complete relaxation is reached after a time $\tau_{relax} = 2\gamma/\kappa_f = 3.22$ ms. Whereas under the two other compression schemes, the ESE and the optimal, the system reached the new equilibrium state exactly at the time imposed, $t_f = 0.35$ ms. Both accelerate the process effectively, but the dynamics of evolution are very different between the two, this, together with the shape of $\kappa(t)$, the striking differences can be clearly seen in the (s, κ) parameter space, see inset of the figure, and will be reflected in the energy cost discussed below.

5.4.1 Energetics of the optimal protocol

Defining a (s, κ) parameter space is advantageous since the work is clearly half the area beneath the curve $\hat{\kappa}(s)$, see Eq. 5.27.

We analyse the energetic cost associated to each sequence of the optimal protocol described above, and we show the evolution of the measured mean cumulative energetics in the left panel of Fig. 5.8. We can describe the work evolution during the three sequences, depicted in blue in Fig. 5.8:

① The quantity of work $W^{(1)} = s_i(\kappa_i^+ - \kappa_i)/2$ is injected instantaneously into the system at the time t_i as the trap is suddenly stiffened from κ_i to κ_i^+.

② The injection of work continues as the trapping volume is progressively reduced, reaching $W^{(2)} = W_{\rm QS} + \sqrt{\gamma/\lambda}\left[(s_i^{3/2} - s_f^{3/2})/3 - (s_i^{1/2} - s_f^{1/2})/2\right]$ at $t = t_f^-$, when $\kappa = \kappa_f^-$.

③ The trap is suddenly expanded at $t = t_f$, and the system instantly reaches its final equilibrium state, delivering to the thermal bath a quantity of work equal to $W^{(3)} = s_f(\kappa_f - \kappa_f^-)/2$. For $t > t_f$, the thermal steady state is characterized by $W = Q$.

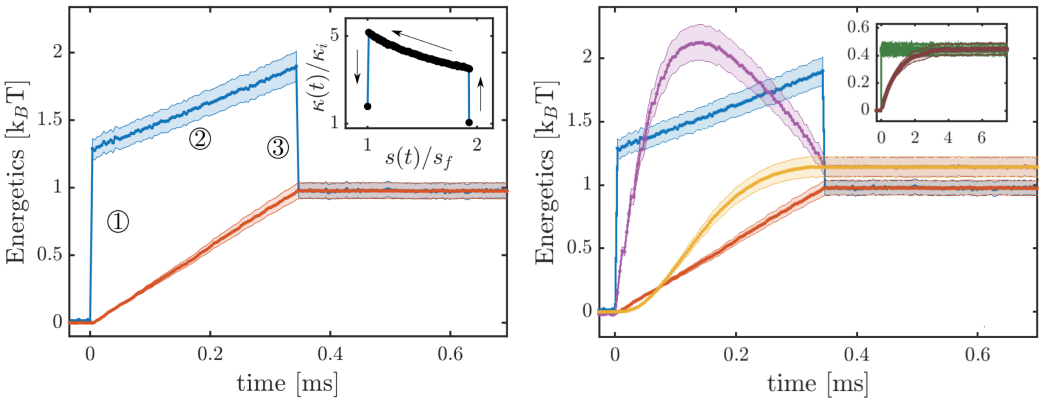

FIGURE 5.8: Left panel: Temporal evolution of the mean cumulative energetics of the optimal protocol. $W_{\text{opt}}(t)$ is plotted in blue and $Q_{\text{opt}}(t)$ in orange. Inset: The protocol in the (s, κ)-space with the sens of the arrows indicating the order of the sequences ① → ② → ③ (or the time). Right panel: Comparison of the energetics of the optimal protocol with the ESE and the STEP (bottom inset) described previously. $W_{\text{ESE}}(t)$ is represented by the pink curve, $Q_{\text{ESE}}(t)$ is displayed in yellow. Shaded areas represent 95% confidence levels.

We evaluate our optimal protocol with respect to our reference, the STEP protocol, and the accelerated protocol, ESE. The results are shown on the right panel of figure 5.8 above. The evolution of the mean cumulative energetics associated to the STEP protocol are shown in the inset of the right panel. Both protocols, the optimal and ESE, attain the equilibrium, given by $W = Q$ precisely at $\Delta t = t_f = 3.47 \times 10^{-4}$ s. Since the ESE protocol is not optimal, to perform the same acceleration as the optimal protocol, confinement has to be increased even beyond the maximum value attained by $\kappa_{\text{opt}}(t)$, and thus, as shown in the curves, more work has to be expended and dissipated. The non-optimal character of the ESE protocol is directly measured with excess work $\Delta W_{\text{ESE}} = W_{\text{ESE}} - \Delta F = 0.81 \pm 0.08\ k_{\text{B}}T$ larger than the optimal value $\Delta W_{\text{opt}} = W_{\text{opt}} - \Delta F = 0.65 \pm 0.07\ k_{\text{B}}T$. In both cases, the acceleration is limited by the maximum laser intensity, therefore for a system limited by the experimental conditions, from a practical point of view, implementing the optimal protocol is also advantageous as it allows to accelerate more, since $\kappa_{\text{ESE}}^{\max} > \kappa_{\text{opt}}^{\max}$ to achieve the same $t_f = \tau_{relax}/n$.

5.5 Universal time-energy bound

From the expressions $\Delta t_{\text{opt}} = \sqrt{\gamma\lambda}\left(s_i^{1/2} - s_f^{1/2}\right)$ and $W_{\text{opt}} = W_{\text{QS}} + \sqrt{\gamma/\lambda}\left(s_i^{1/2} - s_f^{1/2}\right)$, derived as Eqs. 5.33 and 5.34, we can notice that the two values depend only on the difference between initial and final equilibrium states, $s_{i,f}$ and the Lagrange multiplier λ, to which a more intuitive expression can be attributed:

$$\lambda = \frac{\Delta t_{\text{opt}}}{W_{\text{opt}} - W_{\text{QS}}}, \tag{5.39}$$

making very explicit the trade-off between transition time and expended work. This leads us to define the "*excess work*" of the optimal protocol as:

$$\Delta W_{\text{opt}} = W_{\text{opt}} - W_{\text{QS}} \tag{5.40}$$

which corresponds to the dissipative work discussed in the previous chapter, but in this new context of "fast and cheap" protocols results a more convenient terminology.

The central result relies on the product $\Delta t_{\text{opt}}\,\Delta W_{\text{opt}} = \gamma/2(s_i^{1/2} - s_f^{1/2})^2$, which is independent of λ. In other words, it only depends on the difference between the initial and final states. From this remarkable result, we can define a mutually exclusive relation between the transfer duration and the expended work, and it corresponds to the frontier value of a universal exclusion region:

$$\Delta t\,\Delta W \geq \gamma/2(\sqrt{s_i} - \sqrt{s_f})^2, \tag{5.41}$$

that bounds from below all protocols that are not optimal. In order to draw this frontier experimentally, we perform 8 optimal protocols of different durations $\Delta t_{\text{opt}} = \tau_{relax}/n$, with $n \sim 34, 30, 22, 16, 10, 6, 3, 2$, keeping the same choice of κ_i and κ_f for all. We extract the different ΔW_{opt} associated to the different Δt_{opt}. For each protocol, ΔW_{opt} is normalized by the corresponding measured value $\gamma/2(\sqrt{s_i} - \sqrt{s_f})^2$, considering that from experiment to experiment the values of $s_{i,f}$ vary slightly, since experiments are not performed the same day under the same calibration or since when performing various experiments one after the other, a slight degradation from the initial calibration can take place. However, the ratios κ_f/κ_i or s_i/s_f are not affected. We can emphasize that our procedures involve $\Delta\kappa/\Delta t$ ratios, which are unaffected by systematic errors that act equally in all stiffnesses and are therefore compensated in such $\Delta\kappa$ terms. This an important asset of our approach, which becomes insensitive to absolute values.

With the above discussion in consideration, the frontier of the universal exclusion region can be verified experimentally, see Fig. 5.9 by observing that all the coordinates, $\{\Delta t, \Delta W_{\text{opt}}/(\gamma/2(\sqrt{s_i} - \sqrt{s_f})^2)\}$ precisely fall (within error bars) on the $1/\Delta t$ curve.

The universal character of the bound is further explored, by placing the values of excess work normalized respectively, and Δt obtained from other protocols that are non-optimal, such as the ESE protocol, the STEP and the smooth protocols defined in Appendix 3. We observe that all these fall above the optimal bound.

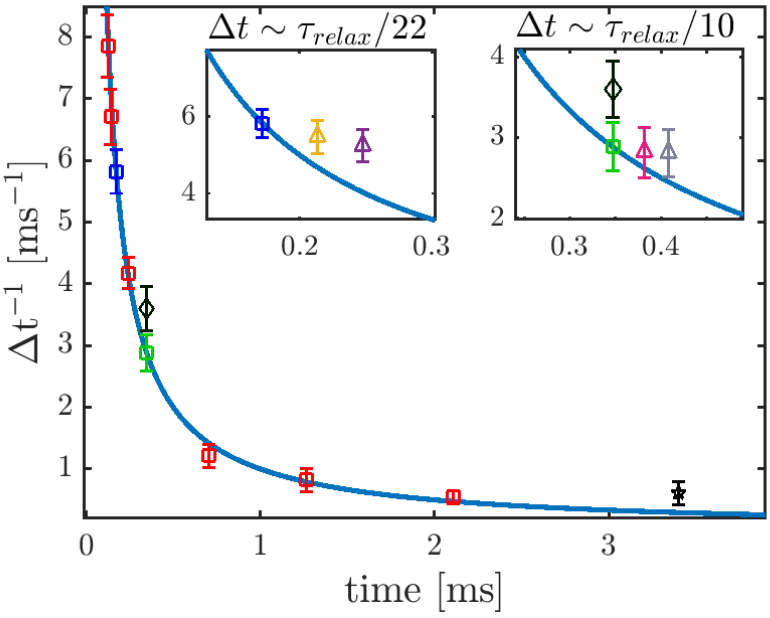

FIGURE 5.9: Experimental verification of the universal time-energy exclusion relation. The continuous solid blue line represents $1/t$. The red markers with errorbars are the normalized values of ΔW_{opt} for the optimal protocols mentioned in the main text. The blue and green markers also correspond to optimal values, and they appear in the insets along with the values obtained by the smooth protocols. The black diamond represents the normalized value associated to the ESE protocol discussed above, and the black star with the STEP.

5.6 Normality tests

Under modulation of the stiffness of the trapping potential, it is crucial to verify that the PDF of positions of the trapped particle remains Gaussian. A straightforward way to assess the normality of the experimental is by calculating the kurtosis at all times of the cycle. The kurtosis is a statistical measure, which determines the degree of concentration presented by the values of a variable around the central area of the distribution, it is defined as:

$$\text{kurtosis}(x) = \frac{\mu_4(x)}{\sigma^4(x)} \tag{5.42}$$

where $\mu_4(x)$ is the fourth central moment and $\sigma(x)$ the standard deviation of the probability distribution $p(x)$. For a Gaussian distribution it is verified that $\mu_4 = 3\sigma^4$, therefore we verify that kurtosis $= 3$ for our data. Small fluctuations of the kurtosis around 3 are expected.

In the figure 5.10 below, we show the measured kurtosis as a function of time, for the entire evolution of the PDF of the system, constructed by the ensemble of trajectories shown in Fig. 5.6. The PDF and the associated trapping potentials are

evaluated at the two different times $t_j < t_0$ and $t_j > t_f$ indicated by the two dashed vertical lines in the bottom right panel of Fig. 5.6, with associated trap stiffnesses $\kappa_i = 2.77 \pm 0.08\,\mathrm{pN}/\mu\mathrm{m}$ and $\kappa_f = 5.22 \pm 0.15\mathrm{pN}/\mu\mathrm{m}$, respectively.

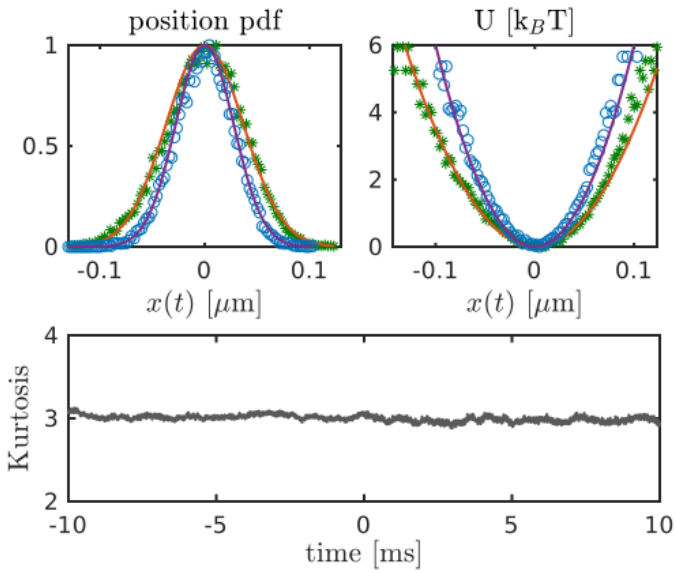

FIGURE 5.10: Top-left panel: Position distribution functions (PDF) built from the ensemble of trajectories at two different times, with associated trap stiffnesses $\kappa_i = 2.78 \pm 0.08$ and $\kappa_f = 5.22 \pm 0.15\,\mathrm{pN}/\mu\mathrm{m}$ respectively. Top-right panel: Associated trapping potentials extracted from the PDF as $U(x, t_j) = -k_\mathrm{B}T \log(\rho(x, t_j)) + \mathrm{cst}$. Bottom panel: Measured kurtosis over the full cycle.

For the shortest protocols, one has to be more careful, since due the instantaneous strong changes in $\kappa(t)$ required to accelerate the transition, there is a higher risk that the trapped bead explores regions beyond the harmonic potential. We therefore carefully assess the normality of the system at all times for the shortest protocol $n \sim 34$, of duration $\Delta t = 1.22 \times 10^{-4}$s which is shown in the upper panel of Fig. 5.11. As seen in the lower panel, the kurtosis remains very close to 3 throughout the entire protocol. To supplement this kurtosis-based analysis we pick four characteristic times, t_0, t_1, t_2, t_3, t_0 at the jump from $\kappa_i \to \kappa_i'$, t_1 in the middle of the evolution, t_2 at jump from $\kappa_f' \to \kappa_f$ and finally one, $t_3 > t_f$ at the final equilibrium value, $\kappa(t) = \kappa_f$. These times are indicated as vertical grey lines in Fig. 5.11 below. For each of these times, we extract the PDF of positions from the ensemble of trajectories and we fit them with Gaussian distributions, the results are shown in Fig. 5.12.

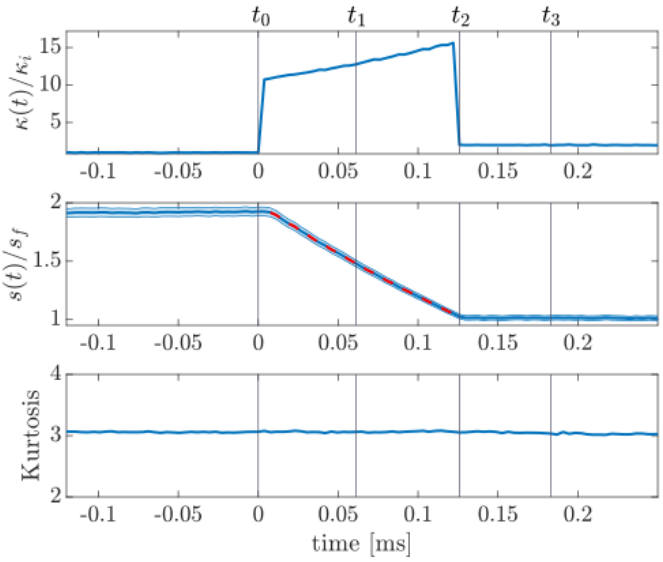

FIGURE 5.11: Top panel: Single cycle of the control parameter $\kappa(t)$ normalized to κ_i for the shortest duration $\Delta t = 1.22 \times 10^{-4}$s protocol. Middle panel: Corresponding time-evolution of the ensemble variance $s(t)$ extracted from the PDF of the ensemble of trajectories, normalized to s_f. The red dashed line, superimposed to $s(t)$ between the transition points, corresponds to the variance extracted from the slopes of the quantile-quantile plots extracted throughout the protocol and shown in the inset of Fig. 5.13. Bottom panel: Kurtosis evaluated throughout the protocol. The vertical lines represent the four times chosen for the analysis of normality.

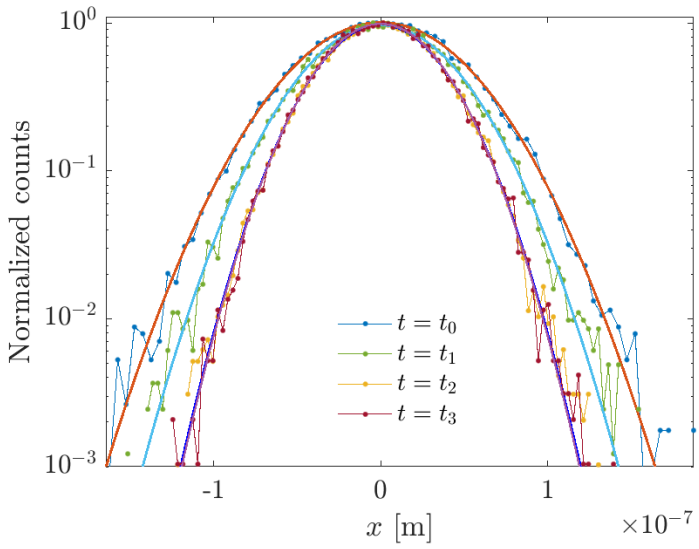

FIGURE 5.12: Normalized PDF represented in log-scale for the four times shown in figure 5.11. The solid lines represent the results of Gaussian fits.

We compare the same family of distributions with varying variance to a Gaussian distribution of zero mean and unitary variance. We plot the quantile-quantile relation

between the standard normal distribution and the for distributions plotted in 5.12 and plot a linear regression to evaluate the departure from normality. The results are displayed in Fig. 5.13 below.

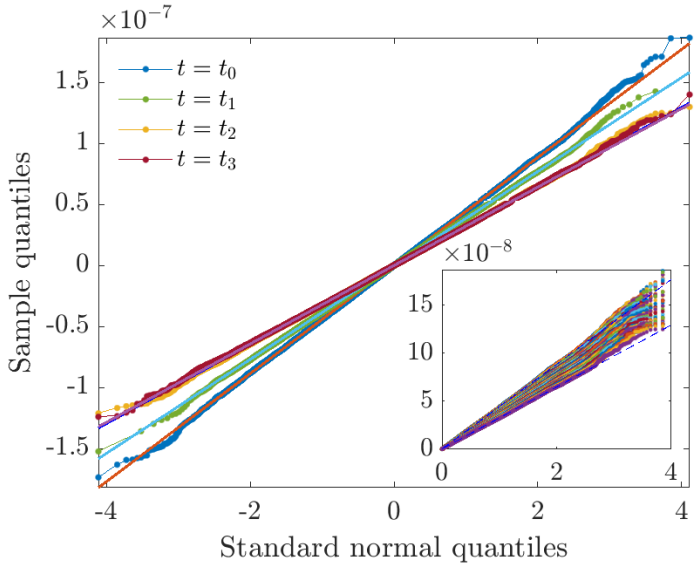

FIGURE 5.13: Quantiles of the PDF at four different times of the protocol as a function of the theoretical quantiles of a standard $\mathcal{N}(0,1)$ normal distribution. Inset: Evolution of the quantile-quantile plot as the stiffness increases with time, the dashed lines represent the linear fits of the quantile-quantile plots of the points at the beginning and end of the protocols.

The intersection of all curves coincides with the 2-quantile, indicating that all distributions are of zero mean, the slope indicates the variance of the distribution, which, as expected, evolves over time through the protocol. For each of these times, despite that most of the data is compatible with a theoretical Gaussian we observe above the fourth quantile, departures of the data from the linear regression. These, depending if they are situated above or below, the regression line, correspond to some of the tails regrouping more or less points, indicating a higher or lower probability of extreme events compared to a perfect normal distribution This is expected given the discrete nature of the data. This does not affect the well-defined mean and variances which are as close as possible to a perfect Gaussian.

For a short protocol, since the transition is much faster than the position relaxation time of the particle, we verify that at all sampling times, $t_0 < t < t_2$, the PDF remains Gaussian and that the variance is well defined. The enveloppe of quantile-quantile plots is displayed in the inset of Fig. 5.13. From the linear fit of each of these relations, we can extract the evolution of the slope of the quantiles as $\kappa(t)$ increases from κ_i to κ_f. From the slopes, we can directly extract the variances, superposed as red-dashed lines in the middle panel of figure 5.11. Besides changing its variance the shape of the PDF does remain the same at all times of the process. We observe that the evolution of the slope corresponds perfectly to the expected evolution of the variance of an optimal

protocol. The variance can therefore be considered as well-defined for our analysis of the time-evolution. Another remarkable feature is that all the curves pass through zero, indicating that the mean of the distribution does not change during the process. The curves remain linear up to the upper quantile, where the points slightly start departing from the linear relation. Overall, therefore this diagrammatic analysis successfully validates that the data to be treated as Gaussian at all points along the transition.

5.7 Discussion and outlook for future works

In this chapter, we have studied the dynamics of a Brownian particle trapped in an optical potential that can vary over time, using the results of stochastic thermodynamics to study the transformations between two equilibrium states of the system. This led us to design protocols for controlling the optical potential so that the transformations between the equilibrium states are done in an optimal way, that is to say, that the relaxation of the particle towards an equilibrium state is done in a fast as possible while guaranteeing a minimal energy dissipation. This is framed within a universal exclusion relation between state transfer duration and expended work.

Our experiments consisted in checking carefully that our initial trapping conditions are harmonic indeed, and that the evolution of the variance of position of the bead follows a Gaussian law throughout the experiments. These verifications are crucial to accurately compare the calculations with the experimental data. These verifications then make it possible to precisely measure the duration, the work and the heat associated with a transformation between two states as functionals of the variance and of the control parameter, which is the stiffness of the trap. To obtain the optimal protocol which minimizes these two quantities, we introduced a Lagrange multiplier between work done by the transformation and duration of this transformation in order to define the minimal amount of work compatible with a given transfer duration.

As stressed in the introduction this capacity for optimizing stochastic processes in rooted in the exceptional control that one can reach with an optical trap. In particular, the possibility to identify both a clear control parameter in the trap stiffness and a clear observable through the motional variance led us to build a (s, κ)-parameter space where optimization through variational calculus can be easily performed.

6 Summary and future perspectives

The adaptability of our optical trapping configuration in synergy with the rich theoretical framework of Langevin equation allowed us to exploit and control the dynamics of an intrinsically noisy system, an optically trapped Brownian particle. First, from a metrology perspective, we have devised through such dynamics a force microscope capable of detecting weak optical forces at the femtonewton scale in water at room temperature. Then, optimal thermodynamic transformations between equilibrium states have been accomplished through a strategy that minimizes the relaxation time and the associated expended work on the Brownian particle in the optical potential subject to compression. Furthermore, stable trapping of single chiral nanoparticles has been achieved using a standing wave trap configuration, and the recognition of the handedness of the trapped object was performed based on the fundamental conservation law of optical chirality [116]. In the following we overview the central results discussed in the manuscript.

Measuring weak optical forces at the thermal limit

Langevin equation offers the possibility to add deterministic terms and to act on each term independently. Optical tweezers offers the possibility to implement experimentally the different terms involved in the Langevin equation in a controlled way while giving access to the instantaneous position of the trapped Brownian particle with spatial resolutions at the level of the angstrom and temporal resolutions below microseconds. This is how we based the construction of a force microscope capable of measuring optical forces at the limit imposed by thermal noise, and how we used this microscope to measure weak radiation pressure force fields.

The first ingredient in these experiments is the probe itself, a gold nanosphere with a diameter of 150 nm. Its characteristics were chosen to maximise the dissipative interaction between the trapped bead and the laser beam generating the radiation pressure. In order to stably confine these particles, we have not used a conventional trap, but we have exploited the standing wave pattern created by the interference between the incident and reflected beam by focalizing the trapping laser close to a reflecting surface. In this configuration, the gold nano spheres are immobilised in the antinodes of the interference pattern. As a reflecting surface, we have used a dichroic mirror which allows the injection of the external radiation pressure beam, which acts on the probe without affecting the trapping dynamics. The intensity of this beam is periodically modulated so that detection is carried out by the spectral analysis of the position of the probe, where the effect of the force appears as a peak at the modulation frequency,

superimposed to the typical power spectrum associated with the trapping dynamics. This allowed us working directly at the thermal limit.

A key feature of such a microscope is the definition of the maximum bandwidth allowed by the stability of the experimental setup. These meticulous checks of the stability conditions led to measuring radiation pressure forces down to 3 fN over a bandwidth of 10 s that ensured the system to remain limited by the termal noise. This resolution is to be compared with the dynamic range offered by our system, which corresponds to a ration of 1/100 between the modulated component and the static component of the force. The measurements were made at different modulation frequencies, reaching sub-angstrom position resolution levels for all drive frequencies for displacement of 10^{-11} m recorded at a modulation frequency close to 100 kHz.

In-situ enantiomeric recognition of single optically trapped chiral nanoparticles

The force microscope described above is of particular interest for measuring chiral optical forces, which are typically 2 orders of magnitude weaker than the conventional optical forces such as gradient forces or radiation pressure. Recently confirmed at the microscale, such forces remain to be measured at the nanoscale, domain in which new strategies for all-optical chiral separation could be developed. Theoretical estimations show typical values of such forces to be of the order of femtonewtons in thermally-limited conditions.

Trapping single chiral nano-objects is the first essential step for measuring such forces. In close collaboration with Lisa V. Poulikakos and Prof. David Norris, from the ETH-Zurich, we have achieved stable trapping of single gold nanopyramids with characteristic sizes of the order of 150 nm. The three-dimensional power spectral analysis of their position fluctuations in the trap indicated stable confinement during times longer than 30 s.

The nanopyramids feature strong signals of circular dichroism peaked at 639 nm and important sign inversions between left and right-handed enantiomers. The adaptability of the experimental setup was also exploited in this context. The standing wave trap guaranteeing the stable trapping of single chiral nano pyramids allows the addition of a polarimetry line. The laser, of wavelength 639 nm serving as a test beam for radiation pressure in the study of force microscopy, is in this case used as a recognition laser.

Our experiments exploited a fundamental result obtained by Lisa V. Poulikakos from David J. Norris' group: A chiral dissipative object illuminated by a non-chiral optical field has to break, in the scattering, the initial balance between right and left polarisation by a means of selective dissipation of electromagnetic energy. It is precisely this breakdown that we were capable of probing in our trap by measuring the

contrast between the left and right polarizations of light scattered by the nanopyramid, from the linearly polarised 639 nm laser. This revealed the capacity of our setup to discriminate, in-situ, the enantiomeric forms of single chiral nanoparticles.

This combination of ingredients –our force microscope, the stable trapping and enantiomeric recognition of nanoparticles with chiral shapes– holds a promising strategy for measuring chiral optical forces at the nanoscale [103], and eventually be able to design all-optical strategies mechanical separation of chiral molecules [131].

Thermodynamic protocols for optimal control of a transfer between two equilibrium states of a Brownian particle.

We have then exploited the capacity of our experimental configuration for creating optical confinement potentials which depend on time. To do this, we modulate the stiffness of the trap (our control parameter) over time by following different protocols. These possibilities allow in particular to study precisely, in the framework of stochastic thermodynamics, the notion of transfer between equilibrium states. An interesting discussion is to consider our optically trapped bead as an analog to a gas-piston model in thermodynamics. Variations in stiffness will correspond to variations in volume of the piston and the consequences on the Brownian fluctuations of our trapped bead will be interpreted as the effects of such piston-gas thermodynamic transformations.

We tackled the problem of accelerating the thermalization of the transfer between two equilibrium states. Usually, accelerating the transfer comes at a high energetic cost, since it is necessary to inject into the system a large amount of work (i.e. a strong intermediate compression of the trap) to quickly thermalize the bead. In collaboration with G. Manfredi and P.A. Hervieux of IPCMS, in Strasbourg, and Laurent Mertz from NYU-Shanghai, we have introduced a new strategy that treats both the duration of the transfer and the expended work in a complete symmetric way, which provides the outstanding capacity to optimally regulate the trade-off between these two quantities. In this way, we were capable of designing a class of optimal protocols. Such protocols reach the best possible compromise between transition time and the energy cost. We were then able to describe experimentally and theoretically all the thermodynamics associated with these constraints, by exploiting the techniques of stochastic thermodynamics. In particular, we have derived a universal energy-time relationship (i.e. dependent only on the initial and final equilibrium conditions) which takes the form of a minimal bound for optimal protocols.

The optimization strategy discussed for transformations between thermodynamic states could be explored for transformations between non-equilibrium steady states (NESS). The most exciting potential application is in the domain of thermal nano-engines, in which it is often desired to have good efficiency at maximum power. An analog strategy could be designed to maximize these two quantities, or simply use thermodynamic cycles that minimize the transfer duration to make shorter cycles that

extract more power while dissipating the minimum to gain in efficiency. For such extent, one could envision to devise a strategy in which an optimal protocol for temperature changes within the cycle (e.g. s in Stilring cycle). Doing so, we could build cycles for which each step, i.e. expansion and compression, together with the temperature transitions, are optimal. Along this line, an interesting prospect would be to control the noise term of the Langevin equation. This has already been explored in [71], but not yet in the context of stochastic optimization.

7 *Résumé de la thèse*

I. Introduction

Le comportement dynamique de nombreux systèmes hors équilibre est considérablement influencé par l'interaction entre la source de bruit et les degrés de liberté déterministes. De telles dynamiques régies par le bruit sont à la base d'une grande partie des processus naturels.

C'est par l'étude de la dynamique d'une microparticule plongée dans un fluide, et donc influencée par la dynamique des degrés de liberté rapides des plus petites particules du fluide que Brown, Smoluchowski, Einstein, Langevin et d'autres ont contribué au développement d'une description complète d'une telle dynamique stochastique. Aujourd'hui elle sert à décrire des nombreux phénomènes dans diverses disciplines. Par exemple: en climatologie pour expliquer les changements climatiques lents comme réponse intégrale à des excitations aléatoires générées par des perturbation rapides météorologiques [165], en génétique pour élucider le fait que notre individualité génétique est due à la fécondation aléatoire, union aléatoire d'une gamète de chaque parent pour former la première cellule de la nouvelle progéniture [18] et comprendre alors comment une telle cellule développe certaines caractéristiques morphologiques. Dans ce cadre génétique, ces processus sont aléatoires précisément parce qu'il y a un mouvement brownien à l'échelle moléculaire des entités biologiques en jeu. Les exemples d'applications du calcul stochastique sont également vastes et divers, allant des prédictions sur des marchés financiers aux descriptions de plusieurs phénomènes des réseaux neuronaux.

L'équation de Langevin décrit la dynamique brownienne comme un équilibre de forces. En reprenant l'exemple d'une particule immergée dans un fluide, cet équilibre de forces s'écrit entre un terme inertiel, un terme visqueux, due au frottement de la bille avec le fluide, et un terme stochastique, connu comme la force thermique ou la force de Langevin, qui représente les effets des collisions aléatoires de la bille avec les molécules du fluide.

L'étude de la dynamique brownienne s'est récemment enrichie d'une technique expérimentale puissante: les pièges optiques. Ces systèmes permettent de piéger optiquement, dans un environnement bien contrôlé, des objets Browniens uniques et d'accéder directement à leurs évolutions stochastiques. Dans ce contexte, les pièges optiques ont permis de réaliser expérimentalement des dynamiques associées à une équation de Langevin où viennent s'ajouter, de manière très contrôlée, des termes déterministes

tels qu'un potentiel d'interaction, qui peut prendre différentes formes, ainsi que des force externes non-conservatives. Globalement, les pièges optiques, par le biais des forces optiques, ont permis l'étude des systèmes Browniens sous des angles nouveaux. L'exemple à ce titre le plus impressionnant a été l'étude et la description des moteurs moléculaires et des machines microbiologiques faites dans les années 1990-2000 par Carlos Bustamante notamment. En parallèle, les pièges optiques ont permis de réaliser (on parle de «simulations» expérimentales) un grand nombres de protocoles récemment prédits et discutés dans le domaine de la thermodynamique stochastique [27], domaine émergeant dans les années 2000 et aujourd'hui très présent dans un grand nombre de laboratoires. Cette thèse porte un intérêt particulier sur ce sujet, d'une part parce qu'il offre la possibilité d'approcher de manière originale plusieurs problématiques étudiées dans notre laboratoire, ensuite parce ces expériences permettent d'être développées en synergie étroite avec une description théorique. Cette synergie permet de tester un grand nombre de résultats théoriques pour lesquels très peu de résultats expérimentaux sont déjà disponibles. C'est dans ce contexte que nous avons étudié la dynamique d'une bille piégé dans un potentiel optique qui peut varier dans le temps, en exploitant les résultats de la thermodynamique stochastique pour étudier les transformations entre deux états d'équilibre du système. Ceci nous a amené à concevoir des protocoles de contrôle du potentiel d'interaction de façon à ce que les transformations entre les états soient faites de façon optimale, c'est-à-dire que la relaxation de la particule vers un état d'équilibre se fait dans un temps plus rapide que l'échelle de temps naturelle de la particule donnée par la viscosité du fluide et la raideur du potentiel tout en garantissant une dissipation d'énergie minimale. Nous avons alors déduit une contrainte universelle imposée par la relation énergie-temps sur de tels protocoles.

II. Résultats et discussions

i) Mesure de forces faibles à la limite thermique

La mesure de forces optiques extrêmement faibles trouve des applications dans divers domaines de la physique. En générale, les méthodes impliquées pour mesurer de telles forces peuvent être utilisées pour la mesure d'autres forces faibles qui ne sont pas d'origine optique, par exemple des forces de Casimir, de Van der Waals, etc. Plusieurs processus naturels impliquent des forces d'intensité de l'ordre des quelques femto-Newtons.

Les pièges optiques donnent accès à la position instantanée de la bille piégé avec des précisions spatiales de l'ordre de l'angström et des résolutions temporelles en dessous de la microseconde. Comme mentionné plus haut, on peut contrôler chaque paramètre de force de l'équation de Langevin et étudier expérimentalement chaque effet indépendamment. C'est ainsi qu'on a basé la construction d'un microscope capable de mesurer des forces optiques à la limite fondamentale imposé par le bruit thermique. Un tel microscope est un piège optique conçu pour permettre l'injection d'une force externe

sans perturber le piège. La force externe, dans notre cas une force de pression de radiation optique, est modulée périodiquement et sondée par la bille. Les dynamiques du piège et de la force sondée étant indépendantes, la détection est faite par une analyse spectrale de la position de la bille à la fréquence de modulation, ce qui nous permet de travailler directement à la limite thermique.

Le premier ingrédient important est la sonde elle-même. Pour nos expériences, il s'agit d'une nano-sphère d'or de 150 nm de diamètre, avec les caractéristiques choisies pour maximiser l'interaction dissipative entre la bille et le faisceau laser générant la pression de radiation que nous souhaitons mesurer. Le piège lui-même n'est pas un piège optique conventionnel. Devant être capable de piéger stablement des telles sondes métalliques, il fonctionne sur le mode d'un piège à onde stationnaire crée par l'interférence entre le faisceau incident et sa réfection sur une surface réfléchissante. C'est dans cette onde stationnaire qu'on arrive à confiner la bille, en la piégeant dans un ventre de l'interférence. En utilisant pour surface réfléchissante un miroir dichroïque, on peut injecter dans le piège le laser externe de pression de radiation. La détection dynamique de la force, modulée sinusoïdalement, se fait directement sur le pic spectral de force superposé au spectre de la fonction d'autocorrélation de la position de la bille d'or piégée ou bien par détection synchrone. Dans nos expériences, nous portons toute notre attention sur la définition de la bande passante maximale autorisée par la stabilité de notre microscope pour mesurer l'amplitude de la force à la limite thermique.

Ces contrôles méticuleux des conditions de stabilité permettent la mesure d'une force de pression de radiation de 3 fN sur une bande passante de 10 s en garantissant que le système reste limité par le bruit thermique. Cette résolution est à mettre en regard avec la grande plage dynamique offerte par notre système et qui correspond à un rapport 1/100 entre la composante modulé et la composante statique de la force.

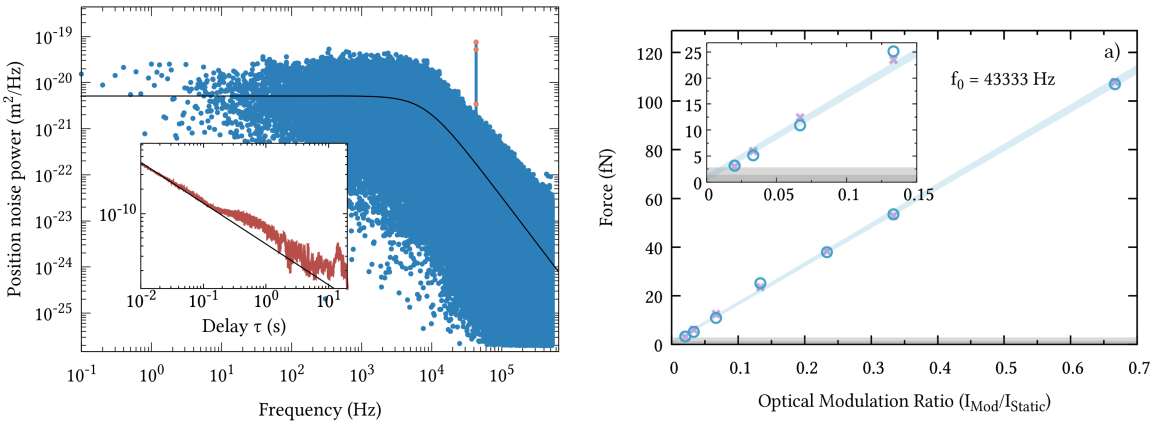

FIGURE 7.1: Panel de gauche: Puissance spectrale du système contenant la signature de la force comme un peak à la fréquence de modulation superposé à la dynamique de la bille dans le piège. En insère: mesure de stabilité globale du système, indiquant la bande passante optimale pour la mesure. Panel de droite: Force mesuré par la méthode montré à gauche, pour différents amplitudes de modulation, avec la plus petite amplitude se trouvant à limite thermique indiquée comme zone grise. verify and rewrite.

ii) Reconnaissance in-situ de nanopyramides chirales uniques piégées

Dans notre laboratoire, un intérêt particulier se porte sur l'influence de la chiralité optique dans les interactions optomécaniques. Une nouvelle classe de forces optiques émergeant de l'interaction entre lumière chirale et matière chirale à l'échelle nanoscopique a été prédite par notre équipe [99]. Récemment confirmées dans le domaine micrométrique par des résultats expérimentaux récents [126, 129], ces forces restent encore à être mesurées dans le régime nanométrique. Une telle démonstration aurait un impact important, révélant la possibilité de nouvelles stratégies «tout-optique» de séparation chirale. Théoriquement pourtant, les estimations faites sur ces forces optiques chirales montrent qu'elles sont typiquement 2 ordres de grandeur plus faibles que les forces optiques conventionnelles (forces de gradient et pression de radiation) et qu'elles atteignent des valeurs typiques de l'ordre du femtoNewton. Dans ce contexte, les caractéristiques de notre piège optique en tant que microscope de force optique, résumées en *i)*, sont extrêmement intéressantes.

Le piégeage optique de nano-objets chiraux uniques est donc une première étape essentielle pour la mise en évidence de ces nouvelles forces. En collaboration avec le groupe du Prof. David Norris, de l'ETH-Zürich, nous avons réussi le piégeage optique stable de nanopyramides d'or de tailles de l'ordre de 150 nm. Une analyse des puissances spectrales de déplacement d'une nanopyramide unique dans les 3 axes du piège indique un confinement stable du nano-objet sur une durée supérieure à 30 s.

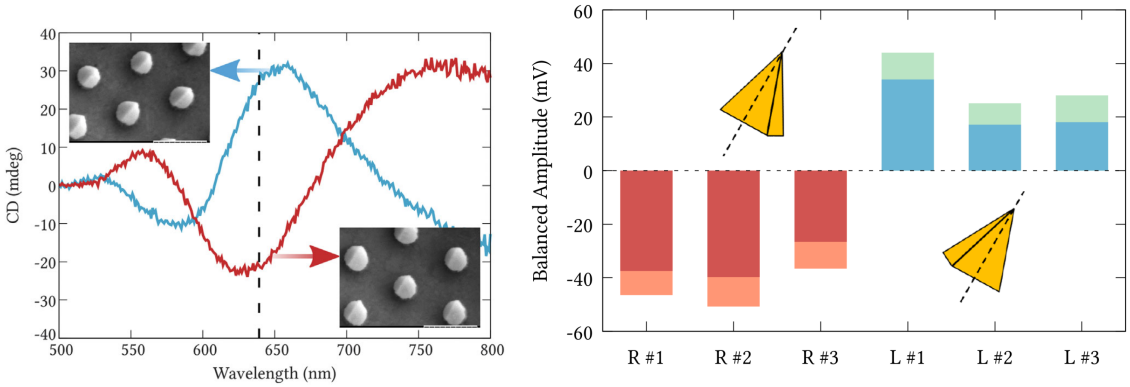

FIGURE 7.2: Panel de gauche: Spectre de dichroïsme circulaire (CD) associé aux nanopyramides apparaissant dans les insères, les formes énantiomères gauches apparaissent au coin supérieur gauche et droites au coin inférieur droit. Panel de droite: Valeurs du paramètre de Stokes de l'intensité de la lumière diffusé par les nanopyramides piégées, utilisées dans les mesures polarimétriques balancés pour deux dispersions des nanoparticules chirales de signe inverse.

Ces nanopyramides sont des objets chiraux particulièrement intéressant pour la nano-optique: ils présentent en effet des signaux des dichroïsme circulaire très importants avec la plus haute amplitude autour d'une longueur d'onde de 639 nm, comme indiqué dans la figure 2. Les spectres indiquent une inversion de signe importante entre les énantiomères gauches et les énantiomères droits. Le laser qui servait en partie ***i)*** de faisceau pousseur pour la mesure de pression de radiation peut être donc utilisé pour la reconnaissance chirale, ayant une longueur d'onde correspondant au maximum du signal CD.

Nos expériences exploitent alors un résultat important obtenu dans le groupe du Prof. D.J. Norris lié à une loi de conservation de chiralité optique. Un objet chiral dissipatif (donc dispersif) illuminé par un champ optique non-chiral doit briser, en diffusion, la balance initiale de polarisation droite et gauche par dissipation sélective en spin de l'énergie électromagnétique. C'est précisément cette brisure que nous avons été capable de sonder dans notre piège en mesurant le contraste de polarisation droite vs. gauche de la diffusion, sur la nanopyramide, du laser à 639 nm polarisé linéairement. Les résultats de ces mesures, effectuées sur 2 énantiomères opposés, sont présentées en Figure 2 et montrent la capacité de notre système à discriminer, in-situ, les formes énantiomériques d'un nano-objet unique.

iii) Protocoles thermodynamiques pour le contrôle optimal d'un transfert entre 2 états d'équilibre d'une particule brownienne

Les lois générales de la thermodynamique régissant les échanges de chaleur, travail et matière entre un système et son environnement sont des lois moyennées, pour lesquelles

les effets des fluctuations thermiques se moyennent à zéro. Mais il est possible de définir ces quantités thermodynamiques en tenant compte de ces fluctuations. Cette possibilité devient très importante lorsque ces fluctuations dominent la dynamique, ce qui est évidemment le cas d'un objet Brownien. Les lois qui régissent alors la chaleur ou le travail, devenus des quantités thermodynamiques fluctuantes, forment un domaine de recherche qui a émergé ces 20 dernières années: la thermodynamique stochastique [12]. Un résultat important de ce domaine est de permettre de comprendre comment émergent les propriétés de thermodynamique «macroscopiques» à partir des effets moyennés des propriétés thermodynamiques «microscopiques». Dans ce contexte, les pièges optiques sont des systèmes extrêmement intéressant à utiliser puisqu'ils permettent d'accéder directement aux dynamiques contrôlées d'objet Browniens uniques. Les travaux de Ken Sekimoto en particulier ont permis d'identifier ces quantités thermodynamiques stochastiques directement à partir d'une description de Langevin [41]. Ces travaux ont ouvert une voie de recherche efficace, directement en lien avec les possibilités expérimentales offertes par les pièges optiques.

Revenant donc à la manipulation des différents termes de l'équation de Langevin, notre configuration expérimentale offre la possibilité de créer des potentiels de confinement optique qui varient dans le temps. Pour ce faire, on module la raideur du piège (notre paramètre de contrôle) au cours du temps en suivant différents protocoles. Ces possibilités permettent en particulier d'étudier précisément dans un cadre de thermodynamique stochastique la notion de transfert entre des états d'équilibre. Une analogie intéressante est de considérer alors notre bille optiquement piégée comme une particule d'un gaz enfermée dans un piston. Les variations de raideur vont correspondre aux variations du volume du piston et les conséquences sur les fluctuations Browniennes de notre bille piégée seront interprétées comme des effets de transformations thermodynamiques. Récemment ainsi, de nouveaux protocoles de modification de raideur ont été proposés pour accélérer la thermalisation entre deux états d'équilibre envisagés comme deux volumes de compression optique différents [160].

Notre travail s'est centré sur ce problème de la thermalisation accélérée, c'est-à-dire la réduction de la durée du transfert. En effet, cette accélération se fait à un prix énergétique très élevé puisqu'il faut injecter dans le système une grande quantité de travail (i.e. une forte compression intermédiaire du piège) pour thermaliser rapidement la bille. Notre travail a été de définir une classe de protocoles de transfert optimaux, c'est-à-dire atteignant le meilleur compromis possible entre raccourcissement de la durée du transfert et réduction du coût énergétique. En collaboration avec Prof. G. Manfredi et Prof. P.A. Hervieux de l'IPCMS, à Strasbourg, et Prof. L. Mertz, à NYU-Shangai, nous avons mis en place une méthode variationnelle qui permet de construire de tels protocoles optimaux dans le contexte de nos expériences [85]. Nous avons pu alors décrire expérimentalement et théoriquement toute la thermodynamique associée à ces contraintes, en exploitant les techniques de la thermodynamique stochastique. En particulier, nous avons dérivé une relation énergie-temps universelle (i.e. ne dépendant que des conditions d'équilibre initiale et finale) qui prend la forme d'une

inégalité minimisée pour les protocoles optimaux.

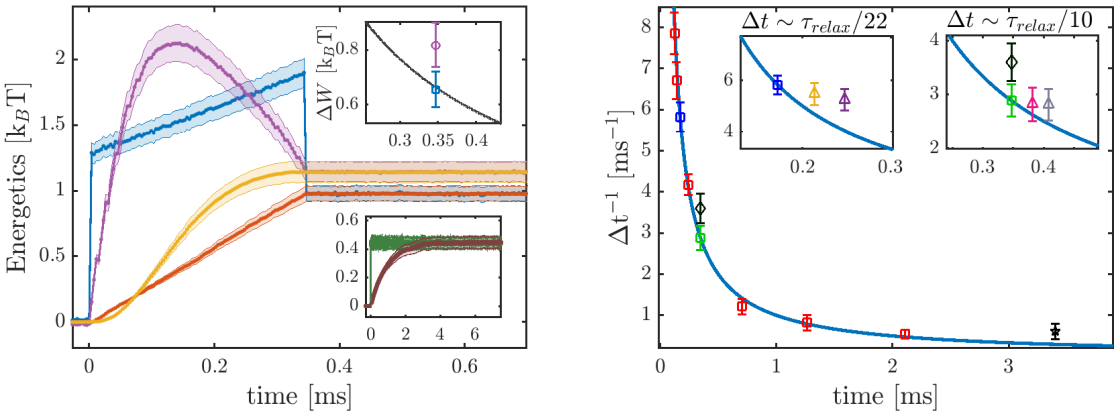

FIGURE 7.3: Panel de gauche:

Cette capacité de définir de tels protocoles optimaux minimisant à la fois la durée de transition et les coûts énergétiques associés, offre évidemment des perspectives d'applications directes pour les nano-dispositifs tels que les nano-machines thermodynamiques. Il devient envisageable de définir des cycles thermodynamiques optimisés en terme de coût énergétique et de durée de cycle. Cet axe constitue une perspective importante de notre travail.

Nos expériences consistent à vérifier soigneusement que nos conditions initiales de piégeage donnent un potentiel harmonique, et que l'évolution de la variance de position de la bille suit bien une loi gaussienne tout au long des expériences. Ces vérifications sont cruciales pour confronter précisément les calculs aux données expérimentales. Ces vérifications permettent alors de mesurer précisément la durée, le travail et la chaleur associés à une transformation entre deux états comme des fonctionnelles de la variance et du paramètre de contrôle, qui est la raideur du piège. Pour obtenir le protocole optimal qui minimise ces deux quantités, nous introduisons un multiplicateur de Lagrange entre travail effectué par la transformation et temps de cette transformation pour réguler leur compromis mutuel et définir ainsi un travail minimal compatible avec un temps de transfert minimal.

En effectuant une série de $N = 2 \times 10^4$ protocoles identiques sur la bille piégée, nous construisons alors un ensemble statistique de trajectoires qui produit une fonction de densité de probabilité de positions dont on peut extraire la variance à tous les temps et construire les quantités thermodynamiques associées, comme montrées en Figure 3. Nous avons également exploré en détail, pour tout un ensemble de protocole, le caractère universel de la limite optimale et vérifié ainsi que seuls les protocoles optimaux sont capables d'atteindre une telle limite.

III. Conclusion

L'adaptabilité d'une part de notre piège optique, et la richesse d'une description par la dynamique de Langevin de notre système nous ont permis dans cette thèse :

- d'explorer des effets de pression de radiation,
- de discuter de la signification de la mesure d'une force faible,
- de piéger un nano-objet chiral unique,
- de vérifier et d'exploiter la loi de conservation de chiralité optique pour une reconnaissance chirale d'un énantiomère nanométrique unique,
- d'utiliser les méthodes de la thermodynamique stochastique pour proposer des protocoles optimisés en temps et en énergie pour le transfert de systèmes Browniens entre 2 équilibres thermiques.

Ces travaux ont fait l'objet de 3 publications [83–85]. La versatilité de notre configuration expérimentale nous a permis cette combinaison de résultats et le fonctionnement harmonique de notre piège une synergie remarquable avec les descriptions théoriques. Cette synergie en particulier s'est révélée fondamentale pour l'étude des protocoles optimaux.

Notre travail ouvre un certain nombre de perspectives intéressantes. Tout d'abord, les résolutions obtenues sur notre «microscope de force» combinées aux capacités de description thermodynamique permettent d'envisager de résoudre, à la fois du point de vue des forces et de la thermodynamique, les effets induits par des champs de forces optiques plus complexes. Ensuite, de chercher à exploiter une approche d'optimisation thermodynamique pour proposer de nouveaux types de cycles thermodynamiques. Les problématiques autour des nano-moteurs sont à l'heure actuelle activement discutées et nous pensons que les approches de contrôle optimal peuvent avoir dans ce cadre un impact important.

A Spectral contribution of the external driving

In Chapter 2 we have seen how difficult has been to observe the mechanical effects of radiation pressure until the invention of the laser, since then, optical tweezers have become the most popular tools to exert and measure forces in the micro and nanoscales with high resolution. However most studies in the optical tweezers community have involved measurement of gradient forces and not genuine radiation pressure in the sens of Maxwell. We have evaluated the capacity of the standing wave trap (SWT) to stably trap relatively large gold nanoparticles, their metallic nature make them excellent probes of radiation pressure. Therefore in Chapter 3 we assessed the capacity of the SWT to measure external radiation pressure and we have qualified the setup as a suitable optical force microscope. In the dynamic mode of operation of our microscope, the intensity of the external laser -exerting radiation pressure on the confined particle- is modulated sinusoidally. Under such driving conditions, on top of the noisy motion of the bead in the potential there is a precises push and pull mechanism that can be directly detected through the Langevin equation. Thus, we have exploited the motion of the bead as our high resolution force transducer. The strategy of the modulation is based on the fact that in the frequency domain, modulating the force at a single frequency will have a clear signature on the power spectrum. Here we present the derivation of such signature.

A.1 A preliminary note on Energy and Power signals

In our experiment, the physical displacement of the trapped particle $z(t)$, modulates the scattered intensity detected by the photodiode. This latter outputs an analog tension which is converted into a digital signal by an analog-to-digital converter integrated in the acquisition card. The experimental signals have a finite duration given by the acquisition time T_{acq} and discrete due to the finite sampling frequency. Therefore, in practice, if we consider $z(t)$ acquired during a finite acquisition time T_{acq}, its Fourier transform $\hat{z}[f]$ is estimated by employing the so-called Finite Fourier Transform, which simply evaluates the integral of eq. A.2 in the finite interval $[0, T_{acq}]$.

For a continuous signal $V(t)$ we can define the energy carried by signal as[1]:

$$E = \int_{\infty}^{+\infty} |V(t)|^2 dt, \tag{A.1}$$

which is consistent with the physical interpretation of energy. Many signals, for example periodic signals, deliver an infinite amount of energy, *i.e.* $E \to \infty$. As a consequence, to describe the energetic properties of such signals it is more convenient to work in terms of average power, which is the rate of production of energy for a signal and is defined as:

$$P = \lim_{T\to\infty} \frac{1}{2T} \int_{-T}^{T} |V(t)|^2 dt \tag{A.2}$$

which is finite.

A.2 Measuring optical forces through their spectral contribution

The Langevin equation taking into account the external force is:

$$\gamma \dot{z}(t) + \kappa z(t) = F_{\text{th}}(t) + F_{\text{ext}}(t) \tag{A.3}$$

with $F_{\text{ext}}(t) = F_{\text{dc}} + F_{\text{ac}} \cos 2\pi f_0 t$.

To compute the respective power spectrum $S_z(f) = 2|\hat{z}(f)|^2$, we first take the Fourier transform of the above expression. For simplicity, we have dropped the influence of F_{dc} since it is a static component:

$$\int_{-\infty}^{+\infty} z(t) e^{-2i\pi f t} dt = \int_{-\infty}^{+\infty} \frac{1}{\kappa} (F_{\text{th}} + F_{\text{ext}}(t)) e^{-2i\pi f t} dt - \int_{-\infty}^{+\infty} \frac{\gamma}{\kappa} \frac{dz}{dt} e^{-2i\pi f t} dt$$

Written explicitly and replacing the integral of z by the FT expression $\hat{z}(f)$

$$\hat{z}(f) = \frac{\sqrt{2k_B T\gamma}}{\kappa} \int_{-\infty}^{+\infty} \eta(t) e^{-2i\pi f t} dt + \frac{F_{\text{ac}}}{\kappa} \int_{-\infty}^{+\infty} \cos(2\pi f_0 t) e^{-2i\pi f t} dt - \frac{\gamma}{\kappa} \int_{-\infty}^{+\infty} \frac{dz}{dt} e^{-2i\pi f t} dt$$

$$\left(1 + \frac{\gamma}{\kappa} 2i\pi f\right) \hat{z}(f) = \frac{\sqrt{2k_B T\gamma}}{\kappa} \int_{-\infty}^{+\infty} \eta(t) e^{-2i\pi f t} dt + \frac{F_{\text{ac}}}{\kappa} \int_{-\infty}^{+\infty} \cos(2\pi f_0 t) e^{-2i\pi f t} dt$$

[1] Which can also be defined for a discrete signal, simply by changing the integrals into sums

The modulus square of Eq. A.2 yields :

$$\big(1-4\pi^2 f^2(\frac{\gamma}{\kappa})^2\big)\langle\hat{z}(f)\hat{z}^*(f)\rangle = \frac{2k_BT\gamma}{\kappa^2}\int_{-\infty}^{+\infty}\int_{-\infty}^{+\infty}\eta(t')\eta(t)e^{-2i\pi ft}e^{2i\pi f't'}\,dt\,dt' - \Big(\frac{F_{\rm ac}}{\kappa}\Big)^2\int_{-\infty}^{+\infty}\int_{-\infty}^{+\infty}\cos(2\pi f_0t')\cos(2\pi f_0t)e^{-2i\pi f't'}e^{2\pi ift}dt\,dt'$$

Performing a change of variable $t' = t - \tau$ the external force term of the previous can be written as:

$$\Big(\frac{F_{\rm ac}}{\kappa}\Big)^2\int_{-\infty}^{+\infty}\int_{-\infty}^{+\infty}\cos(2\pi f_0(t-\tau))\cos(2\pi f_0t)e^{-2i\pi(\tau)}dtdt \tag{A.4}$$

We encounter here, the diverging situation of a signal with infinite energy, (see section A.1). Re-defining the correlation function as[2]:

$$\Gamma(\tau) = \lim_{T\to\infty}\frac{1}{T}\int_{-T}^{+T}\sin(2\pi f_0(t-\tau))\sin(2\pi f_0t)dt \tag{A.5}$$

Where $\Gamma(0)$ is the average power of $\sin(2\pi f_0t)$, and supposing $|\Gamma(\tau)| \leq \Gamma(0)$.

$$\Gamma(0) = \lim_{T\to\infty}\frac{1}{T}\int_{-T}^{+T}\sin^2(2\pi f_0t)dt \tag{A.6}$$

Using: $\sin^2(x) = (1-\cos(x))/2$:

$$\Gamma(0) = \lim_{T\to\infty}\frac{2}{T}\int_{-T/2}^{+T/2}\frac{1-\cos(2\pi f_0t)}{2}dt = \frac{1}{2} + \lim_{T\to\infty}\frac{\sin(2\pi f_0T)}{T} = \frac{1}{2}$$

and the Fourier transform of $\cos(x)$:

$$\int_{-\infty}^{+\infty}\cos(2\pi f_0\tau)e^{-2i\pi f\tau}dt = \int_{-\infty}^{+\infty}\frac{e^{2i\pi f_0\tau}+e^{-2i\pi f_0\tau}}{2}e^{-2i\pi f\tau}dt \tag{A.7}$$

Finally, we obtain:

$$(1-4\pi^2f^2(\frac{\gamma}{\kappa})^2)\langle\hat{z}(f)\hat{z}^*(f)\rangle = \frac{2k_BT\gamma}{\kappa^2} + \frac{F_{\rm ac}^2}{2\kappa^2}\Big(\delta(f-f_0)+\delta(f+f_0)\Big) \tag{A.8}$$

The force is detected by recording the instantaneous position of the nanosphere with

[2]Where we have used the trigonometric identity $\cos(a-b) = \cos(a)\cos(b) - \sin(a)\sin(b)$ to pass from Eq. A.4 to Eq. A.5

a *p-i-n* photodiode, this signal is passed through a low-noise pre-amplifier in which a high pass filter is set at 0.03 Hz to remove the DC contribution. The spectral signature of the injected radiation pressure is a Dirac delta peak superposed to the one-sided power spectrum of the thermal fluctuations of the bead:

$$S_z^d(f) = \frac{1}{(f^2 + f_T^2)}\Big[\frac{D}{\pi^2} + \frac{F_{\rm ac}}{8\pi^2\gamma^2}\delta(f - f_0)\Big] \tag{A.9}$$

B Stochastic Calculus

B.1 Wiener processes

The Langevin equation, which is central to all our experiments, is a differential equation with a salient feature: the random forces $\xi(t)$, which represent the dynamic variables that fluctuate on short time scales compared to any observable. These forces are represented by white Gaussian noise and are characterized by [21]:

$$\langle \xi(t) \rangle = 0 \qquad\qquad \langle \xi(t')\xi(t) \rangle = \delta(t' - t) \tag{B.1}$$

We can define $d\mathcal{W}_t = \xi(t)dt$, a Wiener process, which is a basic mathematical object designed to deal with this kind of processes.

A real stochastic process, $\mathcal{W}_t$ is called Wiener process if:

(i) For $t = 0$, $\mathcal{W}_t = 0$ the process starts at zero.

(ii) For all $t' < t$, $\mathcal{W}_t - \mathcal{W}'_t$ has a normal distribution with zero mean and variance $t - t'$.

(iii) For all $0 < t_1 < t_2 < ... < t_n$, the random variables $\mathcal{W}_{t_1} < \mathcal{W}_{t_2} - \mathcal{W}_{t_1} < ... < \mathcal{W}_{t_n} - \mathcal{W}_{t_{n-1}}$ are independent.

(iv) Is continuous but not differentiable.

At short times it is not well defined. And its variance grows as t.

B.2 Stochastic differential equations

The Langevin equation is a particular case of stochastic differential equations

$$\frac{dx}{dt} = f(x,t) + g(x,t)\xi(t), \tag{B.2}$$

where $g(x,t)$ and $f(x,t)$ are deterministic functions (in our case $g = \sqrt{2\gamma k_B T}$) and $\xi(t)$ is the delta-correlated noise satisfying B.1.

We can write the Langevin equation in the language of Wiener processes [19]:

$$\begin{aligned} dx &= f(x,t) + g(x,t)d\mathcal{W}_t \\ dt &= \langle d\mathcal{W}_t d\mathcal{W}_{t'=t+dt} \rangle \end{aligned}$$

with $d\mathcal{W}_t = \xi(t)dt$.

In a general case, where $g(x,t)$ depends on the stochastic variable $x(t)$, Eq. B.2 is ill-defined because the integral:

$$\int g(x,t')d\mathcal{W}_t \tag{B.3}$$

is not well defined. Depending on the interpretation of the integrals:

$$x(t+\Delta t) - x(t) = \int_t^{t+\Delta t} f(x,t')dt' + \int_t^{t+\Delta t} g(x,t')d\mathcal{W}_t \tag{B.4}$$

However, we can not define integral with a measure $)d\mathcal{W}_t$, since it is not differentiable. Thus one can define the discretization of such an integral as:

$$\int_0^T g(t)d\mathcal{W}_t = \lim_{N\to\infty} \sum_{i=0}^{N-1} g(\tau_i)(\mathcal{W}_{t_i+1} - \mathcal{W}_{t_i}) \tag{B.5}$$

with $\tau_i = (1-\alpha)t_i + \alpha t_{i+1}$, with $0 \leq \alpha \leq 1$. Since $d\mathcal{W}_t$ is not continuous, the result of such integral depends on the choice of α. And this can result in in a generation of non-equivalent stochastic processes.

Let us suppose the case : $g(x,t) = \mathcal{W}_t$, then :

$$\left\langle \int_0^T \mathcal{W}_t d\mathcal{W}_t \right\rangle = \left\langle \int_0^T \int_0^T \xi(t')\xi(t)dt'dt \right\rangle = \alpha \tag{B.6}$$

The most common conventions are:

- Itô calculus: $\alpha = 0$ with $g(x,t) = \mathcal{W}_t$ results in $\mathcal{W}_t d\mathcal{W}_t = 0$.
- Stratonovich calculus: $\alpha = 1/2$

The integral in Itô form can be written as Eq. B.7, and $g(\tau_i)$ uses Riemann sums, whereas with the Stratonovich convention, the sums use the average:

$$\int_0^T g(t) \circ d\mathcal{W}_t = \lim_{N\to\infty} \sum_{i=0}^{N-1} \left(\frac{g(\tau_i) + g(\tau_{i+1})}{2} \right) (\mathcal{W}_{t_i+1} - \mathcal{W}_{t_i}) \tag{B.7}$$

It should be noted that the Stratonovich convention uses the ordinary rules of calculus. There are physical justifications for choosing one differential calculation or another. In particular, in the case of a correlation function $\langle \xi(t')(t) \rangle$, which approximates the Dirac Delta, a differential calculation is obtained that coincides with Stratonovich form. On the other hand, Stratonovich calculus is physically reasonable in cases where Langevin's

forces are external [153]. It should be noted that the Langevin equation, in itself does not make sense, without first specifying a stochastic differential calculation, that is, at which moment the function $g(X, t')$, thus, once the Langevin equation is written down, it has already a chosen interpretation, which in our case is a Stratonovich interpretation.

C Variational calculus

C.1 Calculus of variations

In this appendix we present, in a simple and brief way, a review of the principles of variational calculus, on which our optimization strategy for reducing the relaxation time of the Brownian particle in a potential with the minimum energy cost is based. This section is based on the content of references [163, 166–169].

In some processes, even in simple mechanical systems, it is not trivial to find the equations of motion. The main difficulty of modeling is that the interaction between the elements must be described by means of forces that are not known a priori and that represent restrictions between the variables of the system. They are unknowns of the problem that must be eliminated to get the equations that govern the movement. These constraints are often quite complicated and if there are many to consider, the modeling process is terribly cumbersome. In such cases, a possible alternative is to use energy considerations. This alternative is based on Hamilton's principle of least action that makes use of the calculus of variations.

Functionals

A functional is a mapping from the vector space of functions to the set of real or complex numbers. For example, in $\mathbb{R}$, we can define the functional:

$$J[f(x)] = \int_a^b f(x)dx \tag{C.1}$$

that maps to each function $f(x)$ its integral in the interval $[a, b]$. Formally, if $\mathcal{C}((c, d), \mathbb{R})$ is the vector space of continuous functions in the interval $[c, d]$ with values in $\mathbb{R}$ and $[a, b] \subset [c, d]$ we can write:

$$\begin{aligned} J\colon \mathcal{C}((c,d),\mathbb{R}) &\to \mathbb{R} \\ f &\mapsto \int_a^b f(x)dx \end{aligned}$$

In analytical mechanics, the action of a mechanical system is defined as a functional of the Lagrangian L, which in turn represents the difference of potential and kinetic energies of the system.

Variations

Let the Lagrangian be defined as the mapping:

$$\begin{aligned} L\colon \mathbb{R}\times\mathbb{R}\times\mathbb{R} &\mapsto \mathbb{R} \\ (x,\dot{x},t) &\mapsto L(x,\dot{x},t), \end{aligned}$$

L is a function of three independent variables. Given two points $x_0, x_1 \in \mathbb{R}$, among all the trajectories that are differentiable and satisfy the boundary conditions:

$$x(t_0) = x_0,\ \ x(t_1) = x_1 \tag{C.2}$$

the essential problem of variational calculus can be stated as finding the extremal (could be maximum or minimum) of the functional:

$$S(x(t)) = \int_{t_0}^{t_2} L(x(t),\dot{x}(t),t)dt \tag{C.3}$$

In general, let two differentiable trajectories $x, h \in \mathcal{C}([a,b],\mathbb{R})$. The functional C.3 is differentiable in each function x and the value of its derivative in x is :

$$\delta S(h) = \int_{t_1}^{t_2} \Big[\frac{\partial L}{\partial x} - \frac{d}{dt}\Big(\frac{\partial L}{\partial \dot{x}}\Big)\Big] h(t)\,dt + \frac{\partial L}{\partial \dot{x}} h(t)|_{t_2}^{t_1}, \tag{C.4}$$

this is called a variation. Then, an extremal of S is a curve such that $\delta S(h) = 0$ for all h.

Lemma: If $x(t)$ is an extremal of the functional $S[x(t)]$ on the space of curves satisfying the boundary conditions C.2, then $x(t)$ satisfies the Euler-Lagrange equations:

$$\frac{\partial L}{\partial x} = \frac{d}{dt}\frac{\partial L}{\partial \dot{x}} \tag{C.5}$$

Proof: Let $h(t)$ be any curve satisfying the boundary conditions $h(t_1) = h(t_2) = 0$. And let $x(t)$ an extremal of the functional S. Then let us define a curve :

$$\eta(t,\alpha) = x(t) + \alpha h(t) \tag{C.6}$$

and

$$S[\alpha, t_1, t_2] = \int_{t_1}^{t_2} L(\eta(t,\alpha),\dot{\eta}(t,\alpha),t)dt \tag{C.7}$$

then, if $x(t)$ is an extremal of S then:

$$\frac{dS}{d\alpha}\Big|_{\alpha=0} = 0 \tag{C.8}$$

for any choice of $h(t)$. By using the chain rule and the fact that $\eta(\alpha = 0, t) = x(t)$, we can write Eq. C.8:

$$\begin{aligned} 0 &= \int_{t_1}^{t_2} dt \frac{dL}{d\alpha}\Big|_{\alpha=0} \\ &= \int_{t_1}^{t_2} dt \Big[\frac{\partial L}{\partial \eta}\frac{\partial \eta}{\partial \alpha} + \frac{\partial L}{\partial \dot{\eta}}\frac{\partial \dot{\eta}}{\partial \alpha}\Big]_{\alpha=0} \\ &= \int_{t_1}^{t_2} dt \Big[\frac{\partial L}{\partial x}h(t) + \frac{\partial L}{\partial \dot{x}}\dot{h}(t)\Big], \end{aligned}$$

after integration by parts of the last equality:

$$0 = \int_{t_1}^{t_2} dt \Big[\frac{\partial L}{\partial x} + \frac{d}{dt}\frac{\partial L}{\partial \dot{x}}\Big]h(t) \tag{C.9}$$

Since the function $h(t)$ is arbitrary, the term inside the brackets has to be zero. The fact that $h(t)$ satisfies the boundary conditions $h(t_1) = 0$ and $h(t_2) = 0$ is essential to avoid any contribution to the boundaries and thus in this way the lemma is demonstrated in a simple way, there are of course more formal ways, see refs.

C.2 The method of Lagrange multipliers

Let $f(x_1, x_2, ..., x_n)$ a function of n variables. Supposing that such variables are related by $m < n$ constraints: $g_1(x_1, .., x_n) = 0$, $g_m(x_1, .., x_n) = 0$,...$g_2(x_1, .., x_n) = 0$. Consider a new function $F(x_1, x_2, ..., x_n)$:

$$F(x_1, x_2, ..., x_n) = f(x_1, x_2, ..., x_n) + \sum_{i=1}^{m} \lambda_i g_i(x_1, .., x_n) \tag{C.10}$$

where λ_i are unknown. We can form the set of equations:

$$\begin{cases} \frac{\partial F}{\partial x_1} = 0 \\ \frac{\partial F}{\partial x_2} = 0 \\ ... \\ \frac{\partial F}{\partial x_n} = 0 \end{cases} \tag{C.11}$$

with the m constraints $g_i(x_1, .., x_n) = 0$, determine the m parameters $\lambda_1, \lambda_2, ...\lambda_m$ and the n variables $x_1, ...x_n$ of the extrema of the function $f(x_1, x_2, ..., x_n)$. The parameters λ_i are known as the Lagrange multipliers.

C.3 Smooth protocols

As seen in the previous section, using the Lagrange multiplier method, it is possible to add as many Lagrange multipliers as constraints of the problem. In Chapter **??**, the optimal protocols were found from the solution that minimizes the functional:

$$J[\hat{\kappa}(s)] = \int_{s_i}^{s_f} \frac{\gamma ds}{D\gamma s\hat{\kappa}(s)} - \lambda \int_{s_i}^{s_f} \hat{\kappa}(s) ds \tag{C.12}$$

λ is the Lagrange multiplier and regulates the trade-off between the expended work and transfer duration.

In order to comply with thermally equilibrated initial and final configurations we had to augment sudden jumps to Eq. 5.37. From an experimental point of view, such discontinuities do not constitute a weakness of the procedure, as they correspond to finite and measurable quantities of work exchanged between the bath and the system [170, 171]. Nevertheless, it is possible to generate smooth protocols that are arbitrarily close to the optimal by adding a constraint in the derivatives of $\hat{\kappa}(s)$, and thus, with a second Lagrange multiplier ε, we can write the functional 5.30 with an additional term:

$$J[\hat{\kappa}(s)] = \int_{s_i}^{s_f} \frac{\gamma ds}{D\gamma s\hat{\kappa}(s)} - \lambda \int_{s_i}^{s_f} \hat{\kappa}(s) ds - \varepsilon \int_{s_i}^{s_f} |\hat{\kappa}'(s)|^2 ds, \tag{C.13}$$

ε acts as a regularization parameter by removing the discontinuities in $\hat{\kappa}(s)$. The Euler-Lagrange equation that minimize C.13 yields:

$$2\varepsilon \frac{d^2\hat{\kappa}}{ds^2} = \frac{\gamma s}{(D\gamma - s\hat{\kappa})^2} - \lambda, \tag{C.14}$$

which is a second-order differential equation, and thus needs two independent boundary conditions, enabling us to set $s_i\kappa_i = s_f\kappa_f = D\gamma$, as requested for our protocols. The solution can be obtained numerically and generates a protocol $\hat{\kappa}(s)$ that is continuous in the variable s and that converges towards the optimal protocol as $\varepsilon \to 0$. Through the Lagrange multiplier ε, one can limit the value of such derivative, so that the protocol becomes smoother and smoother as ε increases.

In figure C.1 below, we show the comparison of the cumulative energetics between an optimal protocol defined for $\Delta t = 1.72\times10^{-4}$ s $\sim \tau_{\text{relax}}/22$ and two smooth protocols with $\varepsilon = 5\times10^{-6}$ and $\varepsilon = 10^{-6}$, expressed in units of $s_i^2/(D\kappa_i^2)$, and identical value of $\lambda = (2.97 \pm 0.12)\times10^{16}$ s/J. In the inset of Fig. C.1 are displayed the superimposed evolutions $\kappa(t)$ vs. $s(t)$ for the three protocols, showing the continuous nature of the smooth protocols and illustrating the progressive convergence to the optimal protocol in the $\varepsilon \to 0$ limit. For each protocol, the curves are normalized to the corresponding κ_i for $\kappa(t)$ and s_f for $s(t)$. Although the smooth protocols involve slightly less expended work ($1.36 \pm 0.06\ k_BT$ for $\varepsilon = 5\times10^{-6}$ and $1.65 \pm 0.06\ k_BT$ for $\varepsilon = 10^{-6}$) than the optimal one ($1.69\pm0.06\ k_BT$), they correspond to longer transfer durations (2.48×10^{-4} s for $\varepsilon = 5\times10^{-6}$ and 2.14×10^{-4} s for $\varepsilon = 10^{-6}$). The non-optimal character of the

smooth protocols is clearly seen in the insets of universality curve, Fig. 5.9, where all $\{\Delta t, \Delta W\}$ coordinates lie above the universal bound, and only converge towards it in the $\varepsilon \to 0$ limit.

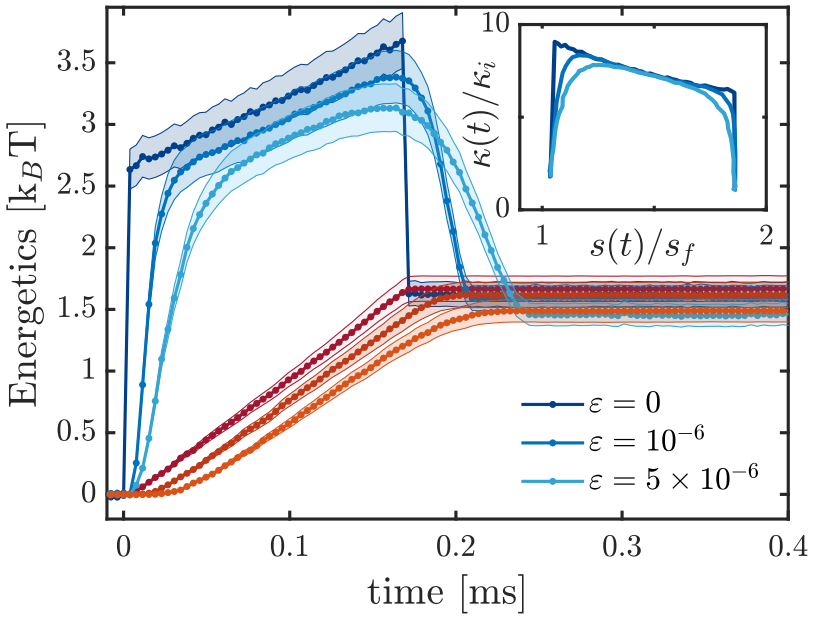

FIGURE C.1: Evolution of the mean cumulative energetics -expended work $W(t)$ (blue curves) and dissipated heat $Q(t)$ (red curves)- between an optimal protocol defined for $\Delta t = \tau_{\text{relax}}/22$ and two smooth protocols with $\varepsilon = 5 \times 10^{-6}$ and $\varepsilon = 10^{-6}$, expressed in units of $s_i^2/(D\kappa_i^2)$. Inset: superimposed evolutions $\kappa(t)$ as a function of $s(t)$ for the three protocols. For each protocol, the curves are normalized to the corresponding κ_i for $\kappa(t)$ and s_f for $s(t)$.

Bibliography

[1] Mark Tuckerman. *Statistical mechanics: theory and molecular simulation*. Oxford university press, 2010.

[2] Daniel M Zuckerman. *Statistical physics of biomolecules: an introduction*. CRC Press, 2010.

[3] Rep Kubo. "The fluctuation-dissipation theorem". In: *Reports on progress in physics* 29.1 (1966), p. 255.

[4] Hidetoshi Nishimori and Gerardo Ortiz. *Elements of phase transitions and critical phenomena*. OUP Oxford, 2010.

[5] Umberto Marini Bettolo Marconi et al. "Fluctuation–dissipation: response theory in statistical physics". In: *Physics reports* 461.4-6 (2008), pp. 111–195.

[6] Ryogo Kubo. "Brownian motion and nonequilibrium statistical mechanics". In: *Science* 233.4761 (1986), pp. 330–334.

[7] Carlos Bustamante, Jan Liphardt, and Felix Ritort. "The nonequilibrium thermodynamics of small systems". In: *arXiv preprint cond-mat/0511629* (2005).

[8] Félix Ritort. "Work fluctuations, transient violations of the second law and free-energy recovery methods: Perspectives in theory and experiments". In: *Poincaré Seminar*. Vol. 2. 2003, pp. 195–229.

[9] Denis J Evans, Debra J Searles, and Stephen R Williams. *Fundamentals of classical statistical thermodynamics*. Wiley Online Library, 2016.

[10] Brad Lee Holian, William G Hoover, and Harald A Posch. "Resolution of Loschmidt's paradox: The origin of irreversible behavior in reversible atomistic dynamics". In: *Physical Review Letters* 59.1 (1987), p. 10.

[11] GM Wang et al. "Experimental demonstration of violations of the second law of thermodynamics for small systems and short time scales". In: *Physical Review Letters* 89.5 (2002), p. 050601.

[12] Denis J Evans, Ezechiel Godert David Cohen, and Gary P Morriss. "Probability of second law violations in shearing steady states". In: *Physical review letters* 71.15 (1993), p. 2401.

[13] Jorge Kurchan. "Fluctuation theorem for stochastic dynamics". In: *Journal of Physics A: Mathematical and General* 31.16 (1998), p. 3719.

[14] Udo Seifert. "Stochastic thermodynamics, fluctuation theorems and molecular machines". In: *Rep. Prog. Phys.* 75.12 (2012), p. 126001. DOI: https://doi.org/10.1088/0034-4885/75/12/126001.

[15] Gavin E Crooks. "Entropy production fluctuation theorem and the nonequilibrium work relation for free energy differences". In: *Physical Review E* 60.3 (1999), p. 2721.

[16] "On the motion of particles suspended in still liquids required by the molecular kinetic theory of heat". In: ().

[17] Albert Einstein. *Investigations on the Theory of the Brownian Movement*. Courier Corporation, 1956.

[18] Erwin Frey and Klaus Kroy. "Brownian motion: a paradigm of soft matter and biological physics". In: *Annalen der Physik* 14.1-3 (2005), pp. 20–50.

[19] Crispin W Gardiner et al. *Handbook of stochastic methods*. Vol. 3. springer Berlin, 1985.

[20] JL Garcia-Palacios. "Introduction to the theory of stochastic processes and Brownian motion problems". In: *arXiv preprint cond-mat/0701242* (2007).

[21] Ken Sekimoto. *Stochastic energetics*. Springer-Verlag, Berlin Heidelberg, 2010. URL: https://link.springer.com/.

[22] William Coffey and Yu P Kalmykov. *The Langevin equation: with applications to stochastic problems in physics, chemistry and electrical engineering*. Vol. 27. World Scientific, 2012.

[23] Wolfgang Paul and Jörg Baschnagel. *Stochastic processes*. Vol. 1. Springer, 2013.

[24] Seth Flaxman et al. "Estimating the number of infections and the impact of nonpharmaceutical interventions on COVID-19 in European countries: technical description update". In: *arXiv preprint arXiv:2004.11342* (2020).

[25] Arthur Ashkin. "Optical trapping and manipulation of neutral particles using lasers". In: *Proceedings of the National Academy of Sciences* 94.10 (1997), pp. 4853–4860.

[26] S Ciliberto. "Experiments in stochastic thermodynamics: Short history and perspectives". In: *Physical Review X* 7.2 (2017), p. 021051.

[27] Udo Seifert. "Stochastic thermodynamics: principles and perspectives". In: *The European Physical Journal B* 64.3-4 (2008), pp. 423–431.

[28] Anthony Bartolotta and Sebastian Deffner. "Jarzynski equality for driven quantum field theories". In: *Physical Review X* 8.1 (2018), p. 011033.

[29] Leonor Saiz, J Miguel Rubi, and Jose MG Vilar. "Inferring the in vivo looping properties of DNA". In: *Proceedings of the National Academy of Sciences* 102.49 (2005), pp. 17642–17645.

[30] Ruyun Zhou et al. "A molecular motor, KIF13A, controls anxiety by transporting the serotonin type 1A receptor". In: *Cell reports* 3.2 (2013), pp. 509–519.

[31] Terence Strick, J-F Allemand, and Vincent Croquette. "The Manipulation of Single Biomolecules." In: *Physics Today* 54.10 (2001), pp. 46–51.

[32] Michelle D Wang et al. "Stretching DNA with optical tweezers." In: *Biophysical journal* 72.3 (1997), p. 1335.

[33] Carlos Bustamante et al. "Single-molecule studies of DNA mechanics". In: *Current opinion in structural biology* 10.3 (2000), pp. 279–285.

[34] Steven M Block, Lawrence SB Goldstein, and Bruce J Schnapp. "Bead movement by single kinesin molecules studied with optical tweezers". In: *Nature* 348.6299 (1990), pp. 348–352.

[35] Georgy Lebon, David Jou, and José Casas-Vázquez. *Understanding non-equilibrium thermodynamics*. Vol. 295. Springer, 2008.

[36] Ignacio A Martínez et al. "Colloidal heat engines: a review". In: *Soft matter* 13.1 (2017), pp. 22–36.

[37] Christian Van den Broeck, Ryoichi Kawai, and Pascal Meurs. "Microscopic analysis of a thermal Brownian motor". In: *Physical review letters* 93.9 (2004), p. 090601.

[38] Ken Sekimoto. "Kinetic characterization of heat bath and the energetics of thermal ratchet models". In: *Journal of the physical society of Japan* 66.5 (1997), pp. 1234–1237.

[39] Christian Van den Broeck, Pascal Meurs, and Ryoichi Kawai. "From Maxwell demon to Brownian motor". In: *New Journal of Physics* 7.1 (2005), p. 10.

[40] Jaehoon Bang et al. "Experimental realization of Feynman's ratchet". In: *New Journal of Physics* 20.10 (2018), p. 103032.

[41] Ken Sekimoto. "Langevin equation and thermodynamics". In: *Progress of Theoretical Physics Supplement* 130 (1998), pp. 17–27.

[42] Udo Seifert. "Entropy production along a stochastic trajectory and an integral fluctuation theorem". In: *Physical review letters* 95.4 (2005), p. 040602.

[43] Christopher Jarzynski. "Comparison of far-from-equilibrium work relations". In: *Comptes Rendus Physique* 8.5-6 (2007), pp. 495–506. DOI: 10.1016/j.crhy.2007.04.010.

[44] Tim Schmiedl and Udo Seifert. "Optimal Finite-Time Processes In Stochastic Thermodynamics". In: *Phys. Rev. Lett.* 98 (10 2007), p. 108301. DOI: 10.1103/PhysRevLett.98.108301. URL: https://link.aps.org/doi/10.1103/PhysRevLett.98.108301.

[45] Jordan M Horowitz and Juan MR Parrondo. "Thermodynamic reversibility in feedback processes". In: *EPL (Europhysics Letters)* 95.1 (2011), p. 10005.

[46] Takahiro Sagawa and Masahito Ueda. "Generalized Jarzynski equality under nonequilibrium feedback control". In: *Physical review letters* 104.9 (2010), p. 090602.

[47] Christopher Jarzynski. "Equalities and inequalities: Irreversibility and the second law of thermodynamics at the nanoscale". In: *Annu. Rev. Condens. Matter Phys.* 2.1 (2011), pp. 329–351.

[48] Pinyu Wu et al. "Direct measurement of the nonconservative force field generated by optical tweezers". In: *Physical review letters* 103.10 (2009), p. 108101.

[49] Tongcang Li et al. "Measurement of the instantaneous velocity of a Brownian particle". In: *Science* 328.5986 (2010), pp. 1673–1675.

[50] Simon Kheifets et al. "Observation of Brownian motion in liquids at short times: instantaneous velocity and memory loss". In: *science* 343.6178 (2014), pp. 1493–1496.

[51] Jasper Chan et al. "Laser cooling of a nanomechanical oscillator into its quantum ground state". In: *Nature* 478.7367 (2011), pp. 89–92.

[52] Jan Gieseler et al. "Subkelvin parametric feedback cooling of a laser-trapped nanoparticle". In: *Physical review letters* 109.10 (2012), p. 103603.

[53] Markus Aspelmeyer, Pierre Meystre, and Keith Schwab. "optomechanics". In: *Phys. Today* 65.7 (2012), p. 29.

[54] Arnaud Gloppe et al. "Bidimensional nano-optomechanics and topological backaction in a non-conservative radiation force field". In: *Nature nanotechnology* 9.11 (2014), p. 920.

[55] James Gleick. *The information: A history, a theory, a flood*. Vintage, 2012.

[56] Rolf Landauer. "Irreversibility and heat generation in the computing process". In: *IBM journal of research and development* 5.3 (1961), pp. 183–191.

[57] Charles H Bennett. "Notes on Landauer's principle, reversible computation, and Maxwell's Demon". In: *Studies In History and Philosophy of Science Part B: Studies In History and Philosophy of Modern Physics* 34.3 (2003), pp. 501–510.

[58] Juan MR Parrondo, Jordan M Horowitz, and Takahiro Sagawa. "Thermodynamics of information". In: *Nature physics* 11.2 (2015), pp. 131–139.

[59] Eric Lutz and Sergio Ciliberto. "From Maxwells demon to Landauers eraser". In: *Phys. Today* 68.9 (2015), p. 30.

[60] Harvey S Leff and Andrew F Rex. *Maxwell's demon: entropy, information, computing*. Princeton University Press, 2014.

[61] Koji Maruyama, Franco Nori, and Vlatko Vedral. "Colloquium: The physics of Maxwell's demon and information". In: *Reviews of Modern Physics* 81.1 (2009), p. 1.

[62] Antoine Bérut et al. "Experimental verification of Landauer's principle linking information and thermodynamics". In: *Nature* 483.7388 (2012), pp. 187–189.

[63] Charles H Bennett. "The thermodynamics of computation—a review". In: *International Journal of Theoretical Physics* 21.12 (1982), pp. 905–940.

[64] Édgar Roldán. *Irreversibility and dissipation in microscopic systems*. Springer, 2014.

[65] Shoichi Toyabe et al. "Experimental demonstration of information-to-energy conversion and validation of the generalized Jarzynski equality". In: *Nature physics* 6.12 (2010), pp. 988–992.

[66] Tamir Admon, Saar Rahav, and Yael Roichman. "Experimental realization of an information machine with tunable temporal correlations". In: *Physical review letters* 121.18 (2018), p. 180601.

[67] Ken Dill and Sarina Bromberg. *Molecular driving forces: statistical thermodynamics in biology, chemistry, physics, and nanoscience*. Garland Science, 2012.

[68] ND Hari Dass. *The principles of thermodynamics*. CRC Press, 2013.

[69] V. Blickle and C. Bechinger. "Realization of a micrometer-sized stochastic heat engine". In: *Nature Phys.* 8 (2011), p. 143. DOI: 10.1038/nphys2163.

[70] Valentin Blickle et al. "Thermodynamics of a colloidal particle in a time-dependent nonharmonic potential". In: *Physical review letters* 96.7 (2006), p. 070603.

[71] Ignacio A Martínez et al. "Adiabatic processes realized with a trapped Brownian particle". In: *Physical review letters* 114.12 (2015), p. 120601.

[72] L Dinis et al. "Thermodynamics at the microscale: from effective heating to the Brownian Carnot engine". In: *Journal of Statistical Mechanics: Theory and Experiment* 2016.5 (2016), p. 054003.

[73] Ignacio A Martínez et al. "Brownian carnot engine". In: *Nature physics* 12.1 (2016), pp. 67–70.

[74] Johannes Roßnagel et al. "Nanoscale heat engine beyond the Carnot limit". In: *Physical review letters* 112.3 (2014), p. 030602.

[75] Ruben Zakine et al. "Stochastic Stirling engine operating in contact with active baths". In: *Entropy* 19.5 (2017), p. 193.

[76] Yu-Shiun Chen, Meng-Yen Hong, and G Steven Huang. "A protein transistor made of an antibody molecule and two gold nanoparticles". In: *Nature nanotechnology* 7.3 (2012), p. 197.

[77] S Velasco et al. "Feynman's ratchet optimization: maximum power and maximum efficiency regimes". In: *Journal of Physics D: Applied Physics* 34.6 (2001), p. 1000.

[78] Luis Dinis. "Optimal sequence for Parrondo games". In: *Physical Review E* 77.2 (2008), p. 021124.

[79] Florian Berger, Tim Schmiedl, and Udo Seifert. "Optimal potentials for temperature ratchets". In: *Physical Review E* 79.3 (2009), p. 031118.

[80] Martin B Tarlie and R Dean Astumian. "Optimal modulation of a Brownian ratchet and enhanced sensitivity to a weak external force". In: *Proceedings of the National Academy of Sciences* 95.5 (1998), pp. 2039–2043.

[81] Patrick Pietzonka and Udo Seifert. "Universal trade-off between power, efficiency, and constancy in steady-state heat engines". In: *Physical review letters* 120.19 (2018), p. 190602.

[82] Alexandre P Solon and Jordan M Horowitz. "Phase transition in protocols minimizing work fluctuations". In: *Physical review letters* 120.18 (2018), p. 180605.

[83] Gabriel Schnoering et al. "Three-Dimensional Enantiomeric Recognition of Optically Trapped Single Chiral Nanoparticles". In: *Phys. Rev. Lett.* 121 (2 2018), p. 023902. DOI: 10.1103/PhysRevLett.121.023902. URL: https://link.aps.org/doi/10.1103/PhysRevLett.121.023902.

[84] Gabriel Schnoering et al. "Thermally Limited Force Microscopy on Optically Trapped Single Metallic Nanoparticles". In: *Phys. Rev. Applied* 11 (3 2019), p. 034023. DOI: 10.1103/PhysRevApplied.11.034023. URL: https://link.aps.org/doi/10.1103/PhysRevApplied.11.034023.

[85] Yoseline Rosales-Cabara et al. "Optimal protocols and universal time-energy bound in Brownian thermodynamics". In: *arXiv preprint arXiv:1906.04171* (2019).

[86] James Clerk Maxwell. *A treatise on electricity and magnetism*. Vol. 1. Clarendon press, 1881.

[87] Peter Lebedev. "Investigations with the pressure of the light". In: *Annalen der Physik* 311.11 (1901), pp. 433–458.

[88] Ernest Fox Nichols and Gordon Ferrie Hull. "A preliminary communication on the pressure of heat and light radiation". In: *Physical Review (Series I)* 13.5 (1901), p. 307.

[89] Arthur Ashkin. "Acceleration and trapping of particles by radiation pressure". In: *Physical review letters* 24.4 (1970), p. 156.

[90] Arthur Ashkin et al. "Observation of a single-beam gradient force optical trap for dielectric particles". In: *Optics letters* 11.5 (1986), pp. 288–290.

[91] Eivind Almaas and Iver Brevik. "Radiation forces on a micrometer-sized sphere in an evanescent field". In: *JOSA B* 12.12 (1995), pp. 2429–2438.

[92] A Mazolli, PA Maia Neto, and HM Nussenzveig. "Theory of trapping forces in optical tweezers". In: *Proceedings of the Royal Society of London. Series A: Mathematical, Physical and Engineering Sciences* 459.2040 (2003), pp. 3021–3041.

[93] Djenan Ganic, Xiaosong Gan, and Min Gu. "Exact radiation trapping force calculation based on vectorial diffraction theory". In: *Optics express* 12.12 (2004), pp. 2670–2675.

[94] Timo A Nieminen et al. "Numerical modelling of optical trapping". In: *Computer Physics Communications* 142.1-3 (2001), pp. 468–471.

[95] TA Nieminen, H Rubinsztein-Dunlop, and NR Heckenberg. "Calculation and optical measurement of laser trapping forces on non-spherical particles". In: *Journal of Quantitative Spectroscopy and Radiative Transfer* 70.4-6 (2001), pp. 627–637.

[96] Yasuhiro Harada and Toshimitsu Asakura. "Radiation forces on a dielectric sphere in the Rayleigh scattering regime". In: *Optics communications* 124.5-6 (1996), pp. 529–541.

[97] Alexander Rohrbach. "Stiffness of optical traps: quantitative agreement between experiment and electromagnetic theory". In: *Physical review letters* 95.16 (2005), p. 168102.

[98] Patrick C Chaumet and Manuel Nieto-Vesperinas. "Time-averaged total force on a dipolar sphere in an electromagnetic field". In: *Optics letters* 25.15 (2000), pp. 1065–1067.

[99] Antoine Canaguier-Durand et al. "Force and torque on an electric dipole by spinning light fields". In: *Physical Review A* 88.3 (2013), p. 033831.

[100] Yohai Roichman et al. "Optical forces arising from phase gradients". In: *Physical review letters* 100.1 (2008), p. 013602.

[101] Giuseppe Pesce et al. "Quantitative assessment of non-conservative radiation forces in an optical trap". In: *EPL (Europhysics Letters)* 86.3 (2009), p. 38002.

[102] Halina Rubinsztein-Dunlop et al. "Optical forces, trapping and manipulation". In: *Photonics: scientific foundations, technology and applications* 3 (2015), pp. 287–339.

[103] Antoine Canaguier-Durand et al. "Mechanical separation of chiral dipoles by chiral light". In: *New Journal of Physics* 15.12 (2013), p. 123037.

[104] P Zemánek et al. "Optical trapping of Rayleigh particles using a Gaussian standing wave". In: *Optics communications* 151.4-6 (1998), pp. 273–285.

[105] A Cuche et al. "Plasmonic coherent drive of an optical trap". In: *Physical review letters* 108.2 (2012), p. 026801.

[106] Gabriel Schnoering and Cyriaque Genet. "Inducing dynamical bistability by reversible compression of an optical piston". In: *Physical Review E* 91.4 (2015), p. 042135.

[107] Gabriel Schnoering. "On the Brownian dynamics of a particle in a bistable optical trap". PhD thesis. Université de Strasbourg, 2016.

[108] Poul Martin Hansen et al. "Expanding the optical trapping range of gold nanoparticles". In: *Nano letters* 5.10 (2005), pp. 1937–1942.

[109] Karel Svoboda and Steven M Block. "Optical trapping of metallic Rayleigh particles". In: *Optics letters* 19.13 (1994), pp. 930–932.

[110] Martin Šiler, Lukáš Chvátal, and Pavel Zemánek. "Metallic nanoparticles in a standing wave: optical force and heating". In: *Journal of Quantitative Spectroscopy and Radiative Transfer* 126 (2013), pp. 84–90.

[111] Kalkbrenner Lindfors et al. "Detection and spectroscopy of gold nanoparticles using supercontinuum white light confocal microscopy". In: *Physical review letters* 93.3 (2004), p. 037401.

[112] Richard W Taylor and Vahid Sandoghdar. "Interferometric Scattering (iSCAT) Microscopy & Related Techniques". In: *arXiv preprint arXiv:1812.10765* (2018).

[113] Gavin Young et al. "Quantitative mass imaging of single biological macromolecules". In: *Science* 360.6387 (2018), pp. 423–427.

[114] Jaime Ortega-Arroyo and Philipp Kukura. "Interferometric scattering microscopy (iSCAT): new frontiers in ultrafast and ultrasensitive optical microscopy". In: *Physical Chemistry Chemical Physics* 14.45 (2012), pp. 15625–15636.

[115] Harry Nyquist. "Thermal agitation of electric charge in conductors". In: *Physical review* 32.1 (1928), p. 110.

[116] Lisa V Poulikakos et al. "Optical chirality flux as a useful far-field probe of chiral near fields". In: *ACS photonics* 3.9 (2016), pp. 1619–1625.

[117] Kevin M McPeak et al. "Complex chiral colloids and surfaces via high-index off-cut silicon". In: *Nano letters* 14.5 (2014), pp. 2934–2940.

[118] Lisa V Poulikakos. "Chiral Light-Matter Interactions in the Near and Far Field". PhD thesis. ETH Zurich, 2018.

[119] Carlos Bustamante, Ignacio Tinoco, and Marcos F Maestre. "Circular differential scattering can be an important part of the circular dichroism of macromolecules". In: *Proceedings of the National Academy of Sciences* 80.12 (1983), pp. 3568–3572.

[120] John David Jackson. *Classical electrodynamics*. 1999.

[121] Daniel M Lipkin. "Existence of a new conservation law in electromagnetic theory". In: *Journal of Mathematical Physics* 5.5 (1964), pp. 696–700.

[122] Yiqiao Tang and Adam E Cohen. "Optical chirality and its interaction with matter". In: *Physical review letters* 104.16 (2010), p. 163901.

[123] A Drezet and C Genet. *Reciprocity and optical chirality*. Pan Stanford Publishing, 2014.

[124] L.V. Poulikakos and D.J. Norris. "In preparation". In: ().

[125] Dennis H Goldstein. *Polarized light*. CRC press, 2017.

[126] Georgiy Tkachenko and Etienne Brasselet. "Optofluidic sorting of material chirality by chiral light". In: *Nature communications* 5.1 (2014), pp. 1–7.

[127] Yang Zhao et al. "Nanoscopic control and quantification of enantioselective optical forces". In: *Nature nanotechnology* 12.11 (2017), p. 1055.

[128] Assaf Ben-Moshe et al. "Chirality and chiroptical effects in inorganic nanocrystal systems with plasmon and exciton resonances". In: *Chemical Society Reviews* 42.16 (2013), pp. 7028–7041.

[129] Yang Zhao, Amr AE Saleh, and Jennifer A Dionne. "Enantioselective optical trapping of chiral nanoparticles with plasmonic tweezers". In: *Acs Photonics* 3.3 (2016), pp. 304–309.

[130] Robert P Cameron, Stephen M Barnett, and Alison M Yao. "Discriminatory optical force for chiral molecules". In: *New Journal of Physics* 16.1 (2014), p. 013020.

[131] Vincent Marichez et al. "Mechanical chiral resolution". In: *Soft matter* 15.23 (2019), pp. 4593–4608.

[132] Gambhir Ranjit et al. "Zeptonewton force sensing with nanospheres in an optical lattice". In: *Physical Review A* 93.5 (2016), p. 053801.

[133] Lulu Liu et al. "Subfemtonewton force spectroscopy at the thermal limit in liquids". In: *Physical review letters* 116.22 (2016), p. 228001.

[134] Philip Ball. "Focus: Detecting Femtonewton Forces in Water". In: *Physics* 9 (2016), p. 61.

[135] LD Landau and EM Lifshitz. *Statistical Physics Vol. 5, 482*. 1959.

[136] William H Press et al. *Numerical recipes 3rd edition: The art of scientific computing*. Cambridge university press, 2007.

[137] C Zensen et al. "Pushing nanoparticles with light—A femtonewton resolved measurement of optical scattering forces". In: *Apl Photonics* 1.2 (2016), p. 026102.

[138] Fabian Czerwinski, Andrew C Richardson, and Lene B Oddershede. "Quantifying noise in optical tweezers by allan variance". In: *Optics express* 17.15 (2009), pp. 13255–13269.

[139] Minghao Li et al. "Subfemtonewton force fields measured with ergodic Brownian ensembles". In: *Physical Review A* 100.6 (2019), p. 063816.

[140] David W Allan. "Statistics of atomic frequency standards". In: *Proceedings of the IEEE* 54.2 (1966), pp. 221–230.

[141] AN Cleland and ML Roukes. "Noise processes in nanomechanical resonators". In: *Journal of applied physics* 92.5 (2002), pp. 2758–2769.

[142] Yoshitsugu Oono and Marco Paniconi. "Steady state thermodynamics". In: *Progress of Theoretical Physics Supplement* 130 (1998), pp. 29–44.

[143] Takahiro Hatano and Shin-ichi Sasa. "Steady-state thermodynamics of Langevin systems". In: *Physical review letters* 86.16 (2001), p. 3463.

[144] T Speck and U Seifert. "Restoring a fluctuation-dissipation theorem in a nonequilibrium steady state". In: *EPL (Europhysics Letters)* 74.3 (2006), p. 391.

[145] GM Wang et al. "Experimental study of the fluctuation theorem in a nonequilibrium steady state". In: *Physical Review E* 71.4 (2005), p. 046142.

[146] EH Trepagnier et al. "Experimental test of Hatano and Sasa's nonequilibrium steady-state equality". In: *Proceedings of the National Academy of Sciences* 101.42 (2004), pp. 15038–15041.

[147] Jan Gieseler et al. "Dynamic relaxation of a levitated nanoparticle from a nonequilibrium steady state". In: *Nature nanotechnology* 9.5 (2014), p. 358.

[148] S. Ciliberto. "Experiments in Stochastic Thermodynamics: Short History and Perspectives". In: *Phys. Rev. X* 7 (2 2017), p. 021051. DOI: 10.1103/PhysRevX.7.021051. URL: https://link.aps.org/doi/10.1103/PhysRevX.7.021051.

[149] Christopher Jarzynski. "Nonequilibrium equality for free energy differences". In: *Physical Review Letters* 78.14 (1997), p. 2690.

[150] Juan MR Parrondo, Christian Van den Broeck, and Ryoichi Kawai. "Entropy production and the arrow of time". In: *New Journal of Physics* 11.7 (2009), p. 073008.

[151] Arnold Sommerfeld. *Thermodynamics and statistical mechanics*. Vol. 5. CUP Archive, 1964.

[152] C Jarzynskia. "Nonequilibrium work relations: foundations and applications". In: *The European Physical Journal B* 64.3-4 (2008), pp. 331–340.

[153] Giovanni Volpe et al. "Influence of noise on force measurements". In: *Physical review letters* 104.17 (2010), p. 170602.

[154] John Taylor. *Introduction to error analysis, the study of uncertainties in physical measurements*. 1997.

[155] Herbert B Callen and Theodore A Welton. "Irreversibility and generalized noise". In: *Physical Review* 83.1 (1951), p. 34.

[156] Jan Liphardt et al. "Equilibrium information from nonequilibrium measurements in an experimental test of Jarzynski's equality". In: *Science* 296.5574 (2002), pp. 1832–1835.

[157] Johan Ludwig William Valdemar Jensen et al. "Sur les fonctions convexes et les inégalités entre les valeurs moyennes". In: *Acta mathematica* 30 (1906), pp. 175–193.

[158] Christopher Jarzynski. "Rare events and the convergence of exponentially averaged work values". In: *Physical Review E* 73.4 (2006), p. 046105.

[159] Jeff Gore, Felix Ritort, and Carlos Bustamante. "Bias and error in estimates of equilibrium free-energy differences from nonequilibrium measurements". In: *Proceedings of the National Academy of Sciences* 100.22 (2003), pp. 12564–12569.

[160] Ignacio A. Martínez et al. "Engineered swift equilibration of a Brownian-particle". In: *Nature Phys.* 12 (2016), p. 843. DOI: 10.1038/nphys3758.

[161] A. Manoliu and C. Kittel. "Correlation in the Langevin theory of Brownian motion". In: *Am. J. Phys.* 47.8 (1979), pp. 678–680. DOI: 10.1119/1.11719.

[162] Anne Le Cunuder et al. "Fast equilibrium switch of a micro mechanical oscillator". In: *Appl. Phys. Lett.* 109.11 (2016), p. 113502. DOI: 10.1063/1.4962825.

[163] Vladimir Igorevich Arnol'd. *Mathematical methods of classical mechanics*. Vol. 60. Springer Science & Business Media, 2013.

[164] T. Schmiedl and U. Seifert. "Efficiency at maximum power: An analytically solvable model for stochastic heat engines". In: *Europhys. Lett.* 81.2 (2008), p. 20003. DOI: 10.1209/0295-5075/81/20003.

[165] Klaus Hasselmann. "Stochastic climate models part I. Theory". In: *tellus* 28.6 (1976), pp. 473–485.

[166] Donald E Kirk. *Optimal control theory: an introduction*. Courier Corporation, 2004.

[167] Karl Johan Åström and Richard M Murray. *Feedback systems: an introduction for scientists and engineers*. Princeton university press, 2010.

[168] ML Krasov, A Kiselev, and Grigorij I Makarenko. "Problems and Exercises in the Calculus of Variations". In: (1975).

[169] Ion Zaballa. *Teoría de Control*. 2019. URL: http://www.ehu.eus/izaballa/Control/control.htm.

[170] Erik Aurell, Carlos Mejía-Monasterio, and Paolo Muratore-Ginanneschi. "Boundary layers in stochastic thermodynamics". In: *Phys. Rev. E* 85 (2 2012), p. 020103. DOI: 10.1103/PhysRevE.85.020103. URL: https://link.aps.org/doi/10.1103/PhysRevE.85.020103.

[171] Carlos A. Plata et al. "Optimal work in a harmonic trap with bounded stiffness". In: *Phys. Rev. E* 99 (1 2019), p. 012140. DOI: 10.1103/PhysRevE.99.012140. URL: https://link.aps.org/doi/10.1103/PhysRevE.99.012140.

Yoseline ROSALES CABARA

Acting on a Brownian probe: from optical forces to optimal thermodynamic protocols

Résumé

Cette thèse explore le comportement d'une particule Brownienne piégée optiquement, à la fois comme sonde de forces optiques et de protocoles thermodynamiques. Un piège optique particulier est développé permettant la mesure en mode dynamique de forces de pression de radiation à l'échelle du femtonewton. Nous piégeons également des nanopyramides métalliques chirales dont la forme énantiomérique peut être reconnue in situ par une mesure polarimétrique couplée au piège. Ce travail ouvre la voie aux mesures de forces optiques chirales nanométrique à l'échelle nanométrique. Enfin, nous étudions les protocoles contrôlant la relaxation de la particule piégée entre deux états d'équilibre. Nous identifions théoriquement des protocoles optimisés du point de vue du temps de transfert entre 2 équilibres et de la dépense énergétique associée. Nous implémentons expérimentalement ces protocoles et démontrons leur caractère optimal au travers d'une relation d'exclusion temps-énergie universelle.

Mots clés : pièges optiques, forces faibles, chiralité, thermodynamique stochastique, contôle optimale

Résumé en anglais

This thesis explores the behaviour of an optically trapped Brownian particle, both as a probe of optical forces and thermodynamic protocols. A particular optical trap is developed allowing the dynamic mode measurement of radiation pressure forces at the femtonewton scale. Such configuration allows to stably trap chiral metallic nanopyramides whose enantiomeric form can be recognized in situ by a polarimetric measurement coupled to the trap. This work paves the way for measurements of chiral optical forces at the nanoscale. Finally, we study protocols controlling the relaxation of the trapped particle between two equilibrium states. We theoretically identify protocols optimized from the point of view of the transfer time between the two equilibria and the associated energetic cost. We experimentally implement these protocols and demonstrate their optimality through a universal time-energy exclusion relationship.

Keywords: optical traps, weak forces, chirality, stochastic thermodynamics, optimal control